Energy, Mines and Resources • *Yukon Geological Survey*

YUKON EXPLORATION & GEOLOGY

2012

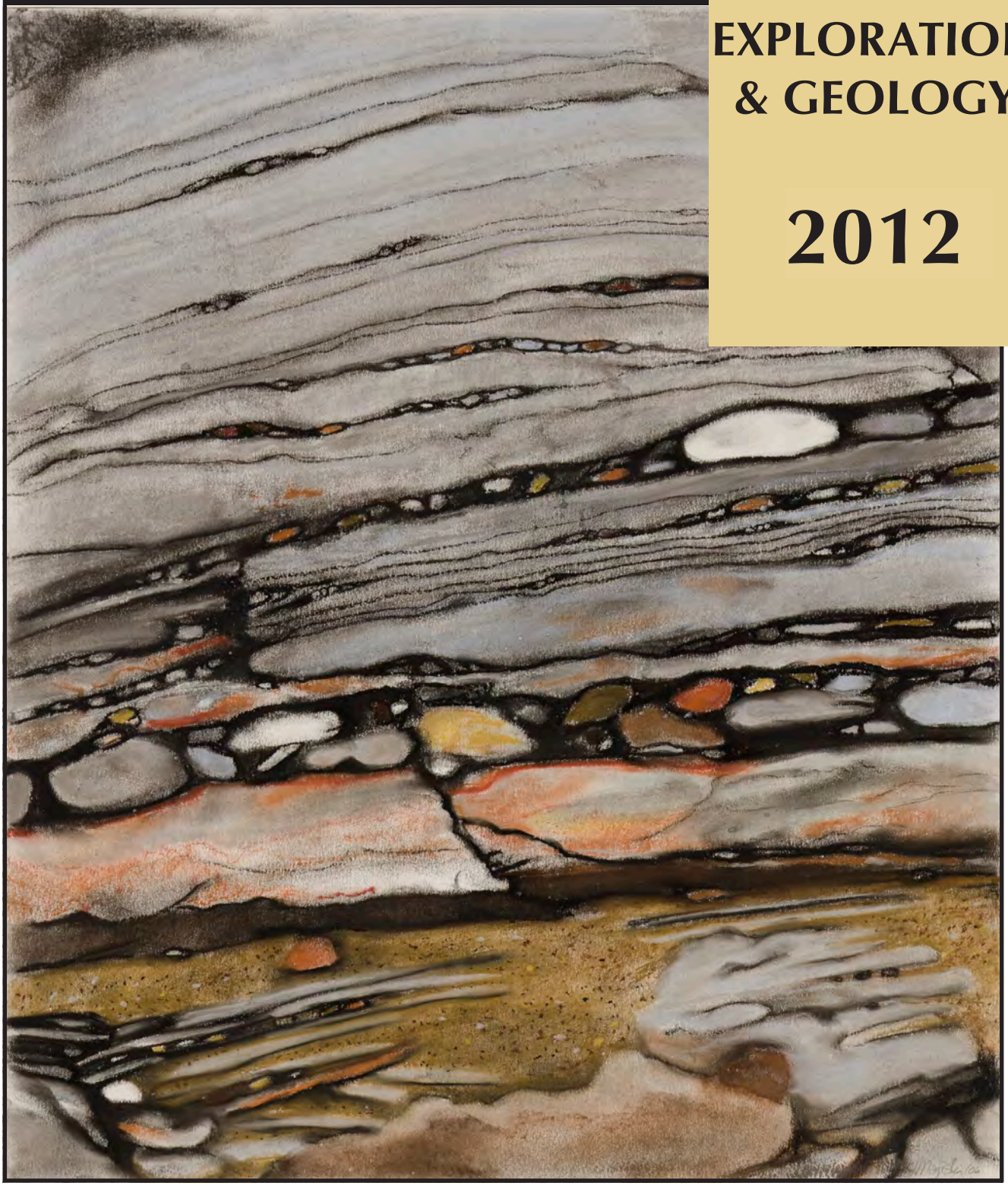

CELEBRATING 20 YEARS
1992-2012
YUKON GEOLOGICAL SURVEY

Yukon
Energy, Mines and Resources

YUKON EXPLORATION & GEOLOGY 2012

Edited by
K.E. MacFarlane, M.G. Nordling, and
P.J. Sack

Yukon Geological Survey
Energy, Mines and Resources
Government of Yukon

Published under the authority of the Department of Energy, Mines and Resources, Government of Yukon ***http://www.emr.gov.yk.ca.***

Printed in Whitehorse, Yukon, 2013.

Publié avec l'autorisation du Ministères de l'Énergie, des Mines et des Ressources du gouvernement du Yukon, ***http://www.emr.gov.yk.ca.***

Imprimé à Whitehorse (Yukon) en 2013.

ISSN 1718-8326 (on-line version)

This, and other Yukon Geological Survey publications, may be obtained from:
Geoscience Information and Sales
Yukon Geological Survey
102-300 Main Street
Box 2703 (K-102)
Whitehorse, Yukon, Canada Y1A 2C6

phone (867) 667-3201, fax (867) 667-3198, e-mail ***geosales@gov.yk.ca***

Visit the Yukon Geological Survey website at ***www.geology.gov.yk.ca.***

In referring to this publication, please use the following citation:
Yukon Exploration and Geology 2012. K.E. MacFarlane, M.G. Nordling, and P.J. Sack (eds.), 2013. Yukon Geological Survey, 178 p.

Papers from this document are available in colour on the Yukon Geological Survey website.

Front cover photograph: Copy of an original chalk pastel drawing by Joyce Majiski. The image was inspired by the geography and geology of the Firth River area, northwest Yukon. The piece was selected to commemorate the 20th anniversary of the Yukon Geological Survey.

PREFACE

Yukon Exploration and Geology (YEG) and the Yukon Exploration and Geology Overview continue to be the main publications of the Yukon Geological Survey (Energy, Mines and Resources, Government of Yukon). Individual YEG papers, with colour images, are available in digital format only and can be downloaded from our website. The YEG Overview is available in print and digital formats.

YEG 2012 contains up-to-date information on mining and mineral exploration activity, studies by industry, and results of recent geological field studies. Information in this volume comes from prospectors, exploration and government geologists, mining companies, and students who are willing to contribute to public geoscience for the benefit of the scientific community, general public, and mineral and petroleum industries of Yukon. Their efforts are appreciated.

I would like to thank my YEG co-editors Monica Nordling and Patrick Sack for not only producing great work, but also providing comic relief and laughter throughout this process. As always, appreciation is extended to Yukon Geological Survey staff who take the time to edit earlier versions of manuscripts; this year I thank Carolyn Relf, Lee Pigage, Maurice Colpron, Steve Israel, Tiffani Fraser, Charlie Roots, and Don Murphy.

We welcome any input or suggestions that you may have to improve future YEG publications. Please contact me at (867) 667-8519, or by e-mail at karen.macfarlane@gov.yk.ca.

Karen MacFarlane

IN MEMORIAM

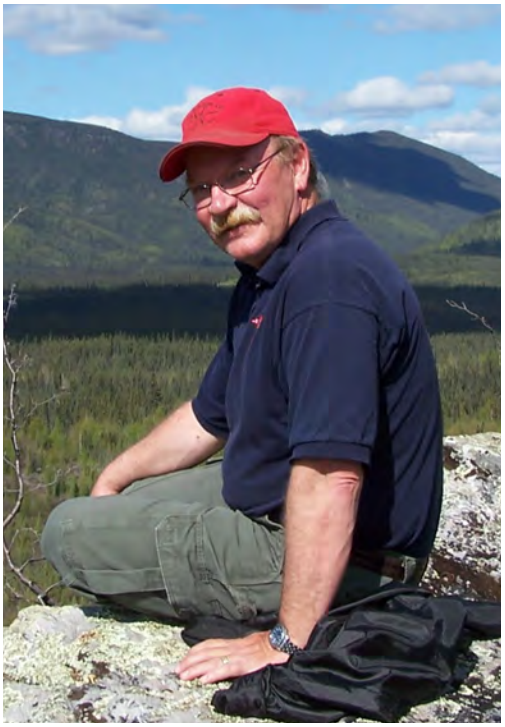

JOHN DAVID WITHAM

On December 14, 2011 the Yukon lost a mining industry legend and friend, Mr. John Witham.

John David Witham was born in Mohall, North Dakota on March 6, 1954. When he was 12 years of age, John and his parents Burt and Louise moved from North Dakota to the wilds of Fort McMurray Alberta, relocating a few years later to Smithers, B.C.

One of John's first real passions in life was flying, and soon after graduating from high school in 1972, he obtained his commercial helicopter licence.

In the early 1970s, at the height of the mineral exploration boom, John moved to Ross River where he met and married Cindy McClymont. Cindy and John raised two children in Ross River, Zackary and Kristen.

Over the course of the next couple of decades, John worked primarily in the Yukon's mining industry. As a testament to his love of flying and dedication to the industry, he proceeded to log almost 30,000 hours of fixed wing and helicopter time.

In 1990, John met Bernadette Etzel, and in 1994 they were married. John and Bernie were loving parents of Vashti and Rafe, and proud grandparents of grandson Drake and granddaughters Deliehla and Danisha.

Drake, who was the apple of grandpa John's eye was born during John's last term as President of the Yukon Chamber of Mines, during the 2006 Yukon GeoScience Forum.

In spite of the many hours he spent flying, John always made time to share with Bernie, the kids, and grandkids some of his many other passions, which included hockey and gardening. When it came to hockey, I am told he had two things in common with Gordie Howe, they both wore skates and they both knew what elbows were really for.

John was also a very accomplished musician, who was always ready and willing to bring life to a party. Whenever he was around, there was usually a guitar, a piano, a harmonica or on occasion even a set of drums somewhere close by. If there wasn't, John would find one or the other and the party was on. Rest assured, if there was music happening, John could be counted on to enthusiastically add one or more of his very accomplished vocal renditions. If he couldn't find a musical instrument nearby, John could always be counted on to entertain with one of his many fairly corny jokes!

Another well-known fact about John is that he was a master story teller, with an uncanny ability to make a story just a bit more interesting and intriguing every time he told it, which was usually quite often.

John's first venture into the private airline industry came as owner/operator of Witham Air Limited. Following that, he spent many years with Trans North Helicopters functioning as Base Pilot in Ross River and Smithers, B.C and subsequently Operations Manager and Marketing Manager in Whitehorse. John was the first CEO of the Kaska Minerals Corporation, he spent several terms as President of the Yukon Chamber of Mines and was also Secretary/Director of the Yukon Chamber

of Commerce. It was as President of the Yukon Chamber of Mines, where along with many other accomplishments, he was instrumental in establishing the Yukon Mine Training Association.

John's list of friends and acquaintances was far reaching, and to a person, they all remember him as a passionate supporter of Yukon's exploration and mining industry. Members of the chamber also remember John as a president that insisted on playing a role in the public consultation process, a trait that he insisted on in private life as well. While John was never shy about providing his own insightful, and always well researched, input on any topic, he was just as eager to consider the perspective of others.

Long-time friend and business associate Rob McIntyre described John as "a class act" and a man of great integrity. He recalls his most enduring memory of John being that while he was plying his profession as a superb helicopter pilot, he always had his ears open to the in-cabin conversations amongst his geologist and prospector clients. While flying, he would often ask meaningful questions and make helpful observations about geological formations, pointing out anomalies in vegetation and weathering patterns. John knew about landscapes, and was well aware of the changes that had taken place in those landscapes from year to year. But, whatever *'gems'* of knowledge John picked up from those many years of in-flight cabin conversations, one could be safe in the knowledge that he would never divulge secrets from company to company, or use that information for personal gain.

On May 8, 2012, the Hon. Brad Cathers, Yukon's Minister of Energy Mines and Resources paid tribute to John in the Yukon Legislative Assembly and quoted from one of John's many Letters to the Editor. "There are many of hundreds of families in the Yukon that depend upon mineral exploration in order to make their mortgage payments, feed themselves, and ensure a proper education and a bright future for their children."

Minister Cathers went on to say "John's letters were always well-written, well-reasoned and often very insightful. In the midst of sometimes very emotional debates, many of us appreciated his thoughtful and always fact-based contributions on our behalf."

In John's honour later that day, Minister Cathers tabled the following Motion in the House;

"Mr. Speaker I rise to give notice of the following motion:

THAT this House urges the Yukon government to continue to respect the fact that there are many hundreds of families in the Yukon that depend upon mineral exploration in order to make their mortgage payments, feed themselves, and ensure a proper education and a bright future for their children; and:

THAT this House urges the Yukon government to continue to support responsible mineral exploration and responsible mining as key elements of a strong diversified Yukon economy."

At the time of his passing, John was Whitehorse Base Manager for Vancouver Island based Peak Helicopters.

Dave Austin

A Long Time Friend

Whitehorse

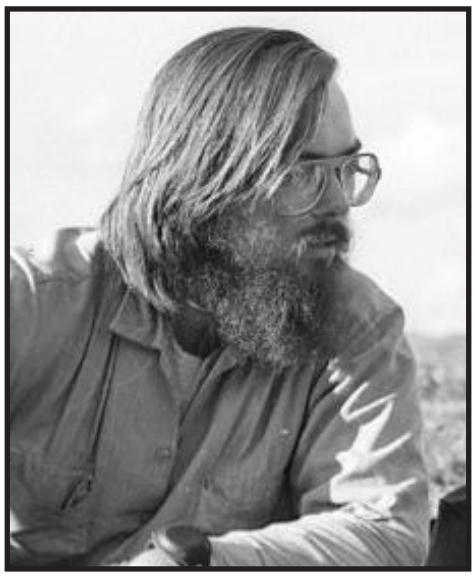

JIM MCFAULL

On April 14, 2012, the Yukon exploration community lost, well known geologist and prospector, Jim McFaull. Born in Regina in 1952, Jim was raised on the road with his family throughout Saskatchewan, Sault St. Marie, Winnipeg and Vancouver. His love of adventure and wild places led him into geology at the University of British Columbia, and he never looked back.

He began working with United Keno Hill Mines in 1970. During his time with UKHM, he was a key player on the mine site exploration team. He helped block out millions of ounces of silver in overlooked resources to supplement production from the Bellkeno, Silver King and Husky underground mines. He was happiest when digging into the archives in the “vault”, looking for overlooked or missed ore shoots. Jim stayed with Keno through thick and thin until the final shutdown in 1990, after which, he began working as an independent, consulting geologist and prospector. He went on to stake and explore ground in the Mayo and Dawson Mining Districts, with a particular passion searching for the source of the Klondike’s rich placer gold deposits.

Jim was a valiant defender of the mining industry, serving as director, vice president, and president of the Yukon Chamber of Mines and the Yukon Prospectors Association. He was a forceful and effective spokesman for the industry during the dark years of the 1990’s.

Jim had a wealth of stories and a truly magnetic personality. He loved the blues and fine Irish whiskey. A lifelong bachelor, he was a generous surrogate uncle to kids in a number of Yukon mining families. He was a true Yukoner in the tradition of the sourdoughs - always on the trail of the next discovery.

ROBERT WILLIAM STROSHEIN

1949-2012

It is with great sadness that we honour the passing of Robert W. Stroshein, a well known and respected geological engineer who spent most of his career in Yukon.

Robert was raised in Wadena, Saskatchewan, the third child in a farming family of six boys. In high school he joined the Wadena army cadets, eventually becoming commander of his cadet corps in grade 12. For three summers following high school, he was a lieutenant working as an instructor at the cadet summer camp held in Vernon, BC.

He graduated from U. of Saskatchewan in 1973 with a BSc in geological engineering. Hiring on with Hudson Bay Exploration and Development (HBED) in Manitoba right after school, he came to Yukon in 1974, and stayed with HBED until 1986. As the project geologist for the last HBED prospecting program using pack horses in Yukon, he witnessed the passing of an era.

Robert's wide field of experience included exploration, feasibility studies, mine development and mining, where he contributed both from a managerial and from a technical perspective. His most significant contributions in Yukon exploration and mining were made in the Whitehorse Copper Belt, in the Mount Nansen and MacPass districts (including the Mount Nansen Mine and the Tom deposit), as well as at Grew Creek, Ketza River and in Yukon Tanana terrane.

He worked for a number of companies in various capacities, as well as for the Yukon government. Since 2003, he worked mostly as a successful independent consultant and contractor through his consulting firm, Protore Geological Services. He served as a director and vice-president of the Yukon Chamber of Mines, and was also a member the Association of Professional Engineers of Yukon Territory, CIMM and SEG. He also served on a number of boards of directors of junior mining companies.

A family man, Robert was married to Breta Chippitt until her death in 2002. Her children became his. With Susan Rousseau, his present spouse, his family grew again. She and her children will miss the partner, father, and grandfather that he so lovingly became.

Robert enjoyed life in the moment and found contentment in the simple pleasures in life. His beautiful Marsh Lake home offered the perfect canvas for good meals with family and friends, walks with the dog, watching the seasons change with a cup of good coffee in hand, listening to his favourite music.

He will be remembered as a very kind man, whose quiet self-confidence, skill, humour, easy-going nature and love of life touched those fortunate enough to be around him. Many good memories and funny stories will hopefully soften the loss of one so dear to many.

YUKON GEOLOGICAL SURVEY

TABLE OF CONTENTS

Yukon Geological Survey staff: (front row, left to right) Sarah Laxton, Johann Slam, Lara Lewis, Olwyn Bruce, Maurice Colpron, Jeff Bond, Tiffani Fraser, and Kristen Kennedy; (back row, left to right) Karen MacFarlane, Carolyn Relf, Bailey Staffen, Laurie Fahr, Aubrey Sicotte, David Moynihan, Steve Israel, Charlie Roots and Robert Deklerk.
Missing from photo: Sue Roy, Derek Torgerson, Lee Pigage, Patrick Sack, Panya Lipovsky, and Don Murphy.

Cache Creek terrane, Stikinia, and overlap assemblages of eastern Whitehorse (NTS 105D) and western Teslin (NTS 105C) map areas

Luke Bickerton
Department of Earth Sciences, Simon Fraser University, Burnaby, BC

Maurice Colpron
Yukon Geological Survey, Whitehorse, YT

Dan Gibson
Department of Earth Sciences, Simon Fraser University, Burnaby, BC

Bickerton, L., Colpron, M., and Gibson, D., 2013. Cache Creek terrane, Stikinia, and overlap assemblages of eastern Whitehorse (NTS 105D) and western Teslin (NTS 105C) map areas. *In*: Yukon Exploration and Geology 2012, K.E. MacFarlane, M.G. Nordling, and P.J. Sack (eds.), Yukon Geological Survey, p. 1-17.

ABSTRACT

Bedrock mapping of parts of the Whitehorse and Teslin map areas in the summer of 2012 has improved upon existing knowledge of the local geology from previous 1:250 000 scale mapping in the respective map sheets. Our mapping characterizes the nature of the Cache Creek terrane in Yukon, including the identification of a previously unknown siliciclastic package, informally named the Michie formation, a gabbroic intrusive complex, and the Marsh Lake intrusive complex, in addition to more typical oceanic lithologies. This mapping helps refine the structural history of the area and define the relationships between Cache Creek terrane and rocks of Stikinia and Whitehorse trough. Two main phases of compressional deformation have been identified: 1) an initial phase of west-verging thrusting, emplacing Cache Creek terrane rocks above rocks of Stikinia and the Whitehorse trough along the Judas Mountain thrust, a northern equivalent to the Nahlin fault; and 2) a subsequent, second phase of thrusting which reshuffles Stikinia and Whitehorse trough rocks onto the Cache Creek terrane along the east-verging Mount Michie thrust. Three main styles of mineralization were observed, associated with either ultramafic bodies or Cretaceous intrusions in the region.

[1]*luke.bickerton@gmail.com*

INTRODUCTION

The Cache Creek terrane is one of the most enigmatic terranes in the Canadian Cordillera. It consists of an accretionary complex made up of a mixture of oceanic and arc volcanic rocks, pelagic sedimentary rocks, ultramafic bodies, and exotic limestone containing Early Permian Tethyan fauna (*e.g.*, Monger and Ross, 1971; Paterson and Harakal, 1974; Gabrielse, 1991; Struik *et al.*, 2001; Orchard *et al.*, 2001). The character of the Cache Creek terrane is known mainly from studies in British Columbia; less is known about the terrane in southern Yukon. To address this gap in knowledge bedrock mapping of an area roughly 680 km^2 in size, and straddling the Michie Creek (NTS 105D/9), Tagish (NTS 105D/8), and Squanga Lake (NTS 105C/5) map areas, was completed in the 2012 summer field season. The area is located approximately 75 km southeast of Whitehorse (Fig. 1) and can largely be accessed from the Alaska Highway along the eastern shore of Marsh Lake. The area lies at the northern termination of the Cache Creek terrane in the Cordillera. The most recent published bedrock maps for this area include parts of the 1:250 000-scale maps of the Whitehorse (NTS 105D; Wheeler, 1961) and Teslin areas (NTS 105C; Gordey and Stevens, 1994). This report summarizes preliminary observations about the nature of the Cache Creek terrane in Yukon, and its relationships with adjacent rocks of Stikinia and Whitehorse trough.

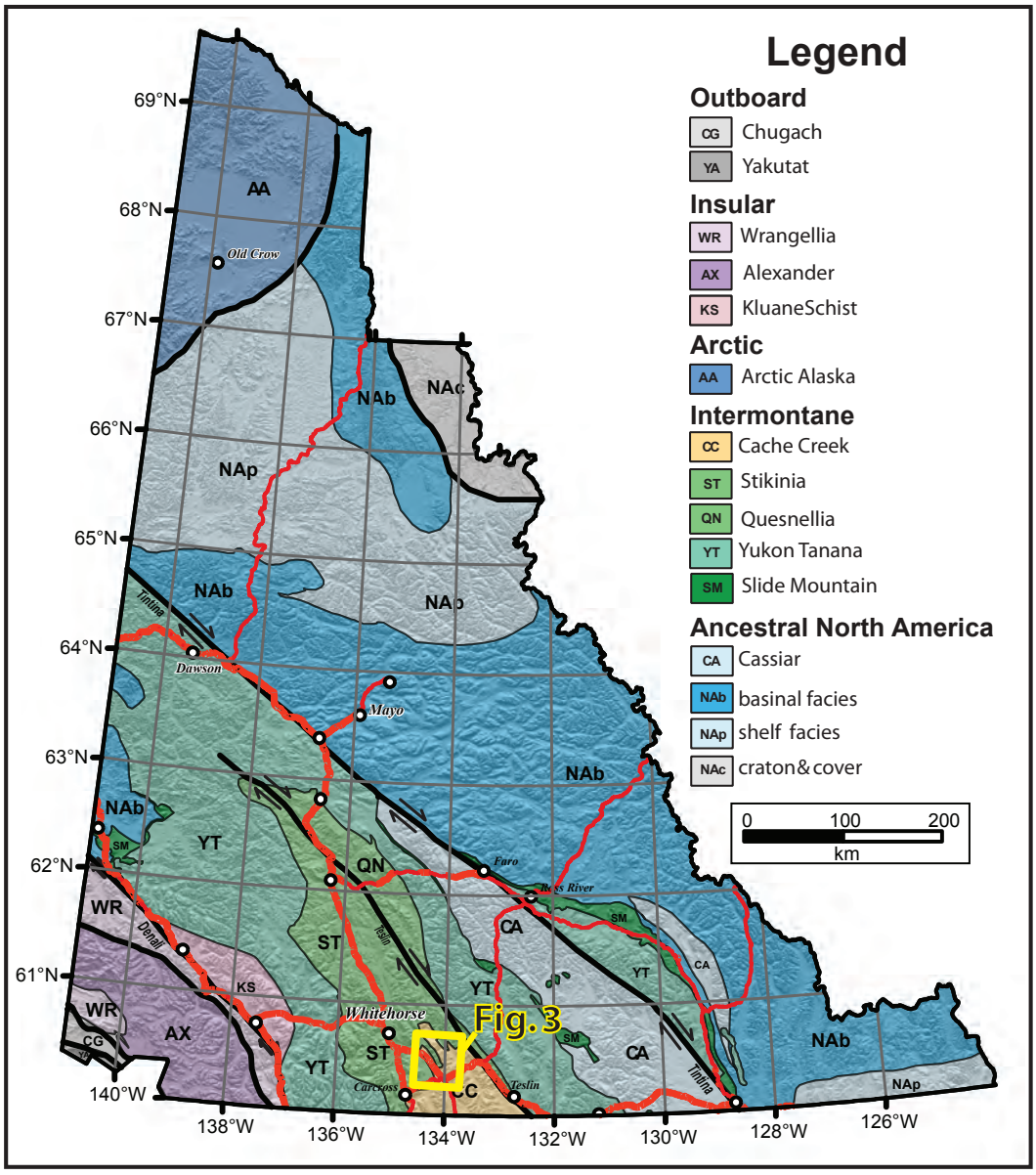

Figure 1. *Regional context of field area, shown on the Yukon terrane map (modified after Colpron and Nelson, 2011). The yellow box outlines the field area and bedrock geology map of Figure 3 centered over the northern termination of the Cache Creek terrane.*

REGIONAL SETTING

South-central Yukon contains multiple segments of terranes accreted to the Laurentian margin in the Cordilleran orogeny. In map-view, the late Paleozoic to early Mesozoic island arc terranes Stikina and Quesnellia, together with the affiliated peri-Laurentian Yukon-Tanana terrane, enclose at the northwestern end pelagic sedimentary rocks, oceanic seamount and ophiolite assemblages, as well as massive carbonate of the exotic Cache Creek terrane (Fig. 1). The thick, regionally extensive limestone of the Cache Creek terrane locally contains distinctive Early Permian fauna of Tethyan affinity (Monger and Ross, 1971). This fauna contrasts with the less exotic McCloud fauna found in limestone of Quesnellia and Stikinia. The presence of limestone with exotic fauna, coupled with local occurrences of Triassic to Lower Jurassic blueschist within mélange in the eastern part of Cache Creek terrane in British Columbia (Paterson and Harakal, 1974; Gabrielse, 1991; Struik *et al.*, 2001; Mihalynuk *et al.*, 2004), has been inferred to indicate a significant amount of Panthalassa lithosphere subducted beneath the Quesnellia-Stikinia arc from Permian to Jurassic time. The contributing factors of exotic Cache Creek *vs.* less exotic Stikinia/Quesnellia fauna, significant subduction beneath these arcs, and the final enclosing geometry, led to the oroclinal entrapment model of Mihalynuk *et al.* (1994).

Throughout the northern Canadian Cordillera, the Cache Creek terrane is typically bounded by major structures that separate it from the adjacent assemblages. In northern British Columbia, the Cache Creek terrane is bound on the east by the Thibert-Kutcho strike-slip fault system (*e.g.*, Gabrielse, 1985, 1991; Evenchick *et al.*, 2005; Gabrielse *et al.*, 2006). The Teslin fault is interpreted to be the northern extension of the Thibert fault in southern Yukon (*e.g.*, Gabrielse *et al.*, 2006; White *et al.*, 2012); it separates the combined Quesnellia and Yukon-Tanana terranes from the Cache Creek terrane. In northern British Columbia, the western boundary of the Cache Creek terrane is the Nahlin fault, which juxtaposes Cache Creek over strata of Whitehorse trough (Gabrielse, 1991, 1998; Mihalynuk, 1999; Mihalynuk *et al.*, 2004; Evenchick *et al.*, 2005). Hart and Radloff (1990) have traced the Nahlin fault into southern Yukon as far north as Carcross where it is cut by a Late Cretaceous pluton and apparently offset by the northeast-trending Crag Lake fault. The nature of the western boundary of the Cache Creek terrane north of the Crag Lake fault is less clear; it has been inferred to be a southwest-verging thrust fault (Gordey and Makepeace, 2001; Colpron, 2011). In northern British Columbia and south-central Yukon, Quesnellia, Cache Creek, Stikinia and Whitehorse trough are imbricated by a series of southwest-verging folds and thrust faults that are dissected by northwest-striking strike-slip faults (Mihalynuk *et al.*, 2004; English and Johnston, 2005; Colpron, 2011; White *et al.*, 2012).

In Yukon, rocks of Stikinia include the Upper Triassic Lewes River Group, which consists of a lower volcanic sequence, the Povoas formation, conformably overlain by a sedimentary sequence, the Aksala formation (Fig. 2; Wheeler, 1961; Tempelman-Kluit, 1984, 2009; Hart, 1997). The Aksala formation comprises a mixed clastic-carbonate assemblage, divisible into three dominant facies: calcareous lithic sandstone (Casca member); locally thick carbonate (Hancock member); and maroon clastic rocks (Mandanna member; Fig. 2; Tempelman-Kluit, 1984, 2009; Long, 2005). The Lewes River Group is unconformably overlain by sandstone, shale, and conglomerate of the Lower to Middle Jurassic Laberge Group of the Whitehorse trough (Wheeler, 1961; Hart, 1997; Lowey *et al.*, 2009). The Whitehorse trough is interpreted as a record of deposition in a forearc setting which evolved into a synorogenic, intermontane piggy-back basin by Middle Jurassic (Mihalynuk *et al.*, 1994, 2004; White *et al.*, 2012). The influx of chert detritus in Middle Jurassic strata of the Laberge Group and in the overlying Middle Jurassic to Lower Cretaceous Tantalus Formation provides evidence for imbrication of the Cache Creek terrane with Stikinia and Whitehorse trough by early Bajocian (*ca.* 171-175 Ma; Mihalynuk *et al.*, 2004; Fig. 2).

The Cache Creek terrane has been extensively studied throughout British Columbia, particularly in northern British Columbia where river incisions of the central Cordilleran plateau have exposed thick sections of Cache Creek terrane rocks. The rock types recognized include tectonized and serpentinized harzburgitic mantle rocks, mafic intrusive and volcanic rocks, hemipelagic chert and shale, and limestone (*e.g.*, Mihalynuk, 1999; Mihalynuk *et al.*, 2003; English *et al.*, 2010; Fig. 2). The age of mantle harzburgite is relatively unconstrained aside from an Early Triassic U-Pb zircon age of 245.4±0.8 Ma from an isolated peridotite body in the Teslin map area, east of the study area (Gordey *et al.*, 1998). In the Atlin area, intrusive rocks include pyroxene gabbro, hornblende diorite, and minor plagiogranite which occur both as lozenges in mélange and as undeformed bodies. The plagiogranite has been dated by U-Pb zircon at *ca.* 261.4±0.3 Ma (Mihalynuk *et al.*, 2003), a Late Permian age which correlates with

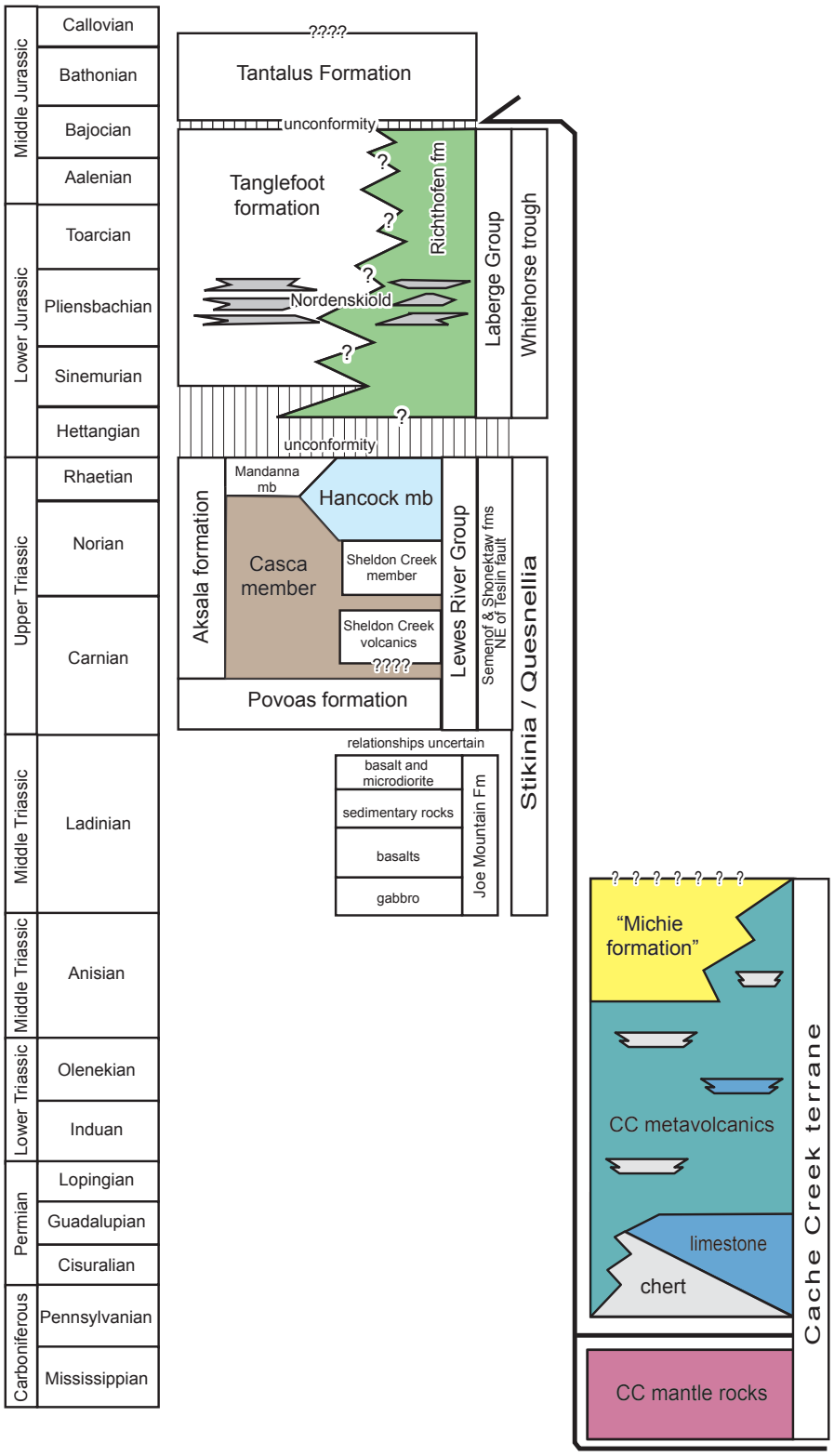

Figure 2. *Composite stratigraphic chart for the Cache Creek terrane, Stikinia, and Whitehorse trough in Yukon (modified after Hart, 1997; Lowey, 2004; White et al., 2012). Note the coloured units are those observed in the mapping area. It should also be noted that many of the stratigraphic units in use for Stikinia and Whitehorse trough are informal. Accordingly, unit terms are not capitalized for informal units here and in the text.*

a U-Pb zircon 263+1/-1.4 Ma age determination of a rhyodacite tuff deposited within the Cache Creek terrane in the French Range, Dease Lake area (Mihalynuk *et al.*, 1999). Mafic volcanic rocks belonging to the Nakina formation in British Columbia comprise fine-grained, massive black basaltic flows, and mint green basaltic tuff and flows (Mihalynuk, 1999). The Nakina formation is thought to have developed during the Late Mississippian to Permian, based on fossil collections from a section of limestone in the Nakina River area (Monger, 1975, 1977). Siliciclastic rocks included in the Cache Creek terrane are called the Kedahda Formation in British Columbia; this formation consists of chert, argillite and fine-grained wacke (*e.g.*, Mihalynuk, 1999) originally thought to range in age from Permian to Upper Triassic (Monger, 1975; Gabrielse, 1994), however, Lower Jurassic radiolarians were also collected from chert mapped as Kedahda Formation in northern British Columbia (Cordey *et al.*, 1991). Carbonate of the Cache Creek terrane is called the Horsefeed Formation in northern British Columbia and occurs as regionally extensive massive pale grey to tan limestone (*e.g.*, Mihalynuk, 1999). This formation hosts Tethyan fusulinid fauna of the family *Verbeekinidae* which range in age from Early Pennsylvanian to Late Permian (Monger, 1975). Southeast of the Nahlin fault, in the Dease Lake area, the King Salmon allochthon contains a sliver of Cache Creek terrane as a structural base, where it is spatially associated with Permo-Triassic bimodal volcanic and volcaniclastic rocks of the Kutcho Assemblage; these rocks are thought to represent a primitive oceanic arc sequence within the Cache Creek terrane and currently represent a partial basement to strata of the Whitehorse trough (Schiarizza, 2011).

The character of the Cache Creek terrane is well documented in British Columbia. Correlative lithologies in Yukon, however, have been less extensively studied. The purpose of this study is to improve our understanding of the Cache Creek terrane in Yukon through bedrock mapping of parts of the Michie Creek/Tagish/Squanga Lake area (Fig. 3).

GEOLOGY OF THE MICHIE CREEK/ TAGISH AREA

CACHE CREEK TERRANE

The Cache Creek terrane in the map area comprises mainly mafic to intermediate metavolcanic rocks with lesser chert and minor limestone throughout the stratigraphy, and extensive metavolcanic rocks grading into a newly recognized siliciclastic unit (informally the Michie formation; Fig 2). Also affiliated with the Cache Creek terrane are ultramafic rocks of variable character, which typically occur as faulted segments, and a mafic intrusive complex. Metamorphism in these rocks reaches predominantly greenschist facies, typically recognized within the extensively chloritized volcanic rocks.

METAVOLCANIC ROCKS

Metavolcanic rocks are the most widespread unit in the Cache Creek terrane in the study area. They are primarily found in the eastern and south-central part of the Michie Creek map area, as well as the eastern and north-central parts of the Tagish map area, near Jakes Corner (Fig. 3). Metavolcanic rocks in the area are mainly composed of plagioclase and clinopyroxene within a chloritic matrix. They locally show pillowed and hyaloclastic textures. The basaltic rocks are typically massive and extensively chloritic. These rocks range from dark grey, medium-grained to aphanitic basalt to light grey, fine-grained andesite. They are commonly thoroughly fractured and silicified, and locally contain amygdules filled with both calcite and silica. The flows exposed in the Marsh Lake and Judas Creek areas typically dip to the southeast. In the eastern part of the Michie Creek map area andesite and basalt are intercalated with green-grey volcaniclastic rocks containing a significant amount of sedimentary lithic clasts, particularly in proximity to the newly described Michie formation (see below).

Sedimentary rocks are locally intercalated with the volcanic rocks, becoming more common near the contact with the Michie formation. These include metre to decimetre-scale lenses of limestone and chert, as well as upwardly increasing amounts of volcaniclastic and siliciclastic rocks in the transition to the Michie formation (Fig. 2).

CHERT

Chert is one of the more distinctive lithologies of the Cache Creek terrane throughout the Cordillera, but is less extensive in the Yukon part of this terrane. Massive chert is locally exposed directly east of Marsh Lake in the north-central part of the Tagish map area and near Jakes Corner where it is intercalated with metavolcanic rocks (Fig. 3). Apart from the more massive occurrences, chert also appears as subordinate lenses within the metavolcanic rocks and as clasts in volcanic breccia of the Cache Creek terrane throughout the map area (Figs. 2 and 4a). Chert units also commonly crop out as ribbon-banded sections, grey-red-brown in colour, and are locally contorted by soft-sediment deformation (Fig. 4b). Chert beds are normally 5 to 10 cm thick with fine-grained argillite interbeds, but thinner bedding is seen in the ribbon-banded outcrops (2-5 cm).

LIMESTONE

In the study area, limestone occurs primarily as lenses within heavily to moderately chloritic basalt and only locally as thickly bedded, massive crystalline limestone to dolostone. Extensive exposures of thickly bedded white limestone, such as found southeast of the Crag Lake fault, do not occur in the study area.

MICHIE FORMATION (INFORMAL; NEW UNIT)

The Michie formation is a previously undocumented stratigraphic unit referring to clastic rocks which overlie mafic metavolcanic rocks in the eastern part of the map area, from east of Mount Michie, extending northwest to the area southwest of Fox Lake (Fig. 3). This formation is composed of a variety of lithologies: beige, coarse-grained sandstone to wacke; clast-supported pebble conglomerate; and dark grey siltstone; (Fig. 5a,b,c). Medium to coarse-grained sandstone to wacke of the Michie formation is typically in sharp contact with the siltstone (Fig. 5c). The sandstone is immature with sub-rounded to angular carbonate and volcanic-lithic clasts. Pebble conglomerate of the Michie formation is found east of Mount Michie, as well as southwest of Fox Lake (Fig. 3). The subrounded to angular clasts in the conglomerate include both mafic and felsic volcanic clasts, limestone, chert, and very fine-grained siltstone clasts (Fig. 5b). Locally, sequences of

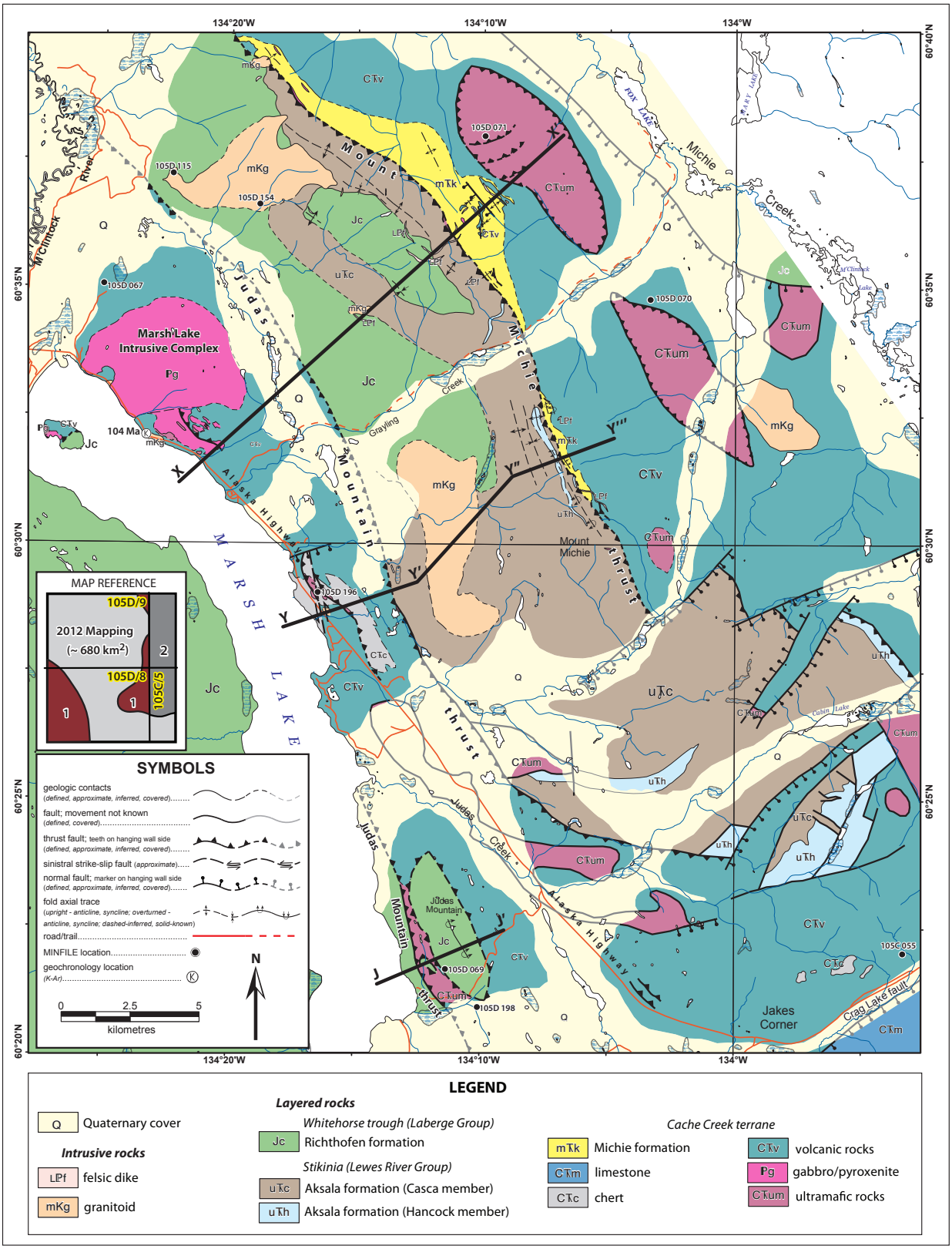

Figure 3. *Simplified bedrock geology map of the study area. Map reference inset shows parts of the map area compiled from 1) Wheeler (1961); and 2) Gordey and Stevens (1994); the author's detailed mapping of an area ~680 km², straddling the Michie Creek (105D/9), Tagish (105D/8), and Squanga Lake (105C/5) map areas is also indicated.*

conglomerate-sandstone-siltstone in conformable contact can be seen with minor normal grading in the sandstone-siltstone transition (Fig. 5c). Siltstone is commonly found coupled with sandstone beds but locally forms massive sections up to 250 m thick. The siltstone is carbonaceous, giving the bed surfaces an iridescent sheen, and is locally interbedded with buff-weathering limestone beds that are 10 to 15 cm in thickness. Southwest of Fox Lake (Fig. 3), a carbonate-rich debris flow unit occurs near an occurrence of limestone interbedded with siltstone. This unit locally includes a limestone olistolith approximately 60 m wide and 250 m long.

The Michie formation is apparently bound by the Mount Michie thrust to the west. The unit terminates to the northwest, east of the M'Clintock River, and to the southeast, near Mount Michie. Thickness estimations from cross sections indicate an apparent thickness of ~100 m where the unit is tapered east of Mount Michie, and a thickness of ~670 m in the area southwest of Fox Lake (Fig. 3).

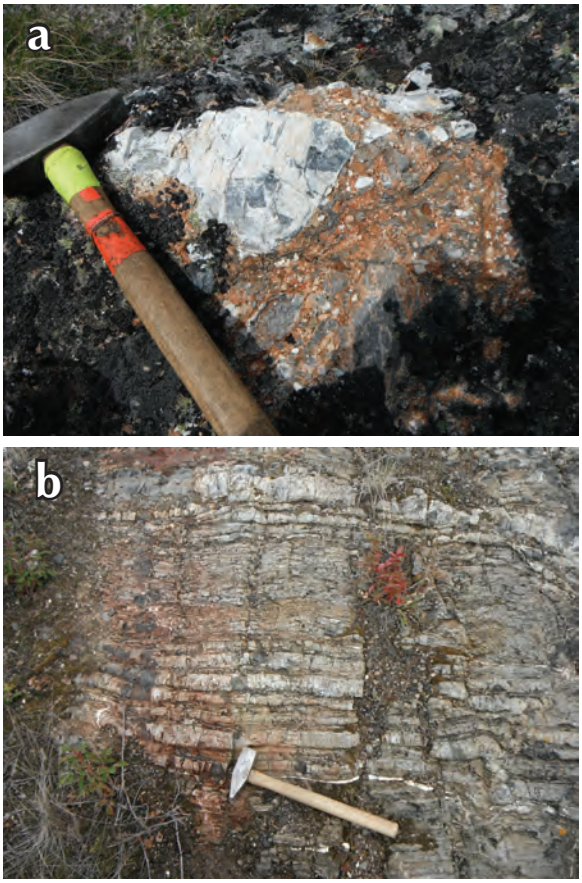

Figure 4. *Outcrop photos of Cache Creek terrane rocks; a) chert clasts within a volcaniclastic matrix, east of Mount Michie; and b) ribbon-banded chert in the Marsh Lake area.*

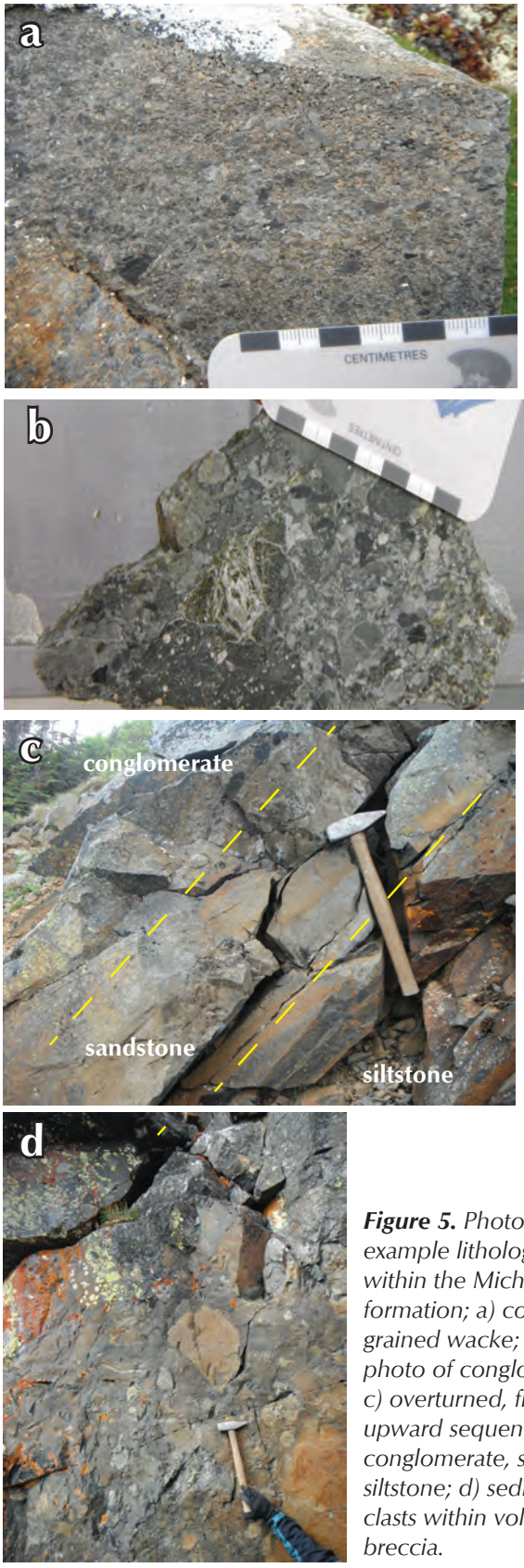

Figure 5. *Photos of example lithologies within the Michie formation; a) coarse-grained wacke; b) slab photo of conglomerate; c) overturned, fining-upward sequence of conglomerate, sandstone, siltstone; d) sedimentary clasts within volcanic breccia.*

ULTRAMAFIC ROCKS

Ultramafic rocks in the Cache Creek terrane are characterized by two main compositions. The ultramafic rocks exposed in the western part of the study area are typically pyroxenite, ranging to serpentinite when in faulted contact with volcanic rocks and chert, or with rocks of the Whitehorse trough in the Judas Mountain and Judas Creek area (Fig. 3). The ultramafic bodies in the eastern part of the map area have the composition of harzburgite to dunite and are typically larger exposures, the most extensive outcrop being ~14 km^2 found to the southwest of Fox Lake.

The typical western ultramafic rocks are exposed near fault contacts and are commonly altered to listwaenite (quartz-carbonate-fuschite). Serpentinite is also commonly found near these fault boundaries where it is locally brecciated (Fig. 6a). Pyroxenite in the western part of the map area is typically non-magnetic, medium grained and dominantly composed of clinopyroxene. These rocks show extensive chlorite and epidote alteration.

The large harzburgite-dunite bodies in the eastern part of the Michie Creek map area are coarse grained and contain abundant magnetite. Locally, harzburgite shows a subtle cumulate texture of olivine with interstitial orthopyroxene; elsewhere, these rocks are sections of rounded blocks in a sheared matrix of heavily altered ultramafic. Veins of antigorite and serpentinite occur throughout theses bodies and also in some areas that are intruded by pegmatite. Typically, olivine crystals are completely replaced by serpentine. The large ultramafic bodies are in fault contact with volcanic rocks of the Cache Creek terrane, but listwaenite alteration is not a prominent feature near these contacts.

MARSH LAKE INTRUSIVE COMPLEX

A gabbroic complex crops out extensively in the south-central part of the Michie Creek map area, near the north end of Marsh Lake. The complex lies between the M'Clintock River and Grayling Creek (Fig. 3), and intrudes exclusively mafic metavolcanic rocks of the Cache Creek terrane. These rocks have extensive chlorite alteration and, locally, are intensely foliated.

Compositions range from hornblende diorite to gabbro to pyroxenite (Fig. 6b). The diorite phases range from microdiorite to hornblende-porphyritic intrusive rocks. Olivine-porphyritic diabase crosscuts the diorite/gabbro throughout the intrusive complex. Plagioclase, clinopyroxene and less commonly olivine-bearing gabbroic intrusive rocks locally grade to clinopyroxene-dominant pyroxenite. The pyroxenite phases are similar in character to the larger bodies of pyroxenite elsewhere in the Cache Creek terrane.

STIKINIA

Only the upper part of Stikinia is exposed in the Michie Creek/Tagish map area comprising two members of the Aksala formation of the Lewes River Group, the Casca and Hancock members (Fig. 2), both of which only reach sub-greenschist facies. Stikinia rocks dominantly crop out along the ridge extending northwest from Mount Michie to east

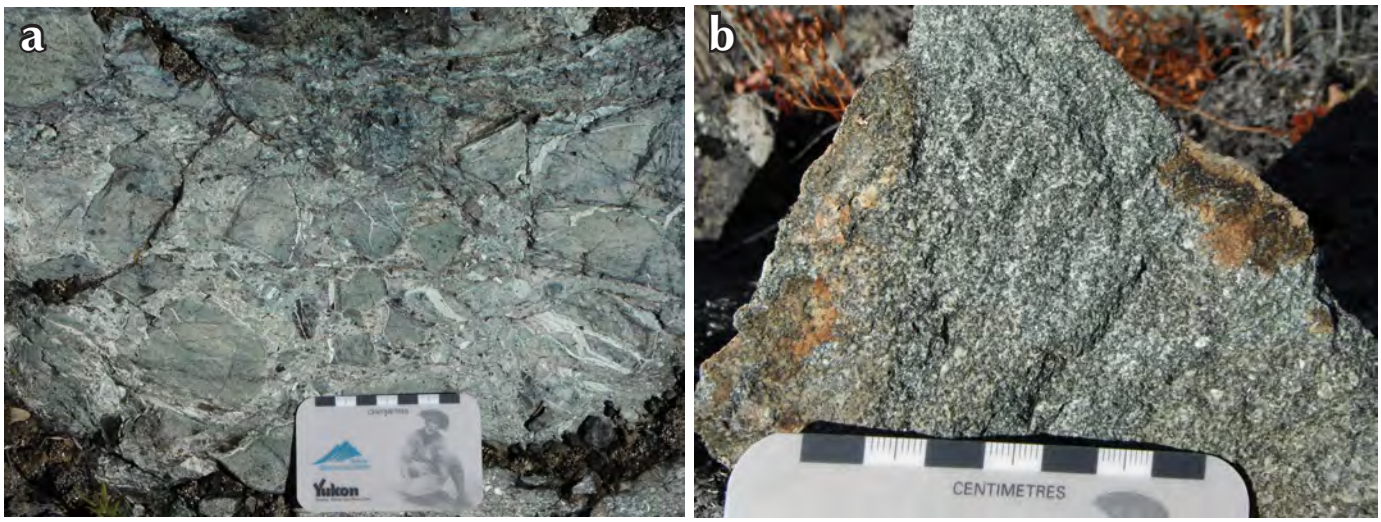

Figure 6. *Outcrop photos of Cache Creek terrane rocks; a) brecciated serpentinite found near Judas Mountain; and b) pyroxene gabbro of the Marsh Lake intrusive complex.*

of the M'Clintock River in the northern part of the Michie Creek map area (Fig. 3). The Aksala formation is ~1000 m thick at its thickest exposure; however, the complete stratigraphic thickness is unknown in the area.

CASCA MEMBER

The Casca member is composed of clastic sedimentary strata varying from coarse-grained, black-grey sandstone to fine-grained, thinly laminated, dark grey argillaceous siltstone. Siltstone units occur as thick, monotonous sections with grey and tan-coloured, very fine-grained sandstone interlaminations. The siltstone beds are commonly graded (Fig. 7a) and contain scour marks, flame structures, rip-up clasts, and locally, trace fossils (Fig. 7b); all indicate that the section is upright. The medium to coarse-grained quartz sandstone of the Casca member has relatively immature grains which are angular to subangular and dominantly poorly sorted. The sandstone is commonly calcareous and occurs as 10 to 20 cm-thick beds among the more dominant argillaceous siltstone.

HANCOCK MEMBER

Carbonate rocks of the Hancock member of the Aksala formation are dominantly found north of Jakes Corner (Fig. 3) as massive, crystalline, locally fossiliferous limestone. These rocks were recognized through the mapping of Gordey and Stevens (1994). Carbonate rocks similar to the Hancock member also appear as locally contiguous, coarsely crystalline limestone to limestone breccia interlayered with siliciclastic rocks at different stratigraphic levels within the Casca member. Limestone clasts within the brecciated sections of the carbonate vary in size from 5 mm to 20 cm and are dominantly subrounded to subangular.

WHITEHORSE TROUGH

Whitehorse trough, in the map area, is represented by the Richthofen formation of the regionally extensive Laberge Group. These rocks are dominantly sub-greenschist facies, and have similar characteristics to the siliciclastic rocks of the Casca member of Stikinia.

RICHTHOFEN FORMATION

The Richthofen formation in the map area comprises dominantly black siltstone and less common greenish-grey sandstone and thick matrix-supported polymictic conglomerate (Fig. 8a,b). The conglomerate within this formation locally reaches an apparent thickness of ~250 m. Rocks typical of the Richthofen formation are found on the Marsh Lake shoreline, to the west of Judas Mountain, and trending parallel to the Mount Michie ridgeline in the north-central part of the area (Fig. 3). The medium to coarse-grained sandstone typically forms beds 5 to 15 cm thick and is coupled with fine-grained green-brown mudstone. Sandstone composition varies from quartz-dominant to micaceous with a strong volcanic-lithic

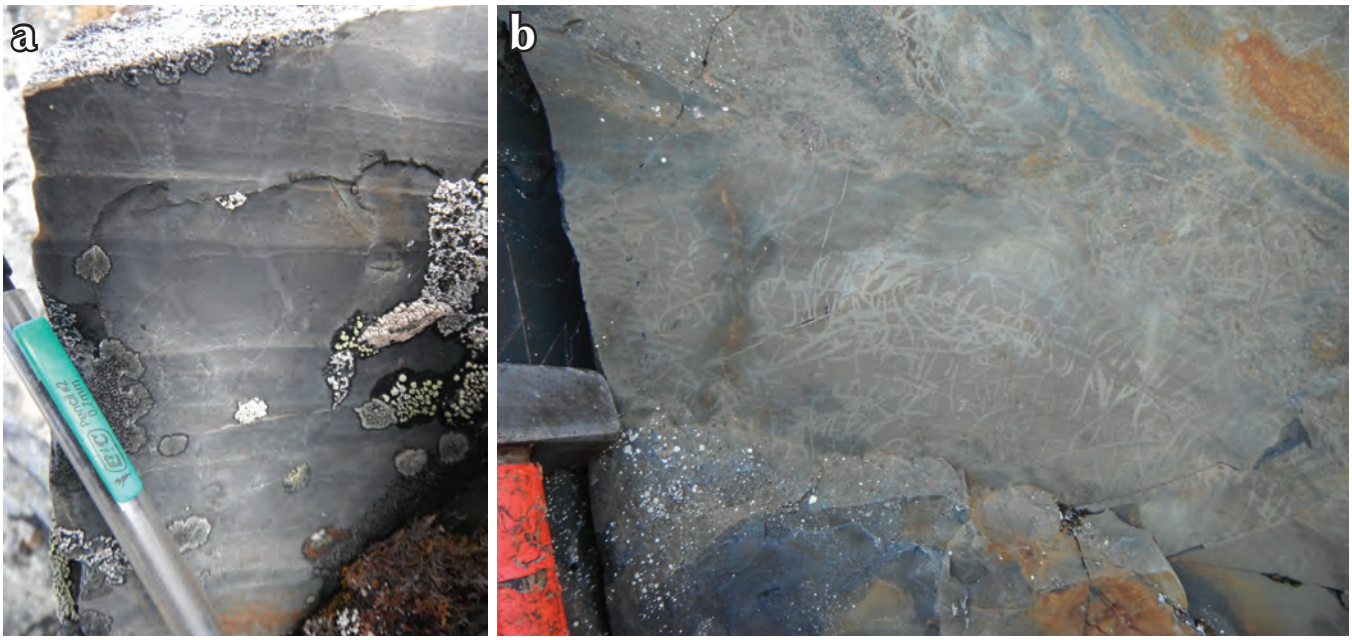

Figure 7. *Layered rocks of Stikinia; a) graded siltstone of the Casca member in the Aksala formation; and b) trace fossils (Chondrites) found within the Casca member of the Aksala formation.*

component. The black siltstone locally forms monotonous strata up to an estimated 1200 m in thickness, locally showing partial Bouma sequences, ranging from C-D to A-D (Fig. 8b). The Richthofen conglomerate is matrix-supported (Fig. 8a) and characterized by polymictic clasts, including grey, very fine-grained siltstone clasts, limestone, felsic plutonic, and less commonly, felsic volcanic clasts which vary from pebble to boulder-sized. The conglomerate rarely crops out as sections thicker than 200-250 m.

POST-ACCRETIONARY INTRUSIVE ROCKS

GRANITOIDS

A number of post-accretionary intrusive rocks outcrop throughout the area and range in composition from granodiorite to quartz monzonite to syenite. These rocks are thought to be mid-Cretaceous in age based on a single K-Ar date of 104±4 Ma (Hart, 1995) from a coarse-grained diorite stock cropping out near the eastern shore of Marsh Lake in the Michie Creek map area (Fig. 3). They are considered part of the Whitehorse plutonic suite (Gordey and Makepeace, 2001; Colpron, 2011).

The igneous body, ranging in composition from granodiorite to quartz monzonite, dominantly contains coarse-grained, equigranular alkali-feldspar and plagioclase, as well as minor quartz and biotite. The body is approximately 6 km wide, east to west, and 3.5 km long, north to south, and occurs in the northern part of the map area. It intrudes both Casca member and Laberge Group (Fig. 3). A small quartz monzonite pluton, located approximately 2 km north of the main granodiorite body, cuts the Mount Michie thrust which juxtaposes the Michie formation and sedimentary rocks of Stikinia and Whitehorse trough (Fig. 2).

A syenite intrusion of intermediate composition ranges from coarse-grained to pegmatitic, is alkali-feldspar dominant, and contains small (5 to 10 mm) books of coarse-grained biotite and muscovite that appear relatively unaltered by chlorite. The body occurs north of the Judas Creek area straddling the Michie Creek and Tagish map areas; it extends approximately 6.5 km north to south, and 1.5 km east to west. The pluton is poorly exposed and its contact is rarely exposed, but it does appear to only be in contact with sedimentary strata of the Laberge Group and the Casca member (Fig. 3); minor hornfels is observed at the contact.

RHYODACITE

Rhyodacitic dikes and plugs occur throughout the map area intruding all map units, making it the youngest unit observed in the map area. The rocks are typically medium to coarse-grained, spherulitic, quartz and feldspar-phyric rhyolite to dacite. The dikes show a well-developed flow-banded texture near their margins and typically have a massive texture and spherulitic feldspar closer to the cores.

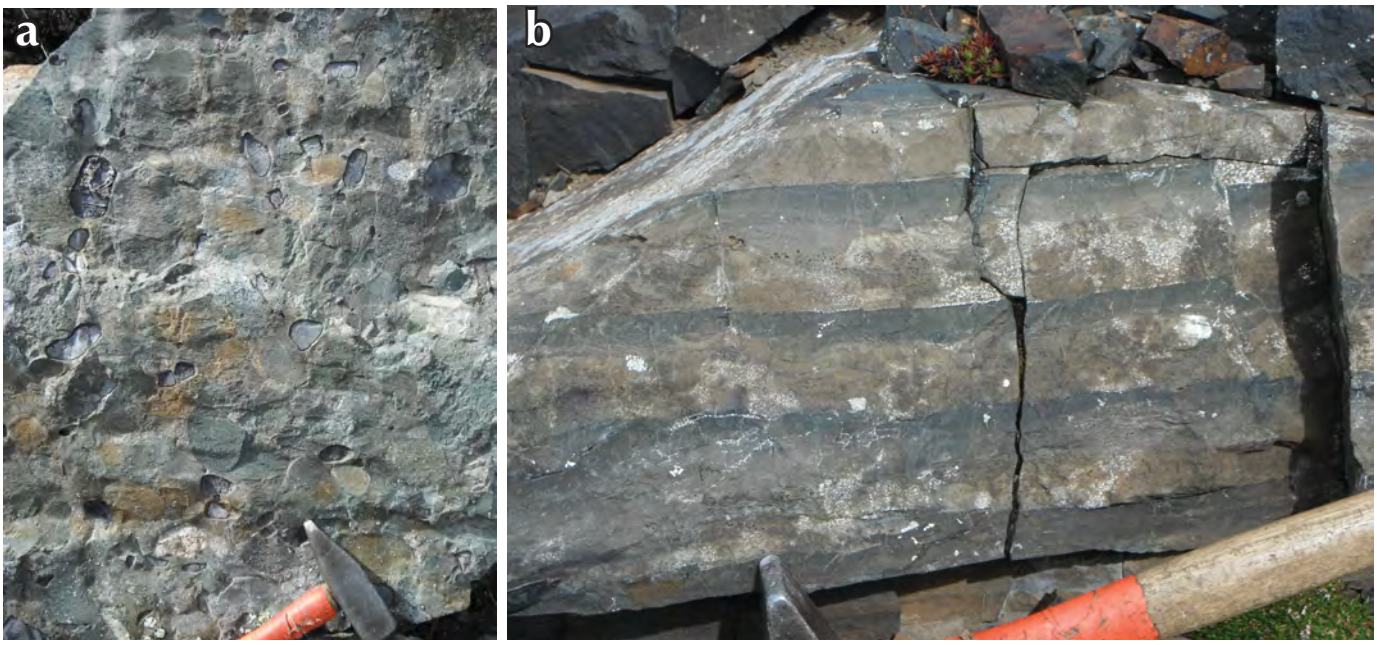

Figure 8. *Layered rocks of the Whitehorse trough; a) polymictic paraconglomerate of the Laberge Group; and b) fining-upwards bedding of sandstone and siltstone in the Laberge Group.*

These intrusive rocks occur as ring dikes, most commonly proximal to the peaks southwest of Fox Lake (Fig. 3). They are similar in character to those recognized in the Atsutla Range of northern British Columbia (Watson and Mathews, 1944; Mathews and Watson, 1953). Regionally, felsic to intermediate intrusive and volcanic rocks, which resemble those seen in the map area, include the early Tertiary Sifton Range volcanic rocks (*e.g.*, Miskovic and Francis, 2004), the Mount Skukum intrusive rocks (*e.g.,* Love *et al.*, 1998) and Eocene Sloko Group volcanic rocks (Souther, 1991; Mihalynuk, 1999) found in northwestern British Columbia and southern Yukon, west of the map area.

STRUCTURE

Due to poor to moderate exposures and the paucity of continuous outcrop, the main structural features in the area are inferred primarily through cleavage-bedding relationships and changes in foliation intensity at isolated outcrops. Offsets of lithology and the local presence of cataclasite and/or listwaenite are also used to determine the structural history of the area. The structural style of the Michie Creek and Tagish map areas is dominated by northwest-trending folds and north-northwest striking thrust faults (Fig. 3). In the southeast part of the map, north of Jakes Corner, Gordey and Stevens (1994) mapped a number of northeast-striking normal faults that delineate the contact between Stikinia/Whitehorse trough rocks to the north and Cache Creek terrane rocks to the south. These structures are similar in style and character to the Crag Lake fault mapped by Hart and Radloff (1990) southwest of the study area.

Two major thrust faults have been identified in the map area: 1) the Judas Mountain thrust, a north-northwest striking, steeply dipping thrust fault juxtaposing rocks of the Cache Creek terrane above sedimentary strata of the Whitehorse trough (Laberge Group), a structure almost entirely concealed at its leading edge by Marsh Lake; and 2) the Mount Michie thrust, a north-northwest striking, steeply west-dipping thrust fault which brings rocks of the Whitehorse trough (Laberge Group) and underlying Lewes River Group (Casca member) above the Cache Creek terrane in the centre of the map area (Fig. 9).

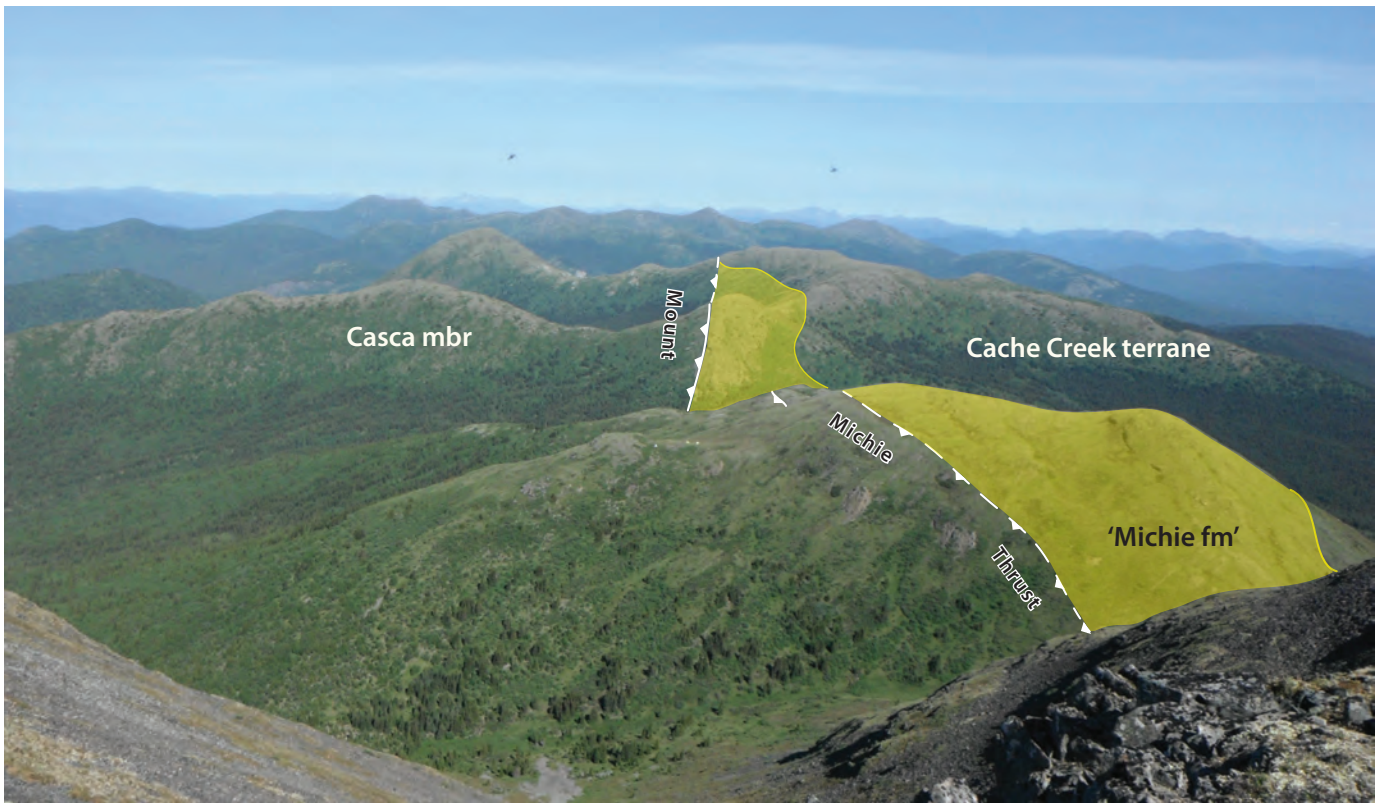

Figure 9. *View to north from Mount Michie; Cache Creek volcanic and ultramafic rocks on right (east), adjacent to exposures of Michie formation shaded in yellow; to the west are rocks of the Casca member (Aksala formation) found within the immediate hanging wall of the Mount Michie thrust, highlighted in white (teeth on hanging wall side).*

The Judas Mountain thrust marks the western structural boundary between the Cache Creek terrane and younger sedimentary strata. The thrust is exposed in the Judas Mountain area where rocks of the Whitehorse trough in the footwall show tight, overturned, southwest-verging folds. In the immediate hanging wall at this location, mafic and ultramafic rocks of the Cache Creek terrane are characterized by foliated listwaenite (e.g., Fig. 10a), serpentinite, and extensive hydrothermal veining. At Judas Mountain, directly east from the leading edge of the Judas Mountain thrust, rocks of the Laberge Group (Richthofen formation) are flanked by intensely foliated ultramafic rocks to the west and metavolcanic rocks of the Cache Creek terrane to the east (Fig. 3). This relationship is interpreted as a fenster of Laberge Group exposed in the footwall of the Judas Mountain thrust. We interpret that the fenster of Laberge Group was exposed through folding and erosion of the thrust contact (Fig. 11). This interpretation is based on the map pattern and structural observations such as steeply dipping foliation and extensive alteration of these rocks in the Judas Mountain area. A fault surface with similar characteristics as the Judas Mountain thrust is recognized to the east-northeast of the Alaska Highway as a northwest striking, steeply dipping structure juxtaposing Cache Creek terrane rocks to the west and sedimentary strata of Stikinia and Whitehorse trough to the east. This surface has little exposure, but is interpreted to be an eastern occurrence of the folded Judas Mountain thrust (Fig. 3). Folding of the Judas Mountain thrust is interpreted to result from a second phase of compression which led to the development of the Mount Michie thrust.

The Mount Michie thrust (Figs. 3 and 9) is characterized by intense foliation development (e.g., Fig. 10a), tight to isoclinal, northeast-verging folds in the immediate hanging wall (Fig. 10b), and the local occurrence of listwaenite and hydrothermally brecciated rocks in the immediate footwall of the boundary between the Cache Creek terrane to the east and Casca member rocks to the west (Fig. 10c). Open folds of sedimentary strata of the Casca member and Laberge Group that are typical in the central part of the

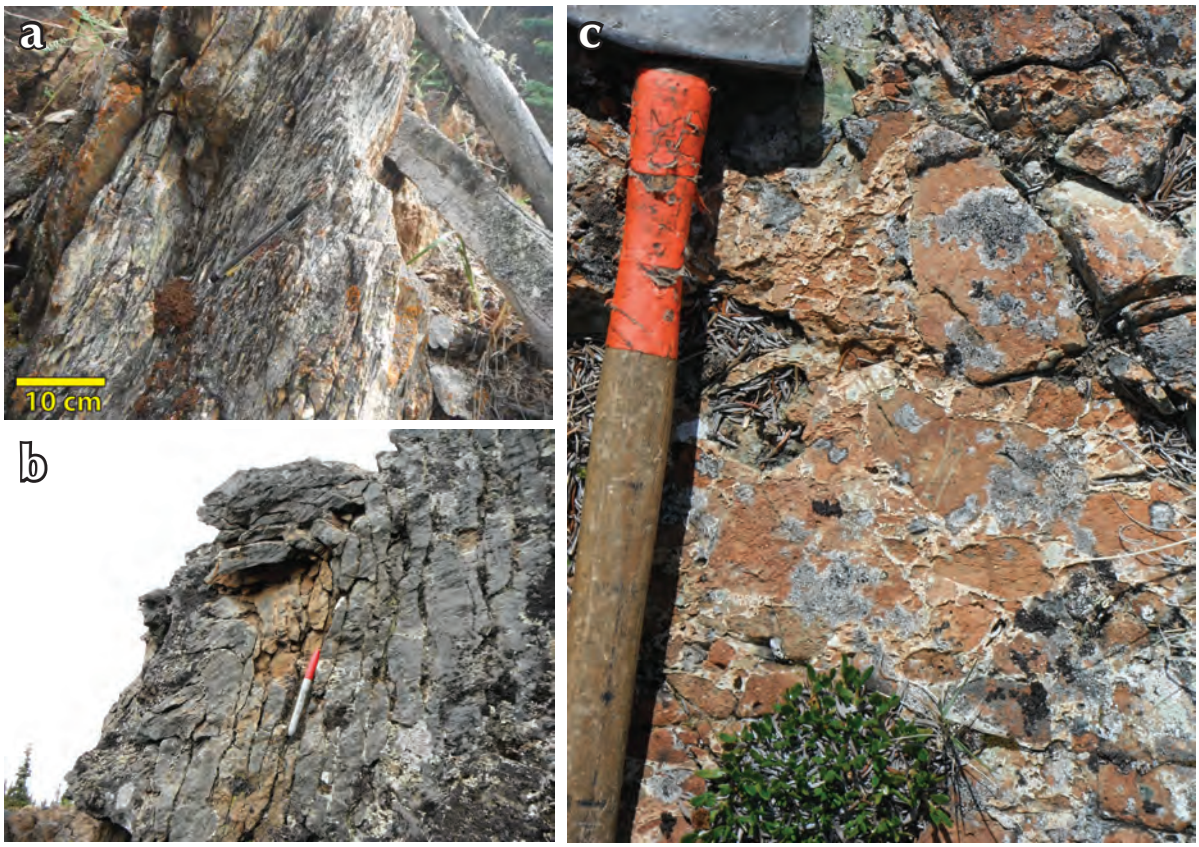

Figure 10. *Outcrop photos of structural features in the field; a) strongly foliated listwaenite of the Cache Creek terrane near a fault contact on Judas Mountain; b) tight northeast-verging chert and argillite of the Cache Creek terrane, Judas Creek area; and c) hydrothermally brecciated volcanic and volcaniclastic rocks of the Cache Creek terrane adjacent to the Mount Michie thrust.*

map area become progressively tight and overturned to the northeast near the Mount Michie thrust (Fig. 11). The hinge lines for these folds typically have a trend paralleling the strike of the Mount Michie thrust.

In summary, the structural evolution of the Michie Creek/Tagish area first involves a phase of southwest-verging folds and thrusts which emplaced rocks of the Cache Creek terrane over Stikinia and Whitehorse trough. This phase is represented by the Judas Mountain thrust, marking the westernmost extent of the Cache Creek terrane in the map area, and a probable northern equivalent of the Nahlin fault recognized in northern British Columbia and southern Yukon (Hart and Radloff, 1990; Mihalynuk, 1999). This phase may also correlate to the thrust faults which juxtapose the harzburgite/dunite bodies structurally above volcanic rocks within the Cache Creek terrane (Figs. 2 and 3). These bodies are interpreted as panels of ultramafic rocks which are thrust from deeper levels of the Cache Creek oceanic crust into contact with the relatively shallow level volcanic rocks.

The Mount Michie thrust is interpreted to be part of a 2nd compressional phase which brought rocks that were formerly in the footwall of the 1st phase Judas Mountain thrust (Stikinia and Whitehorse trough) over its hanging wall rocks (Cache Creek terrane). The second phase of compression also resulted in northeast-verging folds, including the folding of the Judas Mountain thrust, exposing a fenster of Laberge Group rocks (Figs. 3 and 11). A series of late, northeast-striking normal faults locally disrupts this sequence.

MINERAL OCCURRENCES

Three distinct styles of mineralization have been documented in the Michie Creek and parts of Tagish map area. Polymetallic Au-Cu-Ag veins and alteration zones occur in faulted, brecciated, and silicified metavolcanic rocks of the Cache Creek terrane (Yukon MINFILE 105C 055; 105D 067). This type of mineralization has the greatest potential near faults where ultramafic rocks become completely altered (e.g., listwaenite-associated Au-Cu-Ag; Yukon MINFILE 105D 069; 105D 196; 105D 198). Similar to quartz-carbonate lode gold occurrences in northern British Columbia (Ash and Arksey, 1990), polymetallic Au-Cu-Ag veins are found in the southern and the northeastern parts of the map area, trending northwest along the strike of the Mount Michie thrust, where rocks of the Cache Creek terrane are in contact with Stikinia and Whitehorse trough (e.g., Fig. 10a).

Mineralization spatially associated with the Cretaceous granodiorite pluton occurs at two locations in the northern part of the map area (Fig. 3). At one of these localities, lenses of galena with zones of disseminated pyrite and sphalerite are reported (Yukon MINFILE 105D 115). The other occurrence consists of visible gold-bearing veins (Yukon MINFILE 105D 154).

The third type of mineralization recognized in the region consists of base metals in large ultramafic bodies found in the eastern part of the map area. These bodies contain known occurrences of chromite (Yukon MINFILE 105D 070; 105D 071) and the mineralogy and locally unaltered character of the massive ultramafic rocks are prospective

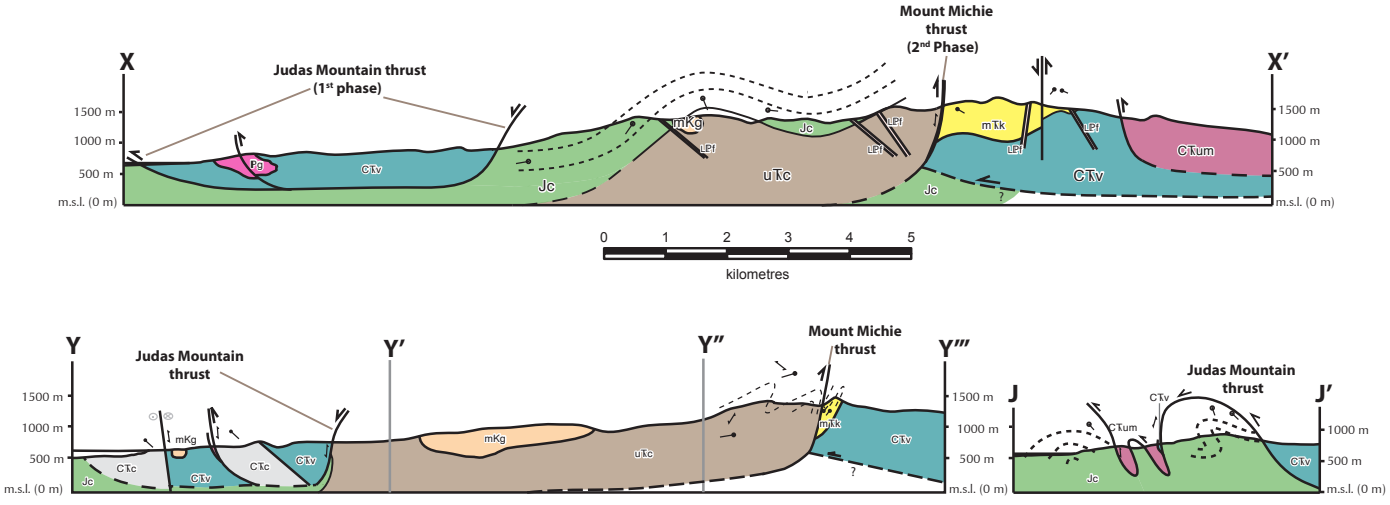

Figure 11. *Cross sections for section lines shown in Figure 3; the same legend applies in this figure as in Figure 3; no vertical exaggeration.*

for nickel-iron alloys (awaruite) and platinum group elements; to date, nearby stream sediment geochemistry has indicated no trace of platinum (Yukon MINFILE 105D 070).

DISCUSSION

Detailed mapping in the Michie Creek and parts of Tagish map area refines and partially redefines the known bedrock geology. One significant new contribution from our mapping is the identification of a previously unrecognized siliciclastic unit, informally defined as the Michie formation, which is stratigraphically intercalated with volcanic and volcaniclastic rocks of the Cache Creek terrane. The Michie formation is a prominent unit within the footwall of the Mount Michie thrust. Preliminary detrital zircon work from this study (not presented here) has so far returned a uniform Early to Middle Triassic age suggesting a source similar to the Kutcho assemblage of northern British Columbia which contains latest Permian-earliest Triassic igneous rocks (Childe and Thompson, 1997; Schiarizza, 2011).

Secondly, we have documented a previously unrecognized mafic igneous intrusive complex emplaced into the Cache Creek terrane at the northern end of Marsh Lake (Fig. 3). The range in composition of this complex, from pyroxenite to diorite with crosscutting diabase, suggests it may have been derived from partial melting of a mantle source, leaving residual rocks with a composition similar to the other ultramafic rocks described in the field area. The harzburgite-dunite ultramafic rocks are inferred to represent the deeper levels of a Cache Creek terrane oceanic assemblage, whereas the igneous complex most likely represents intrusion into the shallow level volcanic rocks, but both may be derived from a similar magma source. Igneous complexes of this character are unusual in the Cache Creek terrane, but one similar occurrence is that of the gabbro-clinopyroxenite Rubyrock igneous complex in central British Columbia, which is interpreted to be part of an ophiolite suite that is upper Paleozoic to Triassic in age (Struik *et al.*, 1998, 2001; MacIntyre and Schiarizza, 1999).

Thirdly, our data suggest a new structural geometry and evolution that differs somewhat from what has been interpreted in northern British Columbia. We have documented two phases of thrust faulting with different kinematics. The first phase of major faulting is interpreted to have thrust rocks of the Cache Creek terrane southwestward over rocks of the Whitehorse trough. The leading thrust of this phase of faulting, the Judas Mountain thrust, has most of its trace covered by Marsh Lake, but is exposed directly west of Judas Mountain in the southern part of the map area and can be recognized on the island at the northern end of Marsh Lake (Fig. 3). A subsequent phase of compression folded the aforementioned thrust contact so that it appears as multiply repeating, steeply-dipping fault contacts (Fig. 11). The main structure associated with this second phase of deformation is the north-northwest-striking, east-verging Mount Michie thrust fault, which places rocks of the Whitehorse trough and Stikinia above those of the Cache Creek terrane (Figs. 9 and 11).

Regionally, the 1st phase Judas Mountain thrust is correlated to the Nahlin fault of northern British Columbia and southernmost Yukon (Hart and Radloff, 1990; Gabrielse, 1991, 1998; Mihalynuk, 1999; Mihalynuk *et al.*, 2004; Evenchick *et al.*, 2005). Faults of similar trend and vergence are also found throughout the Whitehorse trough north of the map area, including the Coghlan, Chain, and Hoochekoo faults (Colpron, 2011; White *et al.*, 2012). Structural features similar in character to the 2nd phase Mount Michie thrust are recorded in the Bowser Basin to the south where rocks which are similar to those of the Whitehorse trough (English and Johnston, 2005) were folded and thrust eastward as early as Oxfordian to Albian time (Skeena fold belt; Evenchick, 1991). The Mount Michie thrust, therefore, most likely developed following the accretionary emplacement of the Cache Creek terrane above strata of Stikinia and the Whitehorse trough, and possibly correlates to the structural features of the Skeena fold belt.

The newly described Michie formation, along with the reinterpreted structural history and presence of a mafic intrusive complex indicate that the northern termination of the Cache Creek terrane in south-central Yukon is more complex than what has been described in previous mapping (*e.g.*, Wheeler, 1961). Future work will attempt to reconcile these complexities within the tectonic framework of the northern Cordillera, and examine the implications they have on previous tectonic models and regional mineral potential.

ACKNOWLEDGEMENTS

Funding for this project was provided by the Yukon Geological Survey (YGS), Northern Scientific Training Program (NSTP) and by National Science and Engineering

Research Council (NSERC) grants to H.D. Gibson and M. Colpron. Thanks to Cam Dorsey and Jaap Verbaas for assistance in the field, Don Murphy for a constructive review and for the support of staff at the YGS and Simon Fraser University.

REFERENCES

Ash, C.H. and Arksey, R.L., 1990. The Atlin ultramafic allochthon: ophiolitic basement within the Cache Creek terrane; tectonic and metallogenic significance (104N/12). BCGS Geological Fieldwork 1989, p. 365-374.

Childe, F. and Thompson, J.F.H., 1997. Geological setting, U-Pb geochronology, and radiogenic characteristics of the Permo-Triassic Kutcho Assemblage, north-central British Columbia. Canadian Journal of Earth Sciences, vol. 34, p. 1310-1324.

Colpron, M., 2011. Geological compilation of Whitehorse trough - Whitehorse (105D), Lake Laberge (105E), and part of Carmacks (115I), Glenlyon (105L), Aishihik Lake (115H), Quiet Lake (105F) and Teslin (105C). Yukon Geological Survey, Geoscience Map 2011-1, 1:250 000.

Colpron, M. and Nelson, J.L., 2011. A Digital Atlas of Terranes for the Northern Cordillera. Accessed online from Yukon Geological Survey (www.geology.gov.yk.ca), April 2012, and British Columbia Geological Survey, BC GeoFile 2011-11.

Cordey, F., Gordey, S.P., and Orchard, M.J., 1991. New biostratigraphic data from the northern Cache Creek terrane, Teslin map area, southern Yukon. *In:* Current Research part E, Geological Survey of Canada, p. 67-76.

English, J.M. and Johnston, S.T., 2005. Collisional orogenesis in the northern Canadian Cordillera: implications for Cordilleran crustal structure, ophiolite emplacement, continental growth, and the terrane hypothesis. Earth and Planetary Science Letters, vol. 232, no. 3, p. 333–344.

English, J.M., Mihalynuk, M.G., and Johnston, S.T., 2010. Geochemistry of the northern Cache Creek terrane and implications for accretionary processes in the Canadian Cordillera. Canadian Journal of Earth Sciences, vol. 47, p. 13-34.

Evenchick, C.A., 1991. Geometry, evolution, and tectonic framework of the Skeena fold belt, north central British Columbia. Tectonics, vol. 10, p. 527–546.

Evenchick, C.A., Gabrielse, H., and Snyder, D., 2005. Crustal structure and lithology of the northern Canadian Cordillera: alternative interpretations of SNORCLE seismic reflection lines 2a and 2b. Canadian Journal of Earth Sciences, vol. 42, p. 1149-1161.

Gabrielse, H., 1985. Major dextral transcurrent displacements along the Northern Rocky Mountain Trench and related lineaments in north-central British Columbia. Geological Society of America Bulletin, vol. 96, p. 1-14.

Gabrielse, H., 1991. Late Paleozoic and Mesozoic terrane interaction in north-central British Columbia. Canadian Journal of Earth Sciences, vol. 28, p. 947-957.

Gabrielse, H., 1994. Geology of Dease Lake (104J/E) and Cry Lake (104I) map areas, north central British Columbia. Geological Survey of Canada, Open File 2779.

Gabrielse, H., 1998. Geology of Dease Lake (104J) and Cry Lake (104I) map areas, north-central British Columbia. Geological Survey of Canada, Bulletin 504.

Gabrielse, H., Murphy, D.C. and Mortensen, J.K., 2006. Cretaceous and Cenozoic dextral orogen-parallel displacements, magmatism and paleogeography, north-central Canadian Cordillera. *In:* Paleogeography of the North American Cordillera: Evidence For and Against Large-Scale Displacements, J.W. Haggart, J.W.H. Monger and R.J. Enkin (eds.), Geological Association of Canada, Special Paper 46, p. 255-276.

Gordey, S.P. and Makepeace, A.J., 2001. Bedrock geology, Yukon Territory. Geological Survey of Canada, Open File 3754, 1:1 000 000. *also: Yukon Geological Survey, Open File 2001-1*.

Gordey, S.P., McNicoll, V.J., and Mortenson, J.K., 1998. New U-Pb ages from the Teslin area, southern Yukon, and their bearing on terrane evolution in the northern Cordillera. *In:* Radiogenic age and isotopic studies. Report 11, Geological Survey of Canada, Current Research no 1998-F, p. 129-148.

Gordey, S.P. and Stevens, R.A., 1994. Geology, Teslin, Yukon Territory. Geological Survey of Canada, Open File 2886, 1:250 000 scale.

Hart, C.J.R., 1995. Magmatic and tectonic evolution of the Intermontane Superterrane and Coast Plutonic Complex in southern Yukon Territory. Unpublished MSc thesis, The University of British Columbia, 198 p.

Hart, C.J.R., 1997. A transect across northern Stikinia: Geology of the northern Whitehorse map area, southern Yukon Territory (105D/13-16). Exploration and Geological Services Division, Yukon Region, Indian and Northern Affairs Canada, Bulletin 8, 112 p.

Hart, C.J.R. and Radloff, J.K., 1990. Geology of the Whitehorse, Alligator Lake, Fenwick Creek, Carcross and part of Robinson map areas (105D/11,6,3,2&7),Yukon Territory. Exploration and Geological Services Division, Yukon Region, Indian and Northern Affairs Canada, Open File 1990-4, 113 p.

Long, D.G.F., 2005. Sedimentology and hydrocarbon potential of fluvial strata in the Tantalus and Aksala formations, northern Whitehorse Trough, Yukon. *In*: Yukon Exploration and Geology 2004, D.S. Edmond, L.L. Lewis and G.D. Bradshaw (eds.), Yukon Geological Survey, p. 167-176.

Love, D.A., Clark, A.H., Hodgon, C.J., Mortensen, J.K., Archibald, D.A., and Farrar, E., 1998. The timing of adularia-sericite-type mineralization and alunite–kaolinite-type alteration, Mount Skukum epithermal gold deposit, Yukon Territory, Canada, ^{40}Ar-^{39}Ar and U–Pb geochronology. Economic Geology, vol. 93, p. 437–462.

Lowey, G.W., 2004. Sedimentology, stratigraphy and source rock potential of the Richthofen formation (Jurassic), northern Whitehorse Trough. *In*: Yukon Exploration and Geology 2004, D.S. Edmond, L.L. Lewis, and G.D. Bradshaw (eds.), Yukon Geological Survey, p. 177-191.

Lowey, G.W., Long, D.G.F., Fowler, M.G., Sweet, A.R., and Orchard, M.J., 2009. Petroleum source rock potential of Whitehorse trough: a frontier basin in south central Yukon. Bulletin of Canadian Petroleum Geology, vol. 57, p. 350-386.

MacIntyre, D.G. and Schiarizza, P., 1999. Bedrock geology, Cunningham Lake (93 K/11,12,13,14). British Columbia Ministry of Energy and Mines, Open File 1999–11.

Mathews, W.H. and Watson, K.D., 1953. Spherulitic alkali rhyolite dikes in the Atsutla Range, northern British Columbia. American Mineralogist, vol. 38, p. 432–447.

Mihalynuk, M.G., 1999. Geology and mineral resources of the Tagish Lake area (NTS 104M/8,9,10E,15 and 104N/12W), Northwestern British Columbia. BCGS Bulletin, vol. 105, p. 293.

Mihalynuk, M.G., Erdmer, P., Ghent, E.D., Archibald, D.A., Friedman, R.M., Cordey, F., Johannson, G.G., and Beanish, J., 1999. Age constraints for emplacement of the northern Cache Creek terrane and implications of blueschist metamorphism. *In*: Geological Fieldwork 1998; British Columbia Ministry of Energy and Mines, p. 127-141.

Mihalynuk, M.G., Erdmer, P., Ghent, E.D., Cordey, F., Archibald, D.A., Friedman, R.M., and Johannson, G.G., 2004. Coherent French Range blueschist; subduction to exhumation in < 2.5 m.y.? Geological Society of America, Bulletin 116, p. 910–922.

Mihalynuk, M.G., Johnston, S.T., English, J.M., Cordey, F., Villeneuve, M.E., Rui, L., and Orchard, M.J., 2003. Atlin TGI, Part II: Regional geology and mineralization of the Nakina area (NTS 104N/2W and 3). *In:* Geological fieldwork 2002; British Columbia Ministry of Energy and Mines, p. 9–37.

Mihalynuk, M.G., Nelson, J., and Diakow, L.J., 1994. Cache Creek terrane entrapment: Oroclinal paradox within the Canadian Cordillera. Tectonics, vol. 13, no. 2, p. 575-595.

Miskovic, A. and Francis. D., 2004. The Early Tertiary Sifton Range volcanic complex, southwestern Yukon. *In:* Yukon Exploration and Geology 2003, D.S. Edmond and L.L. Lewis (eds.), Yukon Geological Survey, p. 143-155.

Monger, J.W.H., 1975. Upper Paleozoic rocks of the Atlin Terrane. Geological Survey of Canada, Paper 74-47, 63 p.

Monger, J.W.H., 1977. Upper Paleozoic rocks of the western Canadian Cordillera and their bearing on Cordilleran evolution. Canadian Journal of Earth Sciences, vol. 14, p. 1832-1859.

Monger, J.W.H. and Ross, C.A., 1971. Distribution of fusulinaceans in the Canadian Cordillera. Canadian Journal of Earth Sciences, vol. 8, p. 770-791.

Orchard, M.J., Cordey, F., Rui, L., Bamber, E.W., Mamet, B., Struik, L.C., Sano, H., and Taylor, H.J., 2001. Biostratigraphic and biogeographic constraints on the Carboniferous to Jurassic Cache Creek Terrane in central British Columbia. Canadian Journal of Earth Sciences, vol. 38, p. 551-578.

Paterson, I.A. and Harakal, J.E., 1974. Potassium-Argon Dating of Blueschists from Pinchi Lake, Central British Columbia. Canadian Journal of Earth Sciences, vol. 11, p. 1007-1011.

Schiarizza, P., 2011. Geology of the Kutcho Assemblage between the Kehlechoa and Tucho Rivers, Northern British Columbia (NTS 104I/01, 02). BCGS Geological Fieldwork 2011, paper 2012-1, p. 75-98.

Souther, J.G., 1991. Volcanic regimes, Chapter 14. *In*: Geology of the Cordilleran orogen in Canada, Gabrielse, H., and Yorath, C. J. (eds.),. Geological Survey of Canada, Geology of Canada, vol. 4, p. 457–490.

Struik, L.C., Cordey, F., Orchard, M.J., and Sano, H., 1998. Stratigraphy, structural stacking, and paleoenvironment of the Cache Creek Complex, central British Columbia. *In*: Current research 1998-E, Geological Survey of Canada, p. 1–10.

Struik, L.C., Schiarizza, P., Orchard, M.J., Cordey, F., Sano, H., MacIntyre, D.G., Lapierre, H., and Tardy, M., 2001. Imbricate architecture of the upper Paleozoic to Jurassic oceanic Cache Creek Terrane, central British Columbia. Canadian Journal of Earth Sciences, vol. 38, p. 495–514.

Tempelman-Kluit, D.J., 1984. Geology, Laberge (105E) and Carmacks (105I), Yukon Territory. Geological Survey of Canada, Open File 1101, 1:250 000.

Tempelman-Kluit, D.J., 2009. Geology of Carmacks and Laberge map areas, central Yukon: Incomplete draft manuscript on stratigraphy, structure and its early interpretation (*ca.* 1986). Geological Survey of Canada, Open File 5982, 399 p.

Watson, K.D. and Mathews, W.H., 1944. The Tuya-Teslin area. British Columbia Department of Mines, Bulletin 19, p. 1-52.

Wheeler, J.O., 1961. Whitehorse map-area, Yukon Territory (105D). Geological Survey of Canada, Memoir, vol. 312, 156 p.

White, D., Colpron, M., and Buffett, G., 2012. Seismic and geological constraints on the structure of the northern Whitehorse trough, Yukon, Canada. Bulletin of Canadian Petroleum Geology, vol. 60, *(in press)*.

Yukon MINFILE, 2012. Yukon MINFILE – A database of mineral occurrences. Yukon Geological Survey, http://www.geology.gov.yk.ca/databases_gis.html [accessed November 22, 2012].

Mount Harper Volcanic Complex, Ogilvie Mountains: A far-flung occurrence of the Franklin Igneous Event?

Grant M. Cox[1]
McGill University, Montreal, Quebec, Canada

Charles F. Roots
Geological Survey of Canada, co-located at Yukon Geological Survey, Whitehorse, Yukon

Galen P. Halverson, William G. Minarik
McGill University, Montreal, Quebec, Canada

Francis A. Macdonald
Harvard University, Massachusetts, U.S.A.

Lucie Hubert-Theou
McGill University, Montreal, Quebec, Canada

Cox, G.M., Roots, C.F., Halverson, G.P., Minarik, W.G., Macdonald, F.A., and Hubert-Theou, L., 2013. Mount Harper Volcanic Complex, Ogilvie Mountains: A far-flung occurrence of the Franklin Igneous Event. *In:* Yukon Exploration and Geology 2012, K.E. MacFarlane, M.G. Nordling, and P.J. Sack (eds.), Yukon Geological Survey, p. 19-36.

ABSTRACT

The middle Neoproterozoic (717 Ma) Mount Harper Volcanic Complex (MHVC) is a calc-alkaline magmatic suite developed within a rift system on the northwestern margin of Laurentia. Based on its low Al_2O_3, Na_2O, and TiO_2 contents, the primary melt was derived from a harzburgitic source, was most likely picritic in composition, and required mantle potential temperatures above those recognized for the ambient mantle. Constraints on mantle melting place the mantle at ~6 km, a depth that would require significant crustal attenuation.

Although the volcanic rocks at Mount Harper are the same age as the Franklin Large Igneous Province, the geochemical trends are distinct. Apart from their age, the only plausible link would be to consider the MHVC as the product of a partial melt at the margin of a dispersed mantle plume.

[1]*grant.cox@mail.mcgill.ca*

INTRODUCTION

Age constraints on Cryogenian volcanism within the Canadian Cordillera indicate that magmatic events are restricted to two principal episodes: the ~780 Ma Gunbarrel Event (Harlan *et al.*, 2003) and the ~720 Ma Franklin Igneous Event (Denyszyn *et al.*, 2009; Heaman *et al.*, 1992). Both of these events produced radiating dike swarms in northern Laurentia. Radiating dikes may represent the physical manifestation of mantle plumes and are often associated with Large Igneous Provinces (LIP) (Ernst and Buchan, 1997, 2001, 2003), although the association of radiating dikes to plumes is contested (McHone *et al.*, 2005). This LIP-plume connection may be a precursor to continental breakup, suggesting that LIP's play an important role in this process (Dalziel *et al.*, 2000; Hill, 1991; Li *et al.*, 2003; Storey, 1995).

The Mount Harper Volcanic Complex (MHVC) consists of basalt to rhyolite which erupted into a half-graben on the broad platform flanking the west side (present coordinates) of Laurentia. Up to 1600 m of lava flows and breccias are preserved and are overlain by diamictite, tuff, and other sediments of the Rapitan Group (Sturtian glaciation). This study was aimed at understanding the evolution of rifted margins using the chemistry of the volcanic rocks to determine the composition of the source magma, its temperature, and the nature of the decompressing mantle. These constraints can then be used to place limits on crustal and lithospheric thicknesses and, by implication, their tectonic setting.

In this paper, new and previously published major element geochemical data are combined for the MHVC, predominantly from the lower ~900 m of basaltic volcanics. A thermodynamic melt model is applied to establish basic constraints on the evolution of the MHVC. These results elucidate the mantle melting regime and place constraints on the thickness of the overlying crust. The MHVC is then compared to the coeval Natkusiak basalts (Victoria Island, Nunavut) which forms a part of the Franklin Igneous Event, attempting to ascertain whether the MHVC could represent a distant manifestation of this magmatic episode.

GEOLOGIC SETTING OF THE MOUNT HARPER VOLCANIC COMPLEX

Mount Harper, 70 km north of Dawson (Fig. 1a,b), is surrounded by 105 km^2 of predominantly sub-aqueous mafic to intermediate volcanic rock with volumetrically minor rhyolite. The mountainous terrain affords clear observation of its nearly conformable attitude atop a shallow marine sedimentary sequence (Mustard and Roots, 1997). The Mount Harper Volcanic Complex (MHVC) sits para-conformably on an alluvial fan wedge (Lower Mount Harper Group) which in turn sits atop the Callison Lake dolostone (Fig. 1b,c), a dominantly carbonate unit with interbedded shales that contain sedimentary talc (Tosca *et al.*, 2011)**.** Different interpretations of the age and sedimentary regime of the Callison Lake dolostone have led to its proposed assignment to 1) the underlying Fifteenmile Group (Thompson *et al.*, 1987), 2) the overlying Mount Harper Group (Macdonald *et al.*, 2011), but is now recognized as 3) a distinct unit, possibly a correlative of the Coates Lake Group in the Mackenzie Mountains (NWT) (Macdonald *et al.*, 2012).

Five kilometres east of Mount Harper, the Lower Mount Harper Group comprises up to 1100 m of mainly conglomerate with interbedded sandstone and red calcareous mudstone. These coarse epiclastic sediments were deposited north of the steeply-dipping syn-sedimentary and syn-volcanic Harper fault (Fig. 1b), partly filling an east-trending half-graben (Mustard and Roots, 1997). The Lower Mount Harper Group thins rapidly to the north, where it transitions into sandstone and mud-cracked siltstones and mudstones of presumed lacustrine affinity (Mustard, 1991; Mustard and Donaldson, 1990; Mustard and Roots, 1997). It is overlain conformably by ~900 m of sub-aqueously extruded basalt flows, which suggests that the MHVC was deposited in a rapidly subsiding basin.

The MHVC is bounded above by glaciogenic diamictite of the Rapitan Group. In a rhyolite flow in the upper Mount Harper Group and in a tuff within the diamictite, radiometric ages on zircons fix the age of this contact at 717 Ma (Macdonald *et al.*, 2010).

MOUNT HARPER VOLCANIC COMPLEX

Roots (1987) and Mustard and Roots (1997) divided the MHVC into six informal units (members A through F; Figs. 1b and 2) based on stratigraphic observations and geochemistry. Members A and B are dominated by pillowed (Fig. 3a) and massive flows, with common chloritic and hematitic alteration. The occurrence of pahoehoe flow textures near the top of member B indicate a sub-aerial eruptive phase in an otherwise dominantly sub-aqueous eruptive sequence. Member C is a lithologic

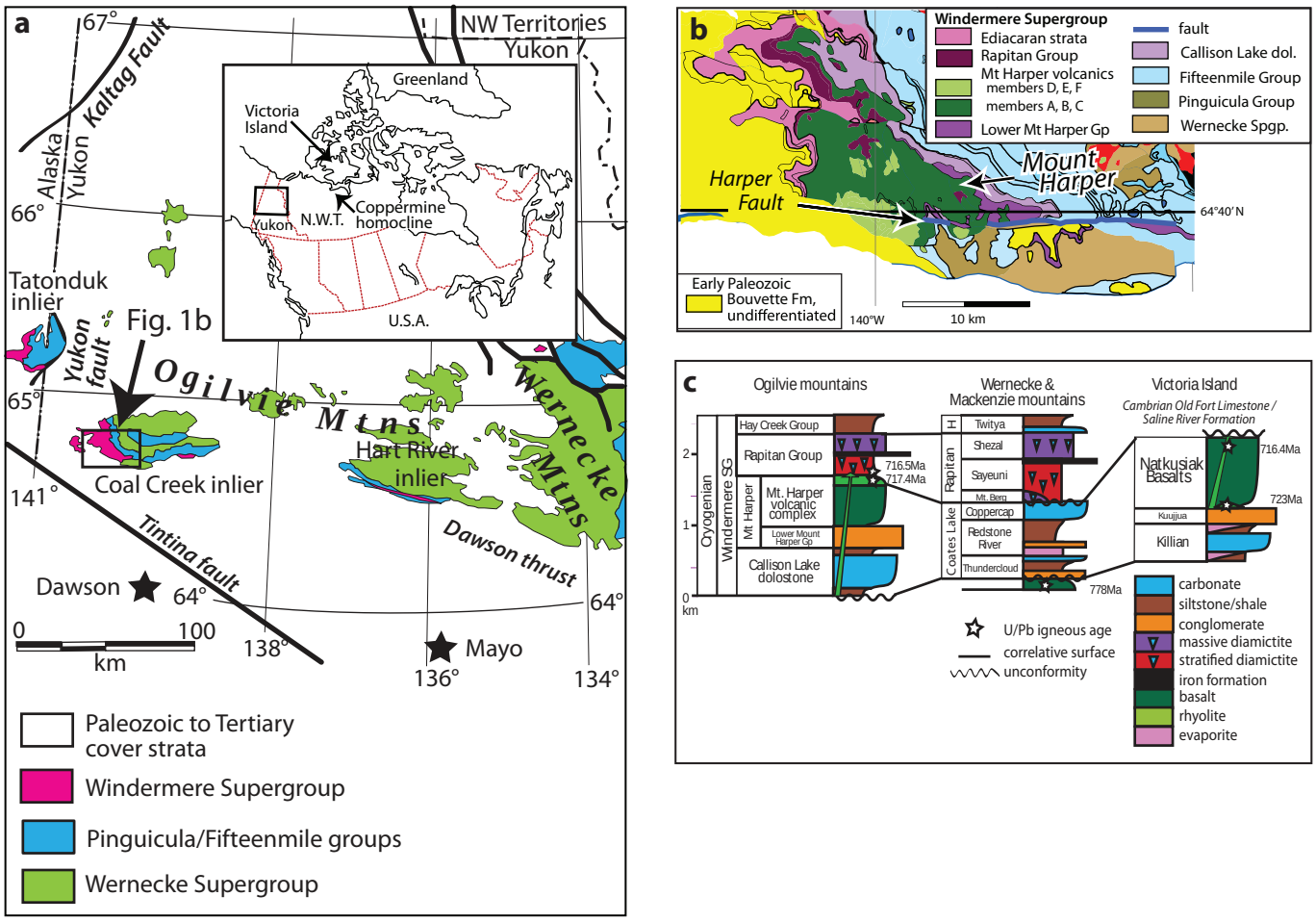

Figure 1. *(a) Regional map for Yukon, NWT, and Alaska; (b) distribution of members of the Mount Harper Volcanic Complex and enclosing units; and (c) stratigraphic column showing stratigraphic correlations with the Wernecke Mountains and Victoria Island (from Macdonald et al., 2012).*

unit: a stratigraphic interval composed almost entirely of sub-aqueous volcanic breccia and tuff that represents a period of explosive volcanism as well as erosional destruction of the member A and B volcanic edifice (Mustard and Roots, 1997). Member D comprises rhyolite flows and domes (Fig. 3b), subsequently partly eroded and succeeded by pillowed and massive andesite flows of member E and then by sub-aqueous basaltic andesite to andesite flows of member F. Mustard and Roots (1997) argued that some lavas in member D were sub-aerial, but definitive evidence is absent.

The original size and extent of the MHVC cannot be ascertained because it is dissected by faults and eroded, including scouring by mid-Cryogenian glaciation. Nevertheless, remnants of the MHVC extend laterally across ~17 km of the Coal Creek inlier (Fig. 1a) and reach a maximum continuous thickness of ~900 m. A composite log of Members A through F (Fig. 2) suggests that the original volcanic edifice was at least ~1600 m thick. Beyond the Coal Creek inlier, volcanic flows at a similar stratigraphic level occur within the Tatonduk and Hart River inliers (Fig. 1a), indicating that the original volcanic field was possibly more extensive.

AGE CONSTRAINTS

The age of the rhyolitic member D is well constrained by a U-Pb zircon age of 717.43±0.14 Ma (Macdonald *et al.*, 2010). A rhyolitic tuff near the base of Rapitan glacial diamictite atop the edifice composed of members

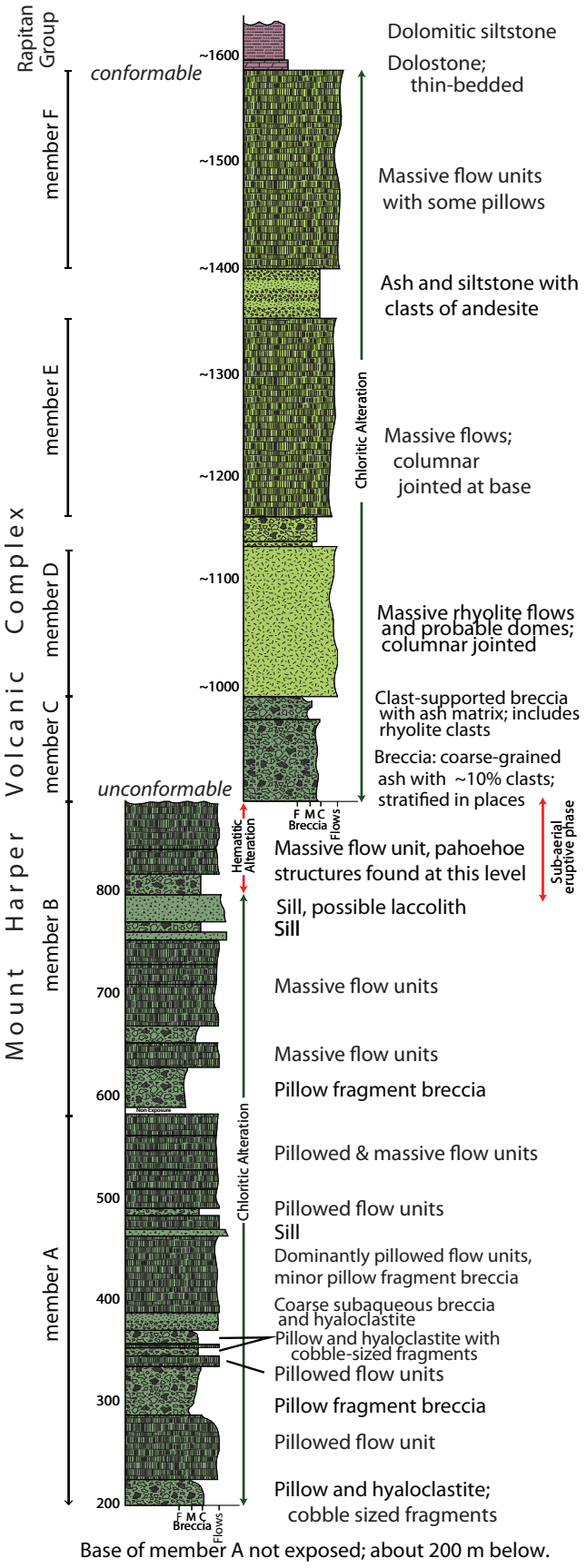

A and B yielded a U-Pb zircon age of 716.47±0.24 Ma (Macdonald *et al.* 2010). This tuff indicates that the initial phase of volcanism was pre- or syn-glacial.

The apparently conformable contacts between members D through F imply that these eruptive phases were continuous. However, the extensive erosional contact separating members A and B from member D may represent a significant time gap between volcanic events. As discussed below, the geochemical characteristics of Member F suggests a return to the melting regime characterized by members A and B. The entire volcanic sequence was therefore most likely erupted during a single magmatic cycle.

ALTERATION

Due to the greenschist facies alteration of these rocks (chlorite and sericite alteration assemblage), many of the rocks are highly hydrated, in particular those of mafic to intermediate compositions. Loss on ignition (LOI) in some samples can be greater than 10%, in which mobile elements such as Ca and Na have been significantly affected. Table S1 (Appendix 1) reports major element data only from rocks with less than 5% LOI; alteration effects are not apparent with no correlation between major element abundances and LOI.

PETROGRAPHY

MEMBERS A AND B

Flows in members A and B contain (micro)phenocrysts of olivine that are pseudomorphed by chlorite. Clinopyroxene (CPX) is abundant along with needles of plagioclase that forms a dense groundmass mesh often containing Fe-Ti oxides. Orthopyroxene (OPX) is absent. An original glassy groundmass is now entirely altered to chlorite±feldspar±sericite. Unlike A, which is chloritic-altered, stratigraphically higher flows of member B are extensively altered to hematite. This zone of hematite

Figure 2. *Composite stratigraphic log of the MHVC. Member B, and possibly member A, were partly eroded before eruption and deposition of members D, E, and F; ~900 m are preserved. Physical volcanic features are described by Roots (1987) and Mustard and Roots (1997).*

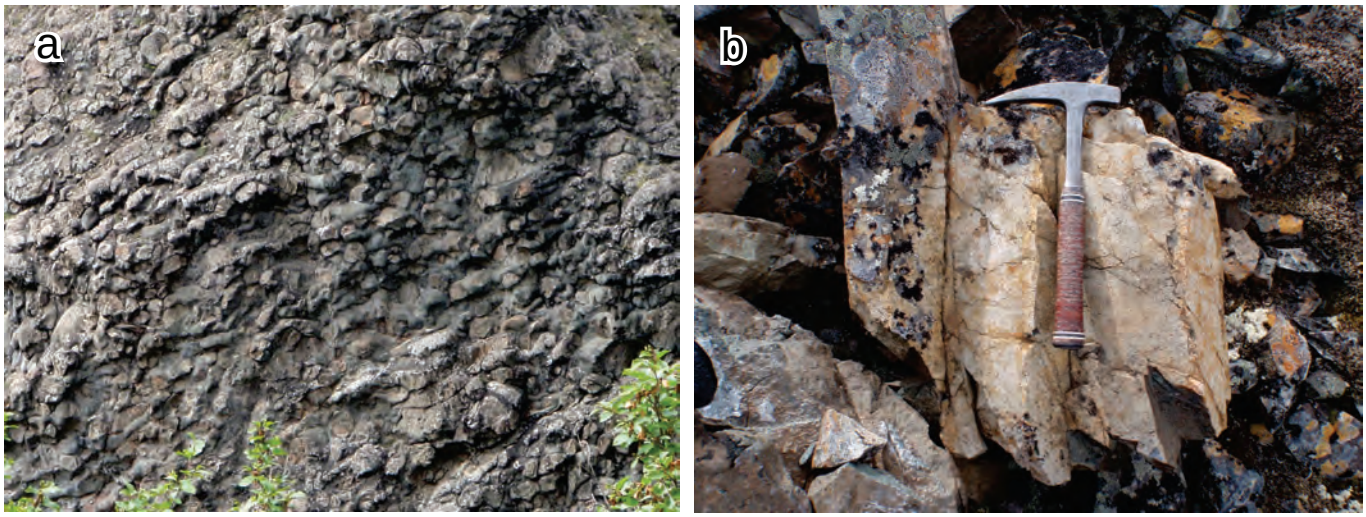

Figure 3. *(a) Cliff face, about 10 m high, exposes rounded pillows in member A (64°40.0'N and 139°54'W; 2 km SW of Mount Harper); (b) columnar rhyolite of member D weathers into conical rubble hills 6.5 km west of Mount Harper.*

alteration coincides with the appearance of pahoehoe flow structures, suggesting that this alteration may be a primary feature related to sub-aerial eruption. The general crystallization sequence for members A and B was likely olivine » clinopyroxene » plagioclase » glass.

MEMBER D

Phenocrystic K-feldspar and plagioclase, commonly saussuritized, are the dominant mineral phases for member D. Minor phases include titanite (I- type index mineral; Chappell and White, 2001), Fe-Ti oxides and zircon, with xenocrystic garnet (Mustard and Roots, 1997; Roots, 1987). An original glassy groundmass is entirely altered to quartz ± sericite ± feldspar.

MEMBER E

The flows are extensively crystallized, plagioclase and minor clinopyroxene being easily distinguishable phases. The groundmass phases include quartz plus Fe-Ti oxides. Olivine is absent.

MEMBER F

Flows are locally seriate and plagioclase-phyric, with visible augite. Voids, into which plagioclase laths project, are filled with secondary silica. The largely indistinguishable groundmass was most likely glass but now contains quartz ± sericite ± feldspar alteration phases. Alteration indicated by chlorite and other clay minerals is extensive.

GEOCHEMICAL CHARACTERISTICS OF MHVC

Major element Harker and Fenner diagrams (Fig. 4) along with alkali vs. silica plots show distinctive geochemical groupings and trends. Members A and B are characterized as basalts to basaltic andesites, member D as rhyolites and both members E and F are andesites but with significantly different bulk compositions (Fig. 4a).

MEMBERS A AND B

While members A and B are defined stratigraphically, they both fall on a compositional trend from basalt to basaltic andesite, with the most primitive examples having MgO contents of ~12%. The combination of low TiO_2, low Al_2O_3, and low Na_2O in these rocks suggests either a depleted mantle source or extensive melting of a fertile source. The liquid line of descent for members A and B is consistent with the fractionation of olivine ± clinopyroxene, and the delay of plagioclase crystallization. A lack of FeO and TiO_2 enrichment with decreasing MgO is consistent with calc-alkaline magmatism.

MEMBER D

Member D reflects a switch from mafic to felsic magmatism within the evolution of the MHVC. These rhyolites are characterized by 70-78% SiO_2 with no intermediate compositions that link them via a liquid line of descent to the extrusion of lower members A and B. Aluminium saturation ratios (Al_2O_3/[CaO + K_2O + Na_2O])

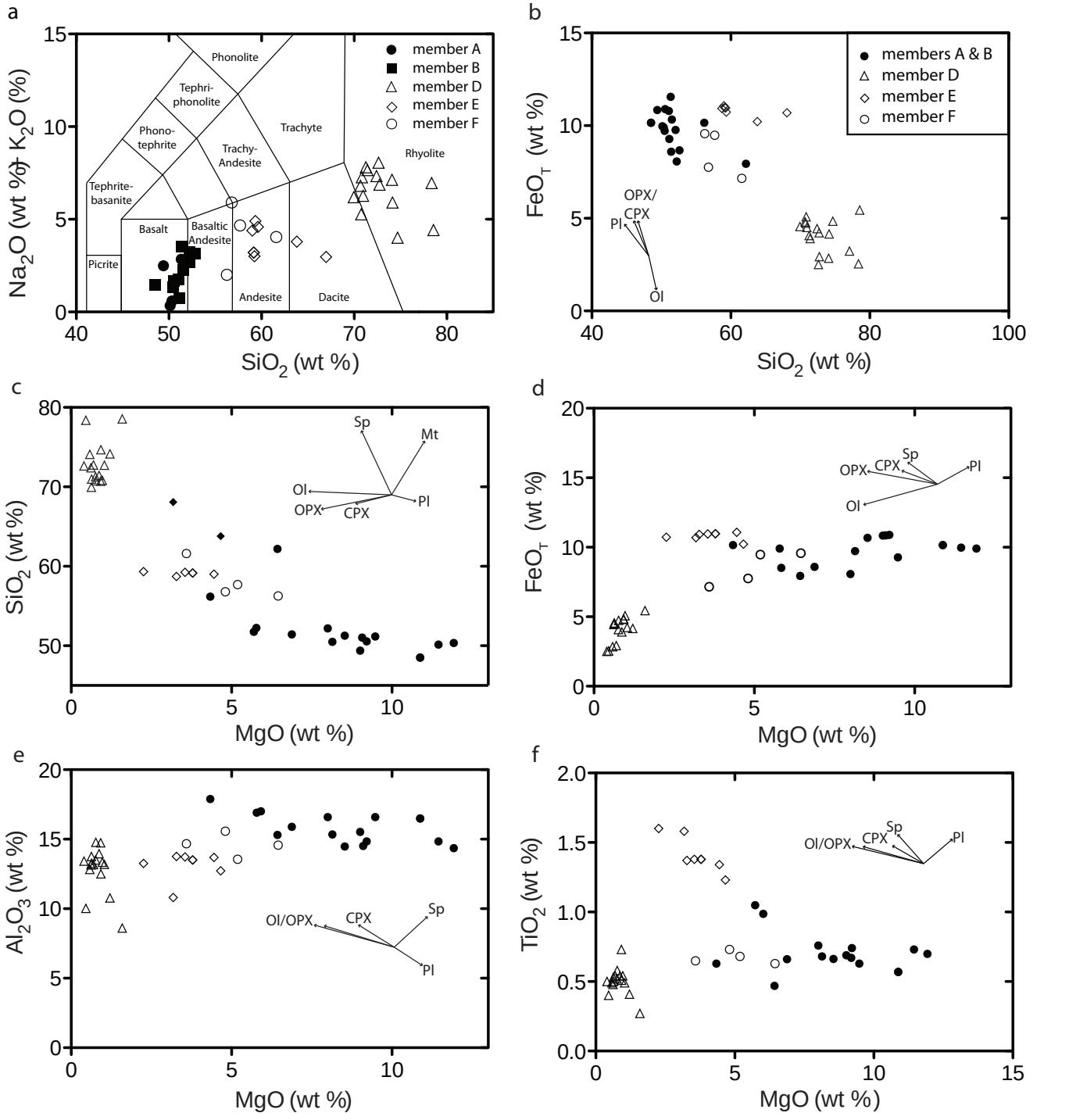

Figure 4. *Major element plots show the distinctive geochemical evolution of the MHVC. Particularly apparent on the Harker diagrams (SiO_2 on the x-axis) is the distinctive geochemical trend represented by members A and B. A silica gap of ~15% (i.e., the "Daly" gap) separates members A and B from the rhyolitic member D. On the Fenner diagrams (MgO on x-axis) members A, B and F define a liquid line of descent characteristic of delayed plagioclase crystallization. Member E lavas are distinct from the mafic to intermediate lavas of members A, B, and F; note the trend to increasing TiO2 and constant FeO. Radiating arrows indicate possible trends resulting from crystallization of normative minerals: CPX – clinopyroxene; Mt – magnetite; Ol - olivine; OPX – orthopyroxene; Pl – plagioclase; Sp - spinel.*

range from metaluminous to peraluminous (0.84 to 1.44) along with normative corundum. However, the occurrence of titanite in the mineral assemblage precludes simple classification as either I or S-type rhyolites (Chappell and White, 2001). Normative compositions projected into the Qz-Ab-Or-H_2O system (Blundy and Cashman, 2001) reveal the dominant role of low pressure polybaric fractionation of albite towards K_2O and SiO_2-rich compositions (Fig. 5).

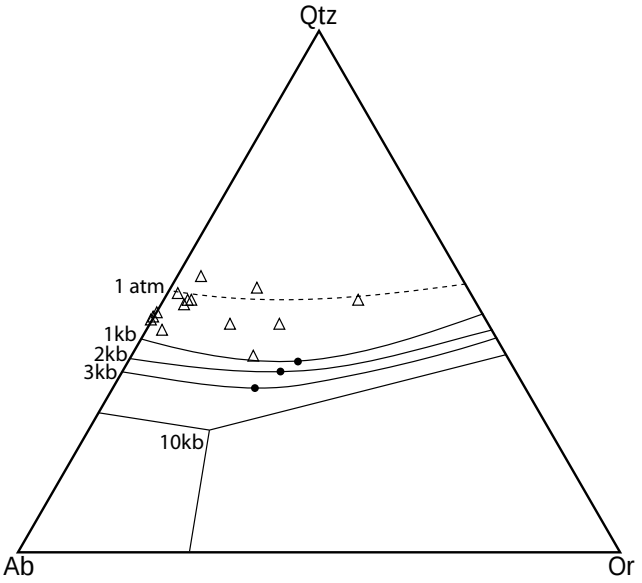

Figure 5. *Projection of the normative composition of member D rhyolites following the method outlined by Blundy and Cashman (2001). This projection reveals a trend of polybaric crystallization dominated by the fractionation of plagioclase. Black dots are the water saturated minimums. Water undersaturation and decreasing pressure move these minimums towards the Qtz-Or join.*

MEMBER E

Member E lavas are andesitic to dacitic but plot well away from the fractionation trend observed in members A and B (Fig. 4f). The major element liquid line of descent for member E is complicated but most likely associated with the fractionation of a gabbroic assemblage (Pl+CPX±Sp). The intermediate nature of member E, coupled with the immediate precursor eruption of rhyolites, possibly indicates the role of magma mixing between a residual member D liquid and a new influx of mafic magma. Simple mixing between members A and B and member D compositions would require that the member D contribution be ~30-40% to achieve the approximate compositional characteristics of the most primitive member E lavas. This compositional fit is far from perfect however, suggesting that petrogenesis of member E was substantially more complicated than a simple mixing model.

MEMBER F

Member F lavas represent the final phase of magmatism of the MHVC, and while these rocks are andesites, they are compositionally distinct from the andesites of member E. At comparable MgO contents, member F lavas have less FeO and TiO_2 and represent evolved members of the calc-alkaline trend defined by members A and B. Unlike member E, which is andesitic to dacitic, the composition of member F is more primitive. Notwithstanding, these compositions suggest that member F flows may reflect a return to the style of magmatism that characterizes members A and B.

THE MOUNT HARPER MELTING REGIME

In the following section we present the results of thermodynamic models aimed at understanding the evolution of the Mount Harper volcanic suite.

MODELING THE LIQUID LINE OF DESCENT

Using alphaMELTS/pHMELTS (Asimow *et al.*, 2004; Ghiorso *et al.*, 2002; Ghiorso and Sack, 1995), it is possible to model the liquid line of descent (LLOD) starting from a parental melt composition. We approximate the parental melt using the Mount Harper sample with the highest MgO content. We have modeled the evolution of a parental melt composition (MgO = ~12%) during decreasing temperature over the pressure range of 1 to 20 kb, with water contents between 0 and 2%, and an oxygen fugacity buffered at FMQ-1 and FMQ.

Regardless of the temperature or oxygen fugacity buffer used, the anhydrous model runs all show enrichments in FeO_T and TiO_2 with decreasing MgO, along with initial decreasing SiO_2 driven by the relatively early appearance of plagioclase on the liquidus. This tholeiitic (Fenner) trend is clearly incompatible with the observed LLOD for members A and B. The addition of water above 1% suppresses FeO_T and TiO_2 enrichment as plagioclase crystallization is impeded.

Trends in both major element and normative compositions (Fig. 6) indicate that members A and B can be successfully

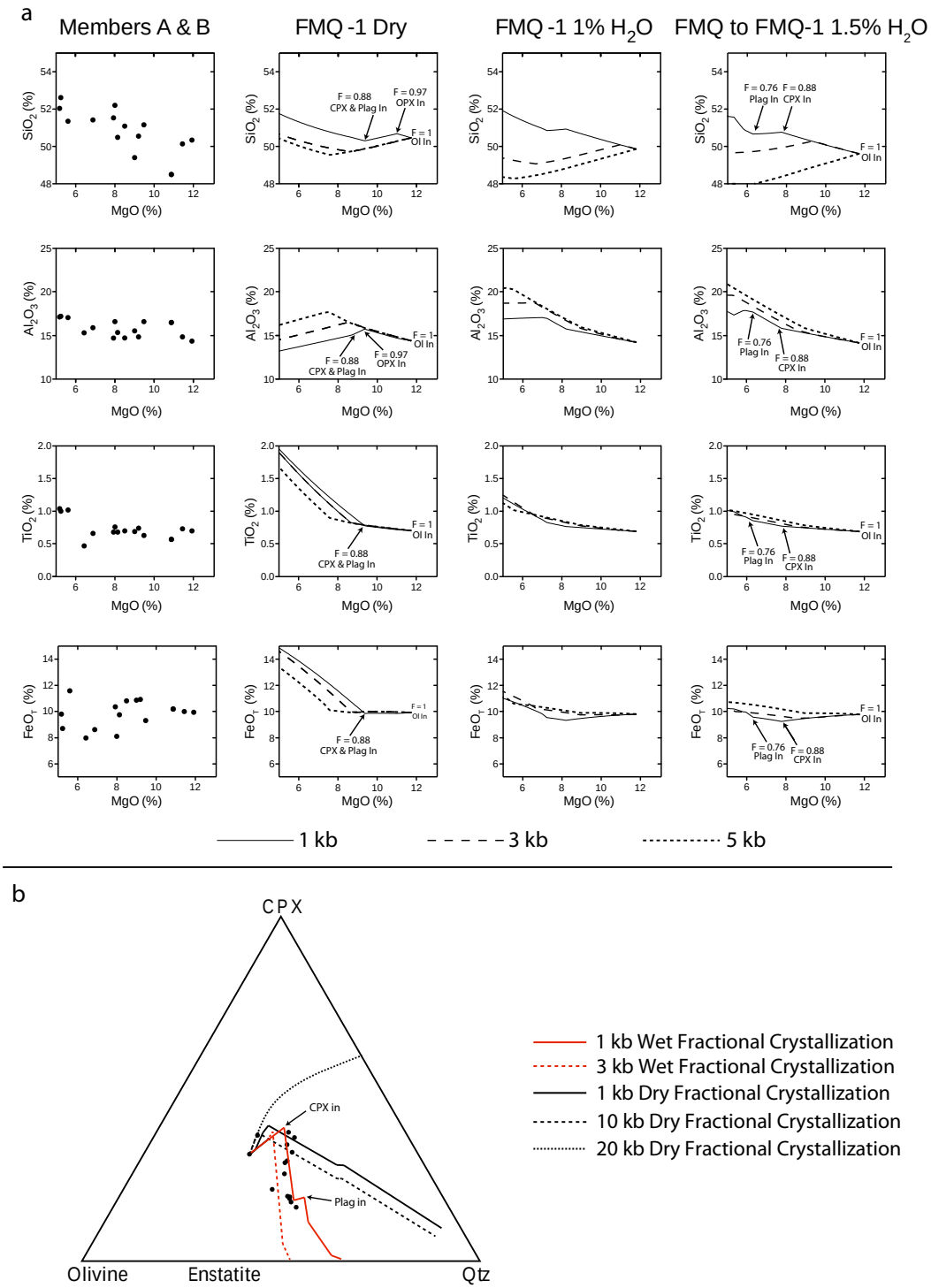

Figure 6. *(a) Major element Fenner diagrams with modeled liquid lines of descent under varied oxygen fugacity constraints. These models demonstrate the requirement for a wet, low pressure melt to suppress the appearance of plagioclase on the liquidus. Such plagioclase suppression results in flat FeO_T and TiO_2, as observed in members A and B. (b) Normative data projected onto the Ol-CPX-Qtz ternary diagram, modeling the liquid line of descent for wet and dry magmas under various pressure regimes. The data best fits that of a low pressure, wet melt. Based on these models, the compositional range observed for members A and B can be explained by the ~30% crystallization of Ol, followed by CPX, and then plagioclase. For fractional crystallization, the melt is held at constant pressure and cooled in increments of 1°C. As crystallization proceeds the solid is immediately removed from the remaining liquid.*

modeled by the low pressure (~1 kb) fractional crystallization of olivine followed by clinopyroxene. The entire compositional range of members A and B between ~12% to ~6% MgO requires approximately 30% fractional crystallization of a wet melt (1-1.5% H_2O) at FMQ-1 to FMQ conditions (Fig. 6a, right column).

These models have focused principally on understanding the petrogenesis of members A and B. However, they demonstrate that the range in composition in member E lavas is successfully modeled by fractionation of the most primitive member E lava (highest MgO%) under anhydrous and low H_2O (*i.e.*, less than 0.5%) conditions. The trend observed for these lavas is compatible with fractionation of CPX+plagioclase of a relatively dry melt (Fig. 6a).

olivine and flags potential errors in the calculation caused by clinopyroxene fractionation or sources possibly characterized by carbonated peridotite and/or pyroxenite components.

The results of the two different approaches are shown in Table 1. There is broad agreement, with both methods calculating picritic primary melts with MgO contents between 14-17% MgO. Based on the calculated MgO contents of these parental melts, and using the equation for calculating mantle potential temperatures (Tp) as outlined by Herzberg *et al.* (2007), the calculated mantle potential temperature[1] for these melts lies between 1440°C and 1511°C , which is ~90°C to 160°C higher than inferred ambient mantle temperature (Herzberg *et al.*,

Table 1. *Primary melt calculations.*

	SiO_2	TiO_2	Al_2O_3	FeO_T	MnO	MgO	CaO	Na_2O	K_2O	P_2O_5	Total	Liquidus T
Starting Composition	50.14	0.73	14.84	9.97	0.19	11.45	12.09	0.21	0.13	0.07	100	1265

Primary Melt	SiO_2	TiO_2	Al_2O_3	FeO_T	MnO	MgO	CaO	Na_2O	K_2O	P_2O_5	Total	Olivine Fo	Tp	% Ol Addition
Method 1 - Fo90	49.47	0.68	13.69	10.16	0.18	14.31	11.18	0.19	0.12	0.06	100	90.0	1442	7.0
Method 2 - PRIMELT2	48.70	0.62	12.59	9.17	0.94	17.17	10.28	0.18	0.11	0.06	100	91.3	1511	16.8

PRIMARY MELT CALCULATIONS

The variation in FeO_T on Figure 4 best demonstrates that samples of members A and B with MgO>9% have only fractionated olivine; this observation is supported by the melt modeling (Fig. 6), as discussed in the previous section. Such a simple fractionation pathway allows for the primary mantle melt to be reconstructed (as a melt in equilibrium with mantle olivine). Two methods have been applied to achieve this primary melt calculation. First, olivine is incrementally added back to the chosen parental melt composition until the liquid is in equilibrium with mantle olivine of ~Fo_{90}, using the FeO/MgO olivine-liquid distribution co-efficient (K_D) of 0.3 (Roeder and Emslie, 1970). Second, we apply the PRIMELT2 model of Herzberg and Asimow (2008), which couples the above inverse model with a forward melting model, such that the intersection of the two indicates the primary mantle melt. Unlike the first model, the PRIMELT2 method does not assume or require the Fo content of coexisting

2007). Of the two methods used, the PRIMELT2 method is preferred as it predicts a harzburgitic source (Fo91.3) which is the best fit for the most primitive lava combining the characteristics of low TiO_2, low Al_2O_3, and low Na_2O (Falloon *et al.*, 1988).

With a reconstructed primary melt composition, critical melting regime characteristics can be evaluated such as percentage melting, melting depth, and source composition. The primary melt composition is projected onto modeled mantle melting curves in Figure 7. The principal variables that affect this calculation include oxygen fugacity, source composition, and pressure during melting (*i.e.,* specifically isobaric *vs.* polybaric path options). Oxygen fugacity is fixed to FMQ-1 based on the calculated fugacity of the Proterozoic upper mantle underlying the Canadian Cordillera as determined from

[1]*The mantle potential temperature (Tp) is the temperature the mantle would have at the earths surface if it ascended along an adiabat without undergoing melting (McKenzie and Bickle, 1988).*

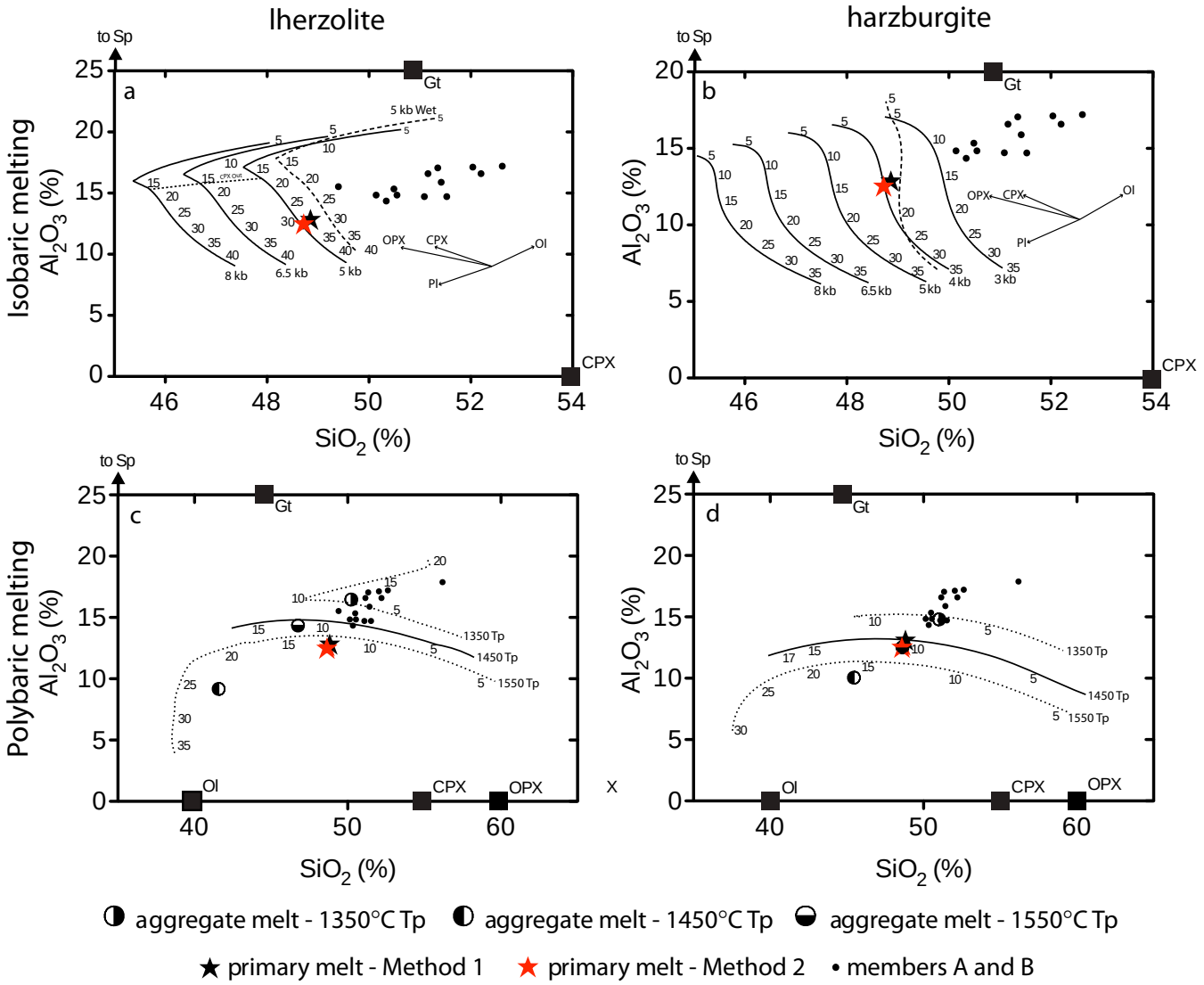

Figure 7. *(a) Isobaric lherzolite melting (b) isobaric harzburgite melting (c) polybaric lherzolite melting (d) polybaric harzburgite melting. The numbers along the melting curves represent percentage melting. Normative minerals: CPX – clinopyroxene; Gt – garnet; Ol - olivine; OPX – orthopyroxene.*

mantle xenoliths (Francis *et al.*, 2010). The nature of the fertile mantle is semi-constrained using a lherzolitic composition as represented by the Kettle River peridotite (Walter, 1998), a sub-lithosphere mantle xenolith from British Columbia. The harzburgitic composition used in this calculation is that of Kettle River peridotite minus ~12% melt. Normative CPX compositions for the respective sources are 16% CPX for the lherzolite and 6% CPX for the harzburgite.

OPTION 1: EQUILIBRIUM ISOBARIC MELTING

Calculated melting curves for a lherzolite source at pressures between 8 kb and 3 kb (24-9 km depth; Fig. 7) reveal that the primary melt composition requires an extraordinary high degree of partial melting (~30%), well past the CPX-out boundary at pressures of 5 kb. Modification of the source to a harzburgitic composition pushes the melting regime to even shallower levels (4 kb) and still requires melting to progress ~10% past the CPX-out boundary.

Several issues arise from these isobaric melting calculations. They imply high degrees of partial melting well beyond the thermal barrier represented by the Sp CPX-out phase boundary, require that the melt be generated entirely within what should be lithospheric mantle, and are based on isobaric mantle melting, which is a doubtful mantle melting process.

OPTION 2: POLYBARIC ISENTROPIC MELTING

It has been shown that polybaric melting of an upwelling mantle source is a fractional melting process due to mantle compaction and the buoyancy of melt with respect to the mantle (Langmuir *et al.*, 1992; McKenzie and Bickle, 1988; McKenzie, 1984; Obata and Nagahara, 1987). Consequently, the fractionation of melt away from the mantle source results in mantle melting being largely isentropic in nature (Asimow *et al.*, 1995). This is more realistic for modeling mantle melting, and so we calculate the P-T path (Fig. 8), the percentage melt, instantaneous melt composition, and aggregate melt composition for both a lherzolite and harzburgite source, rising along adiabats that correspond to mantle potential temperatures of ~1350°C, ~1450°C, and ~1550°C (which bracket the calculated Tp of the primary melt). In the modeling runs, melting begins at the pressure where the corresponding mantle adiabat intersects the respective source solidus and continues up to the base of the lithosphere (which has been adjusted to be between 2 kb and 5 kb for this study (*i.e.*, ~6-15 km depth)).

Figure 7 shows that a lherzolite source is incompatible with the calculated primary melt as it consistently produces aggregate melts that are too high in Al_2O_3. The addition of water, which displaces these melting curves to higher SiO_2 as the peritectic in the Ol-CPX-Qtz ternary system moves towards the CPX-Qtz join, has very little effect on Al_2O_3 contents. The results for a harzburgitic source however show good agreement between the calculated primary melt and the aggregate melt generated by a rising mantle that begins to melt at ~17 kb (Fig. 8). Furthermore, the melt aggregation of this polybaric melting column, at ~2 kb, is consistent with the depth at which the modeled ~1 kb liquid line of descent from the most MgO-rich lava matches the natural variation observed in members A and B.

The largest source of uncertainty in this modeling exercise comes from source composition and the selected thickness of the lithosphere. However, by comparing variations in both the source composition and lithosphere

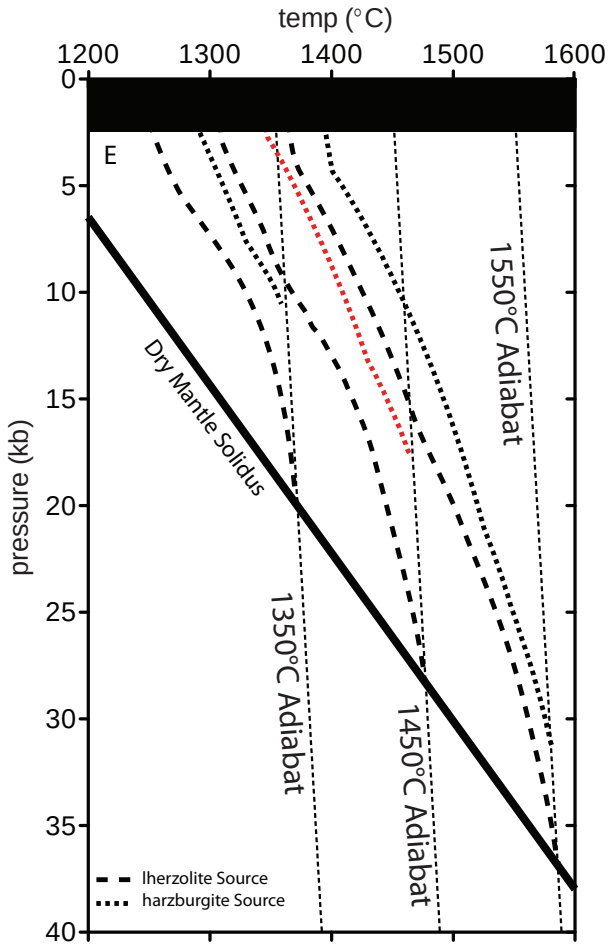

Figure 8. *P/T diagram showing the melt path for the polybaric melting models. Solid black line is the dry solidus for lherzolite mantle (solidus for harzburgite is not shown, but would connect with the high pressure end of the harzburgite melting paths). Path shown in red is for a harzburgite source that intersects the solidus at ~17 kb along a 1450°C adiabat and successfully produces the primary melt composition calculated for members A and B. For the polybaric melting models, the source is maintained at a constant entropy state and melting proceeds under equilibrium conditions until the fraction of melt reaches F=0.005, at which point this melt is removed. The aggregate melt is the summation of these small equilibrium batch melts.*

thickness, we can gauge the sensitivity of the results to changes in these parameters.

It is evident from Figure 9 that the source composition has a larger impact on Al_2O_3 than SiO_2. This is not surprising, considering that Al is effectively incompatible during mantle melting (Falloon *et al.*, 1988). Unlike

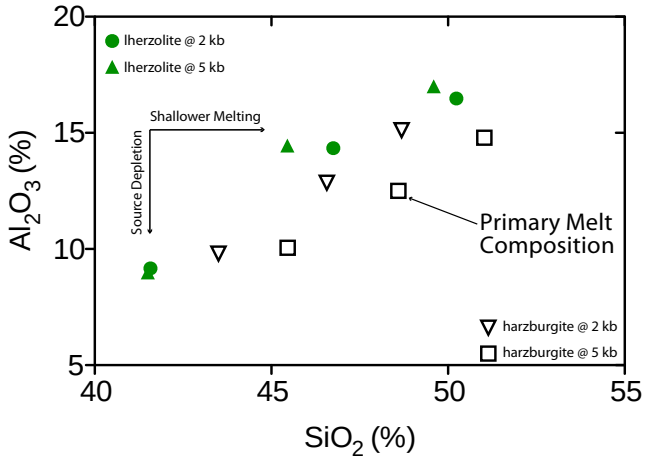

Figure 9. *The effect of changes in source composition and depth to the crust/lithosphere boundary on the polybaric melting models and the effect this has on the ability to constrain these mantle melting parameters. It is evident that SiO_2 is primarily affected by pressure, while Al_2O_3 is affected by source composition, making these two variables independent proxies of these mantle melting variables.*

source composition, the thickness of the lithosphere and hence the pressure of melting has a large impact on SiO_2 and comparatively little impact on Al_2O_3. The increase in SiO_2 is readily explained by the shift of the peritectic and eutectic positions in the Ol-CPX-Qtz system to more SiO_2-rich compositions with decreasing pressure (Bowen and Schairer, 1935; Falloon *et al.*, 1988; Takahashi and Kushiro, 1983). Thus Al_2O_3 and SiO_2 compositions work as semi-independent constraints on the depth of melting and source composition. Other combinations of source composition and depth of the crust/lithosphere will not satisfy the primary melt composition at geologically reasonable mantle potential temperatures. Hence, these models place useful estimates on the melting regime and suggest polybaric melting of harzburgite beneath a lithosphere ~6 km thick (2 kb).

DISCUSSION

TECTONIC SETTING

The models presented here provide quantification of the melt that may have produced the initial volcanic accumulation at Mount Harper. They suggest that the melting that produced the MHVC was a direct result of mantle decompression to pressures of ~2 kb. This pressure implies that the overlying lithosphere was only ~6 km thick. Considering the average thickness of continental crust is ~39 km (Christensen and Mooney, 1995), combined with evidence for significant terrestrial (Lower Mount Harper Group) sedimentation, crustal attenuation by extension was well advanced when volcanism began, clearly pointing to a rift tectonic setting for the MHVC.

A modern analogue for continental transitioning to oceanic rift processes is the East-African-Red Sea-Gulf of Aden rift system. Seismic refraction profiles show significant variability in crustal/lithosphere thicknesses, from ~10 km at the flanks of the Red Sea which transitions to less than 6 km in the Gulf of Aden and the central Red Sea, while the less developed East Africa and Dead Sea rift arms have crustal thicknesses of ~20-30 km (Prodehl *et al.*, 1997). The calculated crustal thickness of ~6 km for the MHVC is consistent with the thickness of the off-axis regions of the Red Sea. While the Red Sea is dominated by a central spreading ridge, many seamounts and volcanic islands can be found along the full length of the central rift (Gass *et al.*, 1973), as well as volcanic centres that flank and onlap onto the coastal zones (*i.e.*, Wiart and Oppenheimer, 2000). Mustard and Roots (1997) originally proposed an East-African rift analogy with incipient low-angle normal faults (Bosworth, 1985). Based on our calculations for the thickness of the lithosphere a more evolved rift setting is appropriate.

A FAR-FLUNG COMPONENT OF THE FRANKLIN LIP?

The Franklin Igneous Province was a LIP manifested by a dike swarm radiating 2500 km across northern Canada and Greenland (Dawes, 1992; Denyszyn *et al.*, 2009; Frisch, 1984a,b,c) and the Natkusiak basalts of Victoria Island (Dostal *et al.*, 1986) at ~720 Ma (Denyszyn *et al.*, 2009; Heaman *et al.*, 1992). The age of the rhyolite (subsequent to members A and B) at MHVC is the same age as the Franklin LIP which leads to conjecture that the MHVC could be part of the Franklin Igneous Province.

The published major element data of Dostal *et al.* (1986) and Denyszyn (2008) show fundamental geochemical differences between the MHVC and Franklin extrusive and intrusive occurrences (Fig. 10). Specifically, Franklin igneous rocks are more evolved, lying along a gabbroic fractionation trend. Additionally, TiO_2 and FeO enrichments indicate a clear tholeiitic evolution in the Franklin volcanics, in contrast to the calc-alkaline evolution of the MHVC.

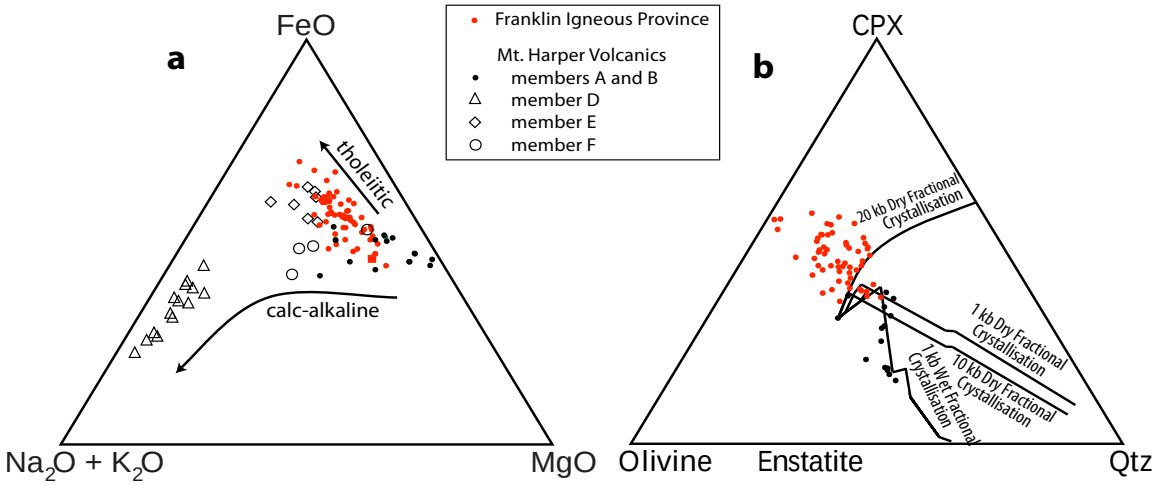

Figure 10. *(a) AFM diagram showing a comparison between major element data for the Franklin LIP in red (Dostal et al., 1986; Denyszyn, 2008), along with our data for the MHVC (black). The Franklin rocks evolved along a tholeiitic pathway, whereas MHVC define a calc-alkaline trajectory. (b) Normative compositions for the Franklin igneous rocks (red) reveal a trend associated with the fractionation of a dry magma from a parental melt, significantly different from the parental melt for members A and B of the MHVC (black). The trend exhibited by the Franklin igneous rocks are similar to that obtained experimentally for fractionation of a basaltic liquid in equilibrium with a lherzolite residue (Villiger et al., 2004).*

This comparison is explored by examining the volcanic suites at similar stages in their evolution. The data sets are normalized to a common MgO% to correct for the effects of fractionation, following the method outlined by Klein and Langmuir (1987). This analysis (Table 2) reveals that, at comparable stages, the MHVC are shifted to higher SiO_2, lower TiO_2, lower FeO, lower CaO, and lower Na_2O. These systematic shifts indicate completely different sources, reinforcing the deduction that the Natkusiak basalts are lherzolite melts (Falloon *et al.*, 1988; Klein and Langmuir, 1987; Turner and Hawkesworth, 1995), whereas the MHVC are harzburgite melts (Falloon *et al.*, 1988; Turner and Hawkesworth, 1995). This conclusion concerning different mantle sources agrees with that reached by Dostal *et al.* (1986), who argued that an N-MORB type source best suited the Natkusiak basalts and our modeling of the MHVC.

Table 2. *Major element values for the Mount Harper Volcanic Complex and Nakusiak basalts corrected to a common value of MgO equals 8% (after Klein and Langmuir, 1987).*

	$Si_{8.0}$	$Ti_{8.0}$	$Al_{8.0}$	$Fe_{8.0}$	$Mn_{8.0}$	$Ca_{8.0}$	$Na_{8.0}$	$K_{8.0}$	$P_{8.0}$
Nakusiak Basalts	50.27	1.40	14.12	12.10	0.20	11.01	2.21	0.52	0.17
MHVC	51.89	0.73	15.99	9.80	0.18	10.57	2.11	0.50	0.08

Systematic differences between the MHVC and Franklin igneous rocks indicate that melt was generated from distinct mantle reservoirs under different conditions. This does not preclude a link between the MHVC and the Franklin volcanics however, if both are considered in the broader context of a plume model proposed for the emplacement of LIP's (Campbell, 2005; Sobolev *et al.*, 2011). The combination of a large radiating dike swarm, high pressure melting (garnet residue; Dostal *et al.*, 1986) and continental doming that preceded the eruption of the Natkusiak basalts (Rainbird, 1993) are consistent with a plume source for the Franklin LIP. A possible plume source for the MHVC is suggested by our calculation of mantle potential temperatures that are 90°C to 160°C above ambient mantle (Herzberg *et al.*, 2007). However, it has been recognized that elevated mantle potential temperatures need not require rising hot asthenosphere, because modeling results suggest that continental insulation can produce an increase in mantle temperatures of at least ~100°C (Anderson, 1982; Coltice *et al.*, 2007; Grigne and Labrosse, 2001). Consequently, the higher mantle potential temperatures calculated for the MHVC are equally compatible with mantle insulation and mantle plume models (Campbell and Griffiths, 1990; Herzberg *et al.*, 2007; Watson and McKenzie, 1991).

An alternative explanation for the discrepancy between the MHVC and the Franklin LIP (Heaman *et al.*, 1992; Rainbird, 1993) may lie in the geographic distance between them and the harzburgitic source required for the MHVC. The thermochemical plume model (Campbell, 2007; Campbell and Griffiths, 1990; Griffiths and Campbell, 1990; Watson and McKenzie, 1991; Wyllie, 1988) posits that hot, adiabatically decompressing mantle impinges on the base of the lithosphere and flattens. Most melting should occur in the rising plume, leaving a melt-depleted mantle that flows radially away from the plume centre along the base of the lithosphere. Consequently a harzburgitic residue related to the Franklin plume might conceivably be the source of the MHVC at the "far flung" fringe of the flattened plume head.

CONCLUSIONS

The composition of igneous rocks of the MHVC can be modeled by polybaric melting of a mantle harzburgite source. The liquid line of descent of this melt would have followed a calc-alkaline differentiation trend characterized by low pressure fractionation of olivine ± clinopyroxene and the delayed appearance of plagioclase. Calculated primary melt composition requires mantle temperatures above those considered normal for the ambient mantle.

This volcanic complex represents a dominantly sub-aqueous magmatic episode, interrupted by a minor interlude of sub-aerial volcanic activity. It would suggest a volcanic island developed in a rift setting, possibly analogous to fringes of the modern Red Sea.

Although the identical ages between the MHVC and the Franklin LIP suggest a synchronous origin for the two, their inferred sources were different. Only by differentiation of a mantle plume as it spread radially, then tapped by a half-graben fault through thinned continental crust, could the MHVC be related to the Franklin Large Igneous Province.

ACKNOWLEDGMENTS

This project has been supported by Yukon Geological Survey and NSERC grants to GPH and a Vanier Fellowship to GMC. Don Francis is thanked for many helpful discussions. Bill Horne re-drafted some figures. This is ESS Contribution number 20120369.

REFERENCES

Anderson, D.L., 1982. Hotspots, polar wander, Mesozoic convection and the geoid. Nature, vol. 297, p. 391-393.

Asimow, P.D., Dixon, J.E., and Langmuir, C.H., 2004. A hydrous melting and fractionation model for mid-ocean ridge basalts: Application to the Mid-Atlantic Ridge near the Azores. Geochemistry, Geophysics, Geosystems, vol. 5, p. Q01E16.

Asimow, P.D., Hirschmann, M.M., Ghiorso, M.S., O'Hara, M.J., and Stolper, E.M., 1995. The effect of pressure-induced solid-solid phase transitions on decompression melting of the mantle. Geochimica et Cosmochimica Acta, vol. 59, p. 4489-4506.

Blundy, J. and Cashman, K., 2001. Ascent-driven crystallisation of dacite magmas at Mount St Helens, 1980-1986. Contributions to Mineralogy and Petrology, vol. 140, p. 631-650.

Bosworth, W., 1985. Geometry of propagating continental rifts. Nature, vol. 316, p. 625-627.

Bowen, N.L. and Schairer, J.F., 1935. The system MgO-FeO-SiO_2. American Journal of Science, Series 5, vol. 29, p. 151-217.

Campbell, I.H., 2005. Large Igneous Provinces and the Mantle Plume Hypothesis. Elements, vol. 1, p. 265-269.

Campbell, I.H, 2007. Testing the plume theory. Chemical Geology, vol. 241, p. 153-176.

Campbell, I.H. and Griffiths, R.W., 1990. Implications of mantle plume structure for the evolution of flood basalts. Earth and Planetary Science Letters, vol. 99, p. 79-93.

Chappell, B.W. and White, A.J.R., 2001. Two contrasting granite types: 25 years later. Australian Journal of Earth Sciences, vol. 48, p. 489-499.

Christensen, N.I. and Mooney, W.D., 1995. Seismic velocity structure and composition of the continental crust: A global view. Journal of Geophysical Research, vol. 100, p. 9761-9788.

Coltice, N., Phillips, B.R., Bertrand, H., Ricard, Y., and Rey, P., 2007. Global warming of the mantle at the origin of flood basalts over supercontinents. Geology, vol. 35, p. 391-394.

Dalziel, I.W.D., Lawver, L.A., and Murphy, J.B., 2000. Plumes, orogenesis, and supercontinental fragmentation. Earth and Planetary Science Letters, vol. 178, p. 1-11.

Dawes, D.W., 1992. Geological compilation map of the Thule area, Greenland. Geological Survey of Greenland, scale 1:500 000.

Denyszyn, S.W., 2008. Paleomagnetism, geochemistry and U-Pb geochronology of Proterozoic mafic intrusions in the High Arctic: Relevance to the Nares Strait problem. PhD dissertation, University of Toronto.

Denyszyn, S.W., Halls, H.C., Davis, D.W., and Evans, D.A.D., 2009. Paleomagnetism and U-Pb geochronology of Franklin dykes in High Artic Canada and Greenland: a revised age and paleomagnetic pole constraining block rotations in the Nares Strait region. Canadian Journal of Earth Sciences, vol. 46, p. 689-705.

Dostal, J., Baragar, W.R.A., and Dupuy, C., 1986. Petrogenesis of the Natkusiak continental basalts, Victoria Island, Northwest Territories, Canada. Canadian Journal of Earth Sciences, vol. 23, p. 622-632.

Ernst, R.E. and Buchan, K.L., 1997. Giant radiating dyke swarms: Their use in identifying pre-Mesozoic large igneous provinces and mantle plumes. *In:* Large Igneous Provinces: Continental, Oceanic, and Planetary Flood Volcanism, J.J. Mahoney and M.F. Coffin (eds.), American Geophysical Union, Washington.

Ernst, R.E. and Buchan, K.L., 2001. The use of mafic dike swarms in identifying and locating mantle plumes. Geological Society of America, Special Papers, vol. 352, p. 247-265.

Ernst, R.E. and Buchan, K.L., 2003. Recognizing mantle plumes in the geological record. Annual Review of Earth and Planetary Sciences, vol. 31, p. 469-523.

Falloon, T.J., Green, D.H., Hatton, C.J., and Harris, K.L., 1988. Anhydrous Partial Melting of a Fertile and Depleted Peridotite from 2 to 30 kb and Application to Basalt Petrogenesis. Journal of Petrology, vol. 29, p. 1257-1282.

Francis, D., Minarik, W., Proenza, Y., and Shi, L., 2010. An overview of the Canadian Cordilleran lithospheric mantle. Canadian Journal of Earth Sciences, vol. 47, p. 353-368.

Frisch, T., 1984a. Geology, Devon Ice Cap, District of Franklin, Northwest Territories. Geological Survey of Canada, scale 1:250 000.

Frisch, T., 1984b. Geology, Mackinson Inlet, District of Franklin, Northwest Territories. Geological Survey of Canada, scale 1:250 000.

Frisch, T., 1984c. Geology, Prince of Wales Mountains, District of Franklin, Northwest Territories. Geological Survey of Canada, scale 1:250 000.

Gass, I.G., Mallick, D.I.J., and Cox, K.G., 1973. Volcanic islands of the Red Sea. Journal of the Geological Society, vol. 129, p. 275-309.

Ghiorso, M.S. and Sack, R.O., 1995. Chemical mass transfer in magmatic processes IV. A revised and internally consistent thermodynamic model for the interpolation and extrapolation of liquid-solid equilibria in magmatic systems at elevated temperatures and pressures. Contributions to Mineralogy and Petrology, vol. 119, p. 197-212.

Ghiorso, M.S., Hirschmann, M.M., Reiners, P.W., and Kress III, V.C., 2002. The pMELTS: A revision of MELTS for improved calculation of phase relations and major element partitioning related to partial melting of the mantle to
3 GPa. Geochemistry, Geophysics, Geosystems, vol. 3, p. 1030.

Griffiths, R.W. and Campbell, I.H., 1990. Stirring and structure in mantle starting plumes. Earth and Planetary Science Letters, vol. 99, p. 66-78.

Grigne, C. and Labrosse, S., 2001. Effects of continents on Earth cooling: Thermal blanketing and depletion in radioactive elements. Geophysical Research. Letters, vol. 28, p. 2707-2710.

Harlan, S.S., Heaman, L., LeCheminant, A.N., and Premo, W.R., 2003. Gunbarrel mafic magmatic event: A key 780 Ma time marker for Rodinia plate reconstructions. Geology, vol. 31, p. 1053-1056.

Heaman, L.M., LeCheminant, A.N., and Rainbird, R.H., 1992. Nature and timing of Franklin igneous events, Canada: Implications for a Late Proterozoic mantle plume and the break-up of Laurentia. Earth and Planetary Science Letters, vol. 109, p. 117-131.

Herzberg, C. and Asimow, P.D., 2008. Petrology of some oceanic island basalts: PRIMELT2.XLS software for primary magma calculation. Geochemistry, Geophysics, Geosystems, vol. 9, p. Q09001.

Herzberg, C., Asimow, P.D., Arndt, N., Niu, Y., Lesher, C.M., Fitton, J.G., Cheadle, M.J., and Saunders, A.D., 2007. Temperatures in ambient mantle and plumes: Constraints from basalts, picrites, and komatiites. Geochemistry, Geophysics, Geosystems, vol. 8, p. Q02006.

Hill, R.I., 1991. Starting plumes and continental break-up. Earth and Planetary Science Letters, vol. 104, p. 398-416.

Klein, E.M. and Langmuir, C.H., 1987. Global Correlations of Ocean Ridge Basalt Chemistry with Axial Depth and Crustal Thickness. Journal of Geophysical Research, vol. 92, p. 8089-8115.

Langmuir, C.H., Klein, E.M., and Plank, T., 1992. Petrological systematics of mid-ocean ridge basalts: Constraints on melt generation beneath ocean ridges, in Mantle Flow and Melt Generation at Mid-Ocean Ridges. AGU Geophysical Monogragh Series, vol. 71, p. 183-280.

Li, Z.X., Kinny, P.D., Wang, J., Zhang, S., and Zhou, H., 2003. Geochronology of Neoproterozoic syn-rift magmatism in the Yangtze Craton, South China and correlations with other continents: evidence for a mantle superplume that broke up Rodinia. Precambrian Research, vol. 122, p. 85-109.

Macdonald, F.A., Halverson, G.P., Strauss, J.V., Smith, E.F., Cox, G.M., Sperling, E.A., and Roots, C.F., 2012. Early Neoproterozoic Basin Formation in Yukon, Canada: Implications for the make-up and break-up of Rodinia. Geoscience Canada, vol. 39, p. 77-99.

Macdonald, F.A., Schmitz, M.D., Crowley, J.L., Roots, C.F., Jones, D.S., Maloof, A.C., Strauss, J.V., Cohen, P.A., Johnston, D.T., and Schrag, D.P., 2010. Calibrating the Cryogenian. Science, vol. 327, p. 1241-1243.

Macdonald, F.A., Smith, E.F., Strauss, J.V., Cox, G.M., Halverson, G.P., and Roots, C.F., 2011. Neoproterozoic and early Paleozoic correlations in the western Ogilvie Mountains. *In:* Yukon Exploration and Geology 2010, K.E. MacFarlane, L.H. Weston, and C. Relf (eds.), Yukon Geological Survey, p. 161-182.

McHone, J.G., Anderson, D.L., Beutel, E.K., and Fialko, Y.A., 2005. Giant dikes, rifts, flood basalts, and plate tectonics: A contention of mantle models. Geological Society of America Special Papers, vol. 388, p. 401-420.

McKenzie, D.A.N., 1984. The Generation and Compaction of Partially Molten Rock. Journal of Petrology, vol. 25, p. 713-765.

McKenzie, D. and Bickle, M.J., 1988. The Volume and Composition of Melt Generated by Extension of the Lithosphere. Journal of Petrology, vol. 29, p. 625-679.

Mustard, P.S., 1991. Normal faulting and alluvial-fan deposition, basal Windermere Tectonic Assemblage, Yukon, Canada. Geological Society of America Bulletin, vol. 103, p. 1346-1364.

Mustard, P.S. and Donaldson, J.A., 1990. Paleokarst breccias, calcretes, silcretes and fault talus breccias at the base of upper Proterozoic "Windermere" strata, northern Canadian Cordillera. Journal of Sedimentary Research, vol. 60, p. 525-539.

Mustard, P.S. and Roots, C.F., 1997. Rift-related volcanism, sedimentation, and tectonic setting of the Mount Harper Group, Ogilvie Mountains, Yukon Territory. Geological Survey of Canada, Bulletin 492.

Obata, M. and Nagahara, N., 1987. Layering of Alpine-Type Peridotite and the Segregation of Partial Melt in the Upper Mantle. Journal of Geophysical Research, vol. 92, p. 3467-3474.

Prodehl, C., Fuchs, K., and Mechie, J., 1997. Seismic-refraction studies of the Afro-Arabian rift system — a brief review. Tectonophysics, vol. 278, p. 1-13.

Rainbird, R.H., 1993. The Sedimentary Record of Mantle Plume Uplift Preceding Eruption of the Neoproterozoic Natkusiak Flood Basalt. The Journal of Geology, vol. 101, p. 305-318.

Roeder, P.L. and Emslie, R.F., 1970. Olivine-liquid equilibrium. Contributions to Mineralogy and Petrology, vol. 29, p. 275-289.

Roots, C.F., 1987. Regional tectonic setting and the evolution of the Late Proterozoic Mount Harper volcanic complex, Ogilvie Mountains, Yukon. Doctoral dissertation, Carleton University, Ottawa, Ontario, 180 p.

Sobolev, S.V., Sobolev, A.V., Kuzmin, D.V., Krivolutskaya, N.A., Petrunin, A.G., Arndt, N.T., Radko, V.A., and Vasiliev, Y.R., 2011. Linking mantle plumes, large igneous provinces and environmental catastrophes. Nature, vol. 477, p. 312-316.

Storey, B.C., 1995. The role of mantle plumes in continental breakup: case histories from Gondwanaland. Nature, vol. 377, p. 301-308.

Takahashi, E. and Kushiro, I., 1983. Melting of a dry peridotite at high pressures and basalt magma genesis. American Mineralogist, vol. 68, p. 859-879.

Thompson, B., Mercier, E., and Roots, C., 1987. Extension and its influence on Canadian Cordilleran passive-margin evolution. Geological Society, London, Special Publications, vol. 28, p. 409-417.

Tosca, N.J., Macdonald, F.A., Strauss, J.V., Johnston, D.T., and Knoll, A.H., 2011. Sedimentary talc in Neoproterozoic carbonate successions. Earth and Planetary Science Letters, vol. 306, p. 11-22.

Turner, S. and Hawkesworth, C., 1995. The nature of the sub-continental mantle: constraints from the major-element composition of continental flood basalts. Chemical Geology, vol. 120, p. 295-314.

Villiger, S., Ulmer, P., Müntener, O., and Thompson, A.B., 2004. The Liquid Line of Descent of Anhydrous, Mantle-Derived, Tholeiitic Liquids by Fractional and Equilibrium Crystallization—an Experimental Study at 1·0 GPa. Journal of Petrology, vol. 45, p. 2369-2388.

Walter, M.J., 1998. Melting of Garnet Peridotite and the Origin of Komatiite and Depleted Lithosphere. Journal of Petrology, vol. 39, p. 29-60.

Watson, S. and McKenzie, D.A.N., 1991. Melt Generation by Plumes: A Study of Hawaiian Volcanism. Journal of Petrology, vol. 32, p. 501-537.

Wiart, P. and Oppenheimer, C., 2000. Largest known historical eruption in Africa: Dubbi volcano, Eritrea, 1861. Geology, vol. 28, p. 291-294.

Wyllie, P.J., 1988. Solidus Curves, Mantle Plumes, and Magma Generation Beneath Hawaii. Journal of Geophysical Research, vol. 93, p. 4171-4181.

APPENDIX 1:

Table S1. *New* major element data for the volcanic rocks of the Mount Harper volcanic complex.*

Sample #	MH10-005	MH10-033	MH10-019	MH10-026	MH10-027	MH10-447	MH10-448	MH10-034	MH10-035	MH10-036	MH10-047	MH10-051	MH10-052B	MH10-054	MH10-059	MH10-071	MH10-072	MH10-064
Member	A	A	B	B	B	B	B	D	D	D	D	D	D	D	D	E	E	F
SiO_2	51.35	49.4	62.18	52.62	52.04	51.53	51.09	71.27	72.41	72.73	78.37	72.63	70.96	74.14	74.09	58.71	59.01	56.79
TiO_2	1.02	0.69	0.47	1.00	1.04	0.68	0.7	0.52	0.48	0.49	0.4	0.5	0.5	0.41	0.49	1.37	1.34	0.73
Al_2O_3	17.06	15.53	15.3	17.21	17.13	14.71	14.72	13.5	13.16	13.19	10.03	13.43	13.27	10.77	12.82	13.76	13.7	15.58
Fe_2O_3	1.95	1.83	1.34	1.46	1.65	1.74	1.82	0.69	0.75	0.71	0.43	0.42	0.76	0.7	0.48	1.84	1.87	1.31
FeO	9.8	9.19	6.74	7.36	8.29	8.76	9.15	3.45	3.78	3.58	2.15	2.12	3.82	3.53	2.42	9.27	9.39	6.58
FeOT	11.55	10.84	7.95	8.67	9.77	10.33	10.79	4.07	4.45	4.22	2.54	2.50	4.50	4.16	2.85	10.93	11.07	7.76
MnO	0.18	0.2	0.07	0.17	0.18	0.18	0.18	0.03	0.03	0.03	0.02	0.05	0.09	0.09	0.07	0.2	0.2	0.13
MgO	5.61	9.01	6.43	5.24	5.18	7.93	8.5	0.76	0.62	1.04	0.46	0.4	0.64	1.21	0.58	3.28	4.45	4.81
CaO	9.91	11.63	2.18	11.59	11.2	12.22	12.02	1.77	1.26	1.15	1.06	2.19	3.5	3.1	1.77	7.07	5.36	8.05
Na_2O	2.22	2.13	4.29	2.18	2.15	1.62	1.49	0.27	1.31	0.17	0.43	2.03	0.38	1.32	0.4	1.53	1.75	4.32
K_2O	0.62	0.36	0.95	1.04	1.02	0.55	0.26	7.54	6.02	6.7	6.53	6.03	5.89	4.58	6.73	2.69	2.64	1.58
P_2O_5	0.27	0.05	0.06	0.12	0.13	0.08	0.08	0.2	0.2	0.21	0.12	0.19	0.19	0.14	0.15	0.29	0.28	0.12
Total	100	100	100	100	100	100	100	100	100	100	100	100	100	100	100	100	100	100
LOI	4.18	2.78	4.61	4.85	4.72	2.41	2.87	3.12	2.46	2.84	1.98	2.69	4.55	4.17	2.99	3.32	3.52	5.73
Normative Minerology																		
Q	3.11	0.00	14.67	3.54	3.05	2.14	2.34	34.23	36.14	40.30	46.91	31.72	35.68	39.41	40.24	16.35	15.75	1.43
or	3.66	2.13	5.61	6.15	6.03	3.25	1.54	44.56	35.57	39.60	38.59	35.64	34.81	27.07	39.77	15.90	15.60	9.34
ab	18.79	18.02	36.30	18.45	18.19	13.71	12.61	2.28	11.08	1.44	3.64	17.18	3.22	11.17	3.38	12.95	14.81	36.56
an	34.76	31.75	10.42	34.11	34.08	31.24	32.71	7.47	4.94	4.33	4.47	9.62	16.12	9.94	7.80	22.73	21.73	18.45
C	0.00	0.00	3.39	0.00	0.00	0.00	0.00	2.16	2.68	4.07	0.61	0.04	0.36	0.00	2.02	0.00	0.00	0.00
di	10.49	20.90	0.00	18.60	17.05	23.60	21.57	0.00	0.00	0.00	0.00	0.00	0.00	3.82	0.00	8.79	2.53	17.03
hy	23.80	13.21	26.64	14.87	16.94	22.06	25.09	6.86	7.13	7.82	4.12	3.81	7.32	6.48	4.81	17.35	23.68	13.63
ol	0.00	9.93	0.00	0.00	0.00	0.00	0.00	0.00	0.00	0.00	0.00	0.00	0.00	0.00	0.00	0.00	0.00	0.00
mt	2.83	2.65	1.94	2.12	2.39	2.52	2.64	1.00	1.09	1.03	0.62	0.61	1.10	1.02	0.70	2.67	2.71	1.90
il	1.94	1.31	0.89	1.90	1.98	1.29	1.33	0.99	0.91	0.93	0.76	0.95	0.95	0.78	0.93	2.60	2.55	1.39
ap	0.63	0.12	0.14	0.28	0.30	0.19	0.19	0.46	0.46	0.49	0.28	0.44	0.44	0.32	0.35	0.67	0.65	0.28

*For results described in this paper, these were combined with data from Mustard and Roots (1997). From this previous work, the following samples were used:

Member A: 127-2, 128-3; Member B: 97a, 118-3, 126-2, 128-15, 129-0, 158-1, 158-2, 162-1.

Member D: 44, 48-1, 103, 138-1, 138-2, 138-3, 138-4, 154, 166; Member E: 72-2, 79-1, 82-4, 99, 144-6; Member F: 121-7; 161

Analytic methods:

Rock samples were first trimmed to remove weathered surfaces and then cut into ~5 cm^3 fragments using a diamond-bladed rock saw. The rocks were crushed to rock chips on a iron jaw crusher. The chips where milled in a hardened steel mill until the powder could pass through a 75 µm mesh. Major and trace element abundances were analysed by X-ray fluorescence using a Philips PW2400 4kW automated XRF spectrometer system with a rhodium 60 kV end window X-ray tube. Major elements, Cr, Ni, and V were analysed using 32 mm diameter fused beads prepared from a 1:5 sample/lithium tetraborate mixture. Sc, Rb, Sr, Zr, Nb, and Y were analysed using 40 mm diameter pressed pellets prepared at a pressure of 20 tonnes from a mixture of 10 g sample powder with 2 g Hoechst Wax C Micropowder. Calibration regression lines were prepared using between 15 and 40 International Standard Reference Materials. Corrections for mass absorption effects were applied on concentration values using a combination of alpha coefficients and/or Compton scatter. The accuracy for silica is within 0.5% absolute, 1% for other majors, and within 5% for trace elements. Instrument precision is within 0.3% relative, generally within 0.23% relative, and the overall precision for beads and pressed pellets is within 0.5% relative.

Besa River Formation in Liard basin, southeast Yukon: Report on 2012 reconnaissance fieldwork

Tiffani Fraser[1]
Yukon Geological Survey

Fil Ferri
Oil and Gas Division, BC Ministry of Energy, Mines and Natural Gas

Kathryn Fiess
Northwest Territories Geoscience Office

Leanne Pyle
VI Geoscience Services Ltd.

Fraser, T., Ferri, F., Fiess, K., and Pyle, L., 2012. Besa River Formation in Liard basin, southeast Yukon: Report on 2012 reconnaissance fieldwork. *In:* Yukon Exploration and Geology 2012, K.E. MacFarlane, M.G. Nordling, and P.J. Sack (eds.), Yukon Geological Survey, p. 37-46.

ABSTRACT

Prospective Devonian - Mississippian shale gas strata in Liard basin are the focus of a new collaborative study among research scientists of the Yukon Geological Survey, Northwest Territories Geoscience Office, and British Columbia Ministry of Energy, Mines and Natural Gas. Reconnaissance fieldwork in July 2012 involved measuring and sampling outcrops in each jurisdiction. One hundred eighty-seven metres of Besa River Formation shale and mudstone was measured and described in the Yukon part of Liard basin (NTS 95C/11). The section comprises three lithofacies: 1) mudstone and shale; 2) silty mudstone and shale; and 3) interbedded mudstone/shale and silty mudstone and shale. Shale is generally recessive, fissile, carbonaceous, very thinly laminated (<1 cm), and black on fresh surfaces. Mudstone is more competent than shale, thin to medium-bedded (1-5 cm), and medium to dark grey on fresh surfaces. Mudstone has variable silt and silica components based on observations of hand samples. Fossils are rare and include cephalopod impressions and unidentified biological fragments. The sampling program involved spectral gamma-radiation readings at one-metre intervals, and chip samples through two-metre intervals for Rock-Eval/total organic carbon, vitrinite reflectance, X-ray diffraction mineralogy, lithogeochemistry, and microfossil biostratigraphy. Laboratory results are anticipated in 2013.

[1]*tiffani.fraser@gov.yk.ca*

INTRODUCTION

The most prospective shale gas exploration targets in western Canada are the widespread organic-rich, Devonian – Mississippian, black shale and mudstone formations of the Western Canadian Sedimentary Basin (Ross and Bustin, 2008). In an effort to improve our understanding of this potential resource in Yukon, the Yukon Geological Survey (YGS) initiated a shale gas study of Devonian - Carboniferous strata in Liard basin. In July 2012, geologists from YGS, Northwest Territories Geoscience Office (NTGO), and British Columbia Ministry of Energy, Mines and Natural Gas (BCMEMNG) visited outcrops of Besa River (Yukon and BC) and Golata Formation (NWT) of the Liard basin to measure and sample one stratigraphic section in each jurisdiction. This paper presents observations from a Besa River Formation section measured in southeast Yukon, NTS mapsheet 95C/11.

STUDY AREA

The area underlain by strata of the Liard basin spans parts of Yukon, British Columbia, and Northwest Territories including parts of NTS 95C, D and 94 J, K, N, O (Fig. 1). The Yukon portion of the basin covers an area of 6500 km^2 and forms the extreme southeastern corner of the territory. Access to the region is by helicopter from either Watson Lake, Yukon or Fort Liard, NWT. A network of access roads to the Kotaneelee gas plant are accessible by barge, west of Liard River. Airstrips exist at Kotaneelee and Beaver River gas fields, the latter on the BC side of the border.

EXPLORATION HISTORY

Exploration in the Liard region began in 1955 with fieldwork by California Standard (later Chevron; National Energy Board, 2001). Drilling began in BC in 1957 on

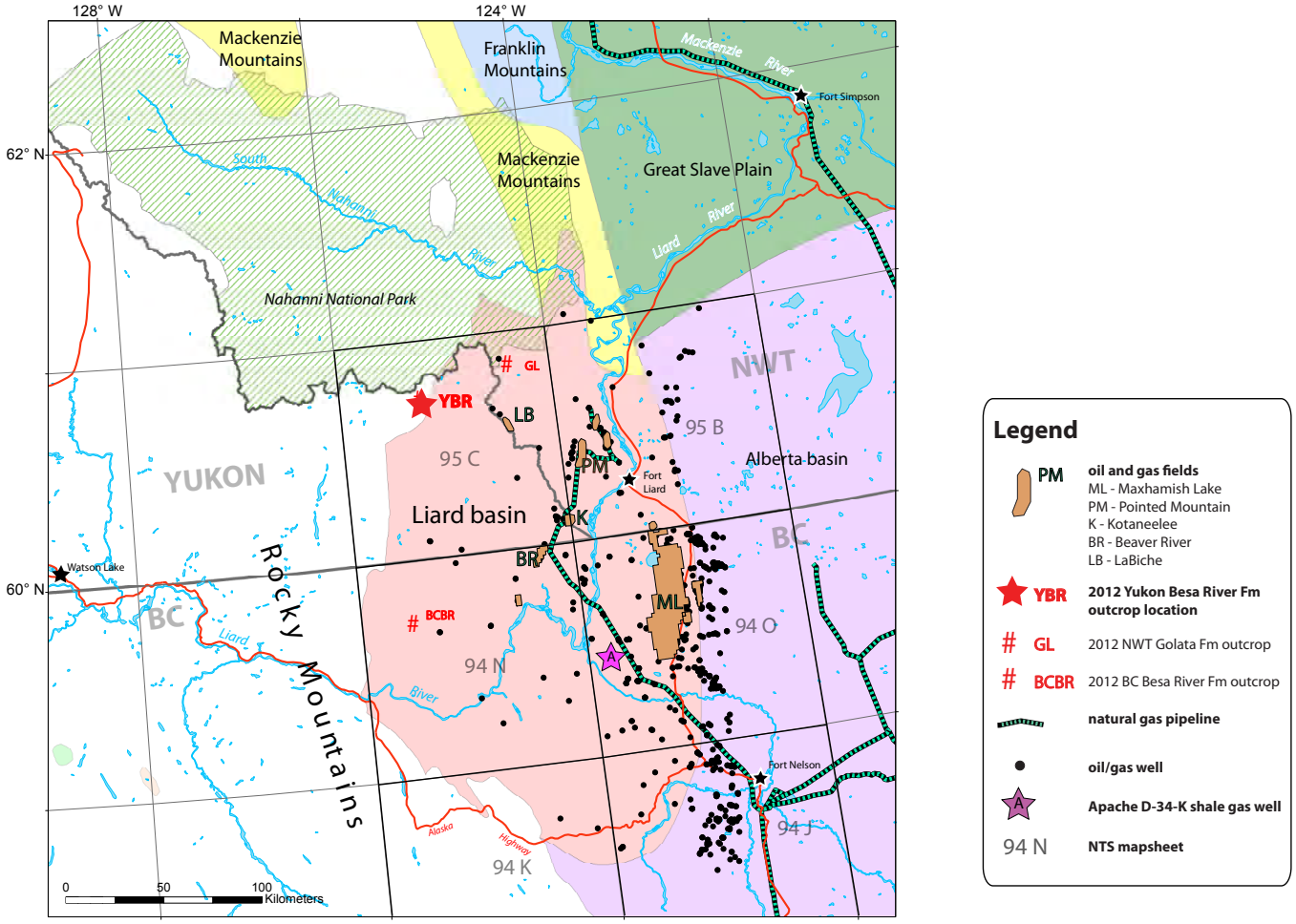

Figure 1. *Location of Liard and adjacent sedimentary basins (after Mossop et al., 2004), oil and gas activity, and 2012 field locations.*

the Beaver River anticline near the Yukon border (Pan Am A-1 Beaver River well). This well is notable for the present study because it encountered a blow-out in fractured shales and siltstone of the Besa River Formation at a depth of 2549 metres below Kelly Bushing. The first well drilled in the Liard area of Yukon was Pan Am et al A-1 Kotaneelee YT P-50 discovery well in 1963, also on the Beaver River structure. Since then, 12 additional wells have been drilled, the most recent of which was in Kotaneelee in 2005 (Devon et al Kotaneelee L-38). Of the thirteen wells, eight are currently abandoned, one is suspended gas, three are flowing gas, and one is a disposal well (Energy, Mines and Resources, 2012). In addition, 570 km of 2D-seismic data have been acquired for the Yukon portion of the basin (Energy, Mines and Resources, 2011). The main exploration target has been the Manetoe hydrothermal dolomite facies in the Middle Devonian Nahanni Formation (Dunedin Formation equivalent).

Portions of three gas fields extend into the Yukon including Kotaneelee, Beaver River, and LaBiche (Fig. 1). Kotaneelee recently suspended gas production in Fall 2012 (J. Ewert, pers comm, 2012). Produced gas was transported to Fort Nelson by the Beaver River lateral pipeline. Current Yukon land dispositions in the region include eight production licenses in Kotaneelee and two special discovery licenses in La Biche.

Liard basin has been explored more actively in NWT and BC. Eighty-one wells have been drilled in NWT to date, and over 400 in BC. BC has recently had a remarkable shale gas discovery in the basin. Apache's D-34-K well (Fig. 1), drilled in 2009, has been called "the most prolific shale gas resource test in the world" (Macedo, 2012). The projected formation is listed as the Upper Devonian Fort Simpson, an equivalent of the Besa River Formation. The well had a 30-day initial production rate of 21.2 MMcf per day and an estimated ultimate recovery of 17.9 Bcf (Macedo, 2012).

REGIONAL GEOLOGY

Liard basin lies within the eastern part of the Canadian Cordillera and consists of broadly folded Paleozoic and Mesozoic strata (Fig. 2). The basin was originally defined on the basis of its thick Carboniferous Mattson Formation (Gabrielse, 1967), but it also preserves a thick Cretaceous section (MacLean and Morrow, 2004). The eastern margin of the basin is marked by the north-trending Bovie fault (Fig. 2; Williams, 1977; Leckie *et al.*, 1991; Wright *et al.*, 1994; MacLean and Morrow, 2004). This feature separates a thicker Paleozoic - Mesozoic succession in Liard basin to the west from a thinner succession in the Interior Plain (Morrow *et al.*, 2006), and has dropped prospective Devonian shale gas horizons much deeper in Liard basin compared with the Horn River basin east of the fault (Ferri *et al.*, 2011; Fig. 3).

STRATIGRAPHY

Liard basin is a sub-basin of the extensive Western Canadian Sedimentary Basin and has a stratigraphic succession comparable to that in neighbouring northeast BC and northwest Alberta. The region preserves a thick (maximum >6000 m) sedimentary package ranging in age from Cambrian to Cretaceous (National Energy Board, 2001). Basement Proterozoic siliciclastic and volcaniclastic sediments are overlain by Cambrian to Middle Devonian carbonate and minor siliciclastic rocks that, from Silurian time, transition westward and northward to basinal shales of the Road River Group (Fallas *et al.*, 2004, 2005). Overlying the carbonates are shales of the Devonian – Mississippian Besa River Formation (Figs. 3 and 4; discussed below). The uppermost Besa River Formation grades eastwardly into Mississippian Golata Formation shale and carbonate (Richards, 1989; Hynes *et al.*, 2003). During the late Mississippian and early Pennsylvanian, a thick package of deltaic sandstone was deposited over the study area (Mattson Formation; Richards, 1989). Pennsylvanian and Permian strata consist of shale and carbonate of the Kindle and Fantasque formations which are overlain by Triassic shale and siltstone of the Toad-Grayling Formation (Pigage, 2006, 2007). The basin is overlain by Cretaceous foreland basin sandstone and shale (Leckie *et al.*, 1991).

This field study focuses on the Middle Devonian to Lower Carboniferous Besa River Formation. The type section is located 1.2 km north of the Muskwa River, in the Kluachesi Lake area (NTS 94G/13) in northeastern BC (Kidd, 1963). In Liard basin, the Besa River Formation contains basinal equivalents to the platform carbonate succession of the Upper Keg River to Debolt formations (Figs. 3 and 4; Ferri *et al.*, 2011). The Besa River Formation also contains facies equivalents of the Horn River, Fort Simpson, Exshaw, and Golata formations. Organic-rich black shale source rocks in the lower part of the Besa River Formation are equivalent to the rich source rocks in the Middle Devonian Horn River Group in Mackenzie Plain area (Morrow *et al.*, 1993). The "first black shale" in the Besa River Formation is another known source

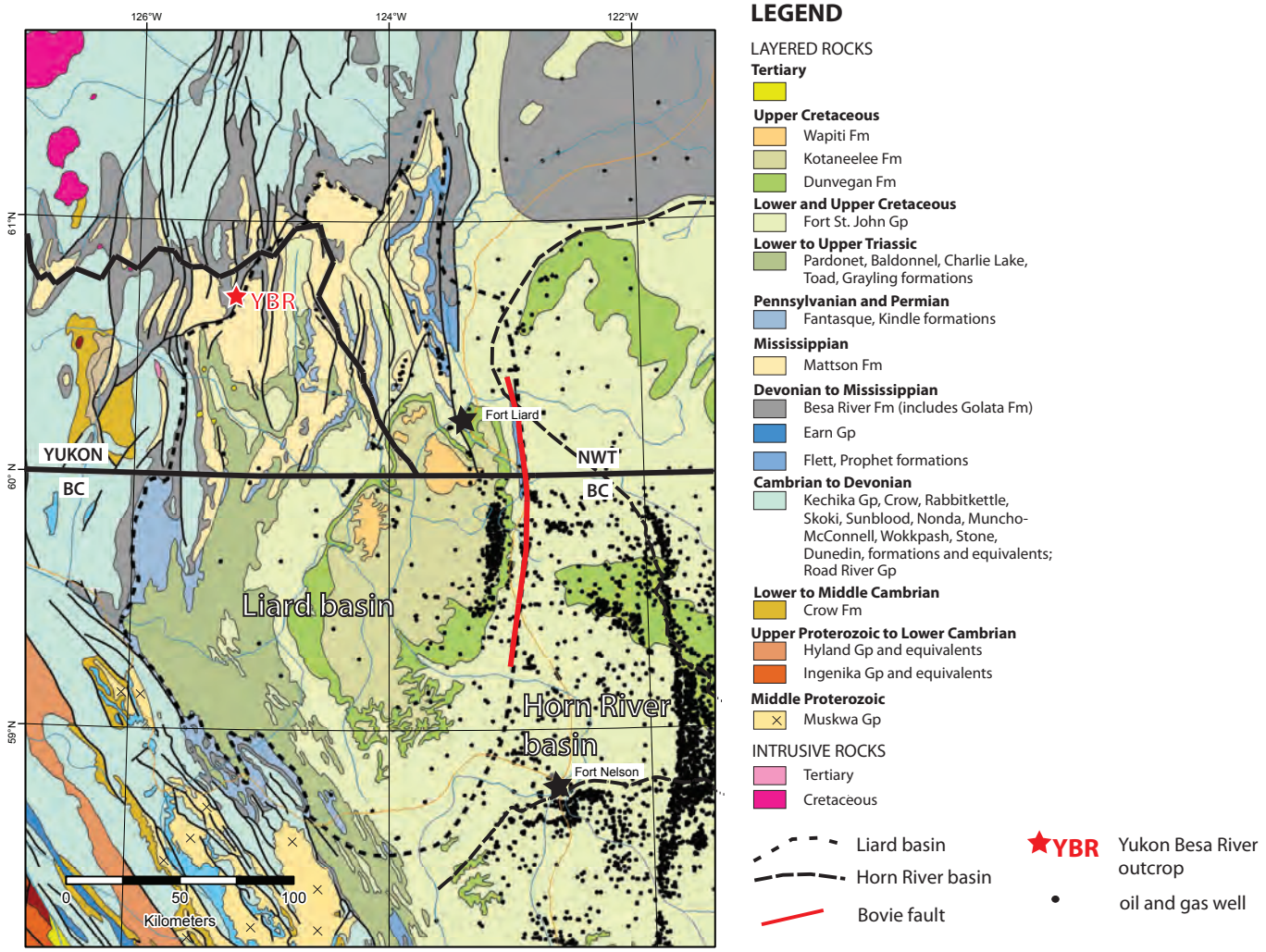

Figure 2. *Geological map of Liard basin region. Also shown is Horn River basin, oil and gas wells, Bovie fault surface trace, and the location of the Yukon Besa River section. Generalized geological map units after Wheeler and McFeeley (1991). Outline of Liard basin is from Mossop et al. (2004). Eastern limit of Horn River basin is eastern limit of Horn River Group shale (Oldale and Munday, 1994).*

rock, a lateral equivalent to the uppermost Devonian to lowermost Carboniferous Exshaw Formation (Fowler *et al.*, 2001). Besa River Formation is conformably overlain by the Middle to Upper Mississippian Mattson Formation (Richards, 1989).

FIELDWORK

Fieldwork was based out of Fort Liard, NWT, in July 2012. One day of aerial reconnaissance identified shale outcrops in NWT and Yukon. As anticipated, the recessive nature of shale posed challenges in finding complete, continuous, and accessible sections. Six days were spent measuring stratigraphic sections in NWT (Golata Formation), Yukon (middle Besa River Formation), and BC (lower Besa River Formation). The Yukon Besa River section, which is the subject of this paper, was measured on July 10th and 11th.

A team of five field workers (4 geologists, 1 assistant) measured, described, and sampled 187 m of Besa River Formation shale and mudstone. The section is located on the north side of an east-west tributary of Whitefish River, NTS 95C/11 (Figs. 1 and 5). The east-southeastwardly dipping section was measured over five segments. Total stratigraphic thickness, including two large covered intervals, is approximately 254 m. The Besa River Formation overlies resistant Devonian carbonate in the region, but the basal contact of the formation is rarely exposed in this area of Yukon, with the exception

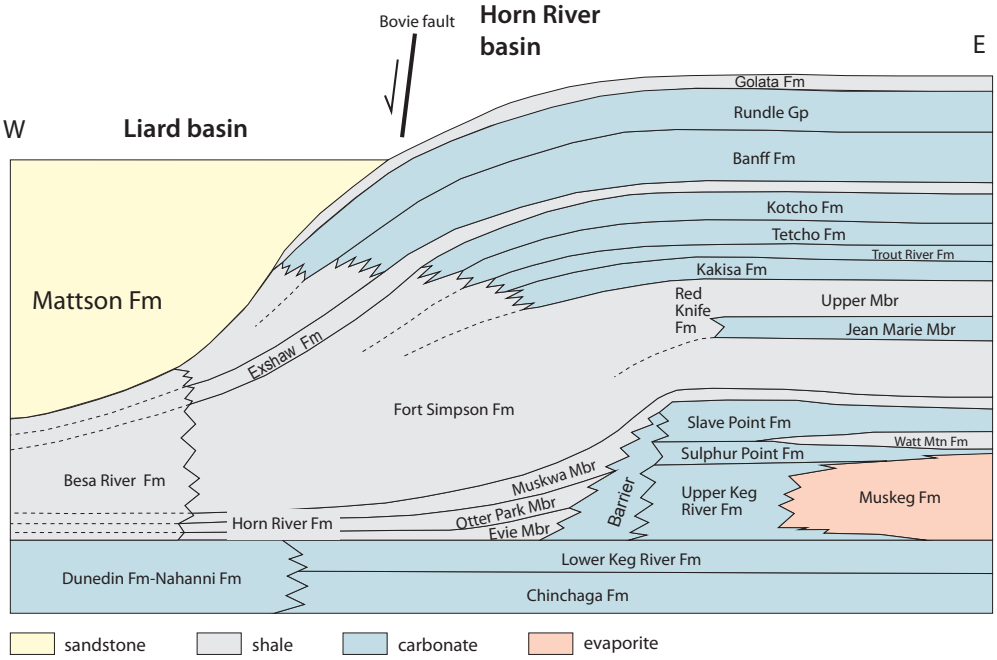

Figure 3. *Schematic diagram showing facies transitions of Middle to Upper Paleozoic shelf and offshelf successions from west to east across Bovie fault (after Ferri et al., 2011). Note that the Besa River facies equivalents include the Horn River, Fort Simpson, Exshaw, and Golata formations. Ages of units indicated in Figure 4.*

of an inaccessible cliff-section in the Pool Creek area (NTS 95C/5). Likewise, the upper contact with the resistant sandstone of the Mattson Formation was also not exposed. The section is thought to be in the middle part of the Besa River Formation, pending further refinement from microfossil dating.

In the field, detailed lithological descriptions were made of the section. Spectral gamma-radiation counts (GR) of uranium, thorium, and potassium were measured with a handheld spectrometer at one-metre intervals. Shale chip samples were collected through two-metre intervals for: Rock-Eval/total organic carbon (RE/TOC); vitrinite reflectance (VR); inductively coupled plasma-emission/mass spectroscopy lithogeochemistry (ICP-ES/MS); x-ray diffraction mineralogy (XRD) and; microfossil biostratigraphy.

FIELD OBSERVATIONS

The graphical log for the Yukon Besa River section (Fig. 6) identifies main rock types and lithofacies, units measured in the field, and locations of chip and microfossil samples. Three main lithofacies were identified in approximately equal proportions: mudstone and shale; silty mudstone and shale and; an interbedded mudstone and shale and silty mudstone and shale.

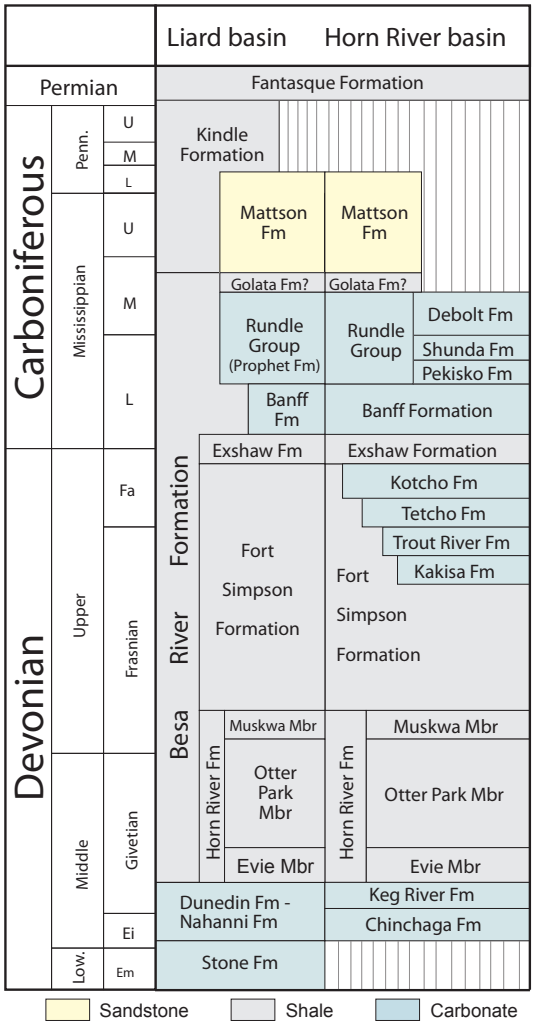

Figure 4. *Time-stratigraphic chart of middle to upper Paleozoic strata of Liard and Horn River basins (after Ferri et al., 2011).*

The mudstone and shale lithofacies is composed of the finest-grained rock types. It is dark grey to black on fresh surfaces, and weathers to a variety of colours including light to medium grey, orange-brown, and blue-grey,

Figure 5. *Besa River Formation outcrop on a tributary of Whitefish River, NTS 095C/11.*

with local yellow-brown coatings (possibly jarosite). This lithofacies contains interbedded mudstone and shale, with shale normally accounting for <50% and often as little as 5% of the unit (e.g., Fig. 7). All beds and laminations are planar. The shale component is fissile to platy, weathering into thin (<1 cm) paper sheets or laminae. It is locally soft and sooty or earthy in nature, crumbling easily (Fig. 8). These sootier intervals are commonly carbonaceous. The mudstone component is more competent in nature than the shale, weathering as plates or blocks up to 5 cm thick. Bedding is 1-5 cm thick on average. Locally, it is highly siliceous in nature, with chert-like properties such as a conchoidal fracture and a characteristic porcelain-breaking sound.

A silty mudstone and shale lithofacies is a marginally coarser grained and overall more competent unit than the mudstone and shale lithofacies. It is dark grey to black on fresh surfaces, and weathers grey, beige, yellow, orange, and rusty brown in colour. The silty mudstone intervals dominate the section with shale forming, thin

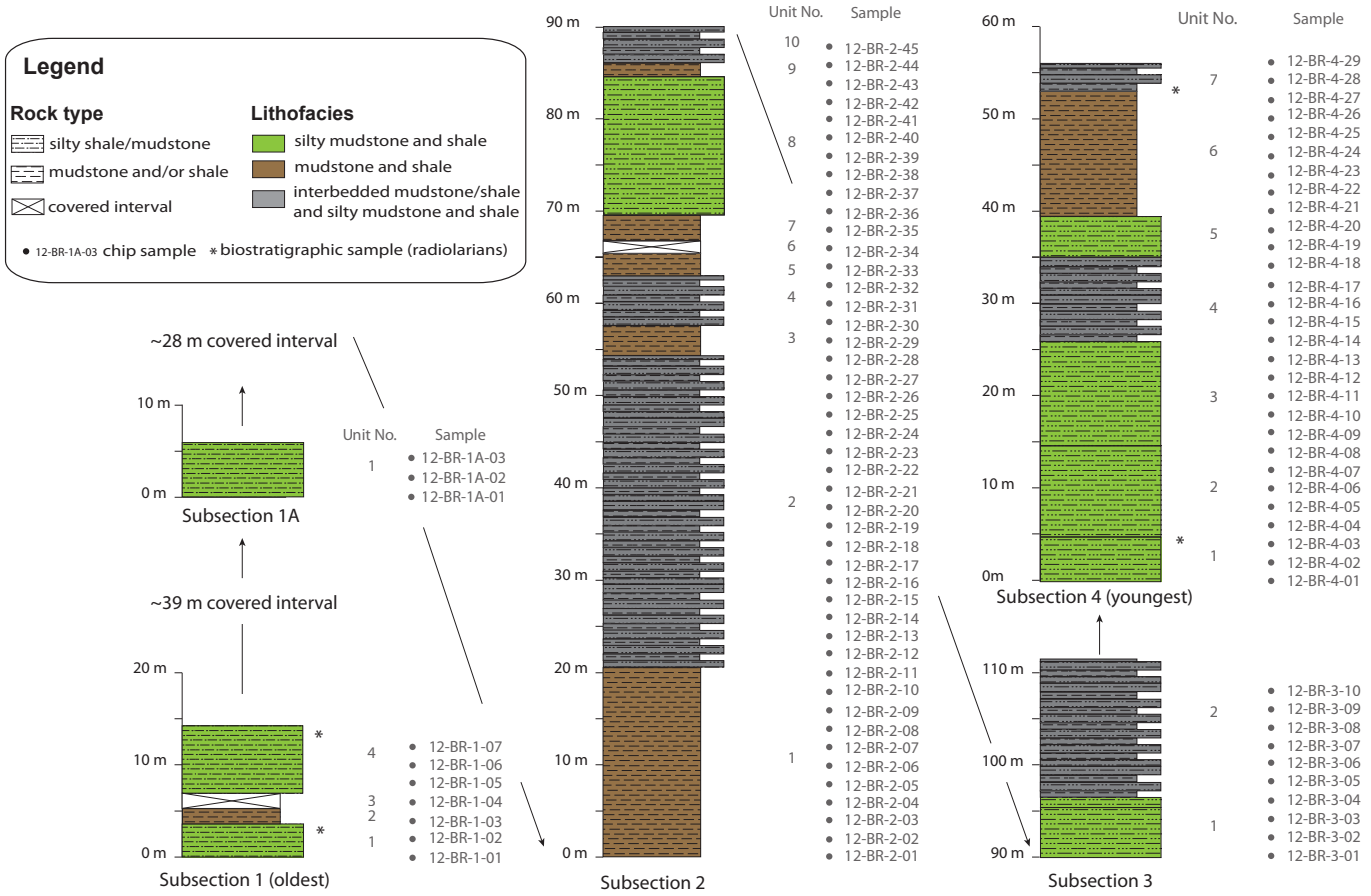

Figure 6. *Measured stratigraphic section from Besa River Formation, shown in Figure 5. All listed samples will be analysed for RockEval/TOC and ICP-ES/MS lithogeochemistry. A subset of these samples will be analysed for VR and XRD mineralogy. Note samples submitted for biostratigraphy (radiolarian identification).*

Figure 7. *Mudstone and shale lithofacies. Mudstone intervals are thicker and more resistant than shale intervals, and weather into blocks. Shale in this section is <10% and forms thin (<1 cm) partings between blockier mudstone beds. Rock hammer for scale.*

Figure 8. *Black, soft, sooty shale interval (near point of hammer) between more resistant mudstone beds.*

(<5 cm) interbeds or partings. Silty mudstone intervals are up to 15 cm thick and weather into thick plates or blocks of this thickness (Fig. 9). Silt-sized silica grains are commonly visible on bedding surfaces. Beds are planar and generally 1-5 cm thick. It is locally carbonaceous, and highly siliceous, forming chert-like beds. Shale interbeds are fissile, recessive, carbonaceous, and weather in thin papery sheets (Fig. 10).

The third lithofacies, interbedded mudstone and shale and silty mudstone and shale, is a combination of the units described above in approximately equal proportions. The lithofacies appears with gradational boundaries between lithologies. Locally, this lithofacies is very competent, particularly in siliceous intervals.

Overall the bedding is planar and homoclinal. Local variations from this occur where beds may be truncated, folded, faulted, and form brecciated zones (Fig. 11), possibly from syn-sedimentary deformation and/or regional tectonics.

The strata are generally barren of macrofossils; however, scree below the section contains rare cephalapod impressions (Fig. 12). Unidentified biological remains were

Figure 9. *Siliceous silty mudstone and shale outcrop. Mudstone is resistant and forms >90% of unit. The silty mudstone weathers into blocks with semi-conchoidal fracture. Shale is observed as thin partings (<1 cm) between mudstone beds.*

Figure 10. *Shale-dominant unit showing thin planar laminations weathering into thin, paper-like sheets.*

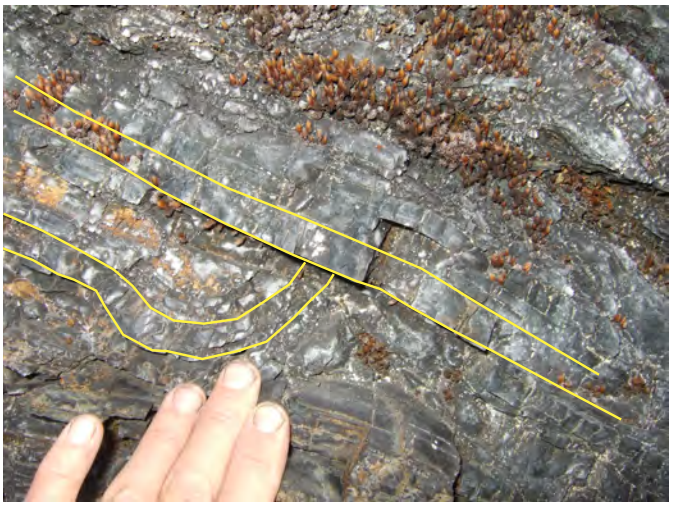

Figure 11. *Zone of deformed strata showing folded, truncated and brecciated shale beds. Yellow lines denote bedding surfaces.*

also seen on bedding surfaces (Fig. 13). Several samples have been submitted for radiolarian biostratigraphy.

Mineralogy is difficult to determine in the field due to the fine-grained nature of the rocks. Silica-dominant zones are identified based on chert-like properties and the competent nature of some intervals. In addition, minor, disseminated pyrite grains occur on bedding surfaces.

Samples for RE/TOC, VR, ICP-MS/ES, XRD, and microfossil biostratigraphy are currently undergoing analysis in respective laboratories.

Figure 12. *Cephalopod fossil impression on bedding surface.*

Figure 13. *Possible fossils on bedding surface of weathered scree. These features occur throughout the section.*

CONCLUSIONS AND FUTURE WORK

A collaborative geoscience study of Devonian to Carboniferous shale units in Liard basin was initiated by YGS, NTGO, and BCMEMNG in 2012 with goals of improving the knowledge of the regional Upper Devonian – Lower Carboniferous geology, including stratigraphy, sedimentology, correlation and distribution of shale units, and hydrocarbon potential. In 2012, one section was measured in each jurisdiction. In southeast Yukon, a 189 m section of middle Besa River Formation was measured on a tributary of Whitefish River, NTS 95C/11. Samples were collected for RE/TOC, VR, ICP-MS/ES lithogeochemistry, XRD mineralogy, and biostratigraphy. Spectral gamma-ray radiation was measured to aid in future correlation with subsurface gamma logs from wells.

Further fieldwork is anticipated for the future. Identifying new Besa River Formation outcrop sections will be critical in moving this project forward. In addition, correlating outcrop sections to subsurface well logs will define the regional distribution of Devonian shale in the Liard basin area. Comments or suggestions on future research in this area are encouraged.

ACKNOWLEDGEMENTS

Funding for the project came from the Yukon Geological Survey, Northwest Territories Geoscience Office, and British Columbia Ministry of Energy, Mines and Natural Gas. Arend Stamhuis provided superior field and lab assistance. The Geological Survey of Canada is

acknowledged for labwork support and the use of the gamma-ray spectrometer. Great Slave Helicopters supplied excellent flying services to field locations. The manuscript was reviewed by Don Murphy, Yukon Geological Survey.

REFERENCES

Energy, Mines and Resources, 2011. Yukon oil and gas, a northern investment opportunity 2011. URL http://www.emr.gov.yk.ca/oilandgas/index.html. Adobe file downloaded December 15, 2012.

Energy, Mines and Resources, 2012. Well activity record. URL http://www.emr.gov.yk.ca/oilandgas/exploration.html. Excel spreadsheet downloaded December 15, 2012.

Fallas, K.M., Pigage, L.C., and MacNaughton, R.B. (comps.), 2004. Geology, LaBiche River southwest (95C/SW), Yukon Territory and British Columbia. Geological Survey of Canada, Open File 4664, 1:100 000, 2 sheets.

Fallas, K.M., Pigage, L.C., and Lane, L.S. (comps.), 2005. Geology, La Biche River northwest (96C/NW), Yukon and Northwest Territories. Geological Survey of Canada, Open File 5018, scale 1:100 000.

Ferri, F., Hickin, A.S., and Huntley, D.H., 2011. Besa River Formation, western Liard basin, British Columbia (NTS 094N); geochemistry and regional correlations. Geoscience Reports 2011, British Columbia Ministry of Energy and Mines, p. 1-18.

Fowler, M.G., Stasiuk, L.D., Hearn, M., and Obermajer, M., 2001. Devonian hydrocarbon source rocks and their derived oils in the Western Canadian Sedimentary Basin. Bulletin of Canadian Petroleum Geology, vol. 49, p. 117-148.

Gabrielse, H., 1967. Tectonic evolution of the northern Canadian Cordillera. Canadian Journal of Earth Sciences, vol. 4, p. 271-298.

Hynes, G.F., Fallas, K.M., and Lane, L.S., 2003. Geology, Etanda Lakes, (95C/16), Northwest Territories and Yukon Territory. Geological Survey of Canada, Open File 1676, scale 1:50 000.

Kidd, F.A., 1963. The Besa River Formation. Bulletin of Canadian Petroleum Geology, vol. 11, p. 369-372.

Leckie, D.A., Potocki, D.J., and Visser, K., 1991. The Lower Cretaceous Chinkeh Formation: a frontier type play in the Liard basin of western Canada. Bulletin of the American Association of Petroleum Geologists, vol. 75, p. 1324-1352.

Macedo, R., 2012. Apache validates new shale play in B.C.'s Liard basin. Daily Oil Bulletin, June 14, 2012.

MacLean, B.C. and Morrow, D.W., 2004. Bovie structure: its evolution and regional context. Bulletin of Canadian Petroleum Geology, vol. 52, p. 302-324.

Morrow, D.W., Potter, J., Richards, B., and Goodarzi, F., 1993. Paleozoic burial and organic maturation in the Liard Basin region, northern Canada. Bulletin of Canadian Petroleum Geology, vol. 41, p. 17-31.

Morrow, D.W., Jones, A.L., and Dixon, J., 2006. Infrastructure and resources of the Northern Canadian Sedimentary Basin. Geological Survey of Canada, Open File 5152, 59 p.

Mossop, G.D., Wallace-Dudley, K.E., Smith, G.G., and Harrison, J.C. (comps.), 2004. Sedimentary basins of Canada; Geological Survey of Canada, Open File Map 4673, scale 1:5 000 000.

National Energy Board, 2001. Petroleum resource assessment of the Liard plateau, Yukon Territory, Canada. Oil and Gas Resources Branch, Department of Economic Development, Government of Yukon.

Oldale, H.S. and Munday, R.J., 1994. Devonian Beaverhill Lake Group of the Western Canada Sedimentary basin (Chapter 11). *In:* Geological Atlas of the Western Canada Sedimentary Basin, G.D. Mossop and I. Shetsen (comps.), Canadian Society of Petroleum Geologists and Alberta Research Council, URL http://www.ags.gov.ab.ca/publications/wcsb_atlas/atlas.html, accessed December 13, 2012.

Pigage, L.C., 2006. Stratigraphy summary for southeast Yukon (NTS 95D/8 and 95C/5). *In:* Yukon Exploration and Geology 2005, D.S. Emond, G.D. Bradshaw, L.L. Lewis, and L.H. Weston (eds.), Yukon Geological Survey, p. 267-285.

Pigage, L., 2007. Yukon Stratigraphic Correlation Chart, v. 3.0. Yukon Geological Survey and Oil and Gas Management Branch, Yukon Geological Survey, Open File 2007-2.

Richards, B.C., 1989. Uppermost Devonian and Lower Carboniferous stratigraphy, sedimentation, and diagenesis, southwestern District of Mackenzie and Southeastern Yukon Territory. Geological Survey of Canada, Bulletin 390.

Ross, D.J.K. and Bustin, R.M., 2008. Characterizing the shale gas resource potential of Devonian-Mississippian strata in the Western Canada sedimentary basin: application of an integrated formation evaluation. American Association of Petroleum Geologists Bulletin, vol. 92, p. 87-125.

Wheeler, J.O. and McFeely, P., 1991. Tectonic Assemblage Map of the Canadian Cordillera and Adjacent Parts of the United States of America: Geological Survey of Canada, Map 1712A, 1:2 000 000.

Williams, G.K., 1977. The Celibeta structure compared with other basement structures on the flanks of the Tathlina high, district of Mackenzie. Geological Survey of Canada, Paper 77-1B, p. 301-310.

Wright, G.N., McMechan, M.E., and Potter, D.E.G., 1994. Structure and architecture of the western Canada Sedimentary basin (Chapter 3). *In:* Geological Atlas of the Western Canada Sedimentary Basin, G.D. Mossop and I. Shetsen (comps.), Canadian Society of Petroleum Geologists and Alberta Research Council. URL http://www.ags.gov.ab.ca/publications/wcsb_atlas/atlas.html. Accessed December 13, 2012.

Foliation development and hydrothermal gold emplacement in metagabbroic rocks, central Yukon, Canada

Doug MacKenzie[1], Dave Craw
Geology Department, University of Otago, Dunedin, New Zealand

Colin Brodie
Mendoza, Argentina

Adrian Fleming
Rockworks Ltd., Vancouver, Canada

MacKenzie, D., Craw, D., Brodie, C., and Fleming, A., 2013. Foliation development and hydrothermal gold emplacement in metagabbroic rocks, central Yukon, Canada. *In:* Yukon Exploration and Geology 2012, K.E. MacFarlane, M.G. Nordling, and P.J. Sack (eds.), Yukon Geological Survey, p. 47-64.

ABSTRACT

Gold mineralization has been identified on the foliated margins of Paleozoic gabbroic intrusions, where a protracted series of structural preparation events has enhanced rock permeability. Rheological contrasts between these mafic rocks and amphibolite facies metasedimentary hosts have resulted in variable foliation development, especially at margins of mafic bodies. Initial foliation development centred on granitoid material in magmatic intrusion breccia, and was enhanced by syn-metamorphic biotite formation. Early mineralized quartz vein development occurred under greenschist facies conditions during and/or after regional Mesozoic thrust stacking of kilometre scale rock slabs. Initial vein emplacement was largely controlled by the foliation in mafic gneiss, and minor chloritic alteration and later hydrothermal generations cut across all structures. Gold mineralization involved only minor introduction of As, Sb, and S, and the hosting quartzite has higher As, Sb, and S content than most mineralized veins. Au is accompanied by elevated Bi, Mo, and Te in quartz veins.

[1]*doug.mackenzie@otago.ac.nz*

INTRODUCTION

Recent research and gold exploration near to new Yukon gold discoveries in the White River area (MacKenzie *et al.,* 2010; Wainwright *et al.,* 2011; Fig. 1) has highlighted the presence of abundant mafic and ultramafic rocks (MacKenzie and Craw 2012); some of these mafic rocks have elevated gold concentrations worthy of serious exploration attention. This style of mafic-hosted gold mineralization required a protracted chain of structural preparation events to enhance rock permeability. The nature of this structural preparation is well displayed in these rocks, and the processes that have occurred are relevant to all metamorphosed mafic bodies around the world. This paper provides an outline of the processes of structural preparation that have led to localized gold enrichment. In particular, foliation development, and its subsequent control on vein emplacement, has been important in gold localization in these mafic bodies. Geochemical observations on the nature of this new

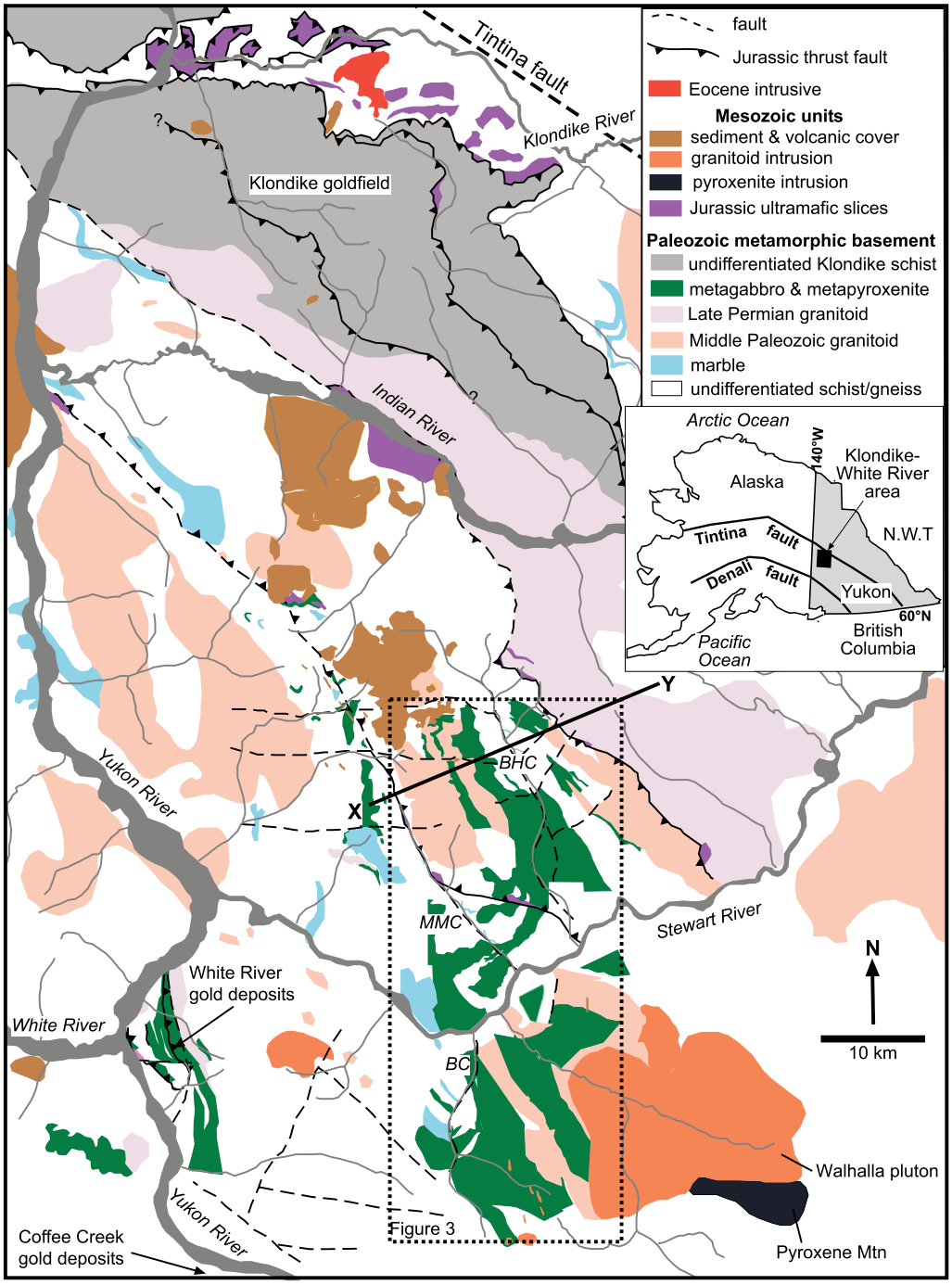

Figure 1. *Summary geological map of the Yukon-Tanana terrane in west-central Yukon, showing the geological relationship between the Klondike gold field and significant new gold deposit discoveries farther south (White River and Coffee Creek deposits). The area of this study is depicted in cross section (line X-Y; Fig. 2a) and in the dotted box (Fig. 3), where significant placer gold bearing creeks (Black Hills Creek (BHC); Maisy May Creek (MMC); Barker Creek (BC)) imply undiscovered deposits. Inset shows the location of this area in NW North America.*

type of hydrothermal gold deposit are provided to help to characterize the hydrothermal system in this largely unexplored part of the Yukon-Tanana terrane.

GENERAL GEOLOGY

The basement rocks in central Yukon are part of the Yukon-Tanana terrane, which is a metamorphic complex including mafic and felsic plutons (Figs. 1 and 2a; Mortensen, 1992, 1996; MacKenzie *et al.,* 2008a, 2010; Table 1). The metamorphic complex consists of metasedimentary rocks, including quartzite, marble, and metaclastic micaceous schist, that were intruded by granitoids and gabbroic rocks prior to and/or during Paleozoic metamorphism (Mortensen, 1992, 1996; Ryan and Gordey, 2004; Ruks *et al.,* 2006). At least three stages of granitoid intrusion occurred between the Devonian and Permian (Ruks *et al.,* 2006), and mafic intrusions apparently accompanied all of these intrusive events. Variable development of foliation during metamorphism yielded a prominent polyphase foliation in most rocks, although some of the more massive rocks have remained unfoliated. Metamorphic grade ranges from greenschist facies in the north, around the main Klondike goldfield (Fig. 1; Mortensen, 1992, 1996; MacKenzie *et al.,* 2008a) to amphibolite facies farther south in the White River and Stewart River areas (Ryan and Gordey, 2004; Ruks *et al.,* 2006; MacKenzie *et al.,* 2010). The present study was conducted entirely in amphibolite facies rocks previously mapped on a regional scale by Ryan and Gordey (2004).

The metamorphic basement was disrupted and stacked on a kilometre scale by thrusting in the Jurassic, and slices of mafic and ultramafic rocks of the Slide Mountain terrane, and some Triassic sedimentary units in the north were incorporated (Figs. 1 and 2a; Table 1; Mortensen, 1990, 1996). This thrust stacking occurred under greenschist facies conditions, along with the associated development of greenschist facies shear and fold zones (MacKenzie *et al.,* 2008a). Minor intrusion of granitoid and associated mafic bodies accompanied this Jurassic collisional orogenesis. However, pyroxenite sills and related amphibolite bodies in the White River area (MacKenzie *et al.,* 2010), previously presumed to be Jurassic in age, are almost certainly part of the suite of Paleozoic mafic bodies described in this study (MacKenzie and Craw, 2012).

Compressional tectonics gave way to regional extension in the Cretaceous, and persisted through to the Eocene (Table 1). Minor mafic and/or felsic volcanism and associated shallow intrusion accompanied this extension (Gabrielse and Yorath, 1991; Mortensen, 1996; Table 1). The Tintina fault, a major regional transcurrent structure (Fig. 1), accommodated mainly Eocene age displacement, which has offset parts of the Yukon-Tanana terrane by ~400 km (Gabrielse *et al.,* 2006). Regional uplift and erosion following movement along the Tintina fault

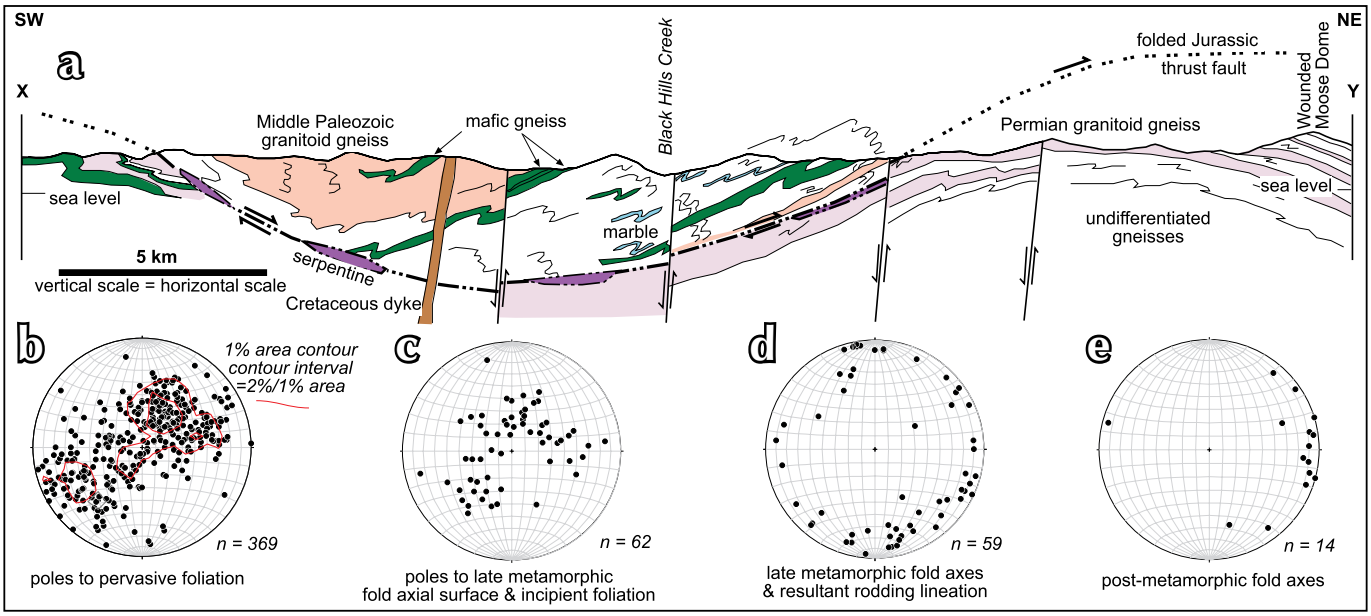

Figure 2. *Cross section and stereonets. a) X-Y line in Fig. 1, rock units depicted in the same colours as Fig. 1. Stereonets: b) lower hemisphere stereographic projection of poles to the pervasive metamorphic foliation; c) poles to late metamorphic planar fabric; d) late metamorphic linear features; and e) post-metamorphic fold axes.*

Table 1. *Summary of the principal geological events affecting mafic rocks and hosting metasediments in the central Yukon-Tanana terrane (Figs. 1 and 3).*

Age	Unit/event	Tectonics (Regional* structural event)	Associated intrusions	Metamorphism	Gold	Structure	Granitoid orthogneiss	Metasediment key minerals	Mafic gneiss key minerals
Pliocene-Recent	White Channel and modern gravels	Regional uplift and erosion		Groundwater alteration	Placer	Fault reactivation with gouge	Fault gouge, cataclasite, chloritic alteration with pyrite, carbonates & clays	Fault gouge, cataclasite, chloritic alteration with carbonates & clays	Fault gouge, cataclasite, chloritic alteration with clays (see Table 3)
Eocene		Regional extension (D_3)	Dykes	Hydrothermal alteration	?	Normal faults with cataclasite & gouge			
Late Cretaceous	Carmacks andesitic volcanism			Hydrothermal alteration	Epithermal				
Middle Cretaceous	Indian River fluvial		Ignimbrites and feeders	Groundwater alteration	Paleoplacer				
Jurassic-Cretaceous?	White River mineralization	?	?	Hydrothermal alteration	Disseminated; veins	Fault-hosted breccias	Hematitic, sericitic alteration ± pyrite	Graphite, pyrrhotite, pyrite (quartzite)	Fuchsite, chlorite, pyrite
Jurassic	Slide Mountain terrane collision and thrusting	(D_4) Orogenic collision, uplift, thrust stacking (D_3)		Hydrothermal alteration	Orogenic veins	Late folds, fractures, breccias	Shearing, with epidote, chlorite, hematite, pyrite, magnetite		Ankerite, pyrite (in Klondike)
			Granite plutons; pyroxenite	Greenschist facies (propylitic)	Localized mobility?	Brittle-ductile shearing		Epidote, quartz, albite, hematite, magnetite (schist); Graphite, pyrrhotite, pyrite (quartzite); diopside, actinolite, epidote (marble)	Epidote, quartz, actinolite, albite, hematite, magnetite; local skarn against marble
				Localized greenschist facies		Ultramafic slice emplacement with shearing			
Permian	Late metamorphic mafic intrusion	Assembly of Yukon-Tanana terrane (D_1-D_2)	Felsic segregations; augen granite	Amphibolite facies		Folding, rodding of foliation	Variable foliation, folding	Garnet, Al-silicates (micaceous schist); hornblende, garnet, graphite (quartzite)	Pyroxene to hornblende (unfoliated); hornblende, biotite, garnet;
Late Paleozoic	Pre-syn metamorphic mafic intrusion		Felsic segregations; augen granite			Main foliation (polyphase)	Variable foliation		
Early Paleozoic?	Host rock sedimentation	?			Syn-depositional enrichment?	Bedding			

*after MacKenzie *et al.*, 2010; MacKenzie and Craw, 2012

has resulted in formation of the productive gold placer deposits of the Klondike area, and tributary valleys of the Stewart River to the south, particularly Black Hills, Maisy May, and Barker creeks (Fig. 3; Fuller and Anderson, 1992; Chapman *et al.,* 2011). The source(s) of the gold for the abundant placer deposits is presumed to be the Jurassic orogenic veins in the Klondike area (Lowey, 2005; MacKenzie *et al.,* 2008a; Chapman *et al.,* 2011) and other scattered hydrothermal deposits of unknown affinity, such as the recently-discovered White River and Coffee Creek deposits (MacKenzie *et al.,* 2010; Wainwright *et al.,* 2011; Fig. 1). The current small size of these newly discovered bedrock deposits points to the probable existence of other undiscovered deposits (Chapman *et al.,* 2011), and this observation has been driving a modern "gold rush" in the area.

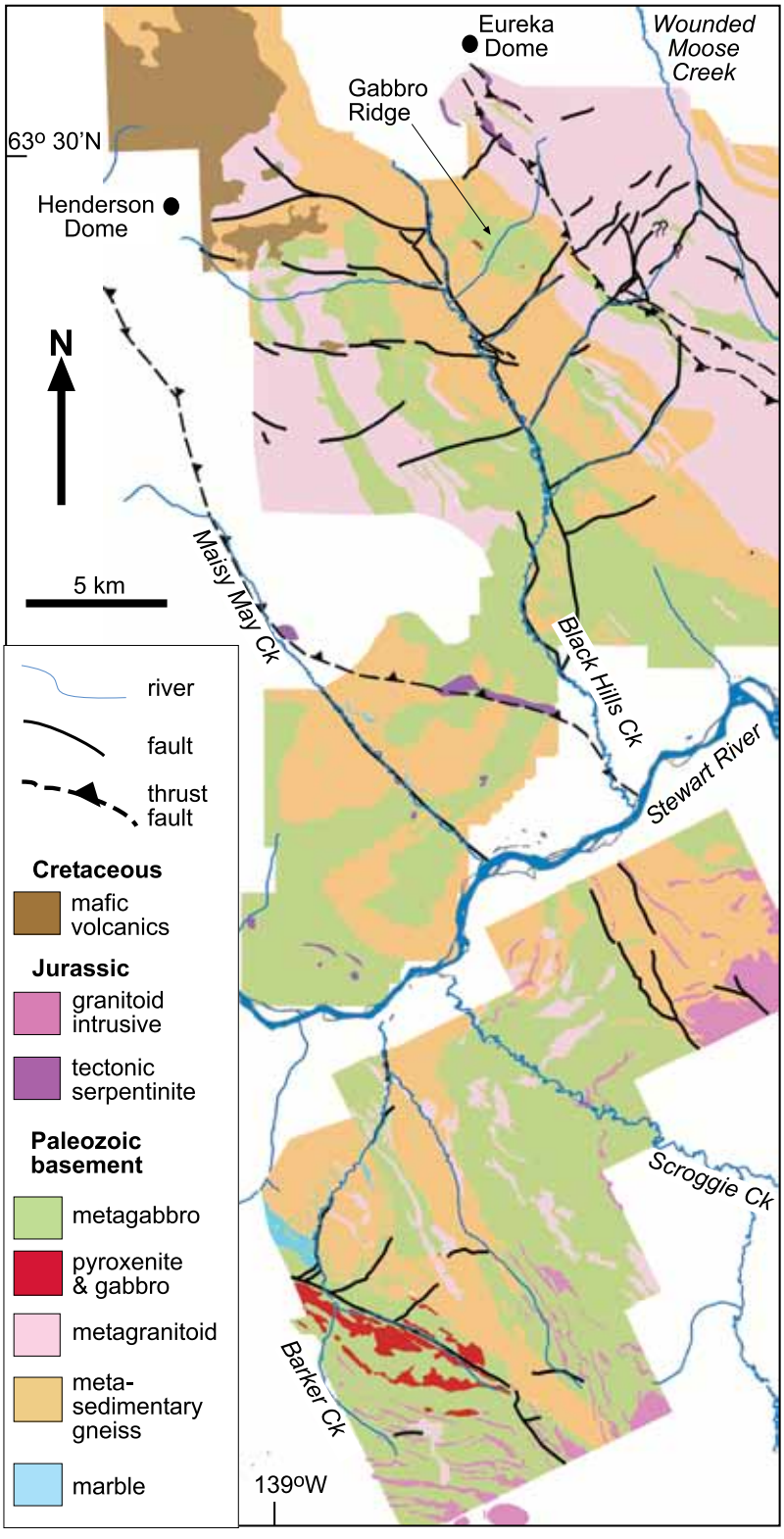

Figure 3. *Geological map of the study area showing the surface distribution of metagabbro (green) and relict pyroxenite (red) in relation to other rock types in the area.*

METHODS

Results of extensive new field mapping, sampling, and geochemical analysis over an area >500 km^2 centred on the auriferous Black Hills Creek and Barker Creek catchments of the Stewart River area, a previously little-studied area near to the White River gold discovery (Figs. 1, 2, and 3) are incorporated in this paper. This research is an extension of a regional scale project on structural and lithological mapping and gold deposit investigations (MacKenzie *et al.,* 2008a, 2010; MacKenzie and Craw, 2012). Field mapping was supplemented by exploration soil geochemistry on ridges and spurs using lithological discriminants. Lateral continuity of rock units was determined from airborne geophysical surveys, of which the magnetic and potassium radiometric data were most useful for map construction (Fig. 3). Rock exposure was created in exploration trenches, and two cored drillholes were emplaced in mafic rocks on Gabbro Ridge (Fig. 3; informal name) where soil, surface rock, and trench mapping and sampling had defined a significant gold anomaly (up to 10 ppm Au). Pulps from samples of altered rock were fused with lithium metaborate, dissolved in nitric acid, and analysed using ICP-MS. Gold was determined to be present in surface rocks and trench wall samples (~50-250 g) by fire assay, using an atomic absorption finish. All analyses were done at Acme Analytical Labs in Vancouver, Canada.

STRUCTURE

The gneiss in the mapped area has a near-pervasive amphibolite facies metamorphic foliation that has shallow to moderate dips to northeast and southwest (Fig. 2a,b). This foliation defines the fold axial surface to synmetamorphic recumbent ductile folds. Late metamorphic recumbent folding has caused localized disruption of the main foliation, and some development of a new foliation in tight fold hinges. This incipient late foliation also has shallow dips (Fig. 2c), but is oblique to the main foliation. The late metamorphic folding and foliation development has caused a prominent rodding lineation fabric to dominate

some outcrops, due to intersection of the two foliations. Late metamorphic fold axes and the associated rodding lineations have a wide range of orientations (Fig. 2d), which have been controlled by local rheological differences in the rock mass rather than regional tectonic stress orientations.

The metamorphic structure has been disrupted by greenschist facies shearing, most of which is concentrated into narrow zones associated with Jurassic thrust faults (Figs. 1, 2a, and 3). These sheared and retrogressed zones include sporadic slices of variably serpentinized ultramafic rock that is internally sheared into phacoidal blocks on the 1-10 m scale. Subordinate greenschist facies shear zones, brecciated fault zones, and veins hosted in these structures, cut steeply across the amphibolite facies gneiss between the shallow-dipping thrust faults. The gneissic foliation and the Jurassic thrust faults have been folded into broad (10 km scale) open upright antiforms and synforms by post-metamorphic compressional deformation (Fig. 2a). This folding is partly responsible for the great-circle scattering of foliation orientations, with a general northwest fold axis trend (Figs. 1 and 2a), although most of this scatter is a result of late-metamorphic folding (Fig. 2a,c). Minor folding of foliation, associated with this deformation, occurs at outcrop scale but these structures are relatively rare and have widely-varying trends (Fig. 2e). The regional upright folds are disrupted by numerous normal faults spaced on the 1-10 km scale, with irregular and intersecting orientations (Figs. 1, 2a, and 3).

HOST ROCKS FOR MAFIC INTRUSIONS

The metasedimentary gneiss host rocks are dominated by quartzite, which ranges from almost pure quartz to muscovite-rich (~10%) variants. The quartzite is apparently derived from quartz-rich clastic sediments, as relict pebbles and sand grains are rarely preserved in low-strain domains (Fig. 4a). However, most quartzite is pervasively recrystallized and is variably foliated, depending on the muscovite content. Minor metamorphic graphite accompanies muscovite in the foliation, along with scattered pyrrhotite, pyrite, sphalerite, galena, arsenopyrite, and chalcopyrite. Interlayered micaceous schist includes muscovite-rich and biotite-rich variants, and both types locally contain subordinate garnet and kyanite or sillimanite. Micaceous schist is strongly foliated, and late metamorphic folding has induced a near-pervasive late metamorphic fold axial surface foliation that largely obscures the earlier metamorphic foliation(s) in some outcrops. The schist in these refoliated zones is commonly strongly lineated parallel to the intersection of the foliations (Fig. 2d).

Marble is less common than quartzite, but is locally interleaved with quartzite on the 1-50 m scale (Figs. 1, 2a, and 3). The marble is calcite-rich, with subordinate muscovite, biotite, and quartz. Some calcareous quartzite horizons (1-5 m) occur where quartzite and marble are interlayered. Foliation is typically weakly developed because of the relative paucity of micas, but layering defined by mineralogical variations has been folded and refolded during complex structural and metamorphic reconstitution.

Gneissic metagranitoid intrusions into the metasedimentary host rocks (Table 1; Figs. 1, 2a, and 3) locally form host rocks for the mafic gneiss, although the metamorphic overprint generally obscures the relative timing of emplacement of these intrusive rocks. The metagranitoid rocks are dominated by plagioclase, quartz, biotite, and hornblende, and potassium feldspar augen in some bodies. Foliation-parallel horizons of gneissic metagranitoid rocks are interleaved with mafic gneiss on the centimetre to metre scale, and vice versa.

MAFIC INTRUSIONS

Mafic gneiss bodies are widespread in the study area, and locally dominate outcrop over large areas (Fig. 3). This dominance in map pattern is partly a result of the shallow dipping foliation (Fig. 2a,b) and the relative resistance of mafic gneiss to erosion. This has left many ridges made up of mafic rocks, and they are underlain by less resistant rock types that have eroded to form valleys (Fig. 3). The contact between the mafic rocks and their hosting metasedimentary gneiss, one of the principal topics of this study, is therefore a shallow-dipping and sinuous feature around the modern topography (Fig. 3). Likewise, the relationship between mafic gneiss and metagranitoid bodies is generally relatively simple foliation-parallel interlamination (Fig. 2a), although the topographic effects lead to a complex map pattern (Fig. 3).

Synmetamorphic deformation is inhomogeneous in the basement rocks, and some portions of the mafic bodies are preserved with little or no overprinting foliation. The most intact bodies are those that were emplaced late in the metamorphic sequence, after the main foliation development. These late-stage bodies are variably foliated

internally and on their margins, but still retain undeformed pods on the 0.5 to 100 m scale in which the metamorphic overprint is minor. The undeformed pods occur within zones of mafic gneiss that can be several kilometres wide in map view (Fig. 3), with maximum thickness poorly defined.

Undeformed pods in mafic bodies commonly consist of unfoliated gabbro with coarse grained (cm scale) clinopyroxene, orthopyroxene, and/or hornblende, and variable amounts of plagioclase (Figs. 5 and 6). No olivine has been observed in these rocks. Pyrrhotite is a common accessory mineral (typically 1-5%) within even the least-deformed and metamorphosed metagabbro and pyroxenite, and may have been a primary magmatic mineral. Mafic intrusion breccia is abundant, in which previously-emplaced mafic rocks have been invaded and disrupted by later mafic intrusive rocks. Pyroxenite sills up to 5 m thick are preserved where they have been intruded parallel to late metamorphic fold axial surfaces, with only minor (<1 m) marginal recrystallization and foliation development.

Mafic intrusions are almost invariably accompanied by conspicuous granitoid intrusive rocks, forming xenolithic breccia with a granitoid matrix (Fig. 5c). The xenolithic breccia generally has a wide range of clast types, including mixtures of metagabbro, pyroxenite, earlier granitoid rocks (Fig. 5c), and some metasedimentary xenoliths. Some mafic clasts have a biotite-rich reaction zone (mm scale) on their rims (Fig 5c). The granitoid matrix is dominated by plagioclase and quartz, with subordinate biotite and hornblende. Similar granitoid rocks also cut across the mafic bodies as centimetre to metre scale dykes with irregular orientations, or are locally emplaced as sills parallel to pre-intrusion foliation.

All the mafic bodies have some degree of foliation development on their margins, and foliated zones occur throughout the bodies on the 1-10 m scale. Hornblende recrystallization and biotite growth are key drivers of foliation development (Fig. 6). Granitoid rocks within the mafic bodies become foliated before immediately adjacent metagabbro, because of the primary biotite and quartz content (Fig. 7a). Foliation development in mafic rocks is enhanced by recrystallization and alignment of biotite on the margins of mafic clasts in xenolithic breccia (Fig. 7b,c). Pyrrhotite in mafic rocks has been recrystallized into parallelism with the developing foliation, and locally forms veins that cut across the foliation, and is commonly accompanied by minor pyrite. Later pyrite veinlets cut across pyrrhotite-rich rocks.

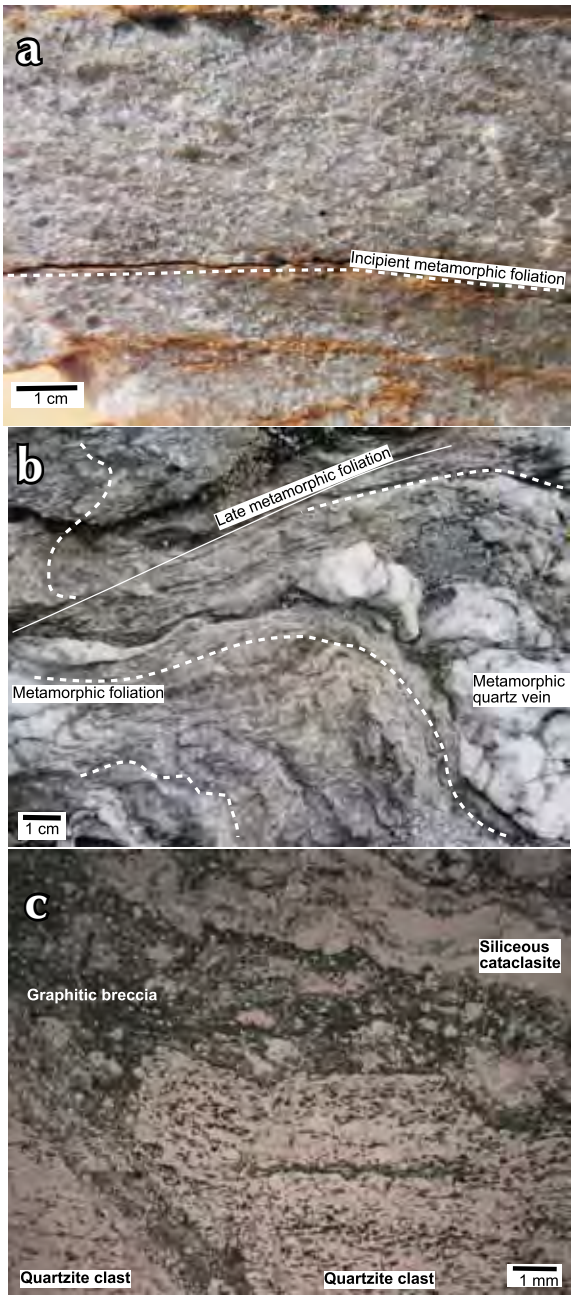

Figure 4. *Photographs of textures of quartzite host rocks to metagabbro. a) Little-deformed pod of quartzite showing remnants of clastic texture, with only incipient foliation development (white dashed line). b) Fully recrystallized quartzite with a late metamorphic fold of the metamorphic foliation (white dashed line) and a metamorphic foliation-parallel quartz vein. Incipient late metamorphic foliation (solid white line) has developed parallel to the fold axial surface. c) Photomicrograph (plane polarized light) of brecciated graphitic quartzite at the margin of a metagabbro body. Amphibolite facies graphitic foliation (black visible in the clast at bottom); the matrix consists of breccia cemented by hydrothermal graphite, and siliceous cataclasite.*

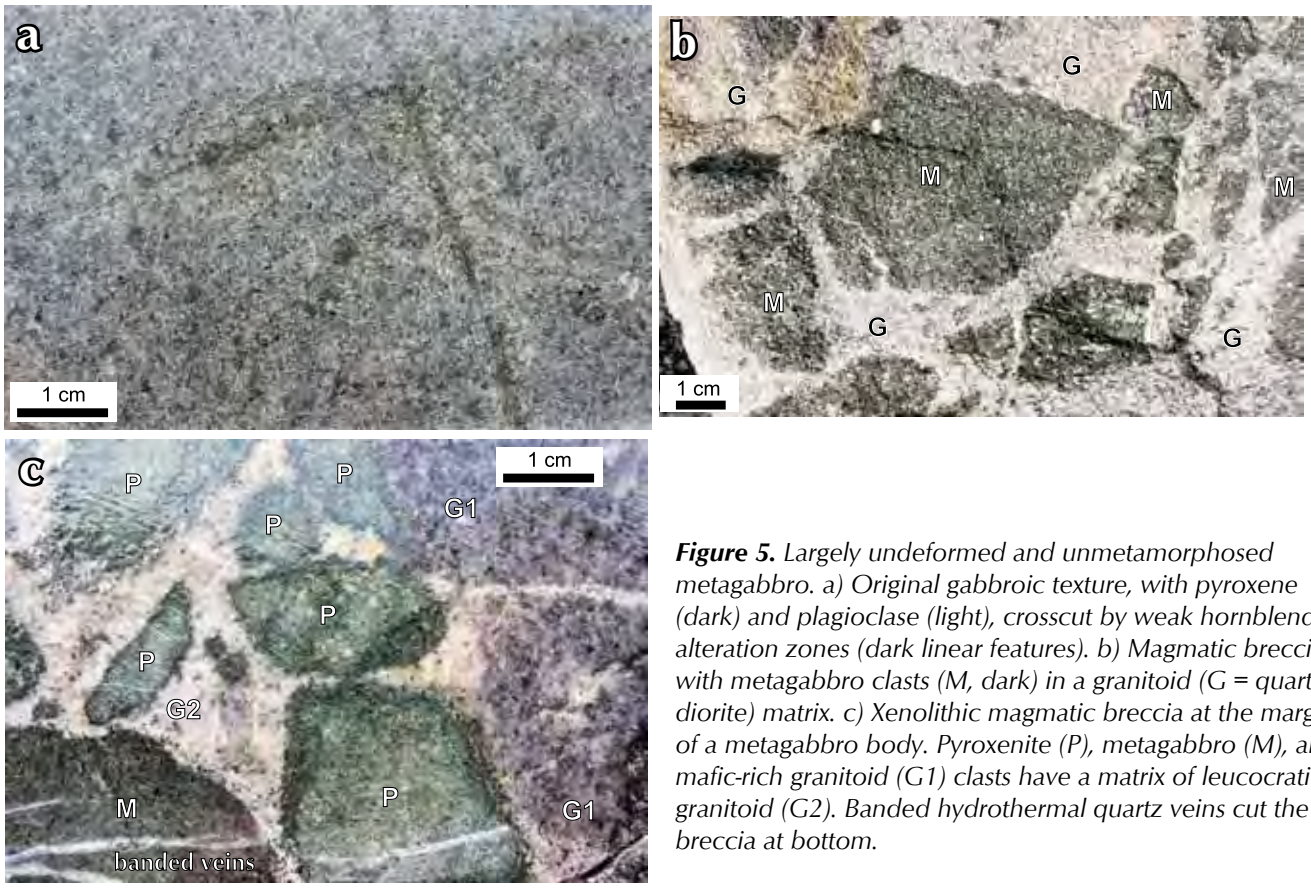

Figure 5. *Largely undeformed and unmetamorphosed metagabbro. a) Original gabbroic texture, with pyroxene (dark) and plagioclase (light), crosscut by weak hornblende alteration zones (dark linear features). b) Magmatic breccia, with metagabbro clasts (M, dark) in a granitoid (G = quartz diorite) matrix. c) Xenolithic magmatic breccia at the margin of a metagabbro body. Pyroxenite (P), metagabbro (M), and mafic-rich granitoid (G1) clasts have a matrix of leucocratic granitoid (G2). Banded hydrothermal quartz veins cut the breccia at bottom.*

The amphibolite facies foliation has undergone minor reactivation under greenschist facies conditions, with associated chloritization of biotite and relict hornblende, resulting in narrow (cm to m scale) chloritic shear zones. These are typically discontinuous at the outcrop scale, although they are more common and continuous near to the regional serpentinite-bearing thrust faults that stacked basement rocks in the Jurassic (Fig. 1 and 2a).

BRITTLE DEFORMATION AND HYDROTHERMAL ALTERATION

SHEARS, VEINS, AND BRECCIA

The late metamorphic structural zones within, and along the margins of, metagabbro bodies are the locus for subsequent more brittle deformation and hydrothermal alteration. This alteration was initiated under greenschist facies metamorphic conditions, with recrystallization of hornblende and biotite to epidote and chlorite, locally with hematite, magnetite and/or pyrite (Tables 1 and 2). The early stages of this alteration occurred along the foliation, with syn-alteration deformation that caused a weak shear foliation to develop locally. This type of alteration spread into veins and adjacent wall rocks of brittle structures such as fractures, breccia, and faults that developed in the metagabbro (Table 1) and adjacent foliated and folded quartzite. Some such quartz veins contain minor pyrite, chalcopyrite, and rare galena.

Several generations of veins and breccia developed after this early evolution to a brittle deformation regime (Tables 1 and 2). The earliest of these generations in the metagabbro bodies does not affect the mafic rocks, but does affect some of the granitoid dykes and granitoid-rich breccia. This hydrothermal generation resulted in emplacement of a set of thin (millimetre scale) massive quartz veins, exhibiting alteration haloes that typically extend for ~1 cm from the veins (Fig. 8a). Alteration is dominated by chloritization of biotite, and associated sericite and minor pyrite. Zones of more extensive rock alteration occur where several haloed veins intersect, and the alteration zones merge into bleached and partially silicified rock with sericite and remnants of chlorite (Fig. 8a). Similar chloritic and sericitic haloes and bleaching occur within some nearby granitoid gneiss, locally with pyritic alteration. This chloritic alteration resembles, but

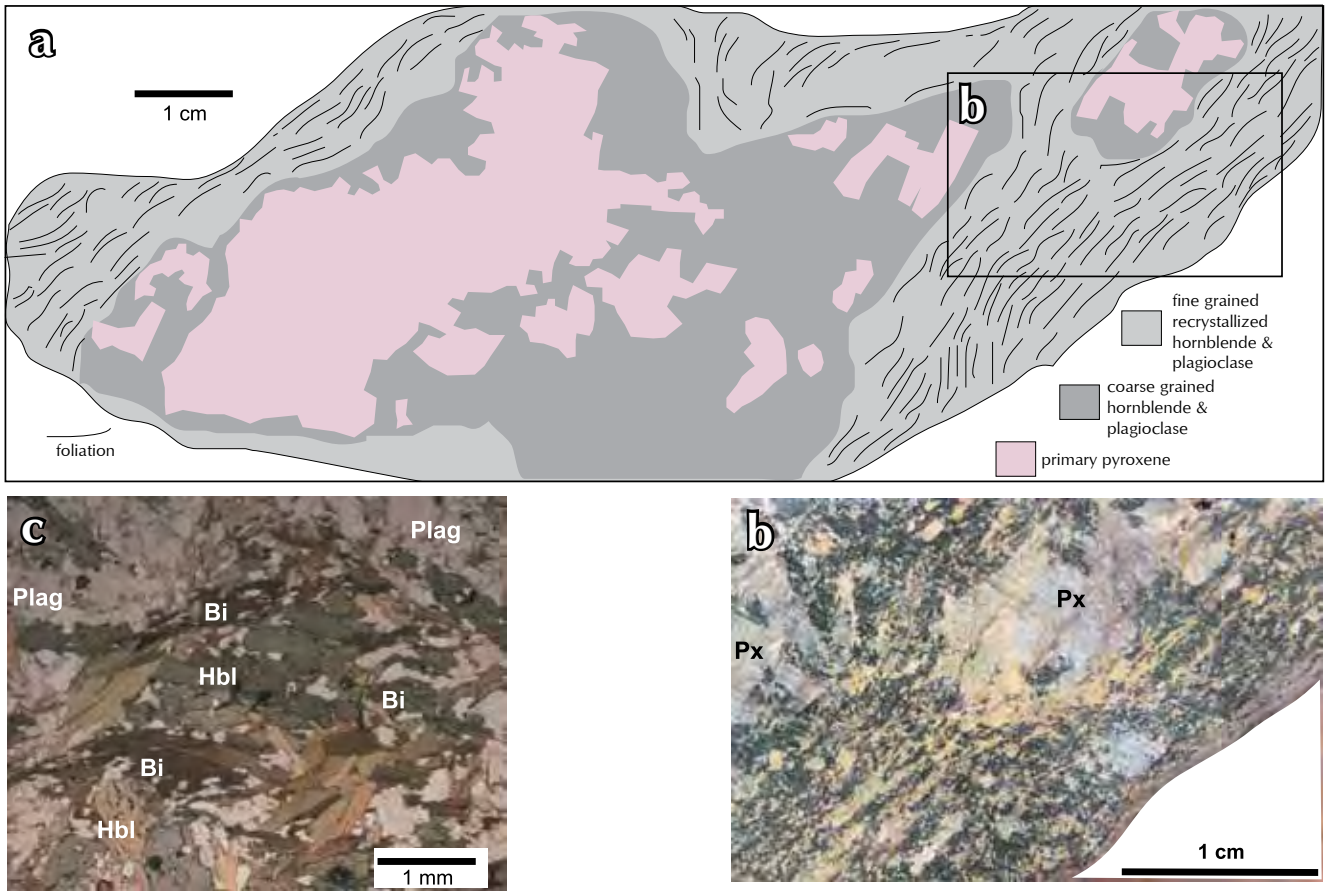

Figure 6. *Textures of metamorphism and foliation development in metagabbro. a) Block from outcrop showing a relict coarse grained pyroxenite core surrounded by unfoliated coarse hornblende metagabbro. Finer grained foliated hornblende metagabbro surrounds the unfoliated rocks. b) Close-up view of a part of the block in (a), showing the steep gradient from primary rock to foliated hornblende metagabbro. c) Photomicrograph (crossed polars) of foliated hornblende metagabbro, showing the localized formation of metamorphic biotite that dominated foliation development.*

structurally post-dates, texturally similar hematitic sericitic alteration of granitoid gneiss that occurs in the same area and, contains gold in the White River area (Table 1).

A later generation of massive quartz veins (Table 2) is more extensive, but lacks distinct alteration haloes (Fig. 8b,c). These massive veins are generally small (millimetre-centimetre scale), and discontinuous, with some included host rock fragments as breccia clasts (Fig. 8b,c). Most of these veins have nucleated in foliated granitoid, or on boundaries between foliated granitoid and variably foliated mafic clasts in xenolithic breccia, where they are largely controlled by foliation (Fig. 8b,c). Margins of these veins, and most breccia fragments, have incipient chloritic alteration of biotite and/or hornblende. Gold-bearing quartz vein material collected from surface zones on mafic rocks contain pyrite and have irregular margins that partially incorporate foliated but weakly chloritized hornblende metagabbro, and formed sub-parallel to foliation. These gold-bearing samples are similar to the massive quartz veins, especially resembling that in Figure 8c.

All rock types in the mafic bodies are crosscut by a prominent but volumetrically small set of quartz veins that are generally banded due to polyphase opening and mineralization history. The banded veins commonly contain prismatic quartz crystals in open cavities, and variable amounts of euhedral pyrite. Most banded veins formed with steep dips, at a high angle to the foliation (Fig. 8b-d). However, these veins also exploit other rock weaknesses, such as foliation and margins of pre-existing veins (Fig. 8c). Some banded veins have formed preferentially in massive rocks such as unfoliated metagabbro and pyroxenite (Fig. 5c).

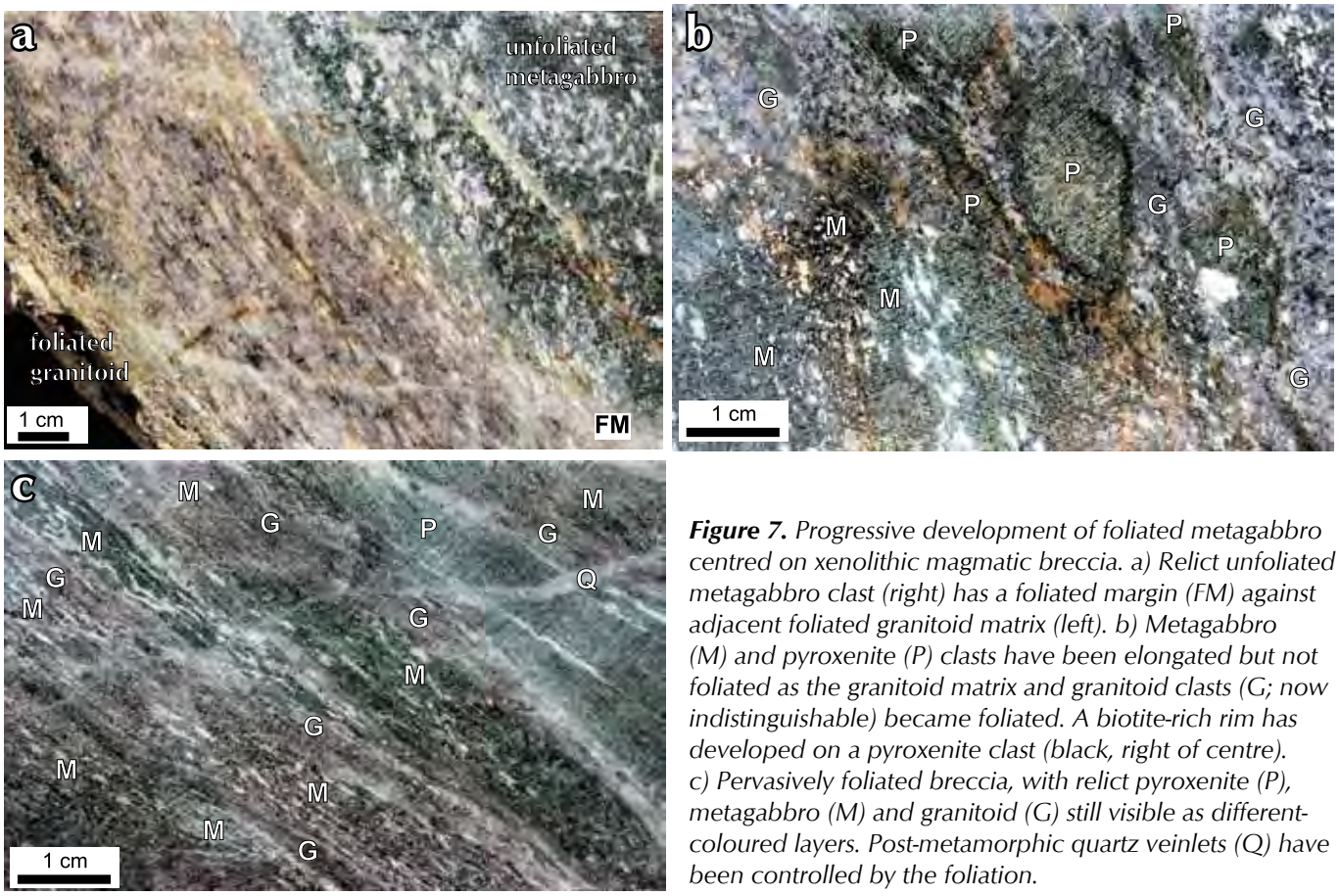

Figure 7. *Progressive development of foliated metagabbro centred on xenolithic magmatic breccia. a) Relict unfoliated metagabbro clast (right) has a foliated margin (FM) against adjacent foliated granitoid matrix (left). b) Metagabbro (M) and pyroxenite (P) clasts have been elongated but not foliated as the granitoid matrix and granitoid clasts (G; now indistinguishable) became foliated. A biotite-rich rim has developed on a pyroxenite clast (black, right of centre). c) Pervasively foliated breccia, with relict pyroxenite (P), metagabbro (M) and granitoid (G) still visible as different-coloured layers. Post-metamorphic quartz veinlets (Q) have been controlled by the foliation.*

Rare veinlets (sub-millimetre scale) containing iron-bearing carbonate cut across the banded veins at a variety of angles in mafic rocks, especially in granitoid-bearing xenolithic breccia. These veinlets also contain minor pyrite and quartz. Late stage pyrite-bearing clay-rich coatings, with disseminated calcite, have formed on fracture surfaces that cut across all of the above vein generations (Table 2).

Brecciated graphitic quartzite, immediately adjacent to metagabbro bodies, is variably silicified and cemented by hydrothermal quartz (Fig. 4c), forming brittle rocks that are locally re-brecciated and re-silicified. Hydrothermal graphite accompanied the silica cementation, and this graphite locally dominates the breccia matrix (Fig. 4c). Scattered micron-scale grains of pyrrhotite and pyrite occur in the graphitic breccia cement.

The mafic/metasediment boundaries, and other foliated zones, were locally reactivated by an unknown number of brittle fault generations that may be as young as Quaternary. These fault zones consist of a complex set of gouge and breccia (metre scale) made up of polyphase soft, clay-rich uncemented cataclasite derived from the immediate wall rocks. Adjacent rocks are generally highly fractured, and hydrothermal fluids have deposited minor quartz (locally prismatic) and scattered euhedral pyrite grains on fracture surfaces. Chlorite-calcite, or hematite-chlorite-calcite coatings occur on shear-polished surfaces in fault zones cutting mafic bodies. Several of these faults cut across the regional metamorphic fabric (Figs. 1, 2, and 3), and associated minor faults have reactivated the foliation in adjacent gneiss, forming foliation-parallel gouge zones.

SKARNS

Localized reaction skarn zones have developed at some boundaries between metagabbro and marble, on the 1-20 m scale. These reaction skarns are larger scale than those that occur in marble xenoliths in metagabbro. In contrast, there is little or no skarn development between marble and interlayered quartzite, or marble and interlayered mafic gneiss, in many other parts of the metamorphic sequence. Most of these marble boundaries

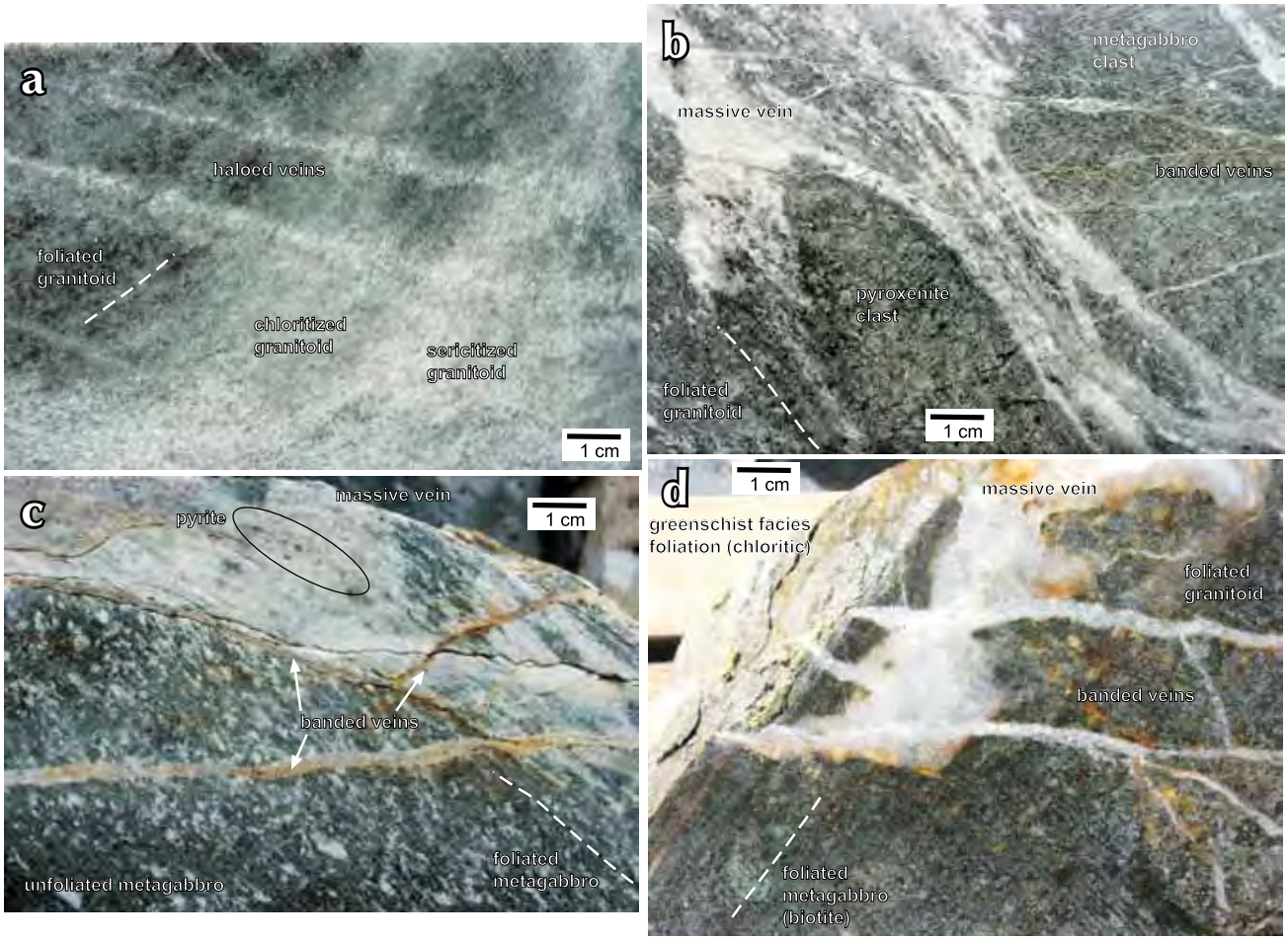

Figure 8. *Hydrothermal vein generations in weakly mineralized metagabbro near a body margin on Gabbro Ridge (Fig. 3). a) Pale chlorite-sericite-quartz seams with alteration haloes cut weakly foliated granitoid in a magmatic breccia. b) Massive quartz veins with minor pyrite have nucleated in foliated granitoid between mafic clasts. Later banded quartz veins cut across all rock types. c) Massive quartz vein with scattered pyrite has developed in the foliated part of metagabbro, with foliated metagabbro breccia clasts (right). A banded quartz vein has formed at the edge of the massive vein, and other banded veins cut all rock types. d) Massive quartz vein with minor pyrite has nucleated near the boundaries between biotite-foliated metagabbro and a chloritic shear zone on left and foliated granitoid on right. Later banded quartz veins cut across all rock types.*

are sharp and unreacted at even the millimetre scale. The reaction skarn zones are unfoliated, and skarn minerals cut across the metamorphic foliation and late metamorphic fold-related structures. Minor skarn recrystallization follows the metamorphic foliation on skarn margins, but skarn minerals have grown across that foliation. These observations suggest that skarn formation occurred during post-metamorphic hydrothermal alteration described in the previous section. The skarns are dominated by actinolite and epidote, with minor diopside, vesuvianite, and garnet. Pyrite and/or pyrrhotite are locally abundant as anhedral masses and veins. The best-developed skarns form massive hard rock zones that transgress the metamorphic foliation, with gradational (<1 m) boundaries to unreacted marble.

CHEMICAL ALTERATION

More than 1000 geochemical analyses of variably altered rocks at and near metagabbro boundaries were examined in this study. Most elements analysed have little variation in the altered rocks and are not useful for distinguishing gold mineralization near these boundaries. Variation of metal content among the variably altered rock types, at and near metagabbro margins and the associated quartz veins, are depicted in Figures 9 and 10. Lower results are omitted from the graphs in Figures 9 and 10 for clarity, especially when the low values are close to the practical detection limit for the analytical methods.

Table 2. *Principal vein generations that cut metagabbro and associated rocks, arranged in chronological order from bottom (oldest) to top (youngest).*

Vein generation	Principal minerals	Metallic minerals	Structure	Shape
late fractures	quartz, clay, calcite	pyrite	fracture-controlled	irregular
Fe carbonate	ankerite, quartz	pyrite	fracture-controlled	lenticular, some breccia
banded	quartz (prismatic, drusy), calcite	pyrite, Au?	mostly steep across foliation; some along foliation, some breccia	parallel-sided, dilational jogs, vein arrays & networks
massive	quartz, calcite, chlorite	pyrite, Au	nucleated in foliation, some breccia	irregular, some diffuse margins
haloed	quartz, chlorite, sericite, calcite	pyrite	steeply cut foliation	diffuse, joint-controlled
epidote	quartz, epidote, chlorite, calcite	hematite, magnetite, pyrite	parallel, perpendicular to foliation	diffuse, joint-controlled

There is a crude positive correlation between As and Sb in the altered rocks and associated quartz veins (Fig. 9a). In particular, the altered quartzite typically has the highest As and Sb content. Elevated As and Sb in altered micaceous schist is generally from samples taken close to, or interlayered with, quartzite; quartz veins with elevated As and Sb are mainly from quartzite host rocks near metagabbro boundaries. Localized hydrothermal mobility of As and Sb from quartzite, having elevated As and Sb backgrounds (MacKenzie *et al.,* 2010), into veins and nearby alteration zones is probably responsible for the widespread nature of the As and Sb anomalies (Fig. 9a). This effect is less pronounced for altered metagabbro samples, some of which have minor As enrichment but little Sb enrichment (Fig. 9a). Altered quartzite is weakly enriched in both Mo and Bi, as well as As (Fig. 9b,c). Some of this enrichment reflects elevated background levels of these metals (MacKenzie *et al.,* 2010). However, some of the quartz veins are enriched in Mo and/or Bi independent of the As content (Fig. 9b,c).

Despite this metallic enrichment, the altered rocks are not strongly enriched in sulphide minerals, and typical S content is near background of 0.1 wt % (Fig. 9d). Some pyritic quartz veins have up to 1.0 wt % S, as does weakly altered and pyritic micaceous schist (Fig. 9d). Elevated S and Fe in weakly altered metagabbro (Fig. 9d) at least partially reflects locally-abundant metamorphic pyrrhotite, although some hydrothermal pyrite occurs in metagabbro as well. Likewise, weakly elevated Cu and Ni in some altered metagabbro (Fig. 9e) at least partially reflect the metamorphic sulphide content: Cu in chalcopyrite, and Ni in solid solution in pyrrhotite in these Ni-rich rocks. There has been little or no enrichment of Cu and Ni in most quartz veins, or in the other altered rocks, apart from some chalcopyrite-bearing veins and altered quartzite (Fig. 9e). Similarly, neither Pb nor Zn are enriched in most veins or altered rocks. However, some quartzite has metamorphic sphalerite and/or galena (MacKenzie *et al.,* 2010), and remobilization of these minerals may have resulted in localized enrichment of Pb and Zn (Fig. 9f). Galena occurs locally in veins in altered metagranitoid, resulting in minor Pb enrichment.

The strongest Au enrichment occurs in quartz veinlets, and there is only minor dissemination of gold in altered host rocks (Fig. 10a). This gold enrichment was not accompanied by significant As enrichment (Fig. 10a). However, gold-bearing veinlets, and some altered quartzite, are distinctly enriched in Mo and Bi (Fig. 10b,c). Likewise, the gold-bearing veins are also enriched in Te (Fig. 10d).

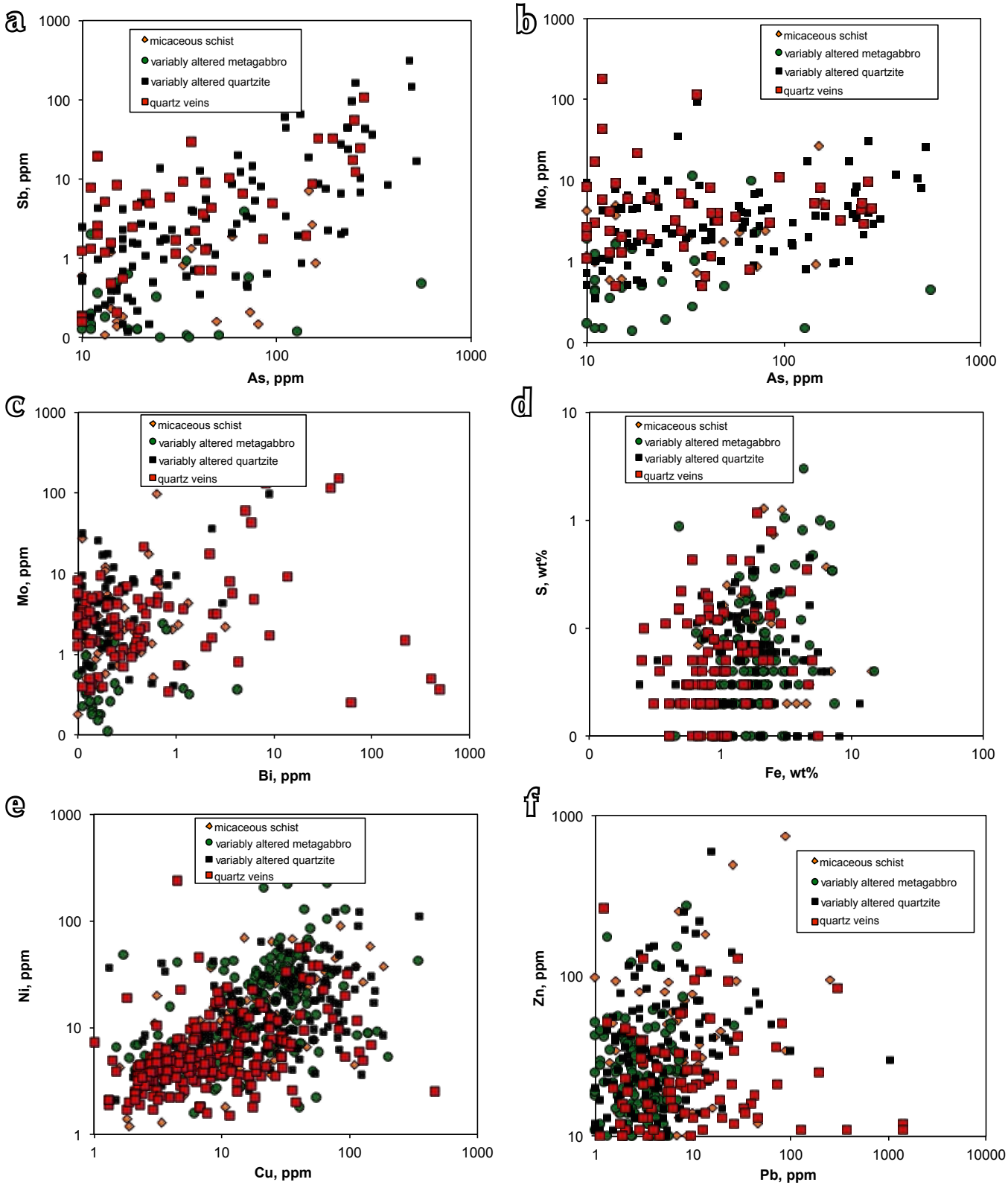

Figure 9. *Geochemical plots of metal contents of variably altered and gold mineralized rocks from near metagabbro boundaries. (a) As vs Sb; (b) As vs Mo; (c) Bi vs Mo; (d) Fe vs S; (e) Cu vs Ni; (f) Pb vs Zn.*

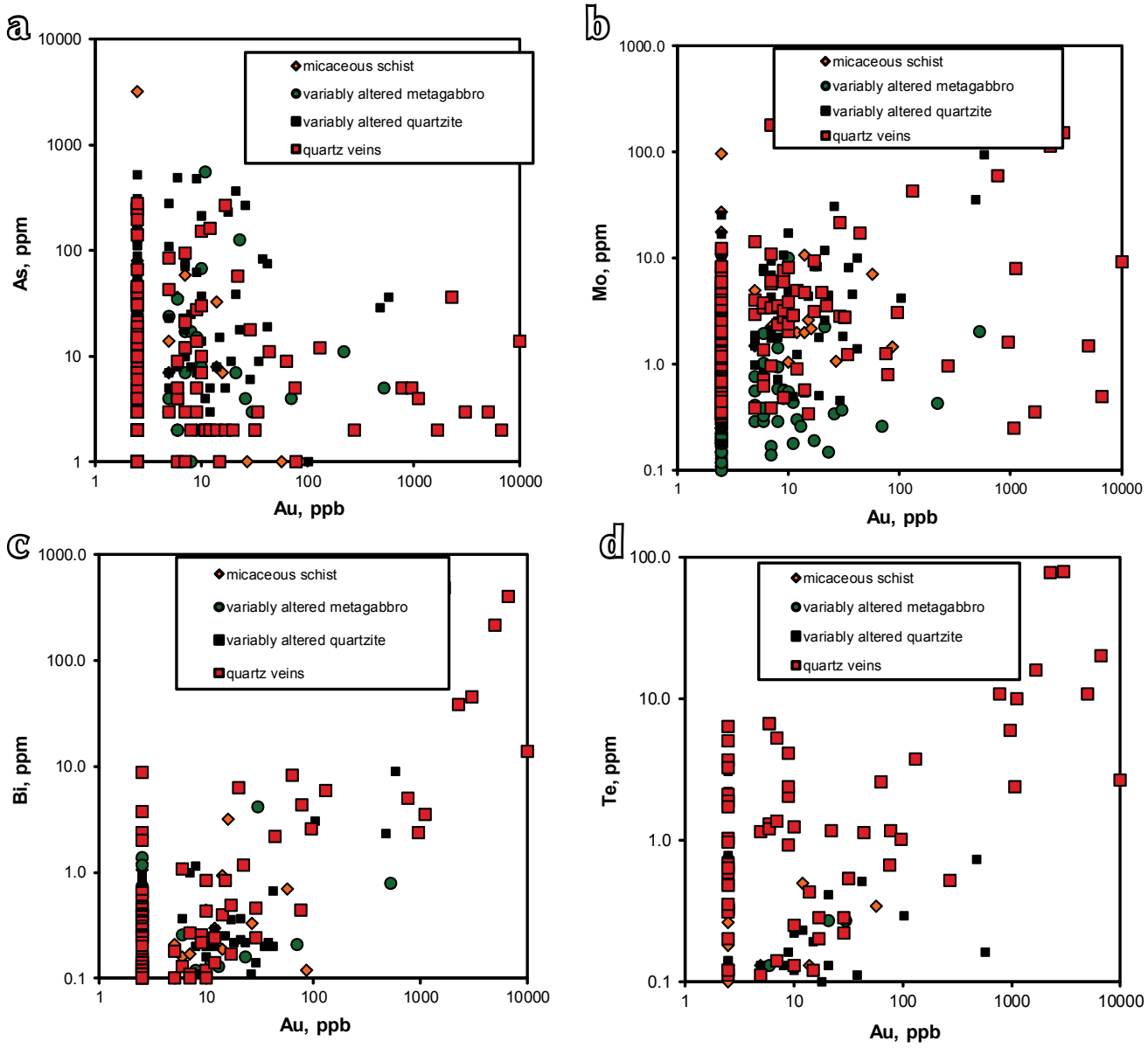

Figure 10. *Gold concentrations in variably altered rocks from near metagabbro boundaries, in relation to: a) As; b) Mo; c) Bi; and d) Te.*

DISCUSSION

CHEMICAL MOBILITY AT MAFIC BODY MARGINS

The metagabbro margins are zones with strong geochemical contrasts, between strongly mafic compositions and siliceous, micaceous, and/or calcareous compositions. Consequently, there has been some elemental exchange between these disparate rock types, on at least the metre scale and possibly greater spatial scales. The details of this migration are difficult to define because the primary rock compositions are unknown and variable. The most obvious manifestation of chemical mobility is that of syn-metamorphic K migration, resulting in development of biotite-rich foliation (Fig. 6c). This K migration must have occurred in zones up to tens of metres wide, both at mafic body margins and within the bodies where granitoid intrusions were deformed along with the mafic rocks. Likewise, metamorphic hornblende in quartzite close to (<10 m from) metagabbro margins reflects migration of mafic major elements such as Fe, Mg, and Ca from the mafic bodies.

Some altered metagabbro is moderately enriched in As compared to background levels (<20 ppm) in unaltered rocks (Fig. 9a). This As has almost certainly migrated from adjacent (<20 m) quartzite that is a relatively As-rich protolith and has As-rich quartz veins (Fig. 9a; MacKenzie *et al.,* 2010). Antimony is also enriched in the quartzite, and apparently has not migrated with the As into the metagabbro.

Graphite is most abundant in quartzite adjacent to (<50 m) metagabbro bodies, and graphite is rare or absent from quartzite more distant from metagabbro. This may be, at least partially, an artifact of poor exposure and/or weathering. However, there may also be a genetic relationship between graphite enrichment and the mafic/metasediment boundaries, facilitated by the chemical gradients at these boundaries. The latter possibility could arise because of geochemical processes that occur at these boundaries during metamorphism and subsequent alteration. Rather than being derived from a primary (sedimentary) carbon source, the graphite may have been deposited by combined oxidation-reduction reactions that occurred in these geochemically diverse boundary zones during metamorphism and/or subsequent hydrothermal alteration (Evans *et al.,* 2006; Huizenga, 2011). One speculative possibility for this process is the recrystallization of pyrrhotite to pyrite (oxidation) combined with reduction of metamorphic carbon dioxide (*e.g.*, from nearby marble), to give a reaction of the form:

1. $4FeS\ (pyrrhotite) + 4H_2S\ (dissolved) + CO_2\ (dissolved) \Rightarrow 4FeS_2\ (pyrite) + C\ (graphite) + 2H_2O + 2H_2$

Syn-metamorphic pyrrhotite is commonly seen to be replaced by late or post-metamorphic pyrite in all rock types of this study, so there is some observational support for this type of reaction. This, or some similar reaction, must have also occurred during post-metamorphic alteration, where substantial hydrothermal graphite addition has occurred in brecciated rocks (Fig. 4c; MacKenzie *et al.,* 2010).

RHEOLOGICAL CONTROL OF DEFORMATION AND FLUID FLOW

The geological history of the metagabbro boundaries is one of progressive localized deformation and rheological weakening that has

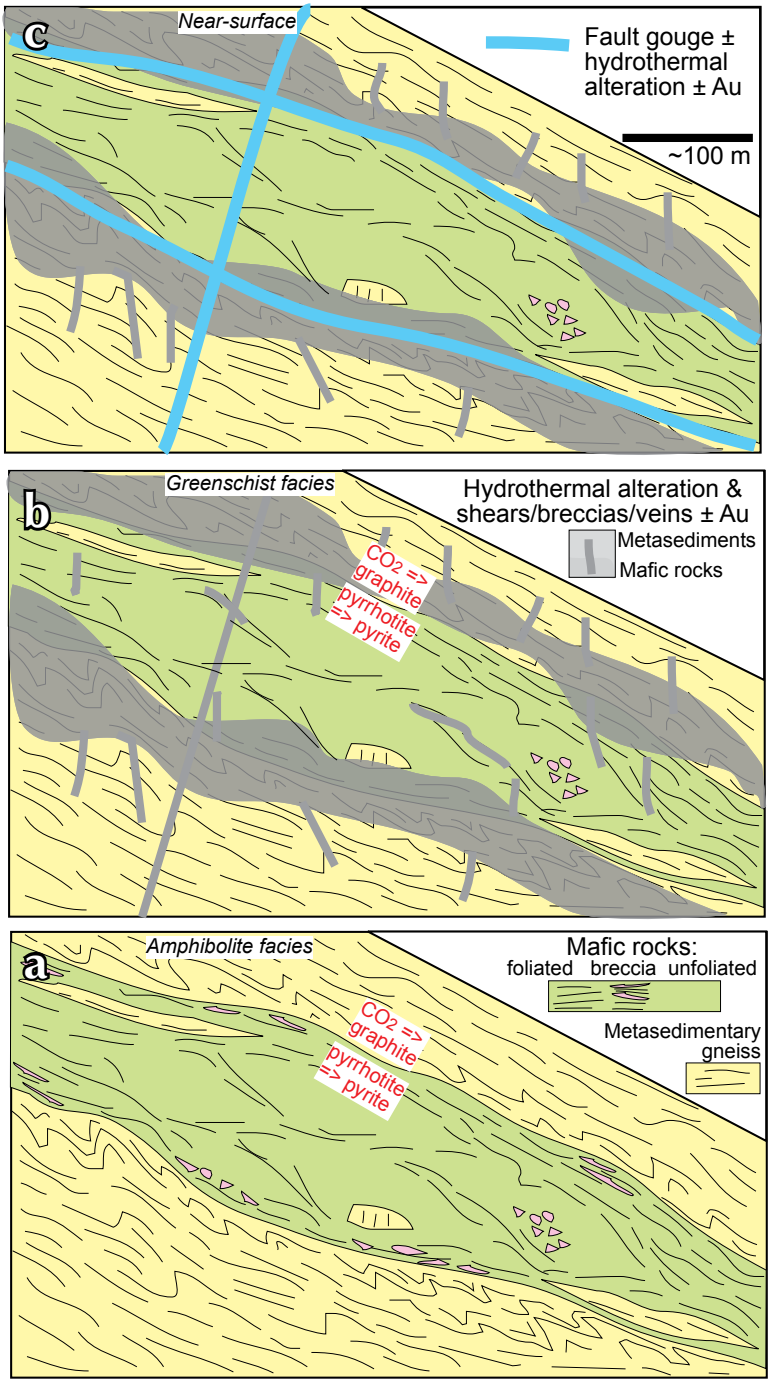

Figure 11. *Cartoon summary of the principal structural preparation events that led to permeability development in metagabbro hosted in quartzite. a) Paleozoic metamorphism and initial foliation development. Late metamorphic folding and foliation development is enhanced at the lithologic boundary and in magmatic breccia (granitoid = pink). b) Mesozoic metamorphic retrogression and hydrothermal alteration is focused in foliated rocks. c) Post-metamorphic brittle deformation and hydrothermal alteration is partly controlled by pre-existing structures.*

resulted in pronounced structural superposition zones on the 1-20 m scale. These structurally weakened zones have facilitated passage of hydrothermal fluids that have deposited veins in extensional sites and altered the immediate host rocks to varying degrees. The geometry of these metagabbro bodies and the sequence of deformation events are summarized in cartoon form in Figure 11a-c.

The earliest stages of deformation of the metagabbro bodies occur during Paleozoic metamorphism (Fig. 11a). The original mafic intrusions were dominated by pyroxene and feldspar, and this resulted in a strong competency contrast between these bodies and adjacent rocks that were rich in quartz, mica, and/or calcite. The resultant high strain gradients at the margins of the metagabbro enhanced metamorphic fluid flow and metamorphic transformations at the boundaries (Fig. 11a). These processes occurred at the centimetre to metre scale in xenolithic breccia (Fig. 7a-c), and at the metre to ten metre scale on gabbro margins (Fig. 11a). Coupled metamorphic reactions between mafic rocks and quartzite resulted in reduction of CO_2 to graphite while pyrrhotite transformed to pyrite (Fig. 11a; equation 1). Pods of some of the metagabbro remained unfoliated (Fig. 11a). Additional localized deformation, elemental mobility, and foliation development occurred around rafts of metasedimentary gneiss at and near the metagabbro margins (Fig. 11a). Late metamorphic deformation focused folding and extra late-stage foliation development in the adjacent host rocks (Fig. 11a).

Foliated metagabbro and associated folded and foliated metasedimentary gneiss were relatively permeable to incursion of hydrothermal fluids that started during greenschist facies overprinting of the metamorphic pile in the Jurassic (Table 1; Fig. 11b). This overprinting is not pervasive, even along the metagabbro margins, and variably affected metagabbro and host rocks. Later, but probably still Mesozoic, hydrothermal fluid flow was controlled by foliation and fractures within the metagabbro bodies, especially those associated with granitoid, and along metagabbro margins. These hydrothermal events (Table 2) evolved to lower temperature orogenic-hydrothermal alteration and vein formation. Veins filled extensional sites in metagabbro, associated granitoid, and immediate host rocks, with minor rock alteration (Fig. 11b). Additional hydrothermal graphite deposition occurred in adjacent quartzite (Figs. 4c and 11b).

The folded, foliated, and hydrothermally altered zones along metagabbro margins, and locally within metagabbro bodies, were subsequently the principal locus for development of late stage faults in the metamorphic rock mass, probably in the Cenozoic (Fig. 11c). These faults apparently had low net displacement, which is largely sub-parallel to the foliation (Fig. 11c). The resultant fault zones are dominated by cataclasite and gouge made up of variably altered and veined rocks from metagabbro and host rocks. This deformation has disrupted parts of the early hydrothermal alteration zones, but additional hydrothermal fluid flow has partially cemented some cataclasite. This late stage hydrothermal mineralization is not as widespread as the earlier stages, and may have been localized by specific crosscutting fault structures, in the same way as the White River gold mineralization was controlled largely by east-striking faults (MacKenzie *et al.,* 2010).

LOCALIZATION AND STYLE OF GOLD MINERALIZATION

The observed quartz veins and associated breccia have structural and textural characteristics of orogenic gold deposits (Goldfarb *et al.,* 2005), albeit only identified at a small scale in the metagabbro bodies thus far. The veins are discontinuous, and fill localized extensional sites in foliated metagabbro bodies. As such, these veins resemble the orogenic veins of the Klondike goldfield, rather than the largely vein-free disseminated gold deposits of the White River area (Fig. 1; MacKenzie *et al.,* 2010). Hydrothermal alteration of Klondike mafic schist host rocks occurred on the metre scale adjacent to veins (MacKenzie *et al.,* 2008b, MacKenzie and Craw, 2012), but hydrothermal fluids obtained only limited penetration into the mafic rocks described in this study, and alteration was extremely limited (cm scale). Some mineralized quartz veins, also with orogenic style, do occur in the margins of metabasic rocks in the White River mineralized zones, similar to those described in this study. However, most hydrothermal interaction with White River mafic rocks resulted in fuchsite alteration and no gold (MacKenzie *et al.,* 2010; Table 1).

There has been little or no As or Sb enrichment associated with hydrothermal gold mineralization at metagabbro margins in this study (Fig. 10a), similar to the As-poor orogenic gold mineralization in the Klondike area (MacKenzie *et al.,* 2008a,b). In contrast, both As and Sb are enriched to varying degrees in the White River hydrothermal gold deposits (MacKenzie *et al.,* 2010). Gold mineralization in this study involved significant Mo and Bi enrichment, both metals that are also enriched at White

River (MacKenzie *et al.,* 2010). Some of the banded pyritic quartz veins described in metagabbro bodies in this study resemble epithermal vein styles, rather than orogenic veins, although no definitive gold anomalies specifically associated with these veins have yet been determined.

CONCLUSIONS

Structurally-induced permeability to hydrothermal fluids developed in mafic intrusions in amphibolite facies basement after a protracted series of events. Paleozoic foliation development in these massive rocks initially required small-scale (centimetre-metre) elemental migration, particularly of potassium, to form biotite from primary pyroxene via metamorphic hornblende. Foliation developed around pods of rheologically more resistant mafic rocks that include coarse-grained pyroxenite differentiates. Quartzite host rocks appear to contain enhanced metamorphic graphite contents near to boundaries between quartzite and mafic bodies. Graphite deposition may have resulted from linking of redox reactions at these boundaries, involving transformation of abundant primary and metamorphic pyrrhotite to pyrite.

The amphibolite facies foliation was reworked by Jurassic deformation under greenschist facies conditions, with replacement of biotite by chlorite and muscovite. Additional graphite deposition occurred in late greenschist facies breccia in quartzite adjacent to mafic bodies, probably from the same linkage of redox reactions involving the pyrrhotite-pyrite transformation. The first stage of gold mineralization occurred during and/or after this retrogressive alteration, with emplacement of massive quartz veinlets controlled by the reworked foliation. Quartz vein emplacement was mediated by rheological contrasts at the mafic body margins, and veins nucleated preferentially in and around metagranitoid in deformed magmatic breccia. These quartz veins contain minor pyrite, and are locally enriched in Au, Bi, Mo, and Te. Gold deposition may have been facilitated by the relatively reduced chemical environment maintained by pyrrhotite-bearing mafic rocks and graphite and pyrrhotite bearing adjacent quartzite.

Later brittle deformation of the mafic rock margins facilitated several further vein formation generations, through to late stage veinlets, breccia, and alteration zones with epithermal style. The occurrence of gold in these generations is unknown, but similar generations of epithermal style alteration zones, breccia, and veins in metagranitoid host rocks near Gabbro Ridge (Fig. 3) do contain gold. It is notable that none of the hydrothermal alteration and vein formation events resulted in significant introduction of As into the mafic rocks, and gold mineralization was not accompanied by addition of anomalous As or Sb. The hosting quartzite has a relatively high As and Sb background, and these elements appear to have been largely immobile throughout the hydrothermal processes that affected the immediately adjacent mafic rocks.

ACKNOWLEDGEMENTS

This research was supported financially by Smash Minerals Corporation, the New Zealand Ministry for Science and Innovation, and the University of Otago. Discussions with Chris Siron, Chris Pennimpede, Phil Smerchanski, Rob Mackie, Dennis Arne, Mike Cooley, Lamont Leatherman, Kristy Long, and Mike Young helped us to develop geological ideas expressed herein. Olivia Brown provided excellent technical assistance.

REFERENCES

Chapman, R.J., Mortensen, J.K., and LeBarge, W.P., 2011. Styles of lode gold mineralization contributing to the placers of the Indian River and Black Hills Creek, Yukon Territory, Canada as deduced from microchemical characterization of placer gold grains. Mineralium Deposita, vol. 46, p. 881-903.

Evans, K.A., Phillips, G.N., and Powell, R., 2006. Rock-buffering of auriferous fluids in altered rocks associated with the Golden Mile-style mineralization, Kalgoorlie gold field, Western Australia. Economic Geology, vol. 101, p. 805-817.

Fuller, E.A. and Andersen, F.J., 1992. Placer geology of Black Hills Creek (parts of 1150/7 &10). Yukon Exploration and Geology 1993, Exploration and Geological Services Division, Indian and Northern Affairs Canada, p. 33–38.

Gabrielse, H., Murphy, D.C., and Mortensen, J.K., 2006. Cretaceous and Cenozoic dextral orogen-parallel displacements, magmatism, and paleogeography, north-central Canadian Cordillera. *In:* Paleogeography of the North American Cordillera: Evidence For and Against Large-Scale Displacments, J.W. Haggart, R. J. Enkin, and J.W.H. Monger (eds.), Geological Association of Canada, Special Paper 46, p. 255-276

Gabrielse, H. and Yorath, C.J., 1991. Tectonic synthesis, Chapter 18. *In:* Geology of the Cordilleran Orogen in Canada, H. Gabrielse and C.J. Yorath (eds.), Geology of Canada, vol. 4, p. 677–705.

Goldfarb, R.J., Baker, T., Dube, B., Groves, D.I., Hart, C.J.R., and Gosselin, P., 2005. Distribution, character and genesis of gold deposits in metamorphic terranes. *In*: Economic Geology 100th Anniversary Volume, J.W. Hedenquist, J.F.H. Thompson, R.J. Goldfarb, and J.P. Richards (eds.), Economic Geology, p. 407-450.

Huizenga, J.-M., 2011. Thermodynamic modelling of a cooling C–O–H fluid–graphite system: implications for hydrothermal graphite precipitation. Mineralium Deposita, vol. 46, p. 23-33.

Lowey, G.W. 2005. The origin and evolution of the Klondike goldfields, Yukon, Canada. Ore Geology Reviews, vol. 28, p. 431-450.

MacKenzie, D., Craw, D., and Mortensen, J.K., 2008a. Structural controls on orogenic gold mineralisation in the Klondike goldfield, Canada. Mineralium Deposita, vol. 43, p. 435-448.

MacKenzie, D., Craw, D., Mortensen, J.K., and Liverton, T., 2008b. Disseminated gold mineralisation associated with orogenic veins in the Klondike Schist, Yukon. *In:* Yukon Exploration and Geology 2007, D.S. Emond, L.R. Blackburn, R.P. Hill, and L.H. Weston (eds.), Yukon Geological Survey, p. 215-224.

MacKenzie, D., Craw, D., Cooley, M., and Fleming, A., 2010. Lithogeochemical localisation of disseminated gold in the White River area, Yukon, Canada. Mineralium Deposita, vol. 45, p. 683-705.

MacKenzie, D. and Craw, D., 2012. Contrasting structural settings of mafic and ultramafic rocks in the Yukon-Tanana terrane. *In:* Yukon Exploration and Geology 2011, K.E. MacFarlane and P.J. Sack (eds.), Yukon Geological Survey, p. 115-127.

Mortensen, J.K., 1990. Geology and U-Pb chronology of the Klondike District, west-central Yukon. Canadian Journal of Earth Sciences, vol. 27, p. 903-914.

Mortensen, J.K., 1992. Pre-mid-Mesozoic tectonic evolution of the Yukon-Tanana Terrane, Yukon and Alaska. Tectonics, vol. 11, p. 836-853.

Mortensen, J.K., 1996. Geological compilation maps of the northern Stewart River map area, Klondike and Sixtymile Districts (115N/15, 16; 1150/13,14; and parts of 1150/15, 16). Exploration and Geological Services Division, Yukon Region, Indian and Northern Affairs Canada, Open File 1996-1(G), 43 p.

Ruks, T.W., Piercey, S.J., Ryan, J.J., Villeneuve, M.E., and Creaser, R.A., 2006. Mid to late Paleozoic K-feldspar augen granitoids of the Yukon-Tanana Terrane, Yukon, Canada: Implications for crustal growth and tectonic evolution of the northern Cordillera. GSA Bulletin 118, p. 1212-1231.

Ryan, J.J. and Gordey, S.P., 2004. Geology, Stewart River Area (Parts of 115 N/1,2,7,8 and 115-O/2–12), Yukon Territory. Geological Survey of Canada, Open File 4641, scale 1:100 000.

Wainwright, A.J., Simmons, A.T., Finnigan, C.S., Smith, T.R., and Carpenter, R.L., 2011. Geology of new gold discoveries in the Coffee Creek area, White Gold district, west-central Yukon. *In:* Yukon Exploration and Geology 2010, K.E. MacFarlane, L.H. Weston and C. Relf (eds.), Yukon Geological Survey, p. 233-247.

Re-Os dating of gold in gold-bearing orogenic vein systems in the Klondike district – progress report

Ryan Mathur[1]
Juniata College, Huntingdon, PA, USA

Jim Mortensen
Earth, Ocean and Atmospheric Sciences, University of British Columbia, Vancouver, BC

Mathur, R. and Mortensen, J., 2013. Re-Os dating of gold in gold-bearing orogenic vein systems in the Klondike district – progress report. *In:* Yukon Exploration and Geology 2012, K.E. MacFarlane, M.G. Nordling, and P.J. Sack (eds.), Yukon Geological Survey, p. 65-72.

ABSTRACT

This is a preliminary study to determine the feasibility of using Re-Os to determine the age of gold in orogenic vein gold of the Klondike district, Yukon. Our objectives were to measure gold from several different vein systems to determine if enough Re and Os exists in native gold samples from the Klondike district to properly date the system. Six samples from different veins contain measurable concentrations of Re and Os and plot with significant variation on a Re-Os isochron diagram. The results indicate the need for detailed sampling of one vein system to better constrain age and source information from Re-Os systematics. Analysis of both native gold and synchronous pyrite from veins may provide enough data to determine age contraints, if native gold is not available.

[1]*mathurr@juniata.edu*

INTRODUCTION

A major impediment to identifying the key controls on formation of orogenic gold deposits is the difficulty in determining the absolute age of the mineralization. Without such information, it is impossible to understand how the timing of vein formation and introduction of gold fits into the structural and thermal evolution of a particular orogenic belt. Many analytical approaches that have proven effective for dating other styles of mineralization are difficult or impossible to apply when investigating orogenic gold systems. For example, there is typically no temporally or genetically related magmatism associated with orogenic gold; hence, it is difficult to closely bracket the age of mineralization by dating pre and post-mineral intrusive rocks. Most orogenic gold veins are hosted in low to medium grade, commonly highly micaceous, country rocks. It is typically difficult, if not impossible, to obtain a pure sample of hydrothermal mica from a vein alteration envelope $^{40}Ar/^{39}Ar$ dating that is unequivocally related to the veining and does not include older mica grains from the wall rock (*e.g.*, Mortensen *et al.*, 2010). Many orogenic veins form by repeated extensional events, producing "crack-seal" textures that include thin septa of micaceous wall rock between ribbons of vein quartz. Much of the mica that occurs locally with orogenic veins is therefore more likely to simply represent a fragment of the wall rock and not hydrothermal in origin. An additional complication in attempting to use $^{40}Ar/^{39}Ar$ methods on micas to date orogenic gold systems is that such veins typically form at a relatively late stage within cooling orogenic belts, and vein fluids show a temperature range that is not very different from the ambient temperature of the host rocks themselves at the time of vein formation. The effective closure temperature of the $^{40}Ar/^{39}Ar$ system in white mica is ~300°C. In at least some cases, both the country rock and any contained orogenic vein systems may not cool through this temperature until sometime after vein formation. In such instances, the resulting ages will reflect regional cooling of the orogen rather than the age of vein formation.

Dating gangue minerals within orogenic veins can potentially avoid some of the pitfalls listed above; however, there are relatively few minerals in such veins that are amenable to precise and accurate dating. As mentioned previously, dating white mica that occurs within some orogenic veins has many obstacles. Rutile is a relatively rare gangue phase in some orogenic veins, and the U-Pb system in rutile has a relatively high effective closure temperature (400-500°C; Blackburn *et al.*, 2011); thus U-Pb rutile dating offers some potential. U-Pb dating of hydrothermal monazite and/or xenotime (either as a gangue phase in the veins themselves or in hydrothermal alteration envelopes surrounding veins) has been used to determine the ages of several Archean and younger orogenic gold deposits (*e.g.*, Veilreicher *et al.*, 2003; Yudovskaya *et al.*, 2011); however, these phosphate minerals occur very rarely in orogenic vein systems. Similarly, although Re-Os dating of molybdenite is one of the most robust methods available for dating many styles of epigenetic mineralization, molybdenite has rarely been reported in orogenic veins, and this method is therefore of limited use.

The ideal solution to the problem would be to devise a method to date the gold in the veins directly. Previous studies (Kirk *et al.*, 2002; Mathur, 2005; Mathur *et al.*, 2003; Schaefer *et al.*, 2010) have shown that gold in a variety of intrusion and non-intrusion related vein systems can contain significant and variable amounts of Re, and that analytically measurable variations in $^{187}Os/^{186}Os$ ratios are generated that can constrain isochrons, from which the depositional age of the gold can be calculated. In this paper, we describe and report preliminary results for a scoping study, initiated in 2012, investigating the possibility of determining the age(s) of gold-bearing veins that were the main source of the rich placer gold deposits in the Klondike district in western Yukon (Chapman *et al.*, 2010a,b).

GEOLOGICAL SETTING AND NATURE OF GOLD-BEARING VEINS

Gold-bearing orogenic quartz veins have been identified in a number of localities in the Klondike (Fig. 1 and veins similar to those described in Chapman *et al.*, 2010a,b), and gold compositional studies by Chapman *et al.* (2010a,b) have demonstrated that these were the main source of the rich placer gold deposits in this area. A concentration of gold-bearing veins has been recognized at the head of rich placer ground on Eldorado and Bonanza creeks (including the Boulder Lode occurrence at the old Lone Star mine and the Nugget zone northeast of Eldorado Creek; Fig. 1). A second concentration of gold-bearing veins in the King Solomon Dome area (including the Sheba occurrence; Fig. 1) was interpreted as the main source for the pay streaks in streams that radiate out from this area, providing most of the gold that has been recovered from Hunker and Dominion creeks and part of the gold mined on Sulphur and Quartz creeks (Chapman *et al.*, 2010). The Virgin

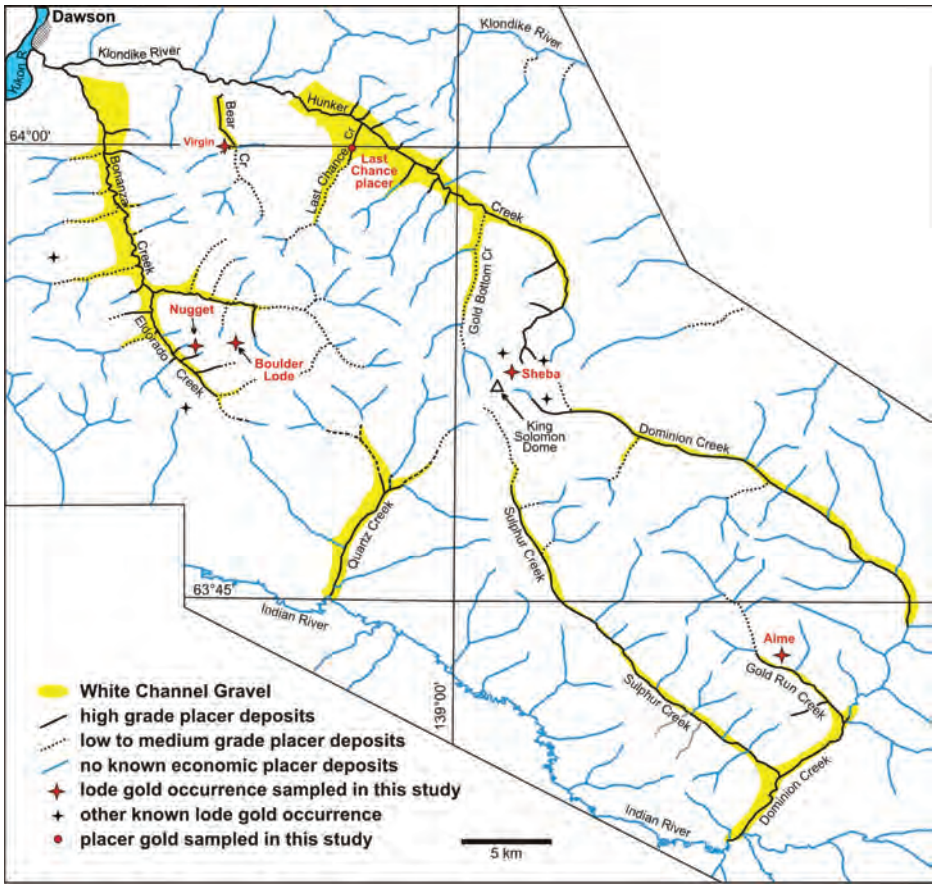

Figure 1. *Map showing the location of the main placer gold deposits in the Klondike District, together with the distribution of the locally gold-bearing White Channel Gravel deposits, and known lode gold deposits. Modified from Chapman et al. 2010a.*

vein occurrence, located on a left limit tributary of Bear Creek (Fig. 1), fed at least part of the Bear Creek placer pay streak. Finally veins on the left limit of lower Gold Run Creek (including the Aime occurrence; Fig. 1) likely contributed at least some of the gold that has been mined from Gold Run and lower Dominion creeks (Chapman *et al.*, 2010).

Gold-bearing veins in the Klondike are typical orogenic veins (Mortensen *et al.*, 1992; Rushton *et al.*, 1993), consisting almost entirely of quartz with only minor carbonate and rare barite and scheelite. They are simple extensional veins, and most represent single stage infillings of open fractures. Ribbon textures reflecting repeated "crack-seal" events during vein formation have been observed at a few localities in the Klondike, but appear to be rare. Sulphide content in the veins is typically low; pyrite concentrations occur in <1 to 2 cm thick selvages along the vein margins, and scattered grains of galena, sphalerite, chalcopyrite, and other sulphides and sulfosalts occur sporadically in the interiors of some veins. Gold is almost entirely confined to the pyritic selvages along the vein margins, and occurs locally as free grains within quartz. Locally sericitic alteration occurs in wall rocks immediately adjacent to the veins. Alteration envelopes, up to several metres wide, containing variable amounts of introduced ferroan carbonate and pyrite occur locally, especially where the veins crosscut mafic schist. Structural controls on the emplacement of gold-bearing veins in the Klondike have been described by MacKenzie *et al.* (2008a). This work showed that most veins formed during the latter stages of, or immediately following, the D_4 deformation event, which is a relatively late stage deformation in the area, characterized by locally developed zones of buckle folds and high-angle reverse faults.

Lead isotopic studies of sulphides from orogenic veins in the Klondike (Mortensen, work in progress) show a high degree of scatter in isotopic compositions and a correlation between the Pb isotopic compositions and compositional ranges from individual vein systems and the lithological composition of the immediate host rocks. This is interpreted to indicate that the lead, and presumably other vein components including gold, were deposited from small-scale hydrothermal systems and were derived from local host rocks, rather than being introduced from external sources, as has been postulated for many other orogenic vein systems (*e.g.*, Goldfarb *et al.*, 2005; Pitcairn *et al.*, 2007; Mortensen *et al.*, 2010).

The characteristics of gold-bearing veins are generally similar throughout the Klondike, and at this point available evidence is most consistent with a single episode of veining in the area. However, the possibility that two or more discrete mineralizing events have occurred cannot be precluded based on available evidence.

PREVIOUS DATING STUDIES OF KLONDIKE VEINS

Metamorphic cooling ages in the Klondike, determined by K-Ar and $^{40}Ar/^{39}Ar$ dating of metamorphic muscovite and biotite, range from *ca.* 185 to 162 Ma (Mortensen, 1990; unpublished data). Two K-Ar ages of 140±2 Ma and 134±1.5 Ma were reported by Mortensen (Hunt and Roddick, 1992) for muscovite that was interpreted to be part of the hydrothermal vein assemblage at the Sheba occurrence in the King Solomon Dome area (Fig. 1). These ages have subsequently been confirmed by $^{40}Ar/^{39}Ar$ methods that yielded ages of 144-145 Ma from muscovite samples both within the vein and from sericitic alteration envelopes (Mortensen, unpublished data). However, rutile from a gold-bearing quartz vein at the Mackay occurrence approximately 2 km east of the Sheba vein, has given a preliminary U-Pb isochron age of *ca.* 160 Ma (Mortensen, work in progress). Veins in the Mackay occurrence are currently interpreted as the same generation as those at the Sheba, raising the possibility that the $^{40}Ar/^{39}Ar$ ages from Sheba may reflect regional uplift and cooling rather than the age of the veining itself. There are presently no other independent constraints on the age(s) of the veins.

PREVIOUS Re-Os DATING OF GOLD

Kirk *et al.* (2002) provide a well developed isochron for gold separates from the Witwatersrand gold deposits in South Africa. The isochron age was interpreted as detrital and is the best evidence that gold in the basin originated from outside of the basin. Schafer *et al.* (2010) carried out a more detailed study of two mines in the Vaal reef in the Witwatersrand which Kirk *et al.* (2002) presented, but demonstrated mixing as a possible interpretation of the data.

Mathur *et al.* (2003; 2005) reported Re-Os data from gold-rich ores and native gold from high temperature, intrusion-related hydrothermal systems, including a Cu-Au porphyry deposit (Grasberg, Indonesia) and high and low sulphidation epithermal veins (Bucaramanga, Columbia). The resulting isochrons were interpreted to correspond to times of sulphide and gold deposition in these deposits, and indicated consistent, but relatively radiogenic, initial Os isotopic compositions for the mineralizing fluids.

GOLD SAMPLES FOR Re-Os DATING

It was anticipated at the outset of this study that Re and Os contents of gold from orogenic veins in the Klondike might be low, which would require relatively large amounts of gold for each analysis. Although gold is present in trace amounts in many of the Klondike veins, it is difficult to obtain sufficient gold from surface exposures for Re-Os analysis. This necessitated targeting veins or parts of veins known from previous work to contain significant amounts of gold, and to specifically sample the pyritic selvages, which typically contain the majority of the gold in any particular vein. A total of eight samples of pyritic selvage material were collected for the study in June, 2012; this included samples from the Boulder Lode and Nugget zones at the Lone Star occurrence (three samples; Fig. 1), the Sheba occurrence in the King Solomon Dome area (three samples; Fig. 1), and the Aime occurrence on lower Gold Run Creek (two samples; Fig. 1). Individual sample sizes ranged from 5-30 kg. These samples were crushed, ground, put over a wet shaking (Wilfley) table, and then flushed through heavy liquids at the University of British Columbia. Although much of the pyrite in these samples was thoroughly oxidized, the concentrates recovered from all of the samples comprised mainly pyrite with a lesser amount of galena. All gold grains present were hand-picked under a binocular microscope. Enough gold for analysis was recovered from the Boulder Lode and Nugget zone samples and two samples from the Aime occurrence. Unfortunately, none of the Sheba occurrence vein samples yielded sufficient gold for analysis. A sixth lode gold sample was obtained by hand panning approximately 200 kg of fine material extracted from a collapsed ore bin at the Virgin vein occurrence on Bear Creek (Fig. 1). An additional sample of panned placer gold was obtained from the right limit of lower Last Chance Creek (Fig. 1). This sample was known to be compositionally homogeneous (based on analytical work reported in Chapman *et al.*, 2010b), and showed a similar compositional range and micro-inclusion suite as the gold from the Virgin lode sample. Gold recovered from the seven vein and placer samples ranged in weight from 0.1 to 0.18 g.

ANALYTICAL METHODS AND RESULTS

Approximately 0.08 to 0.1 g of gold from each sample was loaded into carius tubes for Re-Os isotope analysis. Samples were dissolved in 12 ml of re-aquaregia with the addition of 2 ml of hydrogen peroxide and enriched spikes

of ^{185}Re and ^{190}Os, which were used to determine Re-Os concentrations by the isotope dilution method. Re and Os were purified from the matrix solutions with distillation and further chemistry, as described by Mathur *et al.* (2000). Purified samples of Re and Os were loaded onto filaments and analysed on the negative thermal ionization mass spectrometer at the University of Arizona. Concentrations of Re-Os were low in these samples. The analytical blank can greatly impact the measurement; thus a blank was monitored during the chemical processing of the samples. The Os blank was 0.17 picograms (with $^{187}Os/^{188}Os = 0.19$) and the Re blank was 8 picograms.

A total of seven analyses yielded analytically viable data. The concentration of Os in the gold samples varied between 12 and 257 ppt and Re varied between 0.7 and 4 ppb. The measured $^{187}Os/^{188}Os$ varied between 0.18 and 1.7 and the $^{187}Re/^{188}Os$ varied between 21 and 586. Errors for the samples were determined by varying the blank Os concentration as this is the largest source of error in the analysis. The concentrations of Re and Os in the native samples are similar to Re-Os concentrations observed in gold analyses from porphyry and epithermal sulphide systems. The exception is the placer gold sample from Last Chance Creek which yielded a slightly higher concentration of Os of 267 ppt.

Analytical data from the seven gold analyses are shown on an isochron plot in Figure 2. The implications of the data are discussed below.

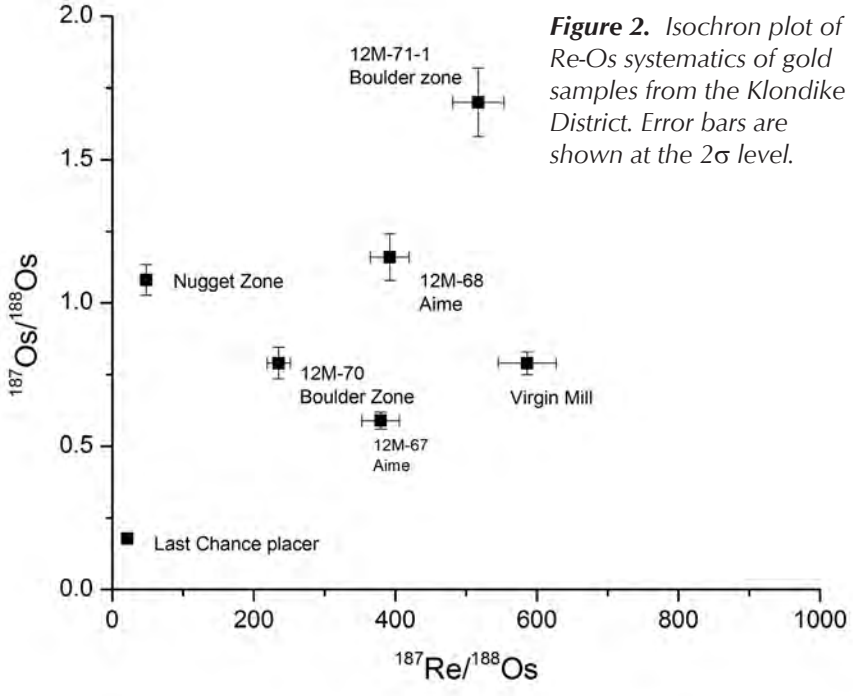

Figure 2. *Isochron plot of Re-Os systematics of gold samples from the Klondike District. Error bars are shown at the 2σ level.*

DISCUSSION

The main goal of this study was to evaluate the possibility of using Re and Os in samples of native gold from the Klondike to determine the age(s) of vein formation and the source(s) of Os (and by inference Au). This method requires that there be measurable amounts of Re and Os in the gold samples, as well as a sufficient range of Re/Os ratios to produce a well-constrained isochron. Three conditions must also be met in order to generate an isochron that is geologically meaningful: a) all samples must have incorporated initial Os of the same isotopic composition; b) the individual samples have to be of the same age and be related to one another (*i.e.*, formed from the same hydrothermal system); and c) the Re-Os isotopic system must have remained undisturbed since the gold was deposited. Initial results of the study have shown that lode gold samples from the Klondike district do contain sufficient concentrations of both Re and Os to permit relatively precise determination of Re and Os isotopic compositions, and our initial sample suite produced a considerable range of $^{187}Re/^{188}Os$ values (21-588). Therefore, in theory, the Re-Os system in gold from the Klondike should be amenable to isochron dating. However, there are several important considerations that potentially bear on the application of this method in the Klondike. First, we cannot be certain that all of the gold-bearing veins in the Klondike formed at the same time as evidenced by petrologic and geologic mapping relationships. Second, gold compositional studies by Chapman *et al.* (2010a,b) suggest that the gold-bearing veins are the products of relatively small hydrothermal systems (scale of <10 km in diameter). The seven samples that were analysed came from localities as much as 45 km apart, and it is therefore unlikely that they represent products of the same hydrothermal system. Third, Pb isotopic studies discussed above suggest that the gold and possibly other contained metals in the veins are derived locally; hence there is no basis to suggest that the Re-Os geochemistry of the vein fluids responsible for the formation of individual veins from different parts of the Klondike would necessarily be related.

There is a high degree of scatter in our data (Fig. 2). Three samples from the Lone Star Ridge area between upper Bonanza

Creek and Eldorado Creek (two samples from the Boulder Lode occurrence and one from the Nugget zone) are all from veins hosted within the same felsic metavolcanic package. The two samples from the Boulder Lode were taken from veins within ~200 m of one another, so might be expected to be closely related and to have formed from the same ore fluid. The Nugget zone sample is from a locality ~2 km farther to the west (Fig. 1). The measured isotopic composition of the Nugget zone gold sample (Fig. 2) indicates that it formed from a mineralizing fluid with a considerably more radiogenic initial Os isotopic composition, and appears to be incompatible with having formed from the same hydrothermal system that produced the Boulder Lode veins. Although some minor differences in the Os isotopic composition of the mineralizing fluids might be expected in view of the variability in Pb isotopic composition within and between individual veins in the Klondike, this amount of heterogeneity was quite unexpected. Two samples from veins ~250 m apart at the Aime occurrence in the southern Klondike (Fig. 1) that are very similar in composition and overall character and are hosted within the same mafic schist package also yield isotopic compositions that indicate that they did not form from the same, isotopically homogeneous ore fluid.

Interpretation of the Re-Os data along with the other trace metal studies is complicated. Osmium has been shown to be immobile in melts and hydrothermal fluids (McCandless *et al.*, 1993; Suzuki *et al.*, 1996, 2000; Woodhead and Brauns, 2004); however, in contrast, Re is very mobile in melts and lower temperature hydrothermal fluids. The variation of the initial Os ratio that we infer from the measured compositions of the Klondike gold samples suggests two possibilities: 1) fluids scavenged osmium from diverse local metal sources; or 2) a single fluid which never reached isotopic equilibrium/closure temperature could be responsible for mineralization. At this point, the first scenario is most likely given the evidence from Pb isotopic studies discussed above. This is significant, because to date, the mobility of Os has not been demonstrated and may be indicated for the first time here in the Klondike gold. The exact mechanism by which variable amounts of initial Os, derived from isotopically distinct, relatively local reservoirs could be mobilized into orogenic veins is unclear. Gold in veins in the Eldorado Creek area (Dysle zone and Violet occurrence) has been shown to include two distinct coexisting gold phases, based on alloy composition (Chapman *et al.*, 2010a), suggesting that the veins formed from distinct pulses of hydrothermal fluid, each of which had different Ag/Au proportions, and may have also had different Os isotopic compositions, implying derivation from distinct sources.

SUGGESTIONS FOR FUTURE WORK

The results of this scoping study suggest that there is a surprisingly large amount of variability in the initial Os isotopic composition of mineralizing fluids responsible for the formation of gold-bearing veins in the Klondike. Although it is unclear whether this is likely to be typical of all orogenic gold systems, it certainly represents a significant challenge for utilizing the Re-Os method to date veins in this area. The main problem appears to be variability between different hydrothermal systems, and perhaps even within closely spaced veins in the same system, related to either very local sources for the Os and/or mixing between ore fluids with somewhat different Os isotopic composition. Our work has shown that there is both adequate amounts of Re and Os in gold from the Klondike veins, and a sufficient range of Re/Os ratios to apply isochron dating methods, if sample suites that meet the criteria for valid isochron dating can be identified. The intimate association between gold and pyrite in most of the veins in the Klondike, and the demonstrated resistance to resetting of the Re-Os system in pyrite (Brenan *et al.*, 2000), suggests that a fruitful approach might be to construct isochrons based on multiple aliquots of gold from a specific part of a single vein, together with multiple fractions of the associated pyrite. The gold to be analysed would have to be examined petrographically and alloy compositions determined using electron microprobe methods in order to preclude any possibility of there being mixed populations of gold alloy phases present. Another very interesting line of research would be to test the source(s) of gold in the orogenic veins in the Boulder Lode area using Re-Os isotopic systematics of the gold and potential sources (especially pyrite in the host schist), which has been suggested by MacKenzie *et al.* (2008b) and Mortensen (unpublished data) to be the ultimate source of the vein gold.

REFERENCES

Blackburn, T., Bowring, S.A., Schoene, B., Mahan, K., and Dudas, F., 2011. U-Pb thermochronology: creating a temporal record of lithosphere thermal evolution. Contributions to Mineralogy and Petrology, doi: 10.1007/s00410-011-0607-6.

Brenan, J.M., Cherniak, D.J., and Rose, L.A., 2000. Diffusion of Os in pyrrhotite and pyrite: implications for closure temperature of the Re-Os system. Earth and Planetary Letters, vol. 180, p. 399-413.

Bucci, L.A., McNaughton, N.J., Fletcher, I.R., Groves, D.I., Kositcin, N., Stein, H.J., and Hagemann, S.G., 2004. Timing and Duration of High-Temperature Gold Mineralization and Spatially Associated Granitoid Magmatism at Chalice, Yilgarn Craton, Western Australia. Economic Geology, vol. 99, no. 6, p. 1123-1144.

Chapman, R.J., Mortensen, J.K., Crawford, E.C., and Lebarge, W.P, 2010a. Microchemical studies of placer and lode gold in the Klondike District, Yukon, Canada: Evidence for a small, gold-rich, orogenic hydrothermal system in the Bonanza and Eldorado Creek area. Economic Geology, vol. 105, p. 1369-1392.

Chapman, R.J., Mortensen, J.K., Crawford, E.C., and Lebarge, W.P., 2010b. Microchemical studies of placer and lode gold in the Klondike District, Yukon, Canada: Constraints on the nature and location of regional lode sources. Economic Geology, vol. 105, p. 1393-1410.

Goldfarb, R.J., Baker, T., Dubé, B., Groves, D.I., Hart, C.J.R., and Gosselin, P., 2005. Distribution, character and genesis of gold deposits in metamorphic terranes. *In:* Economic Geology 100th Anniversary Volume, J.W. Hedenquist, J.F.H. Thompson, R.J. Goldfarb, and J.P. Richards (eds.), p. 407-450.

Hunt, P.A. and Roddick, J.C., 1992. A compilation of K-Ar ages report 21. *In:* Radiogenic age and isotopic studies: report 5. Geological Survey of Canada, Paper no. 91-2, p. 207-261.

Kirk, J., Ruiz, J., Chesley, J., Walshe, J., and England, G., 2002. A Major Archean, Gold- and Crust-Forming Event in the Kaapvaal Craton, South Africa. Science, vol. 297, no. 5588, p. 1856-1858.

MacKenzie, D., Craw, D., and Mortensen, J.K., 2008a. Structural controls on orogenic gold mineralisation in the Klondike goldfield, Canada. Mineralium Deposita, vol. 43, p. 435-448.

MacKenzie, D., Craw, D., Mortensen J.K., and Liverton, T., 2008b. Disseminated gold mineralization associated with orogenic veins in the Klondike Schist, Yukon. *In:* Yukon Exploration and Geology 2007, D.S. Emond, L.R. Blackburn, R.P. Hill, and L.H. Weston (eds.), Yukon Geological Survey, p. 215-224.

Mathur, R., Ruiz, J., Herb, P., Hahn, L., and Burgath, K.P., 2003. Re-Os isotopes applied to the epithermal gold deposits near Bucaramanga, northeastern Colombia. Journal of South American Earth Sciences, vol. 15, no. 7, p. 815-821.

Mathur, R., Ruiz, J., Titley, Gibbons, S., and Margotomo, W., 2000. Different crustal sources for Au-rich and Au-poor ores of the Grasberg Cu-Au porphyry deposit. Earth and Planetary Science Letters, vol. 183, p. 7-14.

Mathur, R., Titley, S., Ruiz, J., Gibbon, S., and Friehauf, K., 2005. A Re-Os isotope study of sedimentary rocks and copper-gold ores from the Ertsberg District, West Papua, Indonesia. Ore Geology Reviews, vol. 26, p. 207-226.

McCandless, T. and Ruiz, J., 1993. Rhenium and Osmium evidence for regional mienralization in southwestern North America. Science, vol. 261, p. 1282-1286.

Mortensen, J.K., 1990. Geology and U-Pb geochronology of the Klondike District, west-central Yukon Territory. Canadian Journal of Earth Sciences, vol. 23, p. 903-914.

Mortensen, J.K., Nesbitt, B.E., and Rushton, R.W., 1992. Preliminary observations on the geology and geochemistry of quartz vein in the Klondike District, west-central Yukon. *In:* Yukon Geology, vol. 3, Indian and Northern Affairs Canada, Exploration and Geological Services Division, Northern Affairs Program, Whitehorse, Yukon, p. 260-270.

Mortensen, J.K., Craw, D., MacKenzie, D.J., Gabites, J.E., and Ullrich, T., 2010. Age and origin of orogenic gold mineralization in the Otago Schist belt, South Island, New Zealand: Constraints from lead isotopic and $^{40}Ar/^{39}Ar$ dating studies. Economic Geology, vol. 105, p. 777-793.

Pitcairn, I.K., Teagle, D.A.H., Craw, D., Olivo, G.R., Kerrich, R.T., and Brewer, T.S., 2007. Sources of metals and fluids in orogenic gold deposits: Insights from the Otago and Alpine schists, New Zealand. Economic Geology, vol. 101, p. 1525-1546.

Rushton, R.W., Nesbitt, B.E., Muehlenbachs, K., and Mortensen, J.K., 1993. A fluid inclusion and stable isotope study of Au-quartz veins in the Klondike District, Yukon Territory, Canada: a section through a mesothermal vein system. Economic Geology, vol. 88, p. 647-678.

Schaefer, B.F., Pearson, D.G., Rogers, N.W., and Barnicoat, A.C., 2010. Re–Os isotope and PGE constraints on the timing and origin of gold mineralisation in the Witwatersrand Basin. Chemical Geology, vol. 276, no. 1-2, p. 88-94.

Suzuki, K., Shimizu, H., and Masuda, A., 1996. Re-Os dating of molybdenites from ore deposits in Japan: Implication for the closure temperature of the Re-Os system for molybdenite and the coiling history of molybdenum ore deposits. Geochmicia et Cosmochimica Acta, vol. 60, p. 3151-3159.

Suzuki, K., Kagi, H., Nara, M., Takano, B., and Nozaki, Y., 2000. Experimental alteration of molybdenite: evaluation of the Re-Os system, infrared spectroscopic profile and polytype. Geochmica et Cosmochimica Acta, vol. 64, p. 223-232.

Veilreicher, N.M., Groves, D.I., Fletcher, I.R., McNaughton, N.J., and Rasmussen, B., 2003. Hydrothermal monazite and xenotime geochronology: A new direction for precise dating of orogenic gold mineralization. Society of Economic Geologists Newsletter, no. 53, April, 2005, p. 1 and 10-15.

Woodhead J. and Brauns, M., 2004. Current limitation to the understanding of Re-Os behavior in subduction systems, with an example from New Britain. Earth and Planetary Science Letters, vol. 221, p. 309-323.

Yudovskaya, M.A., Distler, V.V., Rodionov, N.V., Mokhov, A.V., Antonov, A.V., and Sergeev, S.A., 2011. Relationship between metamorphism and ore formation at the Sukhoi Log gold deposit hosted in black slates from the data of U-Th-Pb isotopic SHRIMP-dating of accessory minerals. Geology of Ore Deposits, vol. 53, p. 27-57.

Mid-Cretaceous orogenic gold and molybdenite mineralization in the Independence Creek area, Dawson Range, parts of NTS 115J/13 and 14

Greg G. McKenzie, Murray M. Allan[1], James K. Mortensen, Craig J.R. Hart, Matías Sánchez
Mineral Deposit Research Unit, University of British Columbia, Vancouver, BC

Robert A. Creaser[2]
Department of Earth & Atmospheric Sciences, University of Alberta, Edmonton, AB

McKenzie, G.G., Allan, M.M., Mortensen, J.K., Hart, C.J.R., Sánchez, M., and Creaser, R.A., 2013. Mid-Cretaceous orogenic gold and molybdenite mineralization in the Independence Creek area, Dawson Range, parts of NTS 115J/13 and 14. *In:* Yukon Exploration and Geology 2012, K.E. MacFarlane, M.G. Nordling, and P.J. Sack (eds.), Yukon Geological Survey, p. 73-97.

ABSTRACT

The Boulevard gold prospect, located in the Independence Creek area of the Dawson Range, comprises sheeted, auriferous quartz-sulphide-carbonate veins and fault breccia, hosted mainly by mafic schist. The nearby Toni Tiger molybdenum showing is characterized by quartz-molybdenite veins cutting Late Permian meta-aplite and garnet-pyroxene skarn of uncertain age. We present geochronological evidence that gold and molybdenum were deposited at 96-95 Ma, approximately 3 m.y. after intrusion of the Dawson Range batholith and Coffee Creek granite. Fluid inclusions from mineralized quartz veins suggests that gold at Boulevard and molybdenite at Toni Tiger were formed from similar H_2O-CO_2-NaCl type fluids between 279 and 310°C and >1 kbar. We conclude that both are part of the same mineralizing system, and that structurally-hosted gold at the nearby Coffee deposit and in the Moosehorn Range of western Yukon may be broadly related, post-arc orogenic systems developed during exhumation of the Dawson Range in mid-Cretaceous time.

[1] *mallan@eos.ubc.ca*

INTRODUCTION

The Independence Creek area is a broad upland plateau within the Dawson Range of west-central Yukon, and is incised by stream systems draining north into the Yukon River. The area is located approximately 140 km south of Dawson, 40 km south of the Golden Saddle gold deposit (Kinross Gold Corp.), which contains 1.4 Moz of gold (Underworld Resources Inc., January 19, 2010 press release), and approximately 10 km southwest of the Coffee gold deposit, which contains 3.2 Moz of gold (Kaminak Gold Corp., December 13, 2012 press release) (Fig. 1).

Gold mineralization of the Boulevard zone was first identified by Rimfire Minerals Corp. in 2007 in the headwaters of the Independence Creek drainage. It is a northwest-trending, 450 m by 1.2 km, gold-arsenic-antimony soil geochemical anomaly with sporadic tellurium and bismuth. Exploration at Boulevard was pursued further by Rimfire in 2008, Silver Quest Resources Ltd. from 2009 to 2011, and Independence Gold Corp. in 2012. Exploration methods at Boulevard have included stream sediment geochemistry, soil geochemistry, trenching, mapping, prospecting, induced polarization and magnetometry surveys, airborne aeromagnetic and radiometric surveys, and diamond drilling.

The Toni Tiger molybdenum showing (Yukon MINFILE 115J 052) is located approximately 2 km east of the Boulevard trend (Fig. 2). Mineralization was discovered by regional silt survey in 1969 by Archer, Cathro and Associates, and the anomaly was attributed to disseminated molybdenite in skarn with associated

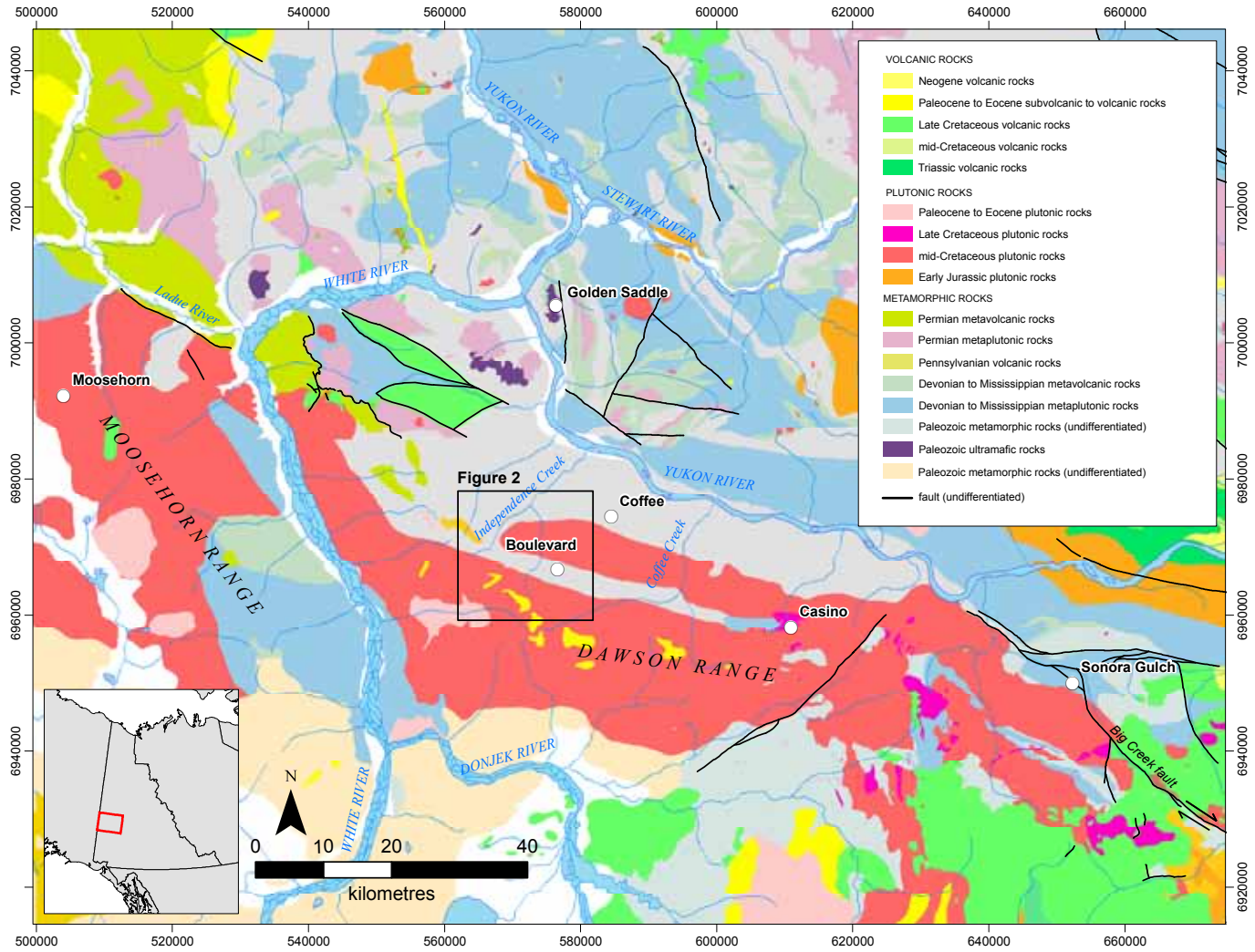

Figure 1. *Geological map of the Dawson Range (in greater Yukon Plateau), showing significant mineral deposits and prospects (geology modified from Gordey and Ryan (2005) and Gordey and Makepeace (2003)). The Independence Creek study area is indicated by the black box. Datum: NAD83; Projection: UTM zone 7N.*

chalcopyrite, arsenopyrite, scheelite, and pyrite (Craig, 1970). Trenching at the prospect exposed quartz-molybdenite veins, and Craig (1970) inferred that molybdenite was associated with, and restricted to, the skarn alteration.

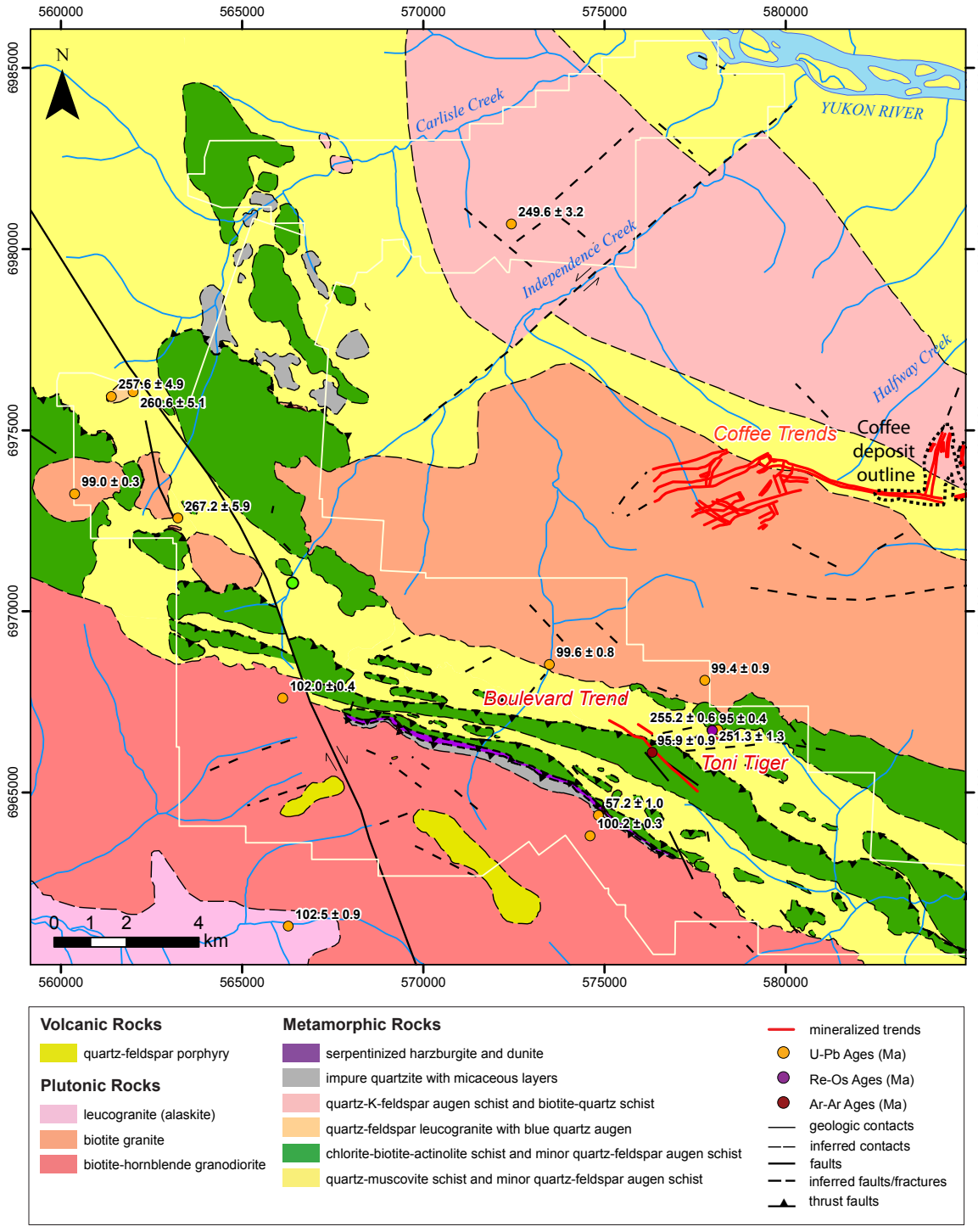

Figure 2. *Geologic map of the Independence Creek area, showing geochronological data and mineralized trends in the Boulevard and Coffee prospects (Datum: NAD83; Projection: zone 7N). Additional sources of information include: Tempelman-Kluit, 1974; Jilson, 2000; Gordey and Ryan, 2005; Chartier et al., 2013; J. Ryan, pers. comm., 2012. The white line defines Silver Quest property limits as of June 2011.*

The Boulevard and Toni Tiger prospects present an opportunity to investigate the age and geological characteristics of two proximal mineralized systems that have contrasting metal associations (Au-As-Sb and Mo-Cu-W, respectively) and uncertain metallogenesis. The geologic relationships presented below are based on mapping, interpretations of airborne magnetic and radiometric data, and detailed observations of diamond drill core. We present U-Pb zircon ages both for metamorphic rocks (including those hosting molybdenite mineralization), and for samples of the Dawson Range batholith, Coffee Creek plutonic suite, and local subvolcanic units. Petrographic observations and reconnaissance-level fluid inclusion data from mineralized veins are also included. Finally, we present $^{40}Ar/^{39}Ar$ muscovite ages for gold-bearing veins at Boulevard and Re-Os molybdenite ages for Toni Tiger, both of which are interpreted to date mineralization directly.

FIELD RELATIONSHIPS

GEOLOGY

The Independence Creek area is underlain by a 3 km-wide, west-northwest-trending belt of predominantly schistose and gneissic rocks (Figs. 1, 2 and 3). This rock package includes the following map units (Fig. 2): (a) serpentinized harzburgite and dunite; (b) variably pyritic chlorite-biotite-actinolite schist, containing minor quartz-feldspar augen schist; (c) quartz-muscovite schist, containing minor calcareous schist; (d) impure quartzite with micaceous layers; (e) foliated quartz-feldspar-muscovite leucogranite and quartz-feldspar augen schist with distinctive blue quartz augen; and (f) quartz-K-feldspar augen schist and minor biotite-quartz schist. Peak metamorphic grade is inferred to be middle greenschist facies on the basis of biotite-chlorite-actinolite assemblages in mafic schists. Lithological heterogeneities are common on the scale of metres to hundreds of metres, due to a combination of original stratigraphic and intrusive contact relationships, and repetition by tight to isoclinal folding and faulting. Ultramafic rocks are exposed as small lenticular bodies near the south margin of the metamorphic package (Figs. 2 and 3f), and are inferred to delineate a major crustal-scale fault (Templeman-Kluit, 1974; Gordey and Makepeace, 2003; Zagorevski *et al.*, 2012).

The metamorphic package is intruded to the south by medium to coarse-grained biotite-hornblende granodiorite of the Dawson Range batholith, a phase of the mid-Cretaceous Whitehorse plutonic suite (Figs. 1, 2, and 3a). The rock is massive to lineated with locally aligned hornblende and stretched quartz. To the north, metamorphic rocks are intruded by the Coffee Creek phase of the Whitehorse plutonic suite (Templeman-Kluit, 1974), which is composed of medium to coarse-grained biotite granite with volumetrically minor aplitic and pegmatitic phases (Figs. 1, 2, and 3b). A garnet-bearing, quartz-phyric porphyry phase is recognized at the western tip of the Coffee Creek granite. No crosscutting relationships are observed between plutonic rocks and gold mineralization at Boulevard or molybdenite-bearing veins at Toni Tiger.

Locally, subcrop of porphyritic rhyodacite and basalt are observed near the northern margin of the Dawson Range batholith (unit too small to represent on Fig. 2). This unit has been mapped and interpreted as a hypabyssal intrusion (J. Ryan, pers. comm., 2012).

STRUCTURES

The principal fabric within metamorphic rock units in the study area strikes 280-290°N and is steeply dipping between ~70 and 90°. West of the Coffee Creek granite, the strike of the regional metamorphic fabric rotates to 315°N (Fig. 2). This structural pattern in the metamorphic rocks mirrors a major change in the regional strike of the Dawson Range batholith approximately 20 km west of the study area (Fig. 1).

The main metamorphic fabric has strongly transposed any original depositional features within the metamorphic rock units. The development of this fabric is likely due to D_1 and D_2 collisional deformation accompanying peak metamorphism of Yukon-Tanana terrane rocks in Late Permian time (Berman *et al.*, 2007; MacKenzie *et al.*, 2008a; Beranek and Mortensen, 2011). Isoclinal, rootless fold hinges and boudinaged quartz veins are interpreted to represent D_2 phase folds that overprint the earlier S_1 fabric.

A third deformation event (D_3) can be recognized as locally developed crenulations (S_3) and tight disharmonic folding of the pre-existing metamorphic fabric, and is best developed within micaceous lithologies. These folds have axial traces that are subparallel to the regional west-northwest map trend of the metamorphic rock package and axial planes that are subvertical. Ultramafic bodies along the northern margin of the Dawson Range define a lineament that extends eastward toward the Casino Cu-Mo-Au porphyry deposit and the Sonora Gulch porphyry prospect (Fig. 1), and are interpreted to define a crustal-

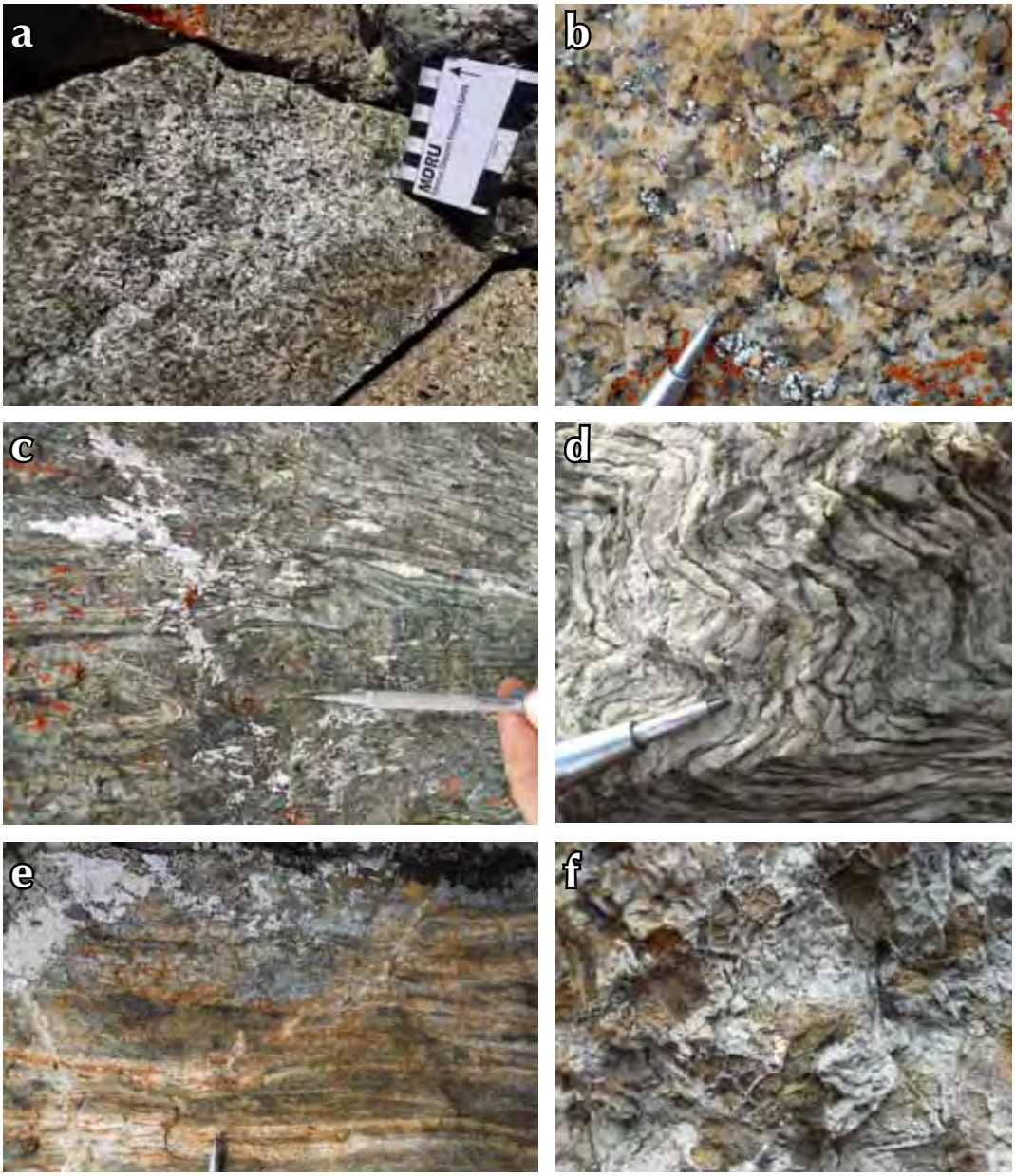

Figure 3. *Typical rock types in the Independence Creek area: (a) biotite hornblende granodiorite of the Dawson Range batholith; (b) biotite granite of the Coffee Creek granite; (c) strongly deformed chloritic schist (typical host rock to gold mineralization); (d) folded metagranite; (e) banded diopside-garnet skarn and biotite schist (typical host rock at the Toni Tiger molybdenum showing); and (f) serpentinitzed harzburgite.*

scale fault that was partially intruded by the Dawson Range batholith (Zagorevski *et al.*, 2012). The origin of this structure is uncertain, but it was likely active in the Early Jurassic, when regional scale thrust faulting imbricated slivers of Slide Mountain oceanic crust within the Yukon-Tanana terrane (MacKenzie *et al.*, 2008a,b; MacKenzie and Craw, 2012).

Locally-developed stretching lineations within the Dawson Range batholith are subhorizontal and parallel to the regional west-northwest strike of metamorphic rocks to the north. The Coffee Creek granite is almost entirely massive, suggesting that either fabrics in the Dawson Range batholith were formed prior to emplacement of the Coffee Creek granite, or that syn to post-magmatic deformation was partitioned more strongly in the Dawson Range batholith.

A fault trending 330°N is obvious in aeromagnetic data, and cuts the metamorphic package and the Dawson Range batholith with 1 km of dextral offset (southwest quadrant of Fig. 2). This fault is the most prominent in a series of northwest to north-northwest-trending structures that truncate the west-northwest-trending magnetic grain of the metamorphic package (Fig. 2). A similar northwest to north-northwest orientation is observed for gold-bearing structures at the Boulevard prospect. The offset of the northern intrusive contact of the Dawson Range batholith by this fault generation indicates that this fault set occurred after emplacement of the Dawson Range batholith in mid-Cretaceous time.

VEINS, ALTERATION, AND MINERALIZATION

Observations on veining, alteration, and mineralization are presented for the Boulevard and Toni Tiger prospects separately, since field relationships do not provide sufficient information about the relative timing of these adjacent systems.

BOULEVARD

Detailed observations of diamond drill core reveal five separate vein generations (Fig. 4), all of which are hosted primarily in biotite-chlorite ± actinolite schist. A paragenetic scheme is presented in Figure 5 and petrographic observations are shown in Figure 6.

V_1: The first vein generation (V_1) comprises sugary quartz ± pyrite veins, and is found in all metamorphic rock types in the study area (Fig. 4a). V_1 veins are typically ~1 cm wide and contain less than 1% pyrite and trace chalcopyrite as inclusions in pyrite. V_1 veins are conformable with the metamorphic fabric, and commonly occur as boudins and rootless hinges in mesoscopic folds. V_1 veins are early and are interpreted to be metamorphic segregations formed during Late Permian tectonism.

V_2: V_2 veins are composed of quartz, pyrrhotite ± chalcopyrite, are 5 to 30 mm wide, have irregular margins, and no alteration envelopes (Fig. 4b). V_2 veins are generally discordant to the S_1/S_2 fabric, suggesting they post-date peak deformation.

V_3: V_3 veins are composed mainly of quartz and ferroan carbonate with muscovite/illite-pyrite-arsenopyrite

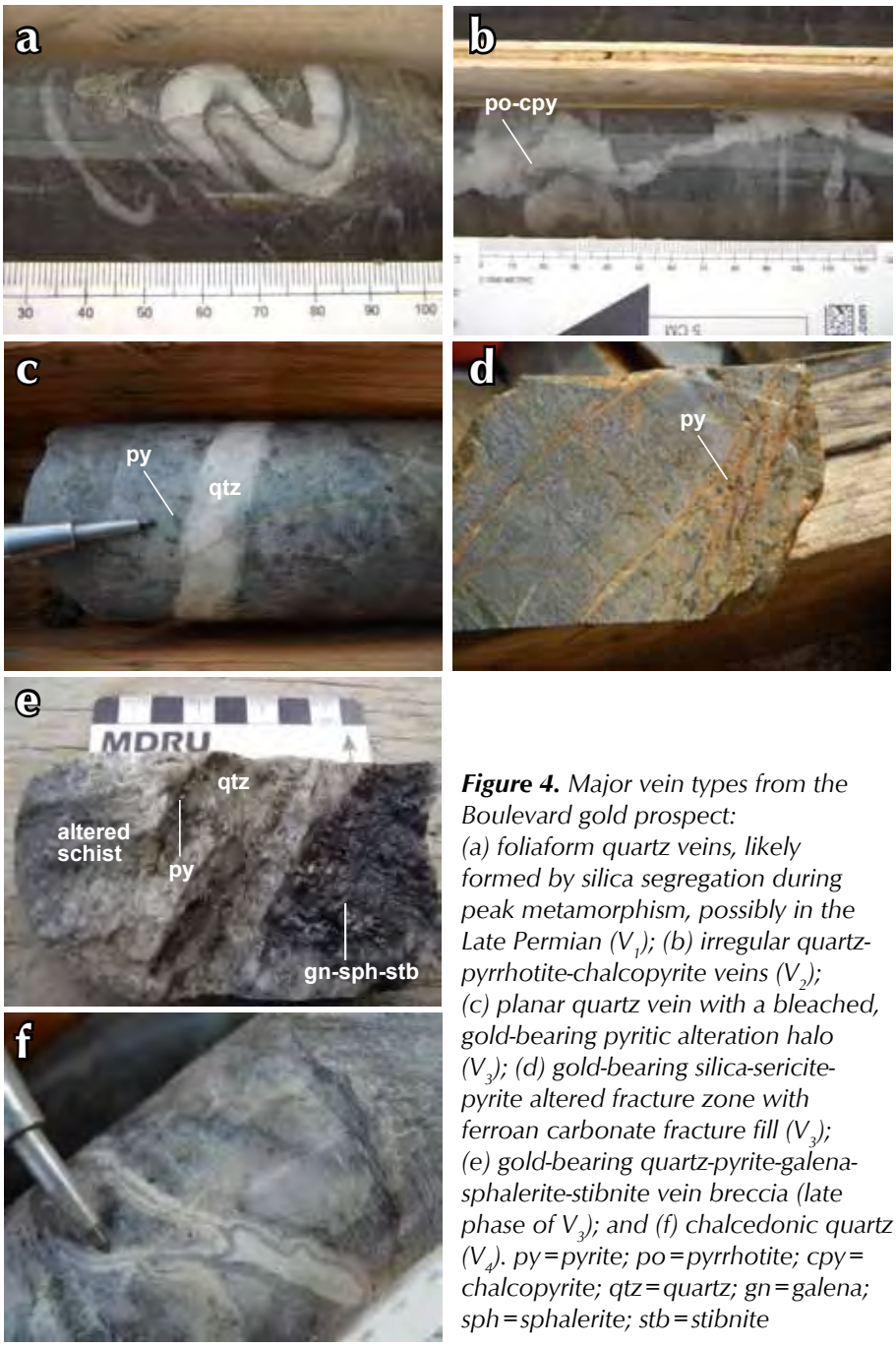

Figure 4. *Major vein types from the Boulevard gold prospect: (a) foliaform quartz veins, likely formed by silica segregation during peak metamorphism, possibly in the Late Permian (V_1); (b) irregular quartz-pyrrhotite-chalcopyrite veins (V_2); (c) planar quartz vein with a bleached, gold-bearing pyritic alteration halo (V_3); (d) gold-bearing silica-sericite-pyrite altered fracture zone with ferroan carbonate fracture fill (V_3); (e) gold-bearing quartz-pyrite-galena-sphalerite-stibnite vein breccia (late phase of V_3); and (f) chalcedonic quartz (V_4). py = pyrite; po = pyrrhotite; cpy = chalcopyrite; qtz = quartz; gn = galena; sph = sphalerite; stb = stibnite*

	V_1	V_2	V_3	V_4	V_5
quartz	———	———	———	———	
ferroan carbonate			———	———	———
pyrite	——	———	——— ——	———	
arsenopyrite			——		
gold			—— —		
pyrrhotite		———			
chalcopyrite	——	———			
sphalerite			—		
galena			—		
stibnite			—		
tetrahedrite			—		

Figure 5. *Mineral paragenesis for veins present in the Boulevard gold prospect.*

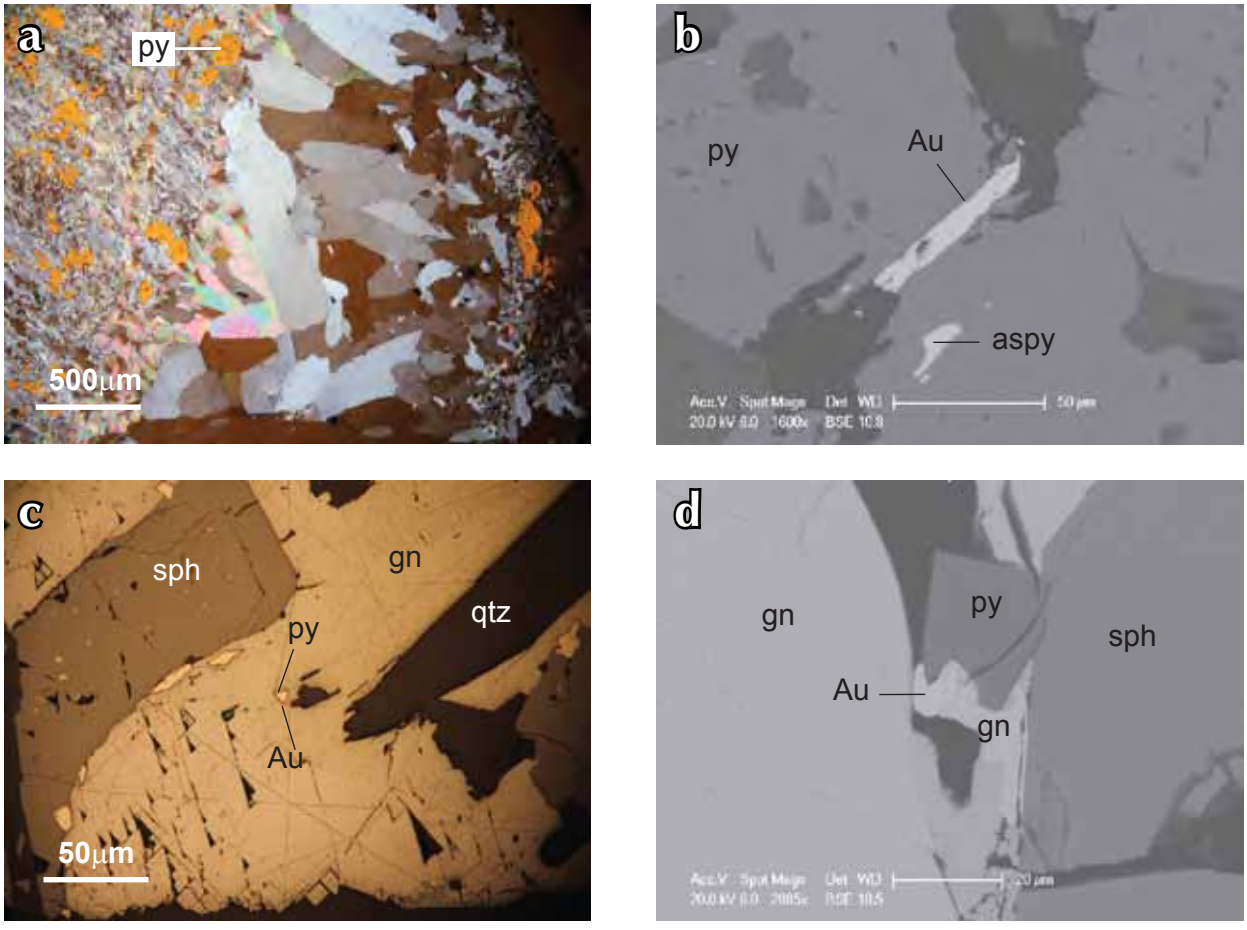

Figure 6. *Examples of gold mineralization from the Boulevard area: (a) typical V_3-generation quartz-carbonate vein with a gold-bearing pyrite halo (combined cross-polarized transmitted light and reflected light); (b) backscattered electron microscope image of gold associated with pyrite and arsenopyrite; (c) reflected light photomicrograph of a <5 µm gold grain as an inclusion in galena; (d) backscattered electron microscope image of a 10 µm gold grain associated with galena, sphalerite and pyrite. aspy = arsenopyrite (other mineral abbreviations as in Figure 4).*

alteration envelopes (Figs. 4c,d, 6a, and 8a). A paragenetically late phase of sphalerite-galena-pyrite-tetrahedrite ± stibnite is observed in some veins, especially where brecciation has also taken place (Fig. 4e). Veins are typically 2 to 20 mm wide, planar, and occur in sheeted sets that cut the S_1/S_2 fabric at a high angle. Approximations of vein orientations (using the local metamorphic fabric as a reference plane in unoriented drill core) yield a predominantly northwest strike and a dip of approximately 30° to the southwest. V_3 vein swarms are spatially related and subparallel to mineralized fault gouge. The faulting is interpreted to post-date V_3 veining since vein fragments have been noted in the fault gouge. Gold has two petrographic associations: (1) inclusions and fracture fillings in pyrite or arsenopyrite in alteration haloes (Fig. 6b); and (2) inclusions in sphalerite-galena-pyrite-tetrahedrite ± stibnite (Fig. 6c,d). Gold grains are typically less than 10 μm.

V_4: A fourth vein generation (V_4) is characterized by thin, colloform banded chalcedonic quartz-carbonate ± pyrite ± chalcopyrite veins (Fig. 4f). They vary in width from 5 to 60 mm. Carbonate is typically pink and manganiferous. V_4 veins crosscut both the metamorphic fabric and V_3 stage veins.

V_5: Thin (1-5 mm) ferroan carbonate veinlets (V_5) cut the metamorphic foliation and all pre-existing vein types. This vein generation has no known association with sulphides or gold.

TONI TIGER

The local host rocks include meta-aplite (Fig. 7a,b), biotite-quartz-feldspar schist (Fig. 7c-e), biotite hornfels, and garnet-diopside skarn (Fig. 7f). All rock types are cut by 1 cm to 1 m-wide, milky white quartz ± molybdenite veins (Figs. 7c-e and 8c) that occupy subvertical, conjugate fracture sets trending north and northeast. Molybdenite is also observed as wall rock disseminations in vein halos in biotite-quartz-feldspar schist and skarn. Veins have biotite-destructive chlorite-muscovite envelopes where they cut biotite-bearing host rocks (Fig. 7c,f). Idiomorphic garnet of hydrothermal origin is common along the margins of quartz ± molybdenite veins cutting the skarn unit.

FLUID INCLUSION PROPERTIES

BOULEVARD

Petrographic observations and a small number of microthermometric analyses were carried out on samples of quartz-hosted fluid inclusions from gold-stage V_3 veins at Boulevard. A homogenous population of aqueous-carbonic fluid was observed, which, based on clathrate melting and CO_2 homogenization temperatures, contains 15 to 24 mol % CO_2, ~2 to 3 wt % NaCl, and a bulk density of 0.8 to 0.85 g/cm³ (Fig. 8a,b). Homogenization temperatures and equation-of-state modeling, using the approach of Allan *et al.* (2011), suggest that fluids were trapped between 280 and 310°C or greater, at a pressure of 1100 bar or more. This pressure corresponds to a minimum depth of approximately 4.0 km at lithostatic pressures (assuming a rock density of 2800 kg/m³).

TONI TIGER

A homogenous population of aqueous-carbonic fluid inclusions was observed in vein quartz from Toni Tiger (Fig. 8c). Microthermometric measures of clathrate melting and CO_2 homogenization demonstrate that this fluid contains ~16 mol % CO_2 and ~3 wt % NaCl, with a bulk density of ~0.88 g/cm³ (Fig. 8d). Fluids were trapped at 280°C or more, at a minimum pressure of 1050 bar (>3.8 km at lithostatic pressure, assuming a rock density of 2800 kg/m³). The composition and trapping conditions of fluid inclusions from Toni Tiger veins are therefore indistinguishable from those in V_3 veins at Boulevard.

U-Pb GEOCHRONOLOGY

SAMPLES AND METHODOLOGY

U-Pb dating of zircon was used to determine the crystallization age of various units in the Independence Creek area, including the metamorphic rock package, Dawson Range batholith, Coffee Creek granite, and subvolcanic rocks. The sample suite includes six samples of metaplutonic rocks, including meta-aplite cut by quartz-molybdenite veins at Toni Tiger (I034207); orthogneiss containing minor disseminated molybdenite (I034224); and quartz-feldspar-biotite schist (GM11-9b, MA11-004BV, MA11-005BV, MA11-006BV). The suite also includes three samples of the Dawson Range batholith (I034239, YGR-BV-004, 99M-106-b); three samples of the Coffee Creek phase (YGR-BV-002, 99M-105, 99M-107); and a single sample of quartz-feldspar rhyodacite porphyry (MA11-001BV).

Zircon grains recovered from plutonic and metaplutonic rocks are all relatively coarse grained (up to 200 μm long) and show a similar range of external morphology and internal structure. Zircons are typically clear, euhedral,

Figure 7. *Rock types and vein features of the Toni Tiger molybdenum occurrence: (a) weakly foliated meta-aplite from the Toni Tiger occurrence; (b) same meta-aplite as in (a), but interfoliated with biotite schist and affected by a later phase of folding; (c) biotite metagranitoid cut by a quartz-molybdenite vein with a chloritic alteration halo; (d) typical milky quartz vein with molybdenite from the Toni Tiger occurrence; (e) milky quartz vein with molybdenite along its margins (and as wall rock disseminations); and (f) pyroxene-garnet skarn with domains of biotite hornfels. moly=molybdenite.*

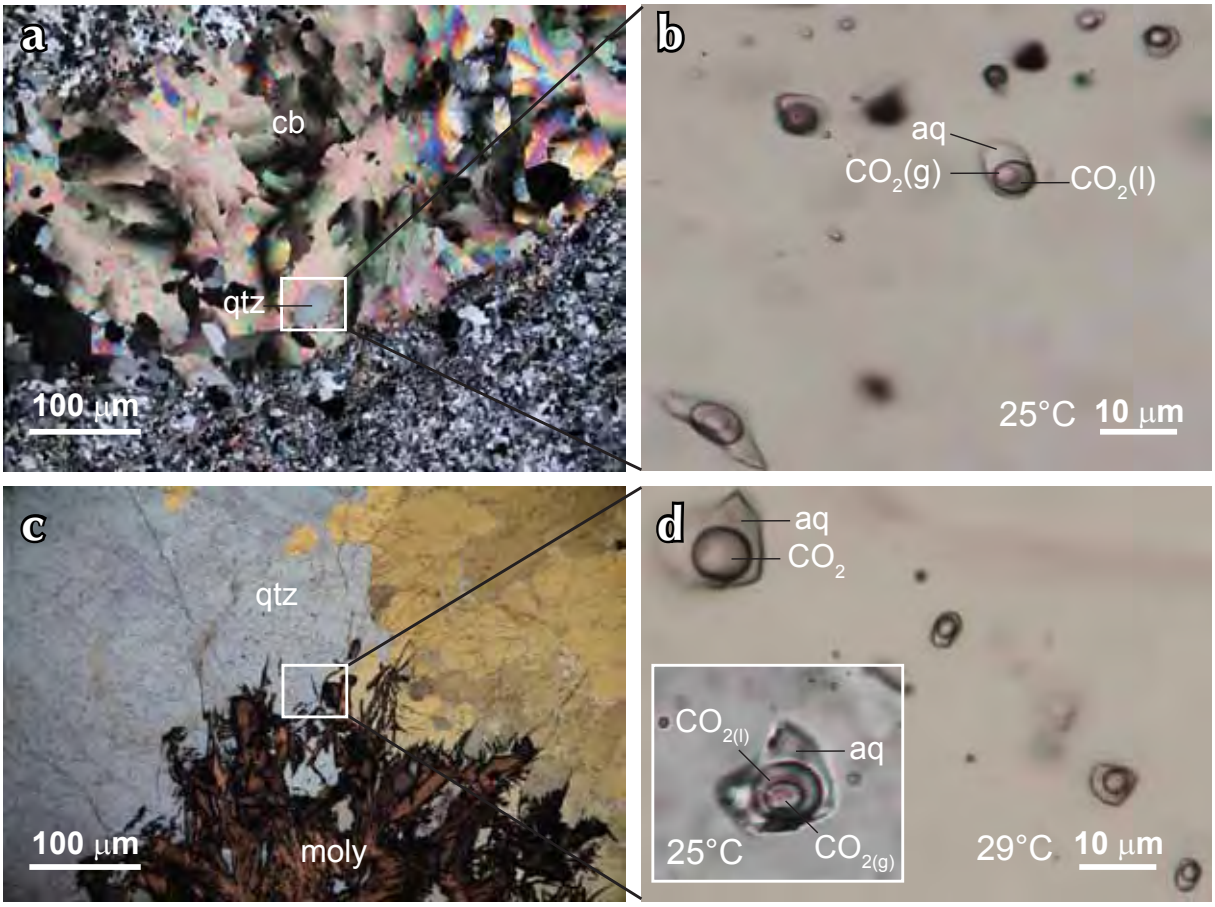

Figure 8. *(a) photomicrograph of a V_3-generation quartz-carbonate vein (cross-polarized light) from the Boulevard gold prospect; (b) quartz-hosted fluid inclusions from the vein in (a), containing aqueous liquid (aq), CO_2 liquid, and CO_2 vapour (photograph taken at 25°C); (c) photomicrograph of molybdenite in quartz from the Toni Tiger occurrence (combined cross-polarized transmitted light and reflected light); (d) photomicrograph of fluid inclusions in quartz associated with molybdenite mineralization in (c). Fluid inclusions contain aqueous liquid and a supercritical CO_2 phase (photograph taken just above the homogenization temperature of the carbonic liquid and vapour phase at 29°C). The inset shows both CO_2 phases below the homogenization temperature (~25°C), for the same large fluid inclusion in (d). cb=carbonate; g=gas phase; l=liquid phase; aq=aqueous phase (other abbreviations as in Figures 4 and 7).*

and colourless to pale yellow-brown. No obvious internal zoning was observed and morphologies range from stubby octahedral prisms to multi-faceted terminations.

The methodology for laser ablation ICP-MS analysis at the Pacific Centre for Isotopic and Geochemical Research (PCIGR), University of British Columbia, follows that described in Tafti *et al.* (2009) and Beranek and Mortensen (2011). The $^{206}Pb/^{238}U$ age is the most precisely determined age for the Phanerozoic zircons in question and is interpreted as the best estimate for the crystallization age of the samples. Assigned ages are based on a weighted average of overlapping, concordant $^{206}Pb/^{238}U$ ages of individual analyses for each sample. Errors are quoted at the 2σ level.

RESULTS

Results are presented in conventional U-Pb concordia plots and weighted average $^{206}Pb/^{238}U$ age summary plots in Figures 9-12 and are shown with sample locations in Table 1. Full analytical data are presented in Appendix 1.

All meta-igneous samples yielded Late Permian crystallization ages in the range of 250 to 267 Ma (Figs. 9 and 10). The molybdenite-bearing, weakly foliated meta-aplite sample (I034207) from Toni Tiger yields a well-constrained age of 251.3 ± 1.3 Ma (Fig. 9b), which suggests that this unit may be part of a post-D_2 intrusive suite of crustally derived intrusions that includes the Jim Creek pluton of the southern Klondike District (Beranek and

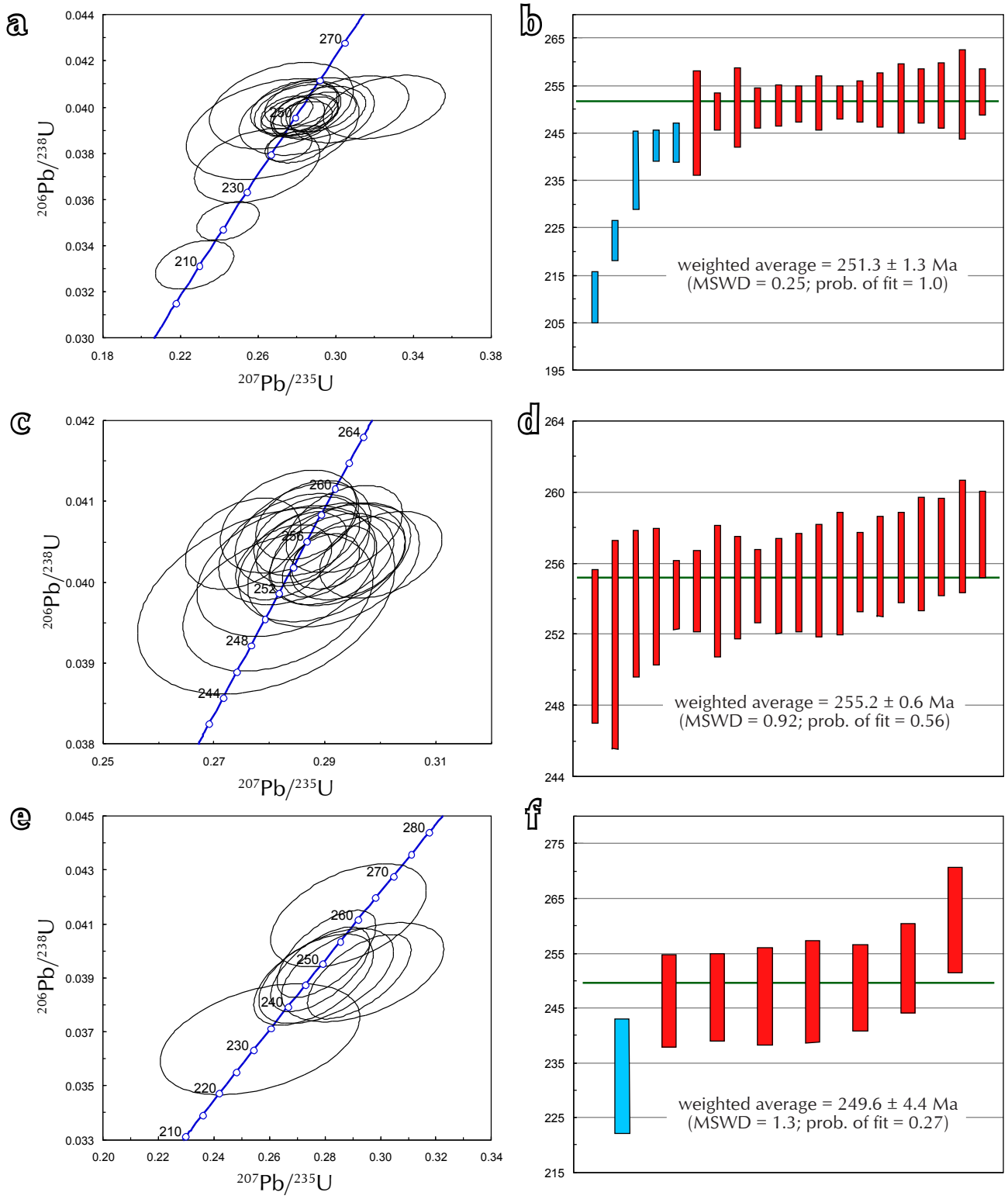

Figure 9. *Conventional concordia diagrams and plots of weighted average $^{206}Pb/^{238}U$ ages for meta-igneous samples from the study area: (a) and (b) sample I034207 – molybdenite-bearing meta-aplite from Toni Tiger; (c) and (d) sample I034224 - orthogneiss with disseminated molybdenite; (e) and (f) sample GM11-9b – quartz-feldspar-biotite schist. Error ellipses on concordia diagrams and error bars on weighted average age plots are shown at 2s level. Red bars on weighted average age plots were used in the age calculation; blue bars were rejected.*

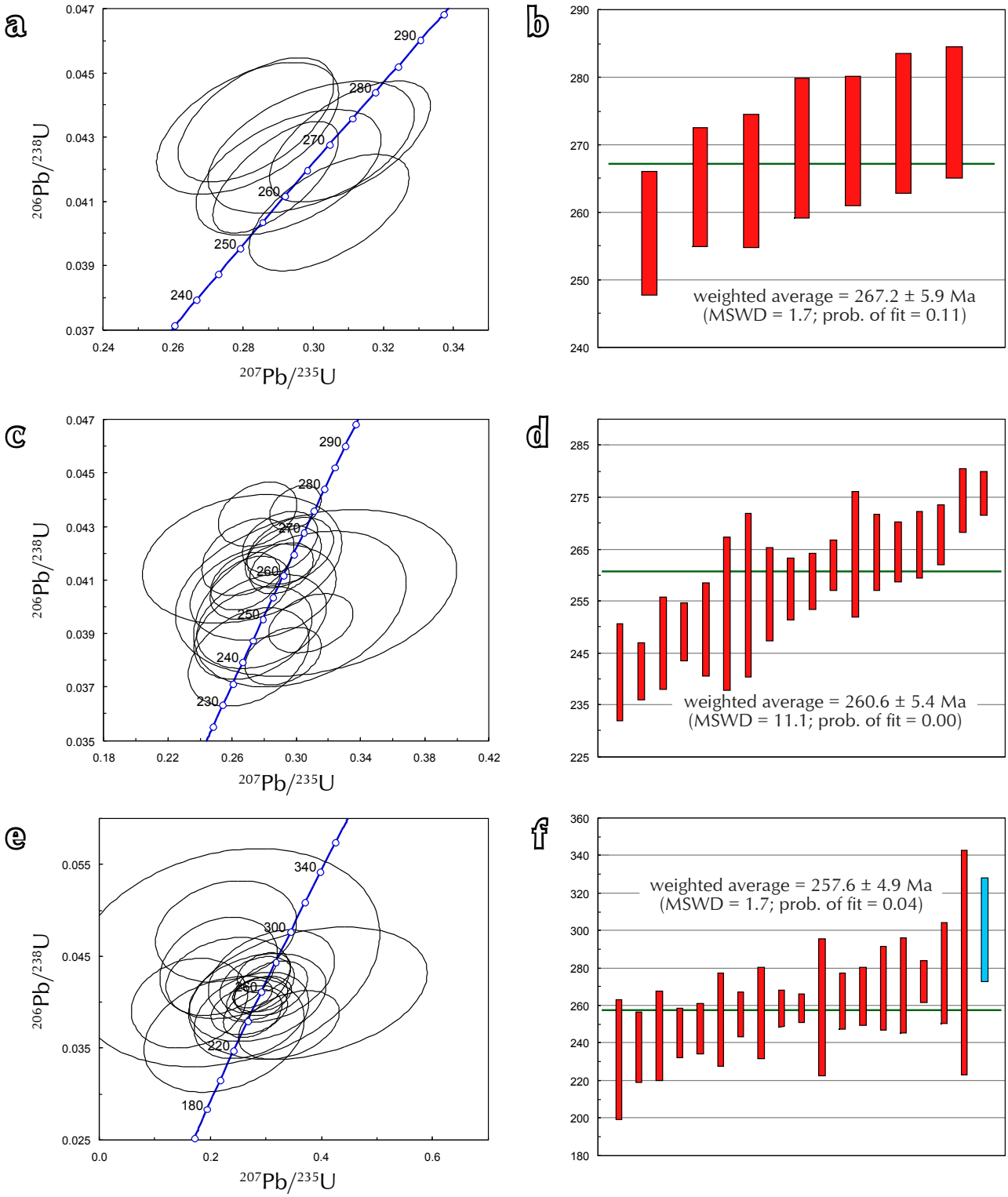

Figure 10. *Conventional concordia diagrams and plots of weighted average $^{206}Pb/^{238}U$ ages for meta-igneous samples from the study area: (a) and (b) sample MA11-004BV - quartz-feldspar-biotite schist; (c) and (d) sample MA11-00BV – quartz-feldspar-biotite schist; (e) and (f) sample MA11-006BV - quartz-feldspar-biotite schist. Symbols as in Figure 9.*

Mortensen, 2011) and the Teacher intrusion in the White Gold area (Mortensen, unpublished data). A sample of quartz-feldspar-biotite schist (GM11-9b) yields a similar age of 249.6±4.4 Ma (Fig. 9f); however, only a small amount of zircon was recovered from this sample and the age is therefore relatively imprecise (based on only seven analyses). All of the other well-foliated meta-igneous rock units yield Late Permian ages ranging from 255 to 267 Ma, which are consistent with ages reported elsewhere for metavolcanic and metaplutonic phases of the Klondike arc assemblage (Mortensen, 1990; Ruks *et al.*, 2006; Beranek and Mortensen, 2011).

Two samples of granodiorite from the Dawson Range batholith give ages of 102.0±0.4 Ma and 100.2±0.3 Ma (Fig. 11b,d). An aplite dyke that cuts Dawson Range granodiorite gives an age of 102.5±0.9 Ma (Fig. 11f). Three biotite granite samples of the Coffee Creek granite give ages ranging from 99 to 100 Ma (Fig. 12b,d,f). The ages are therefore consistent with the Coffee Creek granite being a slightly younger magmatic phase of the Whitehorse plutonic suite than the Dawson Range batholith.

The sample of quartz-feldspar rhyodacite porphyry from subcrop in the study area (sample MA11-001BV) gives an age of 57.2±1.0 Ma (latest Paleocene), which is similar to ages obtained for felsic dykes and plugs throughout the Dawson Range and areas to the north (Mortensen, unpublished data).

$^{40}Ar/^{39}Ar$ GEOCHRONOLOGY

SAMPLE AND METHODOLOGY

$^{40}Ar/^{39}Ar$ geochronology was used to determine the age of a sample of hydrothermal sericite from a quartz-carbonate-stibnite-gold vein with a strong sericite selvage (sample BV23_70.37m from diamond drill core). The hydrothermal sericite is interpreted to have formed at the same time as gold and stibnite mineralization.

Sericite grains were hand-picked from the sample under a binocular microscope, wrapped in aluminum foil, and stacked in an irradiation capsule with similar-aged samples and neutron flux monitors (Fish Canyon Tuff sanidine (FCS); 28.03 Ma (Renne *et al.*, 1998). The methodology used in this study for $^{40}Ar/^{39}Ar$ dating at PCIGR is similar to that described by Mortensen *et al.* (2010). The Boulevard sericite sample was irradiated from May 4 to 5, 2011 at the McMaster Nuclear Reactor in Hamilton, Ontario, for 45 MWH, with a neutron flux of approximately 6×10^{13} neutrons/cm^2/s. Analyses (n=45) of 15 neutron flux monitor positions produced errors of <0.5% in the J value. The sample was split into two separate aliquots after irradiation, and the samples were analysed from June through October 2011 at the Noble Gas Laboratory in the PCIGR.

RESULTS

The first aliquot of hydrothermal sericite yielded a plateau age of 95.9±0.9 Ma (MSWD=0.97, probability=0.41; plateau based on 74.3% of the ^{39}Ar; Fig. 13; Table 2). The duplicate analysis did not settle to enough steps to yield a plateau age, but the results are consistent with the age obtained from the first aliquot.

$^{187}Re/^{187}Os$ GEOCHRONOLOGY

SAMPLES AND METHODOLOGY

$^{187}Re/^{187}Os$ dating methods were utilized to constrain the age of molybdenite mineralization at the Toni Tiger showing. Two samples of molybdenite were dated: (a) a quartz-molybdenite vein crosscutting a meta-aplite (I034208); and (b) a quartz-molybdenite vein crosscutting garnet-actinolite-diopside skarn (I034229). Molybdenite in each sample occurs as coarse-grained rosettes mantled by vein quartz.

Samples were prepared and analysed by R. Creaser at the Radiogenic Isotope Laboratory at the University of Alberta according to the methods described by Selby and Creaser (2004) and Markey *et al.* (2007).

RESULTS

Analytical results for the two samples are given in Table 3. Sample I034208 yielded a Re-Os age of 95.0±0.4 Ma. Sample I034229 contains high common Os, hence the derived age is sensitive to assumed initial $^{187}Os/^{188}Os$ ratio. Assuming an initial $^{187}Os/^{188}Os$ value of 0.3, a somewhat younger age of 92.4±0.7 Ma is determined for this sample.

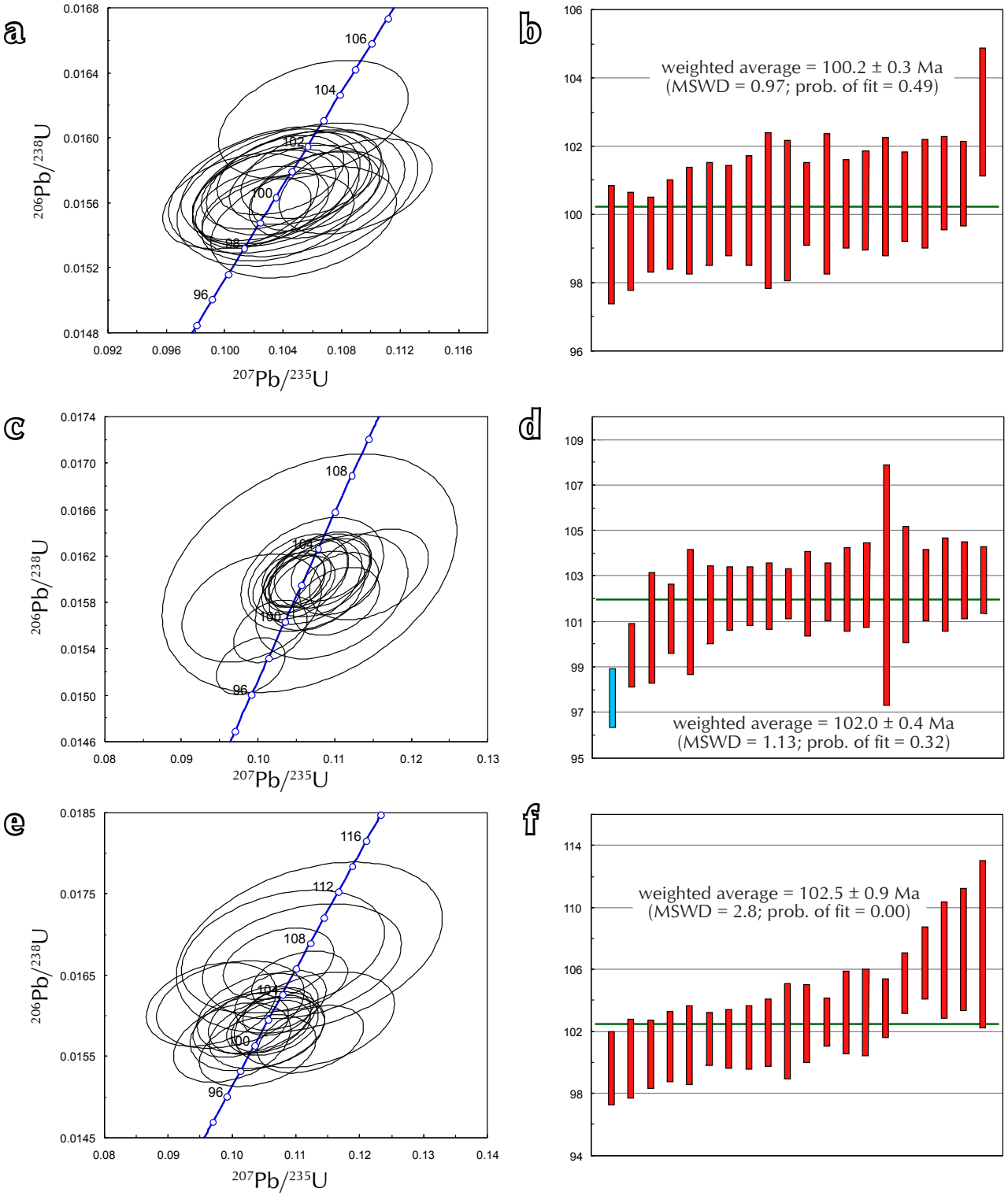

Figure 11. *Conventional concordia diagrams and plots of weighted average $^{206}Pb/^{238}U$ ages for samples of the Dawson Range batholith in the study area: (a) and (b) sample I034239 - biotite-hornblende granodiorite; (c) and (d) sample YGP-BV-004 - biotite-hornblende granodiorite; (e) and (f) sample 99M-106-b – aplite dyke cutting granodiorite. Symbols as in Figure 9.*

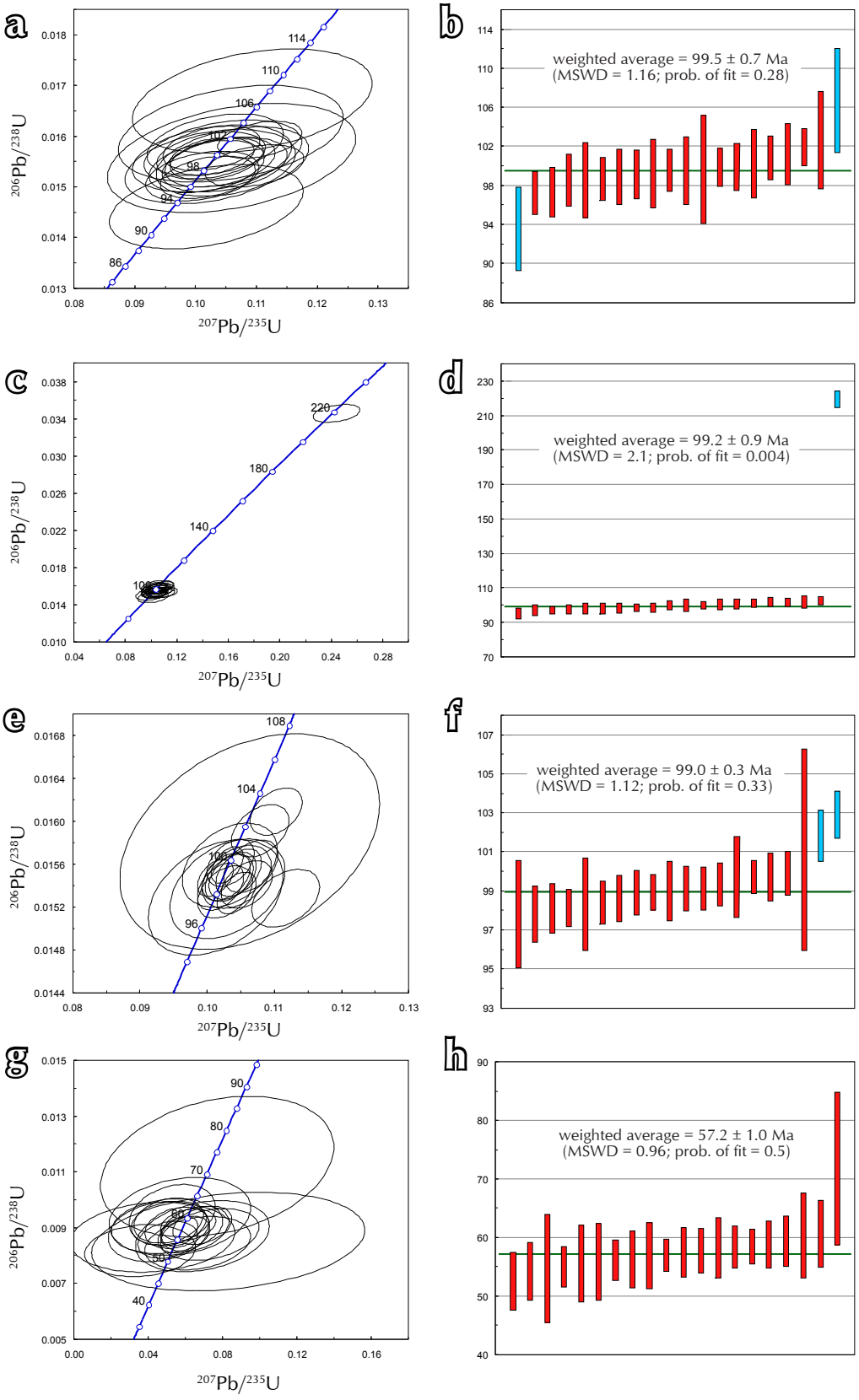

Figure 12. *Conventional concordia diagrams and plots of weighted average $^{206}Pb/^{238}U$ ages for samples of the Coffee Creek intrusions and a young subvolcanic rock in the study area: (a) and (b) sample YGR-BV-002 – biotite granite; (c) and (d) sample 99M-105 – biotite granite; (e) and (f) sample 99M-107 – biotite granite; (g) and (h) sample MA11-001BV - quartz-feldspar rhyodacite porphyry. Symbols as in Figure 9.*

Table 1. *$^{206}Pb/^{238}U$ zircon ages for Independence Creek samples.*

Sample	Rock Description	Unit	Location (NAD83 UTM zone 7N)		Age (Ma)	±2σ
			Easting	Northing		
METAMORPHIC ROCKS						
I034207	meta-aplite*	Klondike assemblage	577980	6966729	251.3	1.3
I034224	felsic orthogneiss*	Klondike assemblage	578139	6966731	255.2	0.6
GM11-9b	quartz-feldspar-biotite schist	Klondike assemblage	572444	6980691	249.6	4.4
MA11-004BV	quartz-feldspar-biotite schist	Klondike assemblage	563229	6972572	267.2	5.9
MA11-005BV	quartz-feldspar-biotite schist	Klondike assemblage	561996	6976060	260.6	5.4
MA11-006BV	quartz-feldspar-biotite schist	Klondike assemblage	561398	6975930	257.6	4.9
PLUTONIC ROCKS						
I034239	biotite-hornblende granodiorite	Dawson Range batholith	574610	6963807	100.2	0.3
YGR-BV-004	biotite-hornblende granodiorite	Dawson Range batholith	566127	6967606	102.0	0.4
99M-106-b	aplite cutting granodiorite	Dawson Range batholith	566278	6961313	102.5	0.9
YGR-BV-002	biotite granite*	Coffee Creek granite	573497	6968539	99.5	0.7
99M-105	biotite granite	Coffee Creek granite	577775	6968097	99.2	0.9
99M-107	biotite granite	Coffee Creek granite	560386	6973241	99.0	0.3
SUBVOLCANIC ROCKS						
MA11-001BV	quartz-feldspar rhyodacite porphyry	Skukum volcanic suite	574845	6964377	57.2	1.0

*molybdenite observed in heavy mineral separates

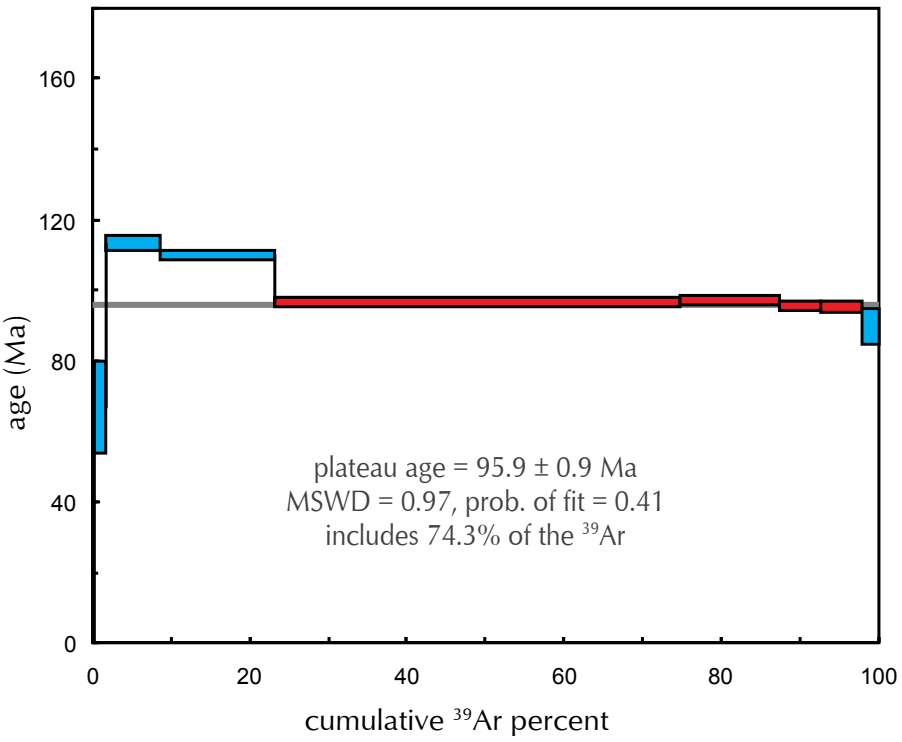

Figure 13. *Age spectra for step-heating of sericite sample BV23-70.37m from the Boulevard property. Error boxes and the calculated age are given at the 2σ level. Steps shown in red define the calculated plateau age; steps in blue were rejected.*

Table 2. *$^{40}Ar/^{39}Ar$ data for Boulevard sericite (Sample BV23_70.37m)*

	Isotope Ratios											
Laser power (%)	**$^{40}Ar/^{39}Ar$**	**1σ**	**$^{37}Ar/^{39}Ar$**	**1σ**	**$^{36}Ar/^{39}Ar$**	**1σ**	**Ca/K**	**%^{40}Ar atm**	**f ^{39}Ar**	**$^{40}Ar^*/^{39}ArK$**	**Age**	**2σ**
2.20 W	22.38	0.40	0.62	0.09	0.067	0.006	1.13	88.77	0.34	2.515	27.44	±39.95
2.60 W	24.21	0.22	0.07	0.03	0.061	0.002	0.12	74.58	1.54	6.154	66.43	±12.64
3.00 W	13.67	0.09	0.47	0.02	0.010	0.000	0.87	22.50	6.68	10.596	112.92	±2.08
3.50 W	10.72	0.07	0.28	0.01	0.002	0.000	0.52	4.35	14.70	10.259	109.44	±1.43
4.00 W	9.20	0.06	0.01	0.00	0.001	0.000	0.02	2.27	51.34	8.987	96.21	±1.17
4.40 W	9.26	0.06	0.01	0.00	0.001	0.000	0.02	2.69	12.50	9.014	96.50	±1.23
5.00 W	9.70	0.06	0.02	0.01	0.003	0.000	0.04	8.38	5.12	8.891	95.22	±1.59
6.00 W	10.11	0.06	0.06	0.01	0.004	0.000	0.10	12.15	5.39	8.883	95.13	±1.61
7.00 W	13.01	0.14	0.02	0.02	0.016	0.001	0.03	35.99	2.39	8.330	89.36	±5.12
J = 0.0060810±0.0000304				Volume ^{39}ArK=0.378			Integrated Date = 99.34±0.58 Ma					
Plateau age=95.93±0.89 Ma (2σ, including J-error of 0.6%)				MSWD=0.97, probability=0.41			Includes 74.3% of the ^{39}Ar (steps 5 through 8)					
Inverse isochron (correlation age) results, plateau steps: Model 1 Solution (±95%-conf.) on 9 points							Age=98.4±7.6 Ma					
Initial $^{40}Ar/^{36}Ar$ =350±170				MSWD=75, probability=0								

Table 3. *Re-Os data for Toni Tiger molybdenite samples.*

Sample	Re (ppm)	±2σ	^{187}Re (ppb)	±2σ	^{187}Os (ppb)	±2σ	Total common Os (pg)	Model Age (Ma)	±2σ
I034208	42.96	0.11	27002	71	42.76	0.04	1.6	95.0	0.4
I034208 (duplicate)	43.00	0.11	27029	70	42.76	0.04	1.6	94.9	0.4
I034228	27.62	0.08	17361	53	26.74	0.16	90.8	92.4	0.7

DISCUSSION

U-Pb GEOCHRONOLOGY

The 250 to 267 Ma age range of meta-igneous rocks in the Independence Creek area overlaps with that of the Late Permian Klondike volcanic arc assemblage and intrusive equivalents (Sulphur Creek orthogneiss) elsewhere in western Yukon (Mortensen, 1990; Ruks *et al.*, 2006; Beranek and Mortensen, 2011). We therefore concur with recent mapping by the Geological Survey of Canada which demonstrates that exposures of Klondike arc rocks in the Ladue River area (NTS 115N) continue eastward along the northern margin of the Dawson Range batholith into the Stevenson Ridge map sheet (NTS 115J) (Ryan *et al.*, in prep.).

The mid-Cretaceous crystallization ages determined for the Dawson Range batholith (*ca.* 100 to 103 Ma) are consistent with current geochronological compilations (Breitspreicher and Mortensen, 2004). The slightly younger 99 to 100 Ma zircon ages for the Coffee Creek granite are consistent with the interpretation of Templeman-Kluit and Wanless (1975) that this unit is a slightly younger intrusive phase of the Whitehorse plutonic suite.

Subvolcanic rocks cutting the Dawson Range batholith were determined to be 57.2±1.0 Ma, and are therefore age-equivalent to the previously mapped Paleocene Skukum volcanic rocks 4 km to the south (Templeman-Kluit, 1974), and volcanic and subvolcanic rocks elsewhere in western Yukon (Breitsprecher and Mortensen, 2004).

TIMING OF MINERALIZATION

The 95.0 ± 0.4 Ma $^{187}Re/^{187}Os$ model age for molybdenite at Toni Tiger overlaps within 2σ error with the 95.9 ± 0.9 Ma $^{40}Ar/^{39}Ar$ cooling age for hydrothermal sericite at Boulevard. While the latter age could be interpreted as a minimum, there is sufficient geological evidence (*e.g.*, common structural style and fluid inclusion properties) that Boulevard and Toni Tiger are related hydrothermal systems. Therefore, we interpret the $^{187}Re/^{187}Os$ and $^{40}Ar/^{39}Ar$ methods as recording coeval mineralizing events at *ca.* 96-95 Ma. Importantly, the mineralization age post-dates crystallization of the Dawson Range batholith and Coffee Creek granite by 3-4 m.y. No younger phase of the Whitehorse plutonic suite has yet been recognized in the Independence Creek area (or anywhere else in western Yukon), nor do the field relationships suggest a magmatic role in mineralization. It is likely that heat and fluid flux related to the emplacement of the Dawson Range batholith and Coffee Creek plutonic suites were responsible for hornfelsing and skarnification in the vicinity of the Toni Tiger showing. However, the geochronologic results of this study suggest that Au-As-Sb-(Pb-Zn-Cu) and Mo mineralization record a distinct and younger event.

The low-salinity, aqueous-carbonic composition of fluids attending mineralization is consistent with orogenic fluids documented worldwide (Groves *et al.*, 2003). The association between gold and pyritic alteration halos to quartz-carbonate veins suggests that wall rock sulphidation is an important gold-precipitating mechanism. Depressurization associated with faulting and brecciation may also play an important role in destabilizing gold-bisulphide complexes (*e.g.*, Wilkinson and Johnston, 1996).

Molybdenite is not commonly reported in orogenic systems; however, the geochronological and fluid inclusion evidence suggests that Toni Tiger is part of the same post-magmatic orogenic system as Boulevard. The association of molybdenite with moderate temperature, moderate pressure, dilute aqueous-carbonic fluids implies that molybdenite transport occurs in nature at *P-T-X* conditions quite dissimilar to those encountered in high-temperature, low-pressure systems such as porphyry Mo deposits. We speculate that molybdenite may have been remobilized from the felsic metaplutonic host rocks, which locally contain significant background concentrations of molybdenite.

REGIONAL SIGNIFICANCE

This study contributes to the metallogenic framework of the Dawson Range, and may be relevant to other structurally-hosted gold prospects, such as the Coffee gold deposit northeast of the Independence Creek drainage (Kaminak Gold Corp.), and gold in the Moosehorn Range (parts of NTS 115N and 115K; Fig. 1). Mineralization in the Coffee area occurs within a series of structural corridors that cut all rock units, including the mid-Cretaceous Coffee Creek granite (Wainwright *et al.*, 2011). A common, *ca.* 96-95 Ma metallogenesis for gold mineralization at Boulevard and Coffee is permissible given field relationships, although Coffee is dominated by brittle (shallow?) features, whereas vein swarms at Boulevard more likely represent deeper crustal levels. In the case of the Moosehorn Range, mineralization has been dated by $^{40}Ar/^{39}Ar$ methods to 93-92 Ma, which post-dates the main phase of the magmatism by ~8 m.y. (Joyce, 2002). Fluid inclusions associated with the Moosehorn veins also overlap strongly in composition and trapping conditions with those at Boulevard. On the basis of currently available geochronological data and geological relationships, we propose a general model in which exhumation of the Dawson Range shortly after cessation of arc magmatism in mid-Cretaceous time was accompanied by brittle deformation, fluid flow, and mineralization. However, the tectonic and structural setting of the Dawson Range at this time is still not completely understood.

ACKNOWLEDGEMENTS

This study is part of GGM's MSc project, which was a component of the Yukon Gold Project, a collaborative research venture between the Mineral Deposit Research Unit (UBC) and a consortium of industry participants, including Aldrin Resource Corp., Barrick Gold Corp., Full Metal Minerals Corp., Gold Fields Canada Exploration, Northern Freegold Resources Ltd., Kinross Gold Corp., Radius Gold Inc., Silver Quest Resources Ltd., Taku Gold Corp., Teck Resources Ltd., and Underworld Resources Inc. The Natural Science and Engineering Research Council of Canada (NSERC) also provided matching funds for the industry contribution. We are grateful for the logistical, financial, scientific, and editorial contributions of Silver Quest Resources (now Independence Gold Corp.) and Equity Exploration Ltd., and in particular Kendra Johnston, Darcy Baker, Dave Pawliuk, Randy Turner, and Ryan Congdon. Jim Ryan of the Geological Survey of Canada is thanked for his thoughtful review and his contributions to the geological understanding of the Dawson Range.

REFERENCES

Allan, M.M., Morrison, G.W., and Yardley, B.W.D., 2011. Physicochemical evolution of a porphyry-breccia system: a laser ablation ICP-MS study of fluid inclusions in the Mount Leyshon Au deposit, Queensland, Australia. Economic Geology, vol. 106, no. 3, p. 413-436.

Beranek, L.P. and Mortensen, J.K., 2011. The timing and provenance record of the Late Permian Klondike orogeny in northwestern Canada and arc-continent collision along western North America. Tectonics, vol. 30, no. 5, p. TC5017.

Berman, R.G., Ryan, J.J., Gordey, S.P., and Villeneuve, M., 2007. Permian to Cretaceous polymetamorphic evolution of the Stewart River region, Yukon-Tanana Terrane, Yukon, Canada; P-T evolution linked with in situ SHRIMP monazite geochronology. Journal of Metamorphic Geology, vol. 25, p. 803-827.

Breitsprecher, K. and Mortensen, J.K. (comps.), 2004. YukonAge 2004: A database of isotopic age determinations for rock units from Yukon Territory. Yukon Geological Survey, CD-ROM.

Craig, D.B., 1970. Toni Tiger report: Soil and rock sampling, bulldozer trenching. Yukon mining assessment report number 060249.

Chartier, D., Couture, J.-F., Sim., R., and Starkey, J., 2013. Mineral resource evaluation, Coffee gold project, Yukon, Canada: Vancouver, Kaminak Gold Corp., 203 p. <http://kaminak.com/projects/sections_and_maps/reports/technical_report/> [accessed February 10, 2013]

Gordey, S.P. and Makepeace, A.J. (comps.), 2003. Yukon Digital Geology. Geological Survey of Canada, Open File 1749 and Yukon Geological Survey, Open File 2003-9(D).

Gordey, S.P. and Ryan, J.J., 2005. Geology, Stewart River area (115N, 115O and part of 115J), Yukon Territory. Geological Survey of Canada, Open File 4970, scale 1:250 000.

Groves, D.I., Goldfarb, R.J., Robert, F., and Hart, C.J.R., 2003. Gold deposits in metamorphic belts: Overview of current understanding, outstanding problems, future research, and exploration significance. Economic Geology, vol. 98, p. 1-29.

Jilson, G., 2000. Geochemical and geological report on the Dan, Man and Indy claims. Yukon mining assessment report number 094174.

Joyce, N.L., 2002. Geologic setting, nature, and structural evolution of intrusion-hosted Au-bearing quartz veins at the Longline occurrence, Moosehorn Range Area, west-central Yukon Territory. Unpublished MSc Thesis, University of British Columbia, Vancouver, 201 p.

MacKenzie, D., Craw, D., and Mortensen, J.K., 2008a. Structural controls on orogenic gold mineralisation in the Klondike goldfield, Canada. Mineralium Deposita, vol. 43, p. 435-448.

MacKenzie, D., Craw, D., and Mortensen J.K., 2008b. Thrust slices and associated deformation in the Klondike goldfields, Yukon. *In:* Yukon Exploration and Geology 2007, D.S. Emond, L.R. Blackburn, R.P. Hill and L.H. Weston (eds.), Yukon Geological Survey, p. 199-213.

MacKenzie, D. and Craw, D., 2012. Contrasting structural settings of mafic and ultramafic rocks in the Yukon-Tanana terrane. *In:* Yukon Exploration and Geology 2011, K.E. MacFarlane and P.J. Sack (eds.), Yukon Geological Survey, p. 115-127.

Markey, R., Stein, H.J., Hannah, J.L., Zimmerman, A., Selby, D. and Creaser, R.A., 2007. Standardizing Re–Os geochronology: A new molybdenite Reference Material (Henderson, USA) and the stoichiometry of Os salts. Chemical Geology, vol. 244, p. 74-87.

Mortensen, J.K., 1990. Geology and U - Pb geochronology of the Klondike District, west - central Yukon Territory. Canadian Journal of Earth Sciences, vol. 27, p. 903–914.

Mortensen, J.K., Craw, D., MacKenzie, D.J., Gabites, J.E., and Ullrich, T., 2010. Age and origin of orogenic gold mineralization in the Otago Schist Belt, South Island, New Zealand: Constraints from lead isotope and $^{40}Ar/^{39}Ar$ dating studies. Economic Geology, vol. 105, p. 777-793.

Renne, P.R., Swisher, C.C., Deino, A.L., Karner, D.B., Owens, T.L., and DePaolo, D.J., 1998. Intercalibration of standards, absolute ages and uncertainties in $^{40}Ar/^{39}Ar$ dating. Chemical Geology, vol. 145, p. 117-152.

Ruks, T.W., Piercey, S.J., Ryan, J.J., Villeneuve, M.E., and Creaser, R.A., 2006. Mid- to late Paleozoic K-feldspar augen granitoids of the Yukon-Tanana terrane, Yukon, Canada: Implications for crustal growth and tectonic evolution of the northern Cordillera. Geological Society of America Bulletin, vol. 118, p. 1212-1231.

Selby, D. and Creaser, R.A., 2004. Macroscale NTIMS and microscale LA-MC-ICP-MS Re-Os isotopic analysis of molybdenite: Testing spatial restrictions for reliable Re-Os age determinations, and implications for the decoupling of Re and Os within molybdenite. Geochimica et Cosmochimica Acta, vol. 68, p. 3897-3908.

Tafti, R., Mortensen, J.K., Lang, J.R., Rebagliati, M., and Oliver, J.L., 2009. Jurassic U-Pb and Re-Os ages for the newly discovered Xietongmen Cu-Au porphyry district, Tibet, PRC: Implications for metallogenic epochs in the southern Gangdese belt. Economic Geology, vol. 104, p. 127-136.

Templeman-Kluit, D.J., 1974. Reconnaissance geology of Aishihik Lake, Snag and part of the Stewart River map areas, west-central Yukon Territory. Geological Survey of Canada, Paper 73-14, 93 p.

Tempelman-Kluit, D. and Wanless, R., 1975. Potassium-argon age determinations of metamorphic and plutonic rocks in the Yukon Crystalline Terrane. Canadian Journal of Earth Sciences, vol. 12, p. 1895-1909.

Wainwright, A.J., Simmons, A.T., Finnigan, C.S., Smith, T.R., and Carpenter, R.L., 2011. Geology of new gold discoveries in the Coffee Creek area, White Gold District, west-central Yukon. *In:* Yukon Exploration and Geology 2010, K.E. MacFarlane, L.H. Weston, and C. Relf (eds.), Yukon Geological Survey, p. 233-247.

Wilkinson, J.J. and Johnston, J.D., 1996. Pressure fluctuations, phase separation, and gold precipitation during seismic fracture propagation. Geology, vol. 24, p. 395-398.

Yukon MINFILE, 2010. Yukon MINFILE - A database of mineral occurrences. Yukon Geological Survey, <www.geology.gov.yk.ca/databases_gis.html> [accessed October 17, 2012].

Zagorevski, A., Ryan, J., Roots, C., and Hayward, N., 2012. Ultramafic rock occurrences in the Dawson Range and their implications for the crustal structure of Yukon-Tanana terrane, Yukon (parts of 115I, J and K), Geological Survey of Canada, Open File 7105, 1 sheet. doi:10.4095/290992.

APPENDIX 1: LA-ICP-MS data for U-Pb analysis of zircons

Fraction	Isotopic Ratios							Isotopic Ages						Background corrected mean counts per second at specified mass							
	$^{207}Pb/^{235}U$	% 1σ	$^{206}Pb/^{238}U$	% 1σ	rho	$^{207}Pb/^{206}Pb$	% 1σ	$^{207}Pb/^{235}U$	± 1σ	$^{206}Pb/^{238}U$	± 1σ	$^{207}Pb/^{206}Pb$	± 1σ	202	204	206	207	208	232	235	238
METAMORPHIC ROCKS																					
Meta-aplite; Toni Tiger (sample I034207)																					
1	0.22732	0.00829	0.03317	0.00043	0.36	0.05211	0.00181	208.0	6.9	210.3	2.7	290.2	77.5	0	13	11263	578	1826	84416	2267	475507
2	0.27569	0.00495	0.03830	0.00026	0.38	0.05298	0.00088	247.2	3.9	242.3	1.6	328.0	37.2	0	0	17138	894	3789	177690	2897	627073
3	0.24444	0.00658	0.03507	0.00034	0.36	0.05150	0.00131	222.0	5.4	222.2	2.1	263.4	57.2	48	0	13996	710	2508	114253	2597	559752
4	0.26753	0.01819	0.03905	0.00089	0.34	0.04842	0.00309	240.7	14.6	247.0	5.5	119.8	143.8	0	0	6711	320	1387	53669	1071	241284
5	0.28094	0.00659	0.03840	0.00033	0.37	0.05353	0.00117	251.4	5.2	242.9	2.1	351.3	48.8	46	19	26356	1391	5864	252194	4437	964482
6	0.28268	0.00636	0.03946	0.00032	0.36	0.05278	0.00110	252.8	5.0	249.5	2.0	319.2	46.5	0	11	16978	884	3336	164531	2808	605635
7	0.28513	0.01423	0.03959	0.00068	0.34	0.05182	0.00242	254.7	11.2	250.3	4.2	277.4	103.3	0	8	4223	216	618	29339	681	150316
8	0.25948	0.01319	0.03747	0.00066	0.35	0.05146	0.00247	234.2	10.6	237.1	4.1	261.5	106.4	0	0	5380	273	914	39886	948	202481
9	0.32504	0.01282	0.04000	0.00056	0.35	0.05560	0.00202	285.8	9.8	252.9	3.5	436.3	79.1	42	6	7064	388	1272	55999	1075	249223
10	0.27494	0.00542	0.03976	0.00029	0.37	0.05091	0.00092	246.6	4.3	251.4	1.8	236.8	41.1	13	0	43533	2190	9528	390740	7184	1546326
11	0.30709	0.01248	0.03991	0.00059	0.36	0.05736	0.00217	271.9	9.7	252.3	3.6	504.9	81.4	15	3	9286	526	1797	73673	1550	329174
12	0.28647	0.00600	0.03972	0.00030	0.36	0.05360	0.00102	255.8	4.7	251.1	1.9	354.0	42.7	3	0	16588	879	3450	164002	2778	591470
13	0.27896	0.00931	0.04000	0.00047	0.35	0.05084	0.00157	249.8	7.4	252.8	2.9	233.6	69.8	31	0	25811	1299	5207	239225	4217	914551
14	0.28211	0.00765	0.04013	0.00039	0.36	0.05188	0.00129	252.3	6.1	253.6	2.4	280.1	56.1	29	0	13773	707	2855	136341	2274	486898
15	0.29159	0.00975	0.03976	0.00047	0.35	0.05268	0.00163	259.8	7.7	251.3	2.9	314.8	68.7	0	6	13969	729	2550	117120	2269	498826
16	0.28043	0.00911	0.03985	0.00046	0.36	0.05221	0.00157	251.0	7.2	251.9	2.8	294.4	66.9	67	12	21147	1094	3089	142233	3550	754747
17	0.29249	0.00732	0.03980	0.00035	0.35	0.05165	0.00117	260.5	5.8	251.6	2.2	269.9	51.2	32	0	22110	1132	5287	241868	3526	790708
18	0.27207	0.01515	0.04006	0.00076	0.34	0.04904	0.00255	244.3	12.1	253.2	4.7	149.6	117.5	0	0	9587	466	1464	62744	1562	341000
19	0.28395	0.00717	0.03967	0.00036	0.36	0.05222	0.00119	253.8	5.7	250.8	2.2	295.1	51.3	0	13	14925	773	2626	124397	2486	536485
20	0.27796	0.00674	0.03959	0.00034	0.35	0.05184	0.00113	249.0	5.4	250.3	2.1	278.5	49.1	17	0	25914	1333	5760	262716	4384	934137
Orthogneiss with disseminated molybdenite (sample I034224)																					
1	0.27938	0.00948	0.03977	0.00047	0.35	0.05117	0.00162	250.2	7.5	251.4	2.9	248.7	71.3	0	17	1927	105	270	10809	396	59986
2	0.28927	0.00285	0.04021	0.00016	0.40	0.05245	0.00048	258.0	2.3	254.2	1.0	305.0	20.8	79	19	20294	1036	1451	49729	3185	488565
3	0.29348	0.00429	0.04066	0.00022	0.37	0.05340	0.00073	261.3	3.4	256.9	1.4	345.6	30.4	16	15	58321	3051	5208	157670	9064	1388549
4	0.29281	0.00518	0.04035	0.00026	0.36	0.05127	0.00084	260.8	4.1	255.0	1.6	253.1	37.3	21	0	31217	1662	2645	81968	4869	734983
5	0.30010	0.00450	0.04034	0.00022	0.36	0.05264	0.00073	266.5	3.5	254.9	1.4	313.3	31.3	24	18	28110	1437	1810	58298	4221	666974
6	0.28341	0.00501	0.04075	0.00026	0.36	0.05049	0.00083	253.4	4.0	257.5	1.6	217.6	37.7	0	32	43875	2370	1536	36805	5034	777004
7	0.28258	0.00353	0.04025	0.00019	0.38	0.05061	0.00059	252.7	2.8	254.4	1.2	223.1	26.7	11	14	28187	1419	2073	68133	4308	662094
8	0.29118	0.00458	0.04029	0.00023	0.36	0.05271	0.00077	259.5	3.6	254.6	1.4	316.2	32.9	76	0	23488	1185	1587	49293	3610	558547
9	0.28938	0.00614	0.04025	0.00030	0.35	0.05150	0.00102	258.1	4.8	254.4	1.9	263.4	44.8	0	6	26627	1399	2116	66524	4137	632458
10	0.28675	0.00391	0.04057	0.00020	0.36	0.05140	0.00065	256.0	3.1	256.3	1.3	258.6	29.0	28	0	10377	532	740	25012	1585	246735
11	0.28576	0.00333	0.04043	0.00018	0.38	0.05193	0.00056	255.2	2.6	255.5	1.1	282.1	24.7	0	13	52149	2800	1735	40924	6054	929877
12	0.27521	0.00424	0.04048	0.00023	0.37	0.05056	0.00073	246.9	3.4	255.8	1.4	220.9	32.9	12	15	40033	2071	3886	124505	6249	947227
13	0.28684	0.00379	0.04077	0.00020	0.37	0.05012	0.00061	256.1	3.0	257.6	1.2	200.8	28.2	29	5	45555	2295	3490	112200	7192	1076595
14	0.28447	0.00556	0.04041	0.00028	0.35	0.05062	0.00092	254.2	4.4	255.4	1.7	223.6	41.6	43	2	29842	1490	1928	65001	4482	700193
15	0.28312	0.00664	0.04014	0.00033	0.35	0.05081	0.00111	253.1	5.3	253.7	2.1	232.0	49.7	17	15	25043	1262	2582	78531	3831	592793
16	0.29153	0.00305	0.04031	0.00016	0.38	0.05340	0.00052	259.8	2.4	254.7	1.0	345.9	21.8	0	40	73133	3808	2400	57873	8370	1291864
17	0.28605	0.00500	0.04059	0.00026	0.37	0.05225	0.00085	255.4	4.0	256.5	1.6	296.4	36.8	13	0	44902	2388	4934	145861	7075	1065334
18	0.29158	0.00633	0.04021	0.00031	0.36	0.05217	0.00105	259.8	5.0	254.1	1.9	292.7	45.5	29	0	17089	889	1773	54829	2685	402584
19	0.28156	0.00701	0.03976	0.00035	0.35	0.05132	0.00119	251.9	5.6	251.3	2.2	255.2	52.6	59	0	11604	602	897	29368	1786	275968
20	0.29416	0.00424	0.04030	0.00021	0.36	0.05251	0.00070	261.8	3.3	254.7	1.3	307.5	30.2	8	0	11765	601	905	29190	1845	282946
Quartz-feldspar-biotite schist (sample GM11-9b)																					
1	0.25657	0.01470	0.03673	0.00084	0.40	0.04957	0.00273	231.9	11.9	232.5	5.2	175.0	123.6	0	0	3079	153	733	41387	542	119334
2	0.29233	0.00763	0.03905	0.00064	0.63	0.05195	0.00131	260.4	6.0	246.9	4.0	283.2	56.4	0	0	7907	413	1103	53709	1283	288676
3	0.28847	0.01147	0.04132	0.00078	0.47	0.05003	0.00189	257.4	9.0	261.0	4.8	196.5	85.7	0	0	5523	277	737	38125	875	190838
4	0.27832	0.00729	0.03932	0.00064	0.62	0.05129	0.00130	249.3	5.8	248.6	4.0	253.9	57.5	0	0	6710	346	1007	46838	1131	243938
5	0.27585	0.00878	0.03894	0.00069	0.56	0.05080	0.00155	247.4	7.0	246.2	4.3	231.9	68.9	30	0	8674	442	1383	66059	1466	320218
6	0.28040	0.00992	0.03907	0.00072	0.52	0.05440	0.00185	251.0	7.9	247.0	4.5	387.7	73.9	64	37	6024	329	1068	52052	1073	221963
7	0.28050	0.00727	0.03989	0.00066	0.64	0.05082	0.00127	251.1	5.8	252.1	4.1	232.7	56.6	0	0	10915	557	1644	86173	1818	394440
8	0.29362	0.01197	0.03921	0.00075	0.47	0.05180	0.00202	261.4	9.4	247.9	4.6	276.7	86.9	0	16	4022	209	382	18062	652	148050
Quartz-feldspar-biotite schist (sample MA11-004BV)																					
1	0.30444	0.00933	0.04065	0.00074	0.59	0.05233	0.00152	269.9	7.3	256.8	4.6	299.8	64.7	14	0	7901	419	1187	49235	1287	296695
2	0.28924	0.00731	0.04175	0.00071	0.67	0.04956	0.00119	258.0	5.8	263.7	4.4	174.6	55.3	0	0	9084	456	1323	60316	1475	331715
3	0.29287	0.01080	0.04190	0.00080	0.52	0.05170	0.00182	260.8	8.5	264.6	5.0	272.3	78.6	43	0	4293	225	608	29029	718	156037
4	0.29939	0.01202	0.04269	0.00084	0.49	0.05247	0.00201	265.9	9.4	269.5	5.2	305.8	84.8	0	8	3209	170	402	16357	533	114527
5	0.31044	0.00937	0.04286	0.00077	0.60	0.05181	0.00148	274.5	7.3	270.5	4.8	276.8	64.1	48	0	6435	338	950	46785	1018	229090

APPENDIX 1 (continued): LA-ICP-MS data for U-Pb analysis of zircons

Fraction	Isotopic Ratios							Isotopic Ages						Background corrected mean counts per second at specified mass							
	$^{207}Pb/^{235}U$	% 1σ	$^{206}Pb/^{238}U$	% 1σ	rho	$^{207}Pb/^{206}Pb$	% 1σ	$^{207}Pb/^{235}U$	± 1σ	$^{206}Pb/^{238}U$	± 1σ	$^{207}Pb/^{206}Pb$	± 1σ	202	204	206	207	208	232	235	238
6	0.28127	0.01061	0.04327	0.00084	0.51	0.04796	0.00172	251.7	8.4	273.1	5.2	96.1	83.7	30	0	7838	381	850	41679	1267	276207
7	0.28356	0.00909	0.04354	0.00079	0.57	0.04854	0.00148	253.5	7.2	274.7	4.9	125.7	70.4	0	0	4986	245	687	34454	809	174536
Quartz-feldspar-biotite schist (sample MA11-00BV)																					
1	0.27302	0.01502	0.03903	0.00071	0.33	0.04866	0.00254	245.1	12.0	246.8	4.4	131.5	118.4	10	0	5428	270	1105	62508	940	211402
2	0.26837	0.00877	0.04095	0.00044	0.33	0.04909	0.00153	241.4	7.0	258.7	2.7	151.9	71.5	72	0	5311	266	900	46700	944	197212
3	0.29940	0.00657	0.04370	0.00034	0.35	0.04979	0.00102	265.9	5.1	275.7	2.1	185.1	47.0	0	0	16053	816	3773	192569	2596	558601
4	0.27581	0.00996	0.04346	0.00049	0.31	0.04858	0.00167	247.3	7.9	274.3	3.1	127.6	79.2	0	0	4741	235	709	32801	812	165891
5	0.29195	0.00965	0.04187	0.00047	0.34	0.05138	0.00161	260.1	7.6	264.4	2.9	257.7	70.2	29	0	6807	356	1568	74478	1165	247295
6	0.26983	0.01171	0.04185	0.00059	0.32	0.04776	0.00197	242.6	9.4	264.3	3.7	86.2	96.0	0	16	5966	290	1128	57105	1027	216958
7	0.26631	0.02535	0.04179	0.00098	0.25	0.04461	0.00414	239.7	20.3	263.9	6.0	0.1	135.3	10	1	1174	53	146	6759	191	42770
8	0.28989	0.00957	0.04241	0.00047	0.34	0.04947	0.00154	258.5	7.5	267.7	2.9	170.0	71.0	0	30	9214	464	2131	113157	1530	330789
9	0.27844	0.01648	0.03946	0.00072	0.31	0.05054	0.00287	249.4	13.1	249.5	4.5	220.0	126.2	0	9	2708	139	592	32543	478	104528
10	0.29632	0.01099	0.04209	0.00051	0.33	0.05297	0.00187	263.5	8.6	265.8	3.2	327.3	78.2	40	0	4220	227	775	40736	734	152722
11	0.27940	0.01856	0.04055	0.00073	0.27	0.05321	0.00345	250.2	14.7	256.3	4.5	337.8	139.8	0	15	1514	81	268	15229	280	56894
12	0.27109	0.01013	0.04071	0.00048	0.32	0.04867	0.00173	243.6	8.1	257.2	3.0	132.1	81.7	0	0	4395	217	651	30191	768	164560
13	0.27030	0.01532	0.03812	0.00075	0.35	0.05249	0.00284	242.9	12.3	241.2	4.7	307.0	118.4	53	0	5329	284	861	41672	1007	213132
14	0.30912	0.01071	0.03938	0.00045	0.33	0.05406	0.00178	273.5	8.3	249.0	2.8	373.5	72.1	10	0	4298	235	847	40381	731	166449
15	0.29082	0.00810	0.04144	0.00039	0.34	0.05104	0.00134	259.2	6.4	261.8	2.4	242.7	59.4	31	20	7698	398	1354	71808	1315	283362
16	0.31232	0.03578	0.04052	0.00127	0.27	0.05512	0.00614	276.0	27.7	256.1	7.9	416.8	231.6	6	2	791	44	123	7043	135	29792
17	0.30215	0.02702	0.03992	0.00119	0.33	0.05659	0.00485	268.1	21.1	252.4	7.4	474.8	179.8	16	0	1687	96	171	10462	307	64522
18	0.29176	0.00974	0.03816	0.00044	0.35	0.05261	0.00166	259.9	7.7	241.4	2.7	312.1	70.0	41	19	8325	443	1254	60535	1462	333064
Quartz-feldspar-biotite schist (sample MA11-006BV)																					
1	0.29397	0.02112	0.04087	0.00079	0.27	0.04900	0.00340	261.7	16.6	258.3	4.9	147.9	155.2	48	22	1394	70	86	4280	225	51587
2	0.37578	0.08776	0.04096	0.00295	0.31	0.06069	0.01352	323.9	64.8	258.8	18.3	628.2	418.9	31	0	634	39	18	1260	99	23428
3	0.21468	0.04316	0.04390	0.00219	0.25	0.04152	0.00817	197.5	36.1	276.9	13.5	0.1	180.6	0	11	1039	44	87	2468	195	35823
4	0.30923	0.02692	0.04150	0.00122	0.34	0.05442	0.00449	273.6	20.9	262.1	7.6	388.4	175.4	94	5	2847	160	252	10733	486	103785
5	0.27573	0.01454	0.04088	0.00062	0.29	0.04785	0.00243	247.3	11.6	258.3	3.9	90.9	117.1	0	8	2428	120	142	4879	409	89877
6	0.22786	0.05184	0.04770	0.00225	0.21	0.03468	0.00770	208.4	42.9	300.4	13.9	0.1	0.0	67	32	927	33	50	1939	137	29422
7	0.27361	0.04224	0.03854	0.00192	0.32	0.05754	0.00862	245.6	33.7	243.8	11.9	511.8	299.6	0	0	1148	68	30	1149	234	45096
8	0.29634	0.01954	0.04320	0.00089	0.31	0.05489	0.00348	263.5	15.3	272.6	5.5	407.8	135.9	0	5	1877	106	173	5424	337	65816
9	0.27598	0.02158	0.03874	0.00106	0.35	0.05634	0.00423	247.5	17.2	245.0	6.6	465.1	159.0	0	17	2970	172	232	5826	588	116121
10	0.22468	0.05914	0.03649	0.00257	0.27	0.04864	0.01257	205.8	49.0	231.0	16.0	130.5	516.1	0	23	807	40	61	4437	169	33507
11	0.16223	0.04266	0.03988	0.00200	0.19	0.03089	0.00802	152.6	37.3	252.1	12.4	0.1	0.0	0	0	905	28	60	1568	167	34402
12	0.22684	0.11359	0.04484	0.00485	0.22	0.04176	0.02057	207.6	94.0	282.8	29.9	0.1	685.5	0	31	406	17	0	1138	72	13726
13	0.28429	0.02248	0.04037	0.00096	0.30	0.04928	0.00374	254.1	17.8	255.1	5.9	161.0	168.4	0	0	1646	83	89	3255	277	61816
14	0.31003	0.04637	0.04282	0.00206	0.32	0.05553	0.00794	274.2	35.9	270.3	12.7	433.2	290.6	49	22	1162	66	45	3492	202	41150
15	0.34142	0.03704	0.03751	0.00152	0.37	0.07186	0.00748	298.3	28.0	237.4	9.4	981.8	198.6	60	0	1561	115	104	6742	319	63137
16	0.26982	0.02803	0.03911	0.00109	0.27	0.04637	0.00466	242.6	22.4	247.3	6.8	16.7	225.5	42	3	1344	63	52	3658	224	52148
17	0.28383	0.02723	0.04190	0.00125	0.31	0.05187	0.00478	253.7	21.5	264.6	7.8	279.9	197.6	0	19	1538	81	83	4189	273	55749
18	0.23190	0.04571	0.04261	0.00181	0.22	0.03718	0.00716	211.8	37.7	269.0	11.2	0.1	0.0	0	0	873	33	77	1843	136	31120
19	0.28504	0.05041	0.04050	0.00196	0.27	0.05263	0.00905	254.6	39.8	255.9	12.2	312.9	350.3	0	0	778	42	47	2667	139	29202
PLUTONIC ROCKS																					
Dawson Range batholith (sample I034239)																					
1	0.10313	0.00219	0.01564	0.00012	0.36	0.04754	0.00101	99.7	2.0	100.0	0.8	75.6	50.5	13	0	11060	552	1631	67944	2216	340250
2	0.10592	0.00196	0.01577	0.00011	0.38	0.04813	0.00089	102.2	1.8	100.9	0.7	105.5	43.2	19	19	8601	406	621	52022	3417	525794
3	0.10620	0.00179	0.01567	0.00010	0.38	0.04850	0.00082	102.5	1.7	100.3	0.6	123.5	39.3	14	2	15138	724	1629	129999	5929	917171
4	0.10254	0.00186	0.01558	0.00010	0.35	0.04795	0.00087	99.1	1.7	99.7	0.7	95.8	43.6	1	6	11681	563	1461	116562	4599	712199
5	0.10218	0.00153	0.01554	0.00009	0.39	0.04795	0.00072	98.8	1.4	99.4	0.6	95.6	36.2	0	0	12086	576	1404	116038	4874	741201
6	0.10434	0.00228	0.01572	0.00013	0.38	0.04865	0.00107	100.8	2.1	100.6	0.8	131.2	50.8	27	0	35287	1856	913	23298	4109	625473
7	0.10313	0.00250	0.01571	0.00014	0.37	0.04807	0.00117	99.7	2.3	100.5	0.9	102.6	56.7	8	35	13151	636	1661	149217	5292	799216
8	0.10644	0.00195	0.01565	0.00011	0.38	0.04958	0.00091	102.7	1.8	100.1	0.7	175.3	42.1	35	31	9257	442	1107	96917	3724	563091
9	0.10351	0.00232	0.01565	0.00013	0.37	0.04824	0.00108	100.0	2.1	100.1	0.8	110.9	52.2	29	0	14203	700	1609	129950	5711	867021
10	0.10109	0.00218	0.01561	0.00012	0.36	0.04731	0.00102	97.8	2.0	99.8	0.8	64.2	51.3	24	3	18249	875	2904	222778	7343	1113660
11	0.10497	0.00337	0.01565	0.00018	0.36	0.04905	0.00158	101.4	3.1	100.1	1.1	150.3	74.0	44	1	20874	1102	523	14160	2398	372224
12	0.10606	0.00265	0.01611	0.00015	0.37	0.04909	0.00123	102.4	2.4	103.0	0.9	152.3	57.8	50	15	4481	218	439	39207	1809	273493
13	0.10540	0.00259	0.01548	0.00014	0.37	0.04897	0.00121	101.7	2.4	99.1	0.9	146.3	56.9	44	4	14555	710	2254	186289	5822	862807
14	0.10895	0.00214	0.01570	0.00012	0.39	0.05040	0.00099	105.0	2.0	100.4	0.7	213.6	44.9	15	33	6719	326	565	47232	2698	414314
15	0.10351	0.00300	0.01568	0.00016	0.35	0.04659	0.00136	100.0	2.8	100.3	1.0	27.9	67.4	7	5	14598	731	2015	164846	5839	887894
16	0.10382	0.00177	0.01577	0.00010	0.37	0.04726	0.00080	100.3	1.6	100.9	0.6	62.0	40.5	3	16	43022	2247	1343	36109	5061	765585

APPENDIX 1 (continued): LA-ICP-MS data for U-Pb analysis of zircons

Fraction	Isotopic Ratios							Isotopic Ages						Background corrected mean counts per second at specified mass							
	$^{207}Pb/^{235}U$	% 1σ	$^{206}Pb/^{238}U$	% 1σ	rho	$^{207}Pb/^{206}Pb$	% 1σ	$^{207}Pb/^{235}U$	± 1σ	$^{206}Pb/^{238}U$	± 1σ	$^{207}Pb/^{206}Pb$	± 1σ	202	204	206	207	208	232	235	238
17	0.10504	0.00297	0.01566	0.00016	0.36	0.04923	0.00140	101.4	2.7	100.1	1.0	158.9	65.2	11	0	13914	653	1554	127026	5480	842157
18	0.10520	0.00199	0.01571	0.00010	0.34	0.04793	0.00090	101.6	1.8	100.5	0.7	94.8	45.0	35	0	9197	449	945	79945	3730	560775
19	0.10363	0.00213	0.01551	0.00011	0.35	0.04764	0.00098	100.1	2.0	99.2	0.7	80.4	48.7	26	1	10141	482	1312	109430	3999	616125
20	0.10300	0.00188	0.01568	0.00010	0.35	0.04738	0.00086	99.5	1.7	100.3	0.7	67.6	43.2	0	19	9439	446	839	73189	3756	580982
Dawson Range batholith (sample YGR-BV-004)																					
1	0.10816	0.00271	0.01604	0.00015	0.37	0.04867	0.00123	104.3	2.5	102.6	0.9	131.9	58.3	47	33	5045	255	828	33112	989	161483
2	0.10517	0.00180	0.01600	0.00010	0.37	0.04730	0.00081	101.5	1.7	102.3	0.6	63.6	41.0	28	0	11730	571	922	75877	4498	701353
3	0.10500	0.00150	0.01599	0.00009	0.39	0.04812	0.00069	101.4	1.4	102.2	0.6	105.2	33.6	0	4	10464	494	1110	90678	4011	627331
4	0.10548	0.00186	0.01596	0.00010	0.36	0.04816	0.00085	101.8	1.7	102.1	0.7	107.4	41.4	0	19	28540	1373	3844	313351	11151	1712402
5	0.10702	0.00266	0.01598	0.00015	0.38	0.04885	0.00123	103.2	2.4	102.2	0.9	140.6	57.9	53	6	9717	468	1049	90530	3784	583817
6	0.10960	0.00406	0.01585	0.00022	0.37	0.04979	0.00186	105.6	3.7	101.4	1.4	185.3	84.8	60	15	50736	2690	1352	32020	5852	909921
7	0.11055	0.00212	0.01596	0.00011	0.36	0.04995	0.00097	106.5	1.9	102.1	0.7	192.8	44.4	42	0	11070	551	1108	84069	4291	669649
8	0.10164	0.00196	0.01555	0.00011	0.37	0.04757	0.00092	98.3	1.8	99.5	0.7	77.2	46.2	70	0	10103	504	859	66958	3896	606866
9	0.10529	0.00267	0.01602	0.00015	0.37	0.04724	0.00120	101.7	2.5	102.4	0.9	60.7	60.1	9	26	9814	466	960	81519	3920	605169
10	0.10671	0.00785	0.01605	0.00042	0.36	0.04770	0.00354	102.9	7.2	102.6	2.7	83.3	167.9	9	1	8261	390	802	61252	3164	494470
11	0.10708	0.00380	0.01604	0.00020	0.35	0.04677	0.00167	103.3	3.5	102.6	1.3	37.1	83.5	0	0	30432	1592	902	22842	3501	547028
12	0.10611	0.00228	0.01605	0.00012	0.35	0.04811	0.00104	102.4	2.1	102.6	0.8	104.6	50.3	7	0	10672	498	1067	86233	3982	637565
13	0.09918	0.00372	0.01575	0.00019	0.32	0.04671	0.00177	96.0	3.4	100.7	1.2	34.1	88.3	37	2	6585	316	610	49382	2551	393340
14	0.10404	0.00192	0.01596	0.00011	0.37	0.04772	0.00089	100.5	1.8	102.0	0.7	84.5	44.4	28	3	7845	366	528	42081	3157	477514
15	0.11022	0.00230	0.01581	0.00012	0.36	0.05038	0.00106	106.2	2.1	101.1	0.8	212.5	47.9	0	19	11944	569	769	63080	4683	717362
16	0.10769	0.00255	0.01590	0.00014	0.37	0.04775	0.00114	103.8	2.3	101.7	0.9	86.0	56.5	17	22	31449	1656	942	22387	3624	562180
17	0.10842	0.00257	0.01607	0.00013	0.34	0.04847	0.00116	104.5	2.4	102.8	0.8	122.1	55.3	16	24	7630	363	637	50748	2894	459903
18	0.10944	0.00210	0.01608	0.00011	0.36	0.04956	0.00096	105.5	1.9	102.8	0.7	174.5	44.3	0	0	5790	280	579	45829	2214	345148
19	0.11449	0.00316	0.01604	0.00016	0.36	0.05032	0.00140	110.1	2.9	102.6	1.0	209.8	63.2	65	12	13560	670	588	48007	5255	807922
20	0.09905	0.00182	0.01525	0.00010	0.36	0.04724	0.00087	95.9	1.7	97.6	0.7	60.7	43.9	0	14	6680	335	754	61826	2513	399033
Dawson Range batholith (sample 99M-106-b)																					
1	0.10799	0.00650	0.01679	0.00031	0.31	0.04620	0.00282	104.1	6.0	107.3	2.0	8.3	140.8	78	11	2679	124	271	27505	1336	199982
2	0.11228	0.00339	0.01571	0.00017	0.36	0.05142	0.00158	108.0	3.1	100.5	1.1	259.7	69.2	140	11	7967	412	1032	115385	4255	636020
3	0.10761	0.00293	0.01619	0.00015	0.34	0.04831	0.00133	103.8	2.7	103.5	1.0	114.3	63.8	90	14	5766	280	699	77492	3020	446698
4	0.10607	0.00254	0.01587	0.00013	0.34	0.04854	0.00118	102.4	2.3	101.5	0.9	125.5	56.2	135	25	7146	349	1324	158411	3817	565069
5	0.09674	0.00415	0.01614	0.00021	0.30	0.04363	0.00190	93.8	3.8	103.2	1.3	0.1	0.0	58	28	4303	189	573	68206	2268	334918
6	0.11060	0.00307	0.01643	0.00015	0.33	0.04825	0.00136	106.5	2.8	105.1	1.0	111.5	65.1	57	7	5408	262	664	76070	2758	413346
7	0.10403	0.00387	0.01603	0.00020	0.34	0.04758	0.00180	100.5	3.6	102.5	1.3	77.5	88.1	92	0	4179	200	536	66458	2236	327551
8	0.10402	0.00373	0.01557	0.00018	0.32	0.04918	0.00179	100.5	3.4	99.6	1.2	156.2	83.2	120	0	4379	217	757	83915	2423	353458
9	0.10636	0.00293	0.01588	0.00015	0.34	0.04808	0.00134	102.6	2.7	101.5	1.0	103.3	64.6	58	8	5301	256	755	85706	2808	420096
10	0.11290	0.00513	0.01595	0.00024	0.33	0.04981	0.00230	108.6	4.7	102.0	1.5	186.0	104.1	71	31	3888	195	488	57385	2011	306718
11	0.11096	0.00635	0.01667	0.00029	0.30	0.04864	0.00283	106.8	5.8	106.6	1.9	130.3	131.3	1	12	2134	104	220	24960	1097	161205
12	0.10729	0.00354	0.01664	0.00018	0.33	0.04719	0.00158	103.5	3.3	106.4	1.2	58.6	78.4	46	1	4184	199	592	61085	2160	316705
13	0.10720	0.00226	0.01605	0.00012	0.35	0.04806	0.00102	103.4	2.1	102.6	0.8	102.4	49.4	0	28	9342	452	2235	243214	4923	733931
14	0.09973	0.00472	0.01614	0.00022	0.29	0.04614	0.00221	96.5	4.4	103.2	1.4	5.1	111.5	59	12	2479	115	325	38244	1349	193759
15	0.10397	0.00431	0.01581	0.00020	0.31	0.04705	0.00198	100.4	4.0	101.1	1.3	51.3	97.6	22	0	3555	168	463	55385	1892	283647
16	0.10139	0.00305	0.01588	0.00016	0.33	0.04648	0.00142	98.1	2.8	101.6	1.0	22.4	70.6	98	21	5410	253	779	80935	2918	429910
17	0.10432	0.00328	0.01594	0.00017	0.34	0.04823	0.00154	100.8	3.0	101.9	1.1	110.5	73.6	111	0	5798	282	978	116648	3159	459489
18	0.10548	0.00368	0.01579	0.00018	0.33	0.04804	0.00170	101.8	3.4	101.0	1.1	101.0	81.6	81	0	3905	189	459	46953	2097	312493
19	0.10001	0.00375	0.01567	0.00020	0.34	0.04799	0.00183	96.8	3.5	100.2	1.3	97.4	89.1	41	8	4915	237	479	55383	2782	396486
20	0.11211	0.00850	0.01684	0.00043	0.34	0.04811	0.00371	107.9	7.8	107.6	2.7	104.6	172.9	123	12	3241	157	379	40863	1641	243420
Coffee Creek granite (sample YGR-BV-002)																					
1	0.10266	0.00283	0.01560	0.00015	0.35	0.04723	0.00130	99.2	2.6	99.8	1.0	60.6	64.8	13	0	5609	271	1092	100851	2652	401905
2	0.10351	0.00314	0.01555	0.00017	0.36	0.04863	0.00148	100.0	2.9	99.5	1.1	130.1	69.9	7	3	5318	264	763	77001	2568	382295
3	0.10254	0.00365	0.01562	0.00019	0.34	0.04667	0.00167	99.1	3.4	99.9	1.2	32.4	83.5	0	0	3415	162	453	40592	1598	244494
4	0.11053	0.00282	0.01593	0.00015	0.37	0.05002	0.00126	106.4	2.6	101.9	1.0	195.8	57.7	1	6	17773	907	3764	409591	8271	1247606
5	0.10181	0.00388	0.01540	0.00021	0.36	0.04756	0.00182	98.4	3.6	98.5	1.3	76.6	89.4	0	0	5155	250	920	82488	2477	374615
6	0.10176	0.00651	0.01461	0.00034	0.36	0.04990	0.00325	98.4	6.0	93.5	2.1	190.5	144.7	33	19	3938	200	888	68418	1987	301834
7	0.10201	0.00320	0.01519	0.00017	0.36	0.04828	0.00152	98.6	3.0	97.2	1.1	113.0	72.4	0	8	10314	506	1247	163869	5025	759997
8	0.10238	0.00573	0.01540	0.00030	0.35	0.04787	0.00271	99.0	5.3	98.5	1.9	91.6	130.0	0	14	3232	157	468	38180	1556	234992
9	0.10402	0.00369	0.01549	0.00020	0.36	0.04827	0.00172	100.5	3.4	99.1	1.2	112.4	81.8	0	10	5025	246	897	79070	2401	363308
10	0.10591	0.00834	0.01557	0.00044	0.36	0.04749	0.00379	102.2	7.7	99.6	2.8	73.3	180.4	13	14	3131	150	458	41514	1447	225312
11	0.10601	0.00512	0.01550	0.00028	0.37	0.05055	0.00247	102.3	4.7	99.2	1.8	220.2	109.3	0	24	7264	372	1020	110609	3571	525287
12	0.10577	0.00755	0.01605	0.00039	0.34	0.04953	0.00359	102.1	6.9	102.6	2.5	173.0	160.7	0	32	1842	92	252	28766	889	128710

APPENDIX 1 (continued): LA-ICP-MS data for U-Pb analysis of zircons

Fraction	Isotopic Ratios							Isotopic Ages						Background corrected mean counts per second at specified mass							
	$^{207}Pb/^{235}U$	% 1σ	$^{206}Pb/^{238}U$	% 1σ	rho	$^{207}Pb/^{206}Pb$	% 1σ	$^{207}Pb/^{235}U$	± 1σ	$^{206}Pb/^{238}U$	± 1σ	$^{207}Pb/^{206}Pb$	± 1σ	202	204	206	207	208	232	235	238
13	0.10266	0.00535	0.01556	0.00027	0.33	0.04777	0.00251	99.2	4.9	99.5	1.7	86.9	121.1	0	0	1877	90	222	24641	901	135331
14	0.10448	0.00529	0.01566	0.00027	0.34	0.04837	0.00247	100.9	4.9	100.2	1.8	117.5	116.2	0	0	2600	127	437	42164	1242	186288
15	0.10965	0.00332	0.01541	0.00017	0.36	0.05158	0.00155	105.6	3.0	98.6	1.1	266.9	67.5	15	0	8753	456	1268	119562	4250	637230
16	0.10322	0.00458	0.01583	0.00025	0.36	0.04664	0.00208	99.7	4.2	101.2	1.6	30.7	103.6	0	15	7782	366	1603	142208	3631	552001
17	0.10932	0.00805	0.01669	0.00042	0.34	0.04707	0.00350	105.3	7.4	106.7	2.7	52.6	168.7	0	13	2355	111	322	30476	1048	158469
18	0.10110	0.00380	0.01521	0.00020	0.35	0.04749	0.00178	97.8	3.5	97.3	1.3	73.1	87.5	0	5	4880	233	737	60813	2368	360274
19	0.10261	0.00326	0.01576	0.00018	0.36	0.04728	0.00149	99.2	3.0	100.8	1.1	62.9	73.7	30	0	7450	354	1101	99325	3548	530908
20	0.10476	0.00421	0.01544	0.00022	0.35	0.04799	0.00193	101.2	3.9	98.8	1.4	97.5	93.7	0	1	10566	509	3189	295478	5004	769069
Coffee Creek granite (sample 99M-105)																					
1	0.10339	0.00320	0.01534	0.00017	0.36	0.04825	0.00143	99.9	3.0	98.1	1.1	111.5	68.4	0	16	11731	580	1990	189507	6334	877776
2	0.10474	0.00312	0.01561	0.00017	0.37	0.04869	0.00138	101.1	2.9	99.8	1.1	132.9	65.2	0	18	20315	1013	3402	333788	10921	1493286
3	0.10824	0.00361	0.01599	0.00020	0.38	0.04963	0.00160	104.4	3.3	102.3	1.2	177.9	73.3	0	6	9917	504	2341	221170	5256	711046
4	0.24398	0.00746	0.03458	0.00039	0.37	0.05149	0.00148	221.7	6.1	219.2	2.4	263.0	64.5	10	20	29189	1538	3079	150998	7117	967439
5	0.10150	0.00486	0.01481	0.00025	0.35	0.04846	0.00231	98.2	4.5	94.8	1.6	121.7	108.4	0	0	3906	193	564	55271	2151	301957
6	0.10009	0.00494	0.01512	0.00027	0.36	0.04837	0.00238	96.9	4.6	96.8	1.7	117.6	112.0	0	0	3919	193	466	45604	2183	296540
7	0.10281	0.00351	0.01514	0.00019	0.37	0.04824	0.00158	99.4	3.2	96.8	1.2	111.0	75.7	31	0	7273	358	1100	109392	3932	549627
8	0.10453	0.00407	0.01566	0.00022	0.36	0.04954	0.00188	101.0	3.8	100.1	1.4	173.3	86.5	0	0	5663	286	1160	106371	3091	413592
9	0.10374	0.00325	0.01577	0.00018	0.36	0.04777	0.00141	100.2	3.0	100.9	1.1	86.8	69.7	0	13	20375	992	4707	441060	10790	1474918
10	0.10281	0.00406	0.01532	0.00022	0.36	0.04854	0.00187	99.4	3.7	98.0	1.4	125.9	88.1	0	0	8598	425	1609	154907	4667	640612
11	0.10473	0.00366	0.01558	0.00020	0.37	0.04814	0.00161	101.1	3.4	99.6	1.3	106.3	77.4	32	20	9424	462	2090	193303	4977	690328
12	0.10300	0.00375	0.01585	0.00021	0.36	0.04675	0.00164	99.5	3.5	101.4	1.3	36.4	82.0	74	14	6636	315	1111	107044	3459	477455
13	0.10514	0.00529	0.01556	0.00028	0.36	0.04927	0.00246	101.5	4.9	99.6	1.8	160.6	112.7	62	20	3412	170	494	50443	1833	249767
14	0.10278	0.00433	0.01529	0.00023	0.36	0.04895	0.00202	99.3	4.0	97.8	1.5	145.7	93.8	74	0	8571	426	1615	149740	4678	638081
15	0.10584	0.00406	0.01537	0.00021	0.36	0.04909	0.00182	102.1	3.7	98.3	1.4	151.9	84.7	26	16	8694	433	1310	122623	4619	643845
16	0.10492	0.00525	0.01590	0.00028	0.35	0.04809	0.00238	101.3	4.8	101.7	1.8	103.5	113.0	0	0	4775	233	710	74355	2505	341546
17	0.10861	0.00392	0.01521	0.00020	0.36	0.05174	0.00178	104.7	3.6	97.3	1.3	273.9	77.1	6	27	20121	1055	6714	612504	10958	1502498
18	0.10907	0.00461	0.01528	0.00023	0.36	0.05120	0.00211	105.1	4.2	97.8	1.5	249.7	92.1	0	12	4319	224	736	67610	2316	320953
19	0.10310	0.00423	0.01568	0.00023	0.36	0.04662	0.00185	99.6	3.9	100.3	1.5	29.9	92.8	0	27	5749	271	821	76380	2969	416182
20	0.10622	0.00358	0.01585	0.00019	0.36	0.04821	0.00153	102.5	3.3	101.4	1.2	109.4	73.2	89	0	61019	2978	22748	2E+06	31613	4368048
Coffee Creek granite (sample 99M-107)																					
1	0.10349	0.00143	0.01561	0.00009	0.42	0.04802	0.00067	100.0	1.3	99.9	0.6	98.9	34.0	45	13	19926	969	3667	404003	10955	1804307
2	0.11027	0.00158	0.01609	0.00009	0.39	0.04912	0.00072	106.2	1.5	102.9	0.6	153.7	33.8	0	0	17501	871	1841	208355	9242	1537814
3	0.10469	0.00139	0.01552	0.00009	0.44	0.04834	0.00065	101.1	1.3	99.3	0.6	115.9	31.6	10	20	27749	1359	7450	900778	15197	2526153
4	0.10338	0.00288	0.01559	0.00016	0.37	0.04798	0.00137	99.9	2.7	99.7	1.0	97.1	67.3	12	0	9618	467	2576	282684	5296	871889
5	0.10283	0.00146	0.01548	0.00009	0.41	0.04811	0.00069	99.4	1.3	99.1	0.6	104.9	33.7	0	21	25962	1265	4034	451622	14426	2368088
6	0.10297	0.00097	0.01559	0.00007	0.48	0.04778	0.00045	99.5	0.9	99.7	0.4	87.6	23.4	21	1	39500	1911	6471	706364	21778	3577980
7	0.10589	0.00156	0.01541	0.00009	0.40	0.04897	0.00073	102.2	1.4	98.6	0.6	146.3	34.8	0	23	18733	929	2609	312858	10297	1716416
8	0.10197	0.00140	0.01539	0.00009	0.43	0.04788	0.00067	98.6	1.3	98.4	0.6	92.3	33.8	0	12	27552	1335	6336	702124	15385	2527561
9	0.10126	0.00409	0.01529	0.00022	0.36	0.04708	0.00194	97.9	3.8	97.8	1.4	53.1	96.0	108	0	4816	229	834	91738	2665	444486
10	0.10266	0.00167	0.01534	0.00010	0.40	0.04808	0.00080	99.2	1.5	98.1	0.6	103.2	38.8	42	44	20654	1005	3880	471386	11518	1899842
11	0.10328	0.00146	0.01547	0.00009	0.41	0.04807	0.00069	99.8	1.3	98.9	0.6	102.8	33.6	43	0	22228	1081	2748	308437	12325	2026927
12	0.10122	0.00108	0.01547	0.00007	0.42	0.04706	0.00051	97.9	1.0	98.9	0.5	51.9	25.0	0	2	29494	1404	4534	532727	16343	2689094
13	0.10438	0.00210	0.01548	0.00012	0.39	0.04815	0.00099	100.8	1.9	99.0	0.8	106.9	47.8	32	0	9946	484	2369	275786	5474	905511
14	0.11169	0.00206	0.01528	0.00011	0.39	0.05171	0.00098	107.5	1.9	97.8	0.7	272.4	42.7	57	12	24701	1291	3507	402829	13647	2278058
15	0.10378	0.00144	0.01549	0.00009	0.42	0.04793	0.00067	100.3	1.3	99.1	0.6	94.6	34.1	18	10	29880	1448	4300	484201	16476	2717852
16	0.10438	0.00118	0.01533	0.00008	0.46	0.04857	0.00056	100.8	1.1	98.1	0.5	127.1	26.8	0	31	28842	1416	4683	531450	16031	2649627
17	0.10634	0.00789	0.01581	0.00041	0.35	0.04827	0.00366	102.6	7.3	101.1	2.6	112.3	170.0	0	22	2477	120	433	51036	1344	220623
18	0.10302	0.00349	0.01537	0.00019	0.36	0.04778	0.00166	99.6	3.2	98.3	1.2	87.3	81.2	62	8	4966	239	1028	121390	2754	454978
19	0.10650	0.00165	0.01558	0.00010	0.41	0.04796	0.00075	102.8	1.5	99.7	0.6	96.3	38.0	0	0	26515	1285	5199	589256	14289	2394737
20	0.10789	0.00175	0.01591	0.00010	0.39	0.04794	0.00079	104.0	1.6	101.8	0.7	95.0	39.8	71	15	17309	838	1980	206543	9207	1530508
SUBVOLCANIC ROCKS																					
Quartz-feldspar rhyodacite porphyry (sample MA11-001BV)																					
1	0.07309	0.01078	0.00875	0.00038	0.29	0.05832	0.00880	71.6	10.2	56.2	2.4	541.0	300.5	0	0	494	28	106	18700	364	82084
2	0.05686	0.00399	0.00887	0.00022	0.35	0.04567	0.00328	56.2	3.8	56.9	1.4	0.1	145.3	33	0	1799	82	367	81481	1336	295312
3	0.04568	0.01112	0.00885	0.00044	0.20	0.03531	0.00869	45.4	10.8	56.8	2.8	0.1	0.0	0	26	512	18	115	24413	366	84420
4	0.05088	0.00764	0.00925	0.00033	0.24	0.03949	0.00601	50.4	7.4	59.3	2.1	0.1	0.0	0	0	921	36	216	47781	662	145440
5	0.06909	0.01472	0.00869	0.00052	0.28	0.06103	0.01331	67.8	14.0	55.8	3.3	640.3	410.5	11	0	337	20	52	14286	276	56818
6	0.07700	0.02564	0.01119	0.00103	0.28	0.05967	0.02033	75.3	24.2	71.7	6.5	591.7	605.3	0	0	249	14	58	13033	179	32723
7	0.05696	0.01555	0.00940	0.00057	0.22	0.04050	0.01119	56.2	14.9	60.3	3.6	0.1	271.6	0	0	452	18	88	18221	299	70736

APPENDIX 1 (continued): LA-ICP-MS data for U-Pb analysis of zircons

Fraction	Isotopic Ratios							Isotopic Ages						Background corrected mean counts per second at specified mass							
	$^{207}Pb/^{235}U$	% 1σ	$^{206}Pb/^{238}U$	% 1σ	rho	$^{207}Pb/^{206}Pb$	% 1σ	$^{207}Pb/^{235}U$	± 1σ	$^{206}Pb/^{238}U$	± 1σ	$^{207}Pb/^{206}Pb$	± 1σ	202	204	206	207	208	232	235	238
8	0.05539	0.00704	0.00899	0.00030	0.26	0.04413	0.00570	54.7	6.8	57.7	1.9	0.1	187.3	0	0	966	42	191	47019	716	158022
9	0.05015	0.01224	0.00905	0.00040	0.18	0.03881	0.00955	49.7	11.8	58.1	2.6	0.1	117.1	23	0	493	19	101	21635	355	80214
10	0.04233	0.01804	0.00865	0.00051	0.14	0.03604	0.01545	42.1	17.6	55.5	3.3	0.1	263.1	41	41	253	9	51	15566	201	43204
11	0.05107	0.00825	0.00916	0.00032	0.22	0.03957	0.00646	50.6	8.0	58.8	2.0	0.1	0.0	4	0	648	25	120	28156	469	104654
12	0.08295	0.03003	0.00850	0.00072	0.23	0.06746	0.02488	80.9	28.2	54.6	4.6	852.1	622.2	40	8	188	12	54	10182	143	32829
13	0.05907	0.00569	0.00875	0.00027	0.32	0.04902	0.00483	58.3	5.5	56.1	1.7	149.0	216.0	61	3	1224	60	173	36942	950	207605
14	0.06656	0.01159	0.00844	0.00039	0.27	0.05989	0.01064	65.4	11.0	54.2	2.5	599.6	344.2	18	2	399	23	61	17326	336	70346
15	0.06503	0.00747	0.00895	0.00033	0.32	0.05622	0.00663	64.0	7.1	57.4	2.1	460.2	242.9	0	13	763	43	103	21803	618	126965
16	0.05293	0.00944	0.00945	0.00045	0.27	0.04176	0.00758	52.4	9.1	60.6	2.9	0.1	163.7	44	16	1003	42	170	41699	743	158430
17	0.05040	0.00656	0.00856	0.00027	0.24	0.04180	0.00552	49.9	6.4	54.9	1.8	0.1	64.9	0	0	855	35	67	19465	666	149306
18	0.06156	0.00602	0.00910	0.00023	0.26	0.04869	0.00483	60.7	5.8	58.4	1.5	133.0	217.8	0	0	957	46	131	29664	712	157333
19	0.03562	0.01216	0.00817	0.00038	0.14	0.03120	0.01071	35.5	11.9	52.4	2.5	0.1	0.0	0	0	433	13	118	21499	357	79560
20	0.06905	0.00647	0.00908	0.00028	0.33	0.05667	0.00544	67.8	6.2	58.3	1.8	477.9	200.1	4	20	882	50	230	43210	682	145736

A preliminary assessment of low pressure, amphibolite-facies metamorphism in the upper Hyland River area (NTS 105H), southeast Yukon

David P. Moynihan[1]
Yukon Geological Survey, Whitehorse, YT

Moynihan, D.P., 2013. A preliminary assessment of low pressure, amphibolite-facies metamorphism in the upper Hyland River area (NTS 105H), southeast Yukon. *In:* Yukon Exploration and Geology 2012, K.E. MacFarlane, M.G. Nordling, and P.J. Sack (eds.), Yukon Geological Survey, p. 99-114.

ABSTRACT

The regional metamorphic grade in southeast Yukon is low, but amphibolite-facies metamorphism has affected regions adjacent to numerous mid-Cretaceous intrusions. In the upper Hyland River area, contact aureoles approximately 300 m wide are developed around the Hyland and Boundary plutons, which are members of the 97-94 Ma Tungsten plutonic suite. Andalusite + cordierite + biotite-bearing assemblages in the aureole of the Hyland pluton imply emplacement at ~2.5-3 kbar, equivalent to a depth of 9 to 11 km. Cordierite + biotite assemblages in the aureole of the adjacent Boundary pluton suggest emplacement at shallower levels (<~2.5 kbar or <9 km). Metamorphism associated with these intrusions took place after most regional deformation. In contrast, rocks adjacent to the older (*ca.* 106 Ma) Mount Billings batholith were metamorphosed syn-kinematically. Staurolite ± andalusite ± sillimanite-bearing assemblages in metapelites east of the Mount Billings batholith indicate metamorphism at deeper levels (~4 kbar, or 15 km depth), coincident with the formation of structures oblique to the regional trend.

[1]*david.moynihan@gov.yk.ca*

INTRODUCTION

In the upper Hyland River area of southeast Yukon (Fig. 1), deformed Neoproterozoic-Mississippian rocks of the Selwyn basin host numerous mid-Cretaceous intrusions of the Hyland and Tungsten plutonic suites (Roots *et al.*, 1966; Hart *et al.*, 2004; Hart and Lewis, 2006). The Hyland suite (106-96 Ma) is represented by large, heterolithic bodies that crop out southwest of the Hyland River, such as the Logan and Mount Billings batholiths (Fig. 1). These intrusions have tabular forms and contacts that are concordant with fabrics in the host rock (Hart and Lewis, 2006). Intrusions belonging to this suite are variably porphyritic, peraluminous or weakly peraluminous, biotite granite and granodiorite; muscovite-bearing phases are also locally present. Hyland suite rocks are weakly oxidized, with moderate magnetic susceptibilities and are associated with W ± Mo, Cu skarns, and distal Ag-Pb-Zn vein mineralization (Hart *et al.*, 2004).

The 97-94 Ma Tungsten suite (Gordey and Anderson, 1993; Hart *et al.*, 2004; Heffernan, 2004; Rasmussen *et al.*, 2006) is represented by small to moderate sized, discordant, biotite granite, monzogranite, and quartz monzonite intrusions. These bodies, which are restricted to the area northeast of the Little Hyland River (Fig. 1), are weakly to moderately peraluminous, ilmenite-bearing, and associated with significant W ± Mo, Cu skarn mineralization (*e.g.*, Cantung; Blusson, 1968).

The metamorphic grade in the Hyland River valley area is low (subgreenschist to lower greenschist-facies; chlorite zone), with the exception of areas directly adjacent to intrusions (Read *et al.*, 1991). Narrow, amphibolite-facies contact metamorphic aureoles surround intrusions of the Tungsten suite (Gordey and Anderson, 1993), whereas there is a large region of schist and gneiss of uncertain origin adjacent to the Mount Billings and Logan batholiths (Roots *et al.*, 1966; McLeod, 1982). In this paper, a preliminary assessment of each of these styles of metamorphism is presented, based on detailed fieldwork in two small areas. Area 1 (Fig. 1) includes part of the contact aureoles of two small, Tungsten suite intrusions. Area 2 (Fig. 1) lies within a region of schist and gneiss to the east of the Mount Billings batholith.

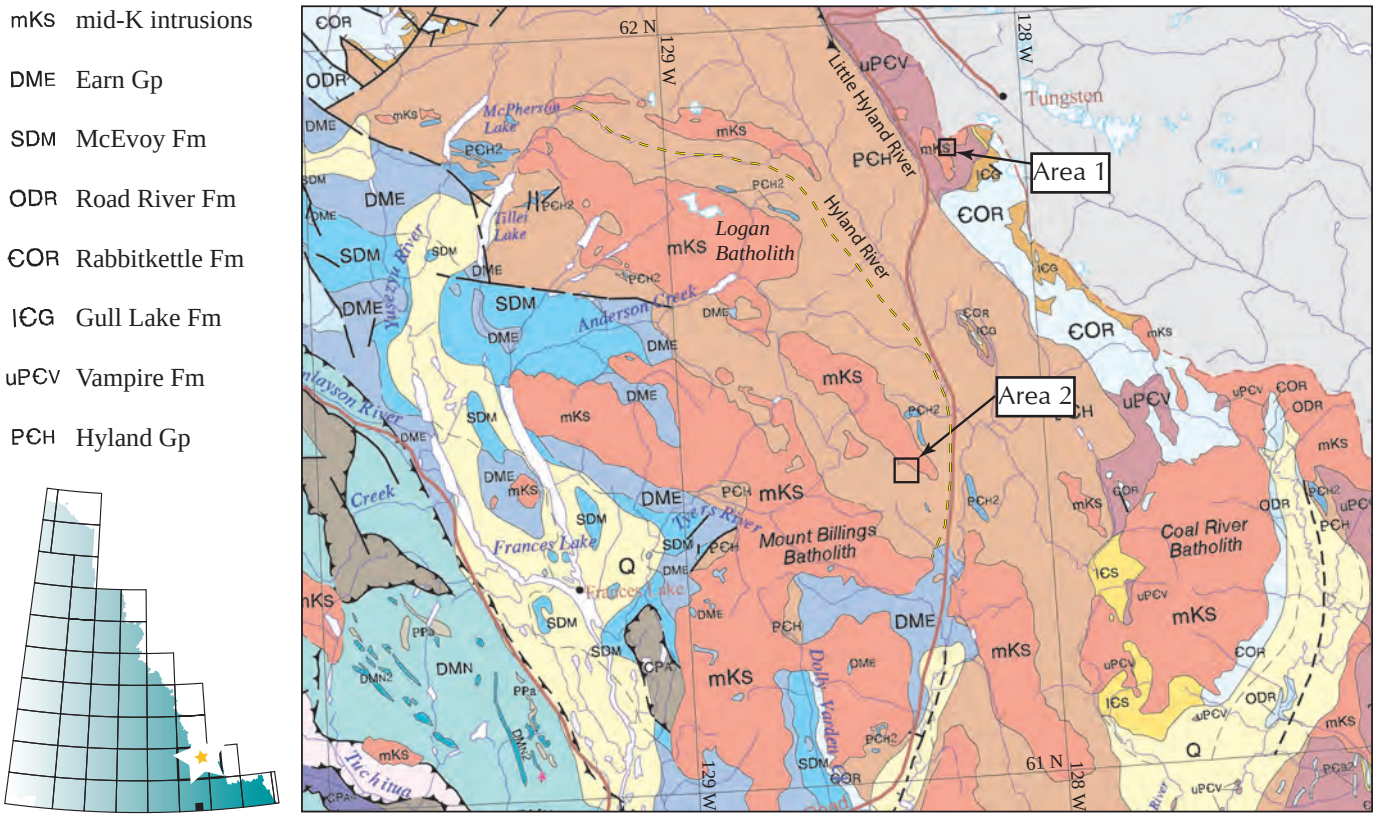

Figure 1. *Geology of the Upper Hyland River area, from Gordey and Makepeace (2003). The locations of the two study areas are marked with black boxes. The dashed yellow line marks the eastern boundary of the schist/gneiss belt adjacent to the Mount Billings and Logan batholiths (Roots et al., 1966).*

Estimates of pressure and temperature conditions during metamorphism are made based on mineral assemblages in metapelites. These assemblages are sensitive discriminants of pressure-temperature conditions and also record timing relationships between metamorphism and deformation.

As contact metamorphism adjacent to simple intrusions is fast in geological terms, pressure-sensitive mineral assemblages in aureoles provide a proxy for their depth of emplacement. In the case of contact aureoles surrounding the two small Tungsten suite intrusions that were studied (Area 1), pressure estimates are valid indicators of emplacement depth. Pressure estimates from rocks east of the Mount Billings batholith (Area 2) cannot be interpreted as providing a direct indication of its emplacement depth, as the timing relationships between metamorphism and plutonism in this area are unclear.

METHODS FOR ESTIMATING P-T CONDITIONS

Pressure-temperature estimates are made by comparing observed mineral assemblages (Table 1) with phase diagrams (equilibrium assemblage diagrams) that show thermodynamically predicted mineral assemblages as a function of pressure and temperature for the bulk composition of interest. For this study, phase diagrams were constructed in the model system K_2O-FeO-MgO-Al_2O_3-SiO_2-H_2O (KFMASH) using THERIAK/DOMINO software (de Capitani and Brown, 1987; de Capitani and Petrakakis, 2010) in conjunction with the thermodynamic database and solution models outlined in Spear and Pyle (2010). The KFMASH system accounts for the major index minerals that record variations in metamorphic grade. Garnet stability is not satisfactorily modelled in KFMASH; however, garnet is absent or a minor phase in the rocks under consideration and is not used for P-T estimates. The bulk composition of representative, homogeneous hand samples was determined by fusion XRF (major elements) and infrared spectroscopy (S, C) at Activation Laboratories Ltd. (Table 2). Samples were milled with mild steel. KFMASH compositions were derived from full compositions by projecting from ilmenite, pyrrhotite, albite and anorthite end-members of plagioclase, and by dropping MnO and P_2O_5. All mineral abbreviations used are from Kretz (1983).

HYLAND AND BOUNDARY PLUTON CONTACT AUREOLES

The Hyland and Boundary plutons are biotite quartz monzonite intrusions located on the east side of the Little Hyland River (Fig. 1; Blusson, 1968). The Hyland pluton (also known as the Tuna stock) lies entirely within Yukon, and the Boundary pluton overlaps the Yukon-NWT border. The two plutons are separated by a narrow septum of low grade country rock, around which this study area is centred (Fig. 2).

The Hyland and Boundary plutons are hosted by the Latest Proterozoic-Early Cambrian Vampire Formation. The Vampire Formation in this region is dominated by uniform, rusty brown weathering and steel grey to dark grey phyllite. Phyllite is locally interbedded with quartzite layers that are generally 1-3 cm thick, but are locally up to 30 cm (Fig. 2b).

The dominant foliation in the area (S_n) strikes NW/SE, parallel to the orogenic trend (Fig. 3). It generally dips NE at 40-70° in the southwest part of the area and dips steeply towards the SW or NE in the northeast part of the area. S_n is locally overprinted by kink bands that have steeply-dipping axial planes and approximately down-dip axes (F_{n+1}). These kink bands post-date development of the contact aureoles and are best developed in low-grade phyllites, which retain a well-defined cleavage.

The pluton-Vampire Fm contact is offset by a number of steeply-dipping, SW-trending normal faults with downthrow to the NW (Fig. 3). These faults are sub-parallel to axial planes of the kink bands, and also have the same orientation as 1) a number of fine-grained, biotite and amphibole-bearing mafic dikes, and 2) an array of quartz-tourmaline veins that transect the Boundary aureole.

HYLAND PLUTON CONTACT AUREOLE

The Hyland pluton, which was emplaced at 97.1 ± 2.0 Ma (U-Pb monazite; Heffernan, 2004), is elongate in a NW direction and underlies an area of approximately 9×2.5 km. The roof of the pluton is preserved around the topographically highest point near the centre of the intrusion. The southwest boundary of the pluton dips steeply, whereas its northeast and southeast boundaries have gentle to moderately steep outward dips. Along the part of the northeast margin that was studied, the pluton-country rock contact dips NE, at an angle of approximately 30-50°, and is locally concordant with the dominant cleavage in the country rock (Fig. 3). The pluton is a biotite quartz monzonite (Streckheisen, 1973); it includes a megacrystic internal phase and an equigranular outer phase. The pluton is undeformed, except around its margin, where a NW-trending foliation and shallowly-plunging lineation is variably developed (Fig. 2c).

Table 1. *Sample locations and mineral assemblages for all samples from which thin-sections were examined.* P *indicates that minerals are pseudomorphed.*

Sample #	UTM E	UTM N	Elev (m)	Grt	Sil	St	And	Crd	Bt	Chl	Ms	Qtz
Area 1												
12-DMO-190	541125	6856906	1442				P	P	X	X	X	X
12-DMO-191	540875	6856771	1512				P	P	X		X	X
12-DMO-192	540710	6856650	1553				X	P	X		X	X
12-DMO-193	540579	6856584	1578				X	P	X		X	X
12-DMO-196	541055	6856405	1461				P	P	X		X	X
12-DMO-197	541283	6857046	1441				P		X	X	X	X
12-DMO-198	541221	6857214	1445							X	X	X
12-DMO-199	541498	6857272	1490							X	X	X
12-DMO-201	542160	6857210	1700							X	X	X
12-DMO-202	542246	6857259	1717					P	X	X	X	X
12-DMO-203	542386	6857284	1707					P	X		X	X
12-DMO-204	542551	6857204	1692					P	X		X	X
12-DMO-205	542510	6857459	1691				X	P	X		X	X
12-DMO-206	542380	6857703	1630				X	P	X		X	X
12-DMO-207	542318	6857732	1584					P	X		X	X
12-DMO-211	541927	6857335	1657							X	X	X
12-DMO-212	541934	6857368	1649					P	X	X	X	X
12-DMO-213	541951	6857403	1651					P	X	X	X	X
12-DMO-216	541772	6858023	1659					P	X		X	X
12-DMO-218	541276	6858182	1750							X	X	X
12-DMO-219	541340	6857925	1724							X	X	X
12-DMO-220	541495	6857879	1675					P	X	X	X	X
12-DMO-222	541686	6857521	1562							X	X	X
12-DMO-224	541737	6856300	1339				P	P	X		X	X
12-DMO-225	541578	6856497	1410				X	X	X		X	X
Area 2												
12-DMO-227A	530954	6810222	1585	X	X	X	X		X			X
12-DMO-227B	530954	6810222	1585		X	X	X		X			X
12-DMO-228A	530758	6810013	1633	X		X			X			X
12-DMO-228B	530758	6810013	1633	X	X	X			X		X	X
12-DMO-229	530766	6809718	1969	X	X	X	X		X		X	X
12-DMO-230	530757	6809486	1966		X	X			X		X	X
12-DMO-231	531024	6809250	1909	X	X	X			X		X	X
12-DMO-232	531285	6809047	1877	X	X	X			X		X	X
12-DMO-234A	531491	6808800	1922		X	X	X		X			X
12-DMO-234B	531491	6808800	1922		X	X	X		X			X
12-DMO-234C	531491	6808800	1922		X	X	X		X		X	X
12-DMO-235	531905	6808626	1936			X	X		X		X	X
12-DMO-236	532298	6808638	1968		X	X	X		X	X	X	X
12-DMO-237	532626	6808641	2015	X		X	X		X			X
12-DMO-238	533099	6808398	2045			X	X		X			X
12-DMO-240	533506	6807835	1962			X	X		X		X	X
12-DMO-241	533398	6807609	1972			X	X		X	X	X	X
12-DMO-242	531600	6809253	1763		X	X	X		X			X

Table 2. *Whole rock compositions from XRF (major elements) and infrared spectroscopy (S, C).*

Sample #	SiO2 %	Al2O3 %	Fe2O3(T) %	MnO %	MgO %	CaO %	Na2O %	K2O %	TiO2 %	P2O5 %	LOI %	Total %	C %	S %	Mg#
12-DMO-190	58.15	21.86	7.29	0.05	1.32	0.22	0.58	4.16	0.96	0.12	3.81	98.56	0.03	0.01	0.29
12-DMO-192	53.65	24.55	8.70	0.18	1.85	0.17	1.08	3.69	0.95	0.13	4.29	99.29	0.02	0.01	0.32
12-DMO-203	59.36	20.22	8.84	0.07	1.97	0.12	0.60	3.43	1.00	0.12	4.00	99.77	< 0.01	< 0.01	0.33
12-DMO-205-2*	40.09	32.81	10.23	0.12	2.54	0.59	0.45	5.68	1.66	0.20	5.03	99.46	0.02	< 0.01	0.37
12-DMO-225-B*	42.00	34.12	7.44	0.09	1.74	0.08	0.54	6.96	1.32	0.06	4.15	98.55	0.03	0.04	0.36
12-DMO-229	49.57	25.34	9.94	0.09	2.26	0.55	2.08	4.41	1.13	0.14	2.98	98.53	0.04	0.12	0.34
12-DMO-231	56.00	22.47	9.14	0.07	2.16	0.40	1.11	3.80	1.08	0.11	2.51	98.89	0.04	0.10	0.35
12-DMO-234A	35.77	35.59	14.72	0.14	3.43	0.21	0.20	3.96	1.95	0.16	3.04	99.25	0.07	0.03	0.35
12-DMO-241	52.12	24.57	8.46	0.05	1.70	0.28	0.89	5.26	1.26	0.10	4.31	99.06	0.26	0.10	0.33
12-DMO-242	40.15	33.43	12.54	0.11	2.91	0.54	1.29	4.28	1.57	0.11	2.35	99.34	0.04	0.07	0.35

Mg# = Mg/(Mg+Fe) in KFMASH
***adjacent to veins, not typical metapelite**

In the low grade area, outside of the contact aureole, metapelite is phyllitic and comprises fine-grained muscovite, chlorite, quartz, ilmenite, and other minor phases. Aligned muscovite and chlorite define a penetrative cleavage; chlorite also forms rounded, slightly elongate porphyroblasts approximately 0.1 mm long (Fig. 4a). The contact aureole includes a phyllitic outer part and a yellow-weathering, hornfelsic inner part. The outer margin of the aureole is marked by the first appearance of small, sparsely distributed spots in the grey phyllite (Fig. 2d). These spots are small porphyroblasts of andalusite and cordierite, whose presence also coincides with the first appearance of tiny biotite crystals (Fig. 4b). Apart from these spots, the rock is similar to phyllites outside the contact aureole, with a well-developed cleavage and phyllitic sheen. With increasing proximity to the pluton, the proportion of chlorite decreases to zero and cordierite, andalusite, and biotite crystals become larger and more abundant (Fig. 4c). Well-preserved cordierite was only observed in a single sample; elsewhere it is pseudomorphed by a fine-grained aggregate rich in chlorite and muscovite. Andalusite is generally partly replaced by muscovite and pokiloblastic, but locally forms well-preserved, idoblastic, inclusion-poor crystals (Fig. 4d). Chlorite-free rocks in the inner parts of the aureole are yellow-brown weathering hornfels with knobbly surfaces due to differential weathering of abundant porphyroblasts (Fig. 2e).

In the outer part of the Crd + And (Chl-free) zone, S_n is discernible but is largely annealed (it does not form a prominent plane of weakness in the rock). In this region, porphyroblasts are superimposed on the matrix foliation (S_n), and there is limited evidence for post-porphyroblast strain in the form of minor deflection of the foliation around porphyroblasts. In most of the Crd + And zone, however, deformation accompanied or post-dated contact metamorphism; cordierite and andalusite porphyroblasts host strain shadows (Fig. 4d), biotite crystals help define the matrix fabric, and curved inclusion trails in andalusite are commonly oblique to, and discontinuous with, the matrix foliation. In well-foliated rocks, micas and deformed pseudomorphs after cordierite define a gently-plunging lineation, approximately parallel to that in the marginal phase of the pluton.

The distance of the And + Crd-in isograd to the pluton contact is approximately 660 m (Fig. 3); however, as the pluton contact dips northeast under this zone, the true thickness is ~270 m (assuming a 40° dip).

The widespread development of Crd + Bt + Ms + Qtz assemblages in the Hyland aureole adjacent to biotite-free, chlorite-bearing phyllites suggests the Crd + And isograd reflects a full-system metamorphic reaction equivalent to the univariant (in KFMASH) reaction:

$$Chl + Ms + Qtz = And + Crd + Bt + H_2O.$$

A single sample with the assemblage Chl + Bt + And + Ms + Qtz on the margin of the aureole suggests the divariant (in KFMASH) reaction:

$$Chl + Ms + Qtz = Bt + And + H_2O.$$

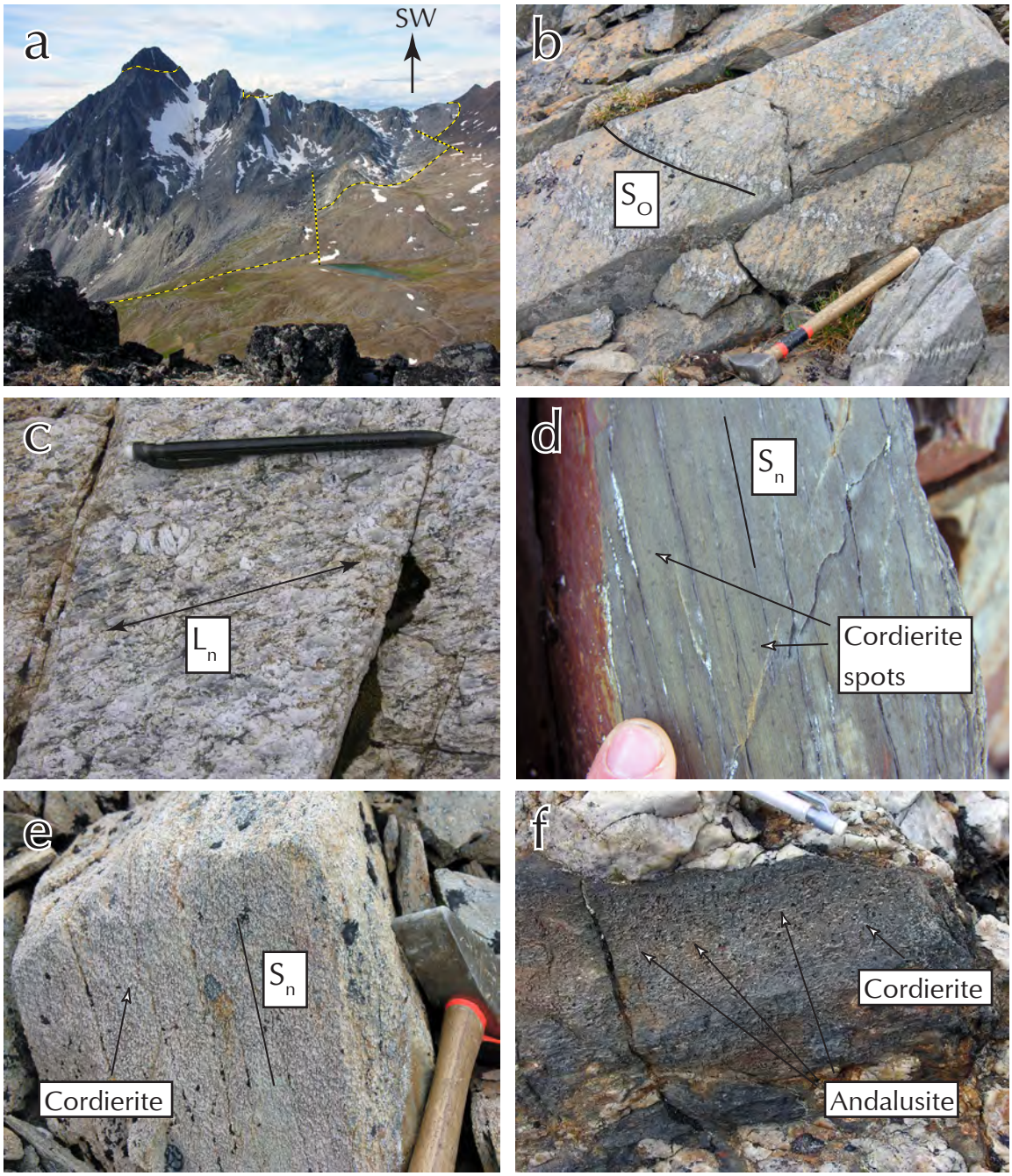

Figure 2. *a) View to the SW towards part of the NE margin of the Hyland pluton. The upper boundary of the pluton dips gently to the NE and is offset by SW-trending faults. Elevation difference between the lake and the peak is approximately 500 m. Pluton outline (long dash) and faults (short dash) are outlined by dashed yellow lines. b) Bedding (S_0) in metasedimentary rock of the Vampire Formation defined by thin, pale grey, fine-grained quartzite layers. The intervening rock is yellow-weathering metapelitic hornfels. Hammer for scale. c) Foliated and lineated, weakly porphyritic marginal phase of the Hyland pluton. The lineation plunges gently to the SE, approximately parallel to the long axis of the intrusion. Pencil for scale. d) Spotted phyllite from the outer part of the contact metamorphic aureole. The rock is a well-cleaved grey phyllite containing scattered small (<1 mm), ovoid cordierite porphyroblasts. Finger for scale. e) Metapelitic hornfels from the inner part of the Boundary pluton aureole. The rock contains abundant mm-scale cordierite porphyroblasts. Foliation is discernible, but the rock is more massive than in regions of lower metamorphic grade. Hammer for scale. f) Elongate andalusite porphyroblasts in metapelite adjacent to a deformed quartz vein. Cordierite is widely developed in the Boundary pluton aureole whereas andalusite is restricted to the margins of veins such as this one. Pencil for scale.*

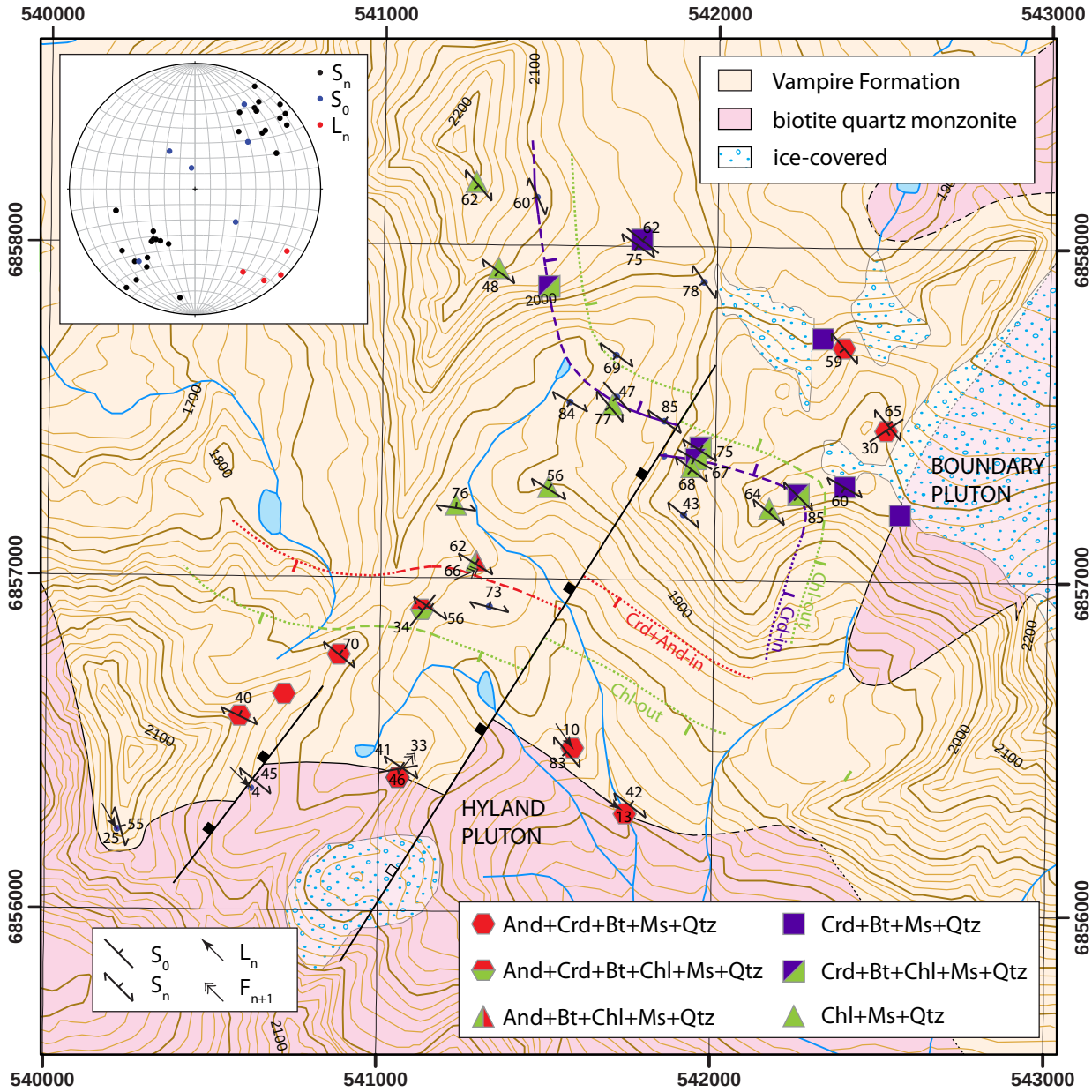

Figure 3. *Map of parts of the Hyland and Boundary plutons and their contact aureoles, showing mineral assemblages and isograds. Structural measurements are compiled on the equal area, lower hemisphere stereonet (inset). Grid lines spaced at 1 km intervals; UTM coordinates are NAD 83.*

BOUNDARY PLUTON CONTACT AUREOLE

The Boundary pluton underlies approximately 9 km^2 on either side of the Yukon-NWT border. It is an equant body with a protrusion on its SW side whose contacts trend SW and dip steeply. The Boundary pluton is an undeformed to weakly deformed biotite quartz monzonite (Streckheisen, 1973) that crosscuts foliation in the country rock (Fig. 8).

The textural changes developed in the Boundary aureole are similar to those described above for the Hyland contact aureole. Unlike the Hyland aureole, however, andalusite is not developed in typical metapelitic rocks. Instead, the assemblage Crd + Bt + Ms + Qtz is widespread, with chlorite also present in the outer parts of the aureole. The distance from the Crd-in isograd to the pluton boundary is approximately 300 m. As is the case in the Hyland aureole, cordierite has been replaced by a fine-grained aggregate rich in chlorite and muscovite.

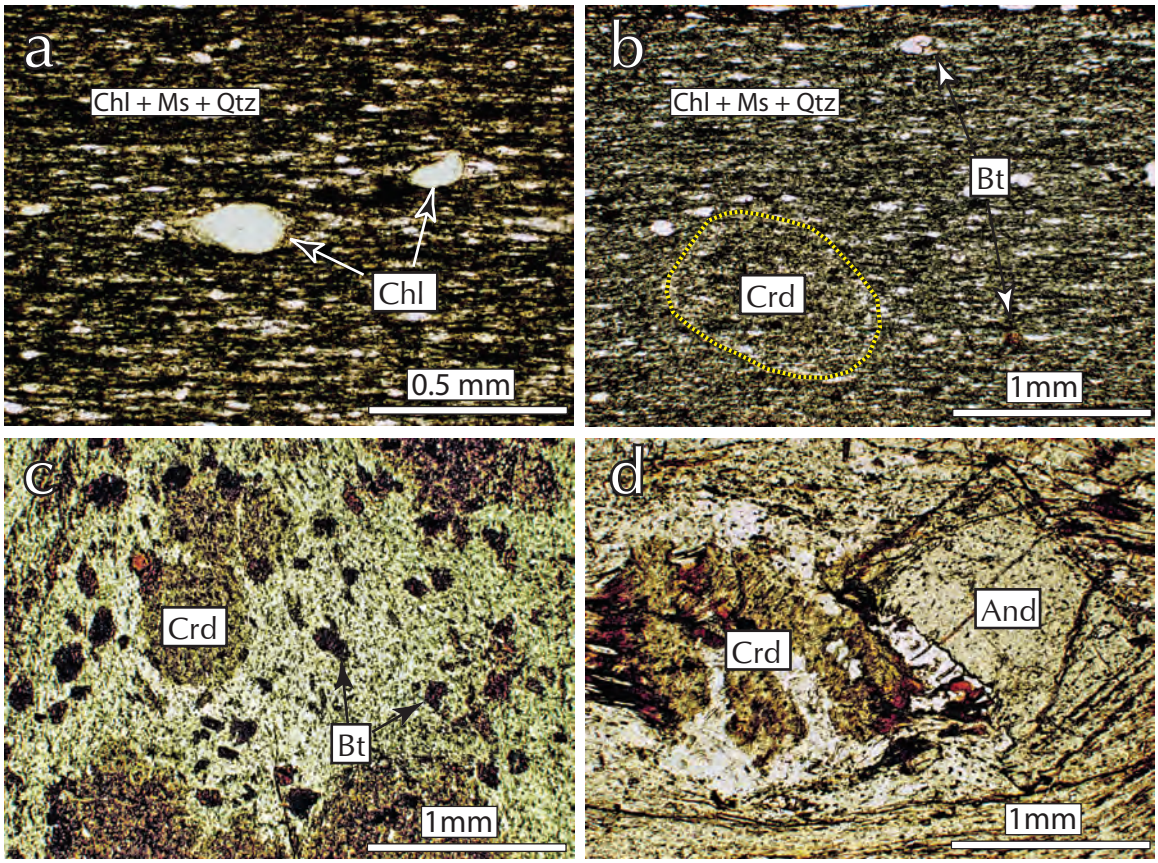

Figure 4. *Photomicrographs of rocks from the contact aureoles of the Hyland and Boundary plutons. All photomicrographs taken in plane polarized light (PPL). a) Phyllite from the low grade area between the Hyland and boundary aureoles. The well-foliated matrix is dominated by fine-grained chlorite, muscovite and quartz, with small rounded chlorite porphyroblasts. b) Spotted phyllite from the outermost part of the Boundary aureole (~at the Crd+Bt isograd). The rock contains sparse, inclusion-rich cordierite porphyroblasts and small biotite crystals. The matrix of the rock is otherwise similar to that outside the aureole, with abundant chlorite. c) Crd+Bt assemblage from the hornfelic inner part of the Boundary aureole. Crd and Bt crystals are larger and more abundant, and there is no primary chlorite. d) Idioblastic andalusite and pseudomorphed cordierite from the Hyland aureole. Syn-kinematic growth is suggested by some wrapping of the porphyroblasts by the matrix but also overgrowth of the matrix foliation (see top of the And crystal).*

There is less evidence for syn-post metamorphic deformation in the Boundary aureole compared with the Hyland aureole. The aureole includes some well-foliated, heavily veined zones but these are uncommon. In general, there is only slight deflection of S_n around cordierite porphyroblasts.

Although andalusite is absent from typical metapelite in the aureole, the assemblage And + Crd + Bt + Ms + Qtz was observed in two locations within the aureole. In each case, andalusite is restricted to a zone of dark grey rock on the margin of deformed quartz veins (Fig. 2f). This rock, which is anomalously Al-rich and Si-poor (12DMO-205-2; Table 2) extends approximately 15 cm from the veins and grades outwards into typical metapelite with a Crd + Bt (And-free) assemblage.

The Crd-in isograd does not conform to the map outline of the Boundary pluton. Instead, an extensive region of Crd + Bt hornfels is developed in the area to the west of the pluton. This suggests that the Boundary pluton extends underneath this region, or that erosion has removed igneous rock from above the land surface.

In the Boundary aureole, the development of the metamorphic assemblage Crd + Bt from Chl + Ms-bearing phyllites suggests a reaction with the form:

$$Chl + Ms + Qtz = Crd + Bt + H_2O$$

(Divariant in KFMASH).

PRESSURE-TEMPERATURE CONDITIONS, HYLAND AND BOUNDARY AUREOLES

The assemblages Crd + Bt + Ms + Qtz and And + Crd + Bt + Ms + Qtz indicate metamorphism at intermediate temperatures and low pressure. The P-T stability range of each of these assemblages is illustrated using an equilibrium assemblage diagram, constructed using a mean composition representative of the Vampire Formation (Fig. 5a). For this composition, And + Crd + Bt + Ms + Qtz is predicted to form in the pressure range 2.5-3 kbar, whereas Crd + Bt + Ms + Qtz assemblages indicate P<~2.5 kbar.

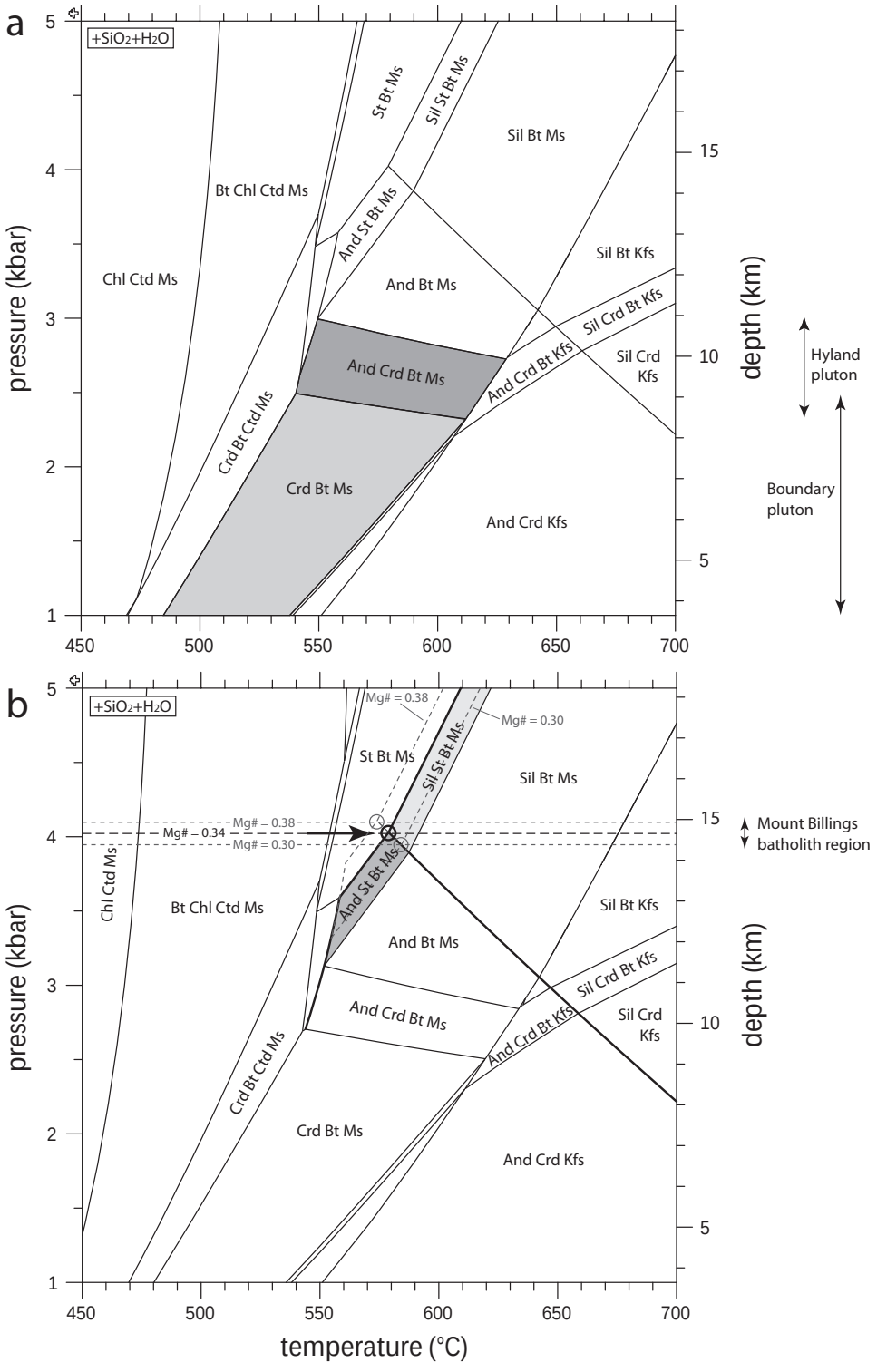

Figure 5. *a) Equilibrium assemblage diagram for the composition representing the mean of three Vampire Fm metapelite samples (Mg/(Mg+Fe)=0.32). b) Equilibrium assemblage diagram for the composition representing the mean of 3 muscovite-bearing Hyland Group metapelites (Mg/(Mg+Fe) = 0.34). The Al_2SiO_5-in and the And-Sil phase boundaries are marked with thick lines. In most rocks, andalusite grew directly from staurolite, but in some samples staurolite breakdown produced sillimanite. This suggests the pressure during metamorphism is approximated by the position of the intersection between the Al_2SiO_5-in and the And-Sil boundaries (~4 kbar, ~15 km depth). The position of the Al_2SiO_5-in boundary is also shown for two modified compositions with Mg/(Mg+Fe) of 0.30 and 0.38, respectively (dashed lines); these compositions were derived by varying the Fe:Mg ratio while keeping values for other elements unchanged. These Mg/(Mg+Fe) values were chosen arbitrarily to illustrate the effect of variation in bulk composition on the P-T position of the intersection between the Al_2SiO_5-in and And-Sil boundaries. See text for discussion.*

Whereas the Hyland aureole contains the assemblage And + Crd + Bt + Ms + Qtz, the Boundary aureole lacks andalusite. This difference can be explained by either a difference in pressure (depth of intrusion), or by a systematic difference in the bulk composition of the host rocks. For a fixed pressure, the andalusite-bearing assemblage is favoured by more Fe and Al-rich compositions. In this case, the close proximity of the isograds in the same phyllite suggests a difference in pressure is the most plausible explanation for the lack of andalusite in the metapelite of the Boundary pluton. A systematic difference in composition is unlikely, as the plutons were intruded across a folded rock sequence and even small, non-systematic differences would complicate a simple trend. The suggestion that the Boundary pluton was intruded at a slightly higher level than the Hyland pluton is compatible with the semi-concordant nature of the Hyland pluton and the higher degree of deformation recorded in the pluton and its aureole.

All of the samples from the Vampire Formation that were analysed by XRF are high-Al metapelites that plot above the garnet-chlorite tie line on an AFM diagram (Fig. 6). Chloritoid is predicted to be stable at low metamorphic grade for each of these measured bulk rock compositions (Fig. 5), but is not present in low-grade rocks between the two contact aureoles. This discrepancy may reflect inadequacies in the projection scheme (Fig. 6), and/or the thermodynamic data and solutions models used (Fig. 5); alternatively, it may indicate relative enrichment in Al due to mass transfer during metamorphism (Ague, 1991). Another possibility, that the low-grade rocks had significantly different primary compositions compared with those within the aureoles, is unlikely.

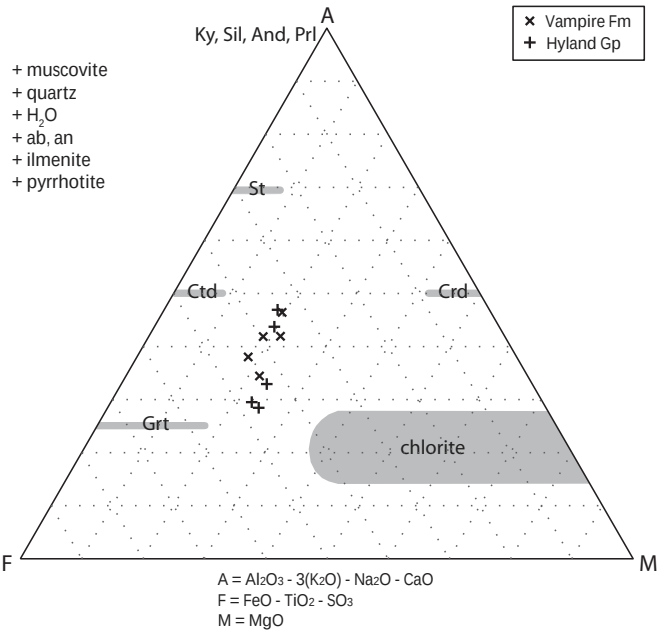

Figure 6. *AFM diagram showing all analysed samples. Mg/(Mg+Fe) in typical metapelite ranges from 0.29-0.34. Samples are projected from end-member muscovite, quartz, H_2O, albite, anorthite, ilmenite, and pyrrhotite. Mineral fields from Spear (1993). Biotite plots below the diagram as it has negative A values.*

METAMORPHISM OF THE HYLAND GROUP EAST OF THE MOUNT BILLINGS BATHOLITH

The second area studied in detail is located northeast of the Mount Billings batholith (Area 2; Fig. 1). This area lies within an extensive region of schist and gneiss that mantles the Logan batholith and the eastern side of the Mount Billings batholith (Roots *et al.*, 1966). Structures in this schist-gneiss belt are discordant with the regional trend and many intrusions have complex border zones up to 400 m wide which contain a mixture of migmatite and inclusions of country rock (*ibid*). Heffernan (2004) reported a U-Pb zircon crystallization age of 106.4 ± 0.4 Ma from the Mount Billings batholith and three U-Pb monazite crystallization ages from the Logan batholith in the range 101-106 Ma.

The country rock, which is assigned to the Hyland Group by Gordey and Makepeace (2003), comprises a monotonous sequence of pelitic and semipelitic schist (Fig. 7a). The schist is pale brownish-yellow with a rusty brown weathering colour. Foliation in the schist dips 20-40° to the southeast and a mineral lineation plunges southeast, approximately down the dip of the foliation. The mineral lineation is defined by mica, and most conspicuously, sillimanite. Locally, crenulations with the same orientation as the mineral lineation are also developed. Compositional layering is generally parallel to the foliation, and high strain is indicated by the presence of rootless isoclinal folds with axial planes parallel to the foliation. These fabrics are crosscut by a weakly deformed biotite granodiorite intrusion of presumed mid-Cretaceous age (northeast corner of Figure 8) and similar smaller bodies. They are also cut by dikes of unfoliated quartz-feldspar porphyry (Fig. 7d) and fine-grained, amphibolite bearing mafic dikes.

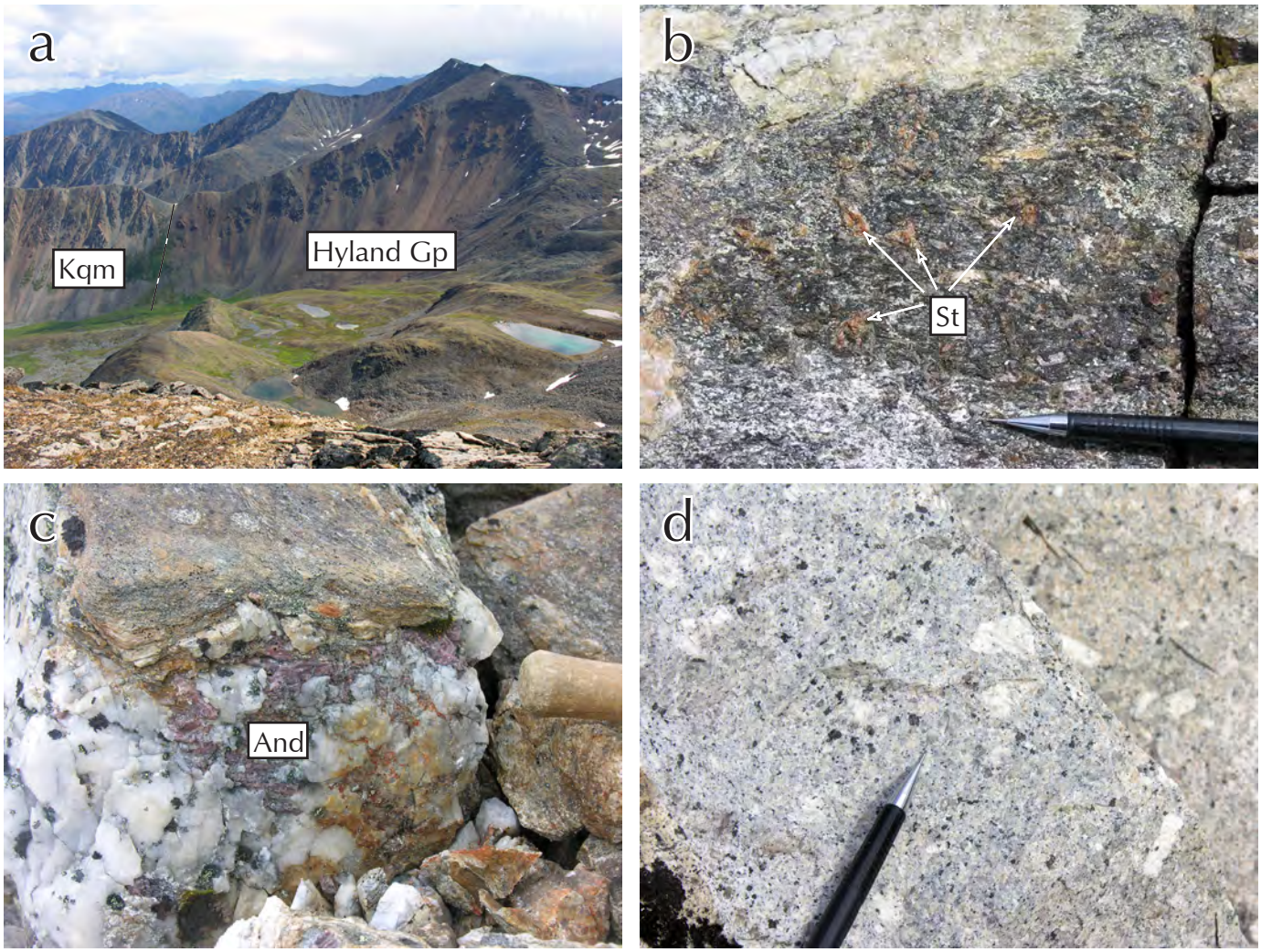

Figure 7. *a) View south towards the contact between rusty brown metapelite of the Hyland Group and a quartz monzonite intrusion of presumed mid-Cretaceous age. The foliation/lineation in the Hyland Group is truncated by the intrusion. Elevation difference between the valley bottom and the peak on the right hand side is approximately 200 m. b) Prominent honey-brown staurolite porphyroblasts in metapelitic schist. Metapelitic rocks in the area also typically contain andalusite, biotite, quartz, plagioclase ± sillimanite ± muscovite ± garnet. Pencil for scale. c) Vein composed of quartz and pink andalusite. Quartz-andalusite veins are common in the metapelitic schists and are deformed within the dominant foliation. Hammer handle for scale. d) Quartz-feldspar porphyry dike that crosscuts the foliation/lineation in metapelitic schists. Phenocrysts of euhedral to corroded quartz, plagioclase, K-feldspar and chloritized mafic phenocrysts sit in a fine-grained quartzofeldspathic matrix. Pencil for scale.*

Metapelitic schists in the area contain Qtz + Plag + Bt + Ilm + St + Al_2SiO_5(Sil and/or And) ± Ms ± Grt ± Sp (Table 1; Figs. 7b and 9). Staurolite forms porphyroblasts with irregular, embayed margins and is generally surrounded by a mantle of andalusite (Fig. 9b,d). In samples that lack andalusite but contain sillimanite (n=4), staurolite is rimmed by muscovite that is generally aligned parallel to S_n (Fig. 9c). Larger staurolite crystals are commonly twinned. Andalusite typically forms large blocky crystals, many with one or more staurolite inclusions. Andalusite is commonly pokiloblastic (Fig. 9d), and in some cases forms extensive, optically continuous, net-textured sheets parallel to compositional layering. Some crystals display pink segments, particularly in their cores (Fig. 9a). In two samples, green spinel is included within andalusite adjacent to embayed staurolite inclusions. Sillimanite occurs in the form of fibrolite in and/or around crystals of biotite (Fig. 9e). Garnet is present in small quantities in some rocks; crystals are generally small and have irregular, embayed margins (Fig. 9f).

The schistosity (S_n) is defined by preferentially aligned biotite and, where present, sillimanite and/or muscovite. Staurolite and andalusite contain inclusion trails, and andalusite crystals are wrapped by S_n. These observations indicate that deformation took place during the growth of staurolite, andalusite, and sillimanite.

Deformed quartz veins hosted by metapelitic schist commonly contain large, zoned crystals of pink andalusite (Fig. 7c). These veins locally crosscut the schistosity but are generally elongated parallel to the schistosity and wrapped by it; this suggests that the veining accompanied formation of S_n.

Metapelites throughout the study area contain andalusite; in contrast, sillimanite is restricted to its northwest part. The orientation of the sillimanite isograd is largely unconstrained due to the location of sampling sites (Fig. 8). Peak metamorphism is not related to the granodiorite body (of presumed mid-Cretaceous age) in the northeast part of the area because the syn-metamorphic schistosity is cut by this intrusion.

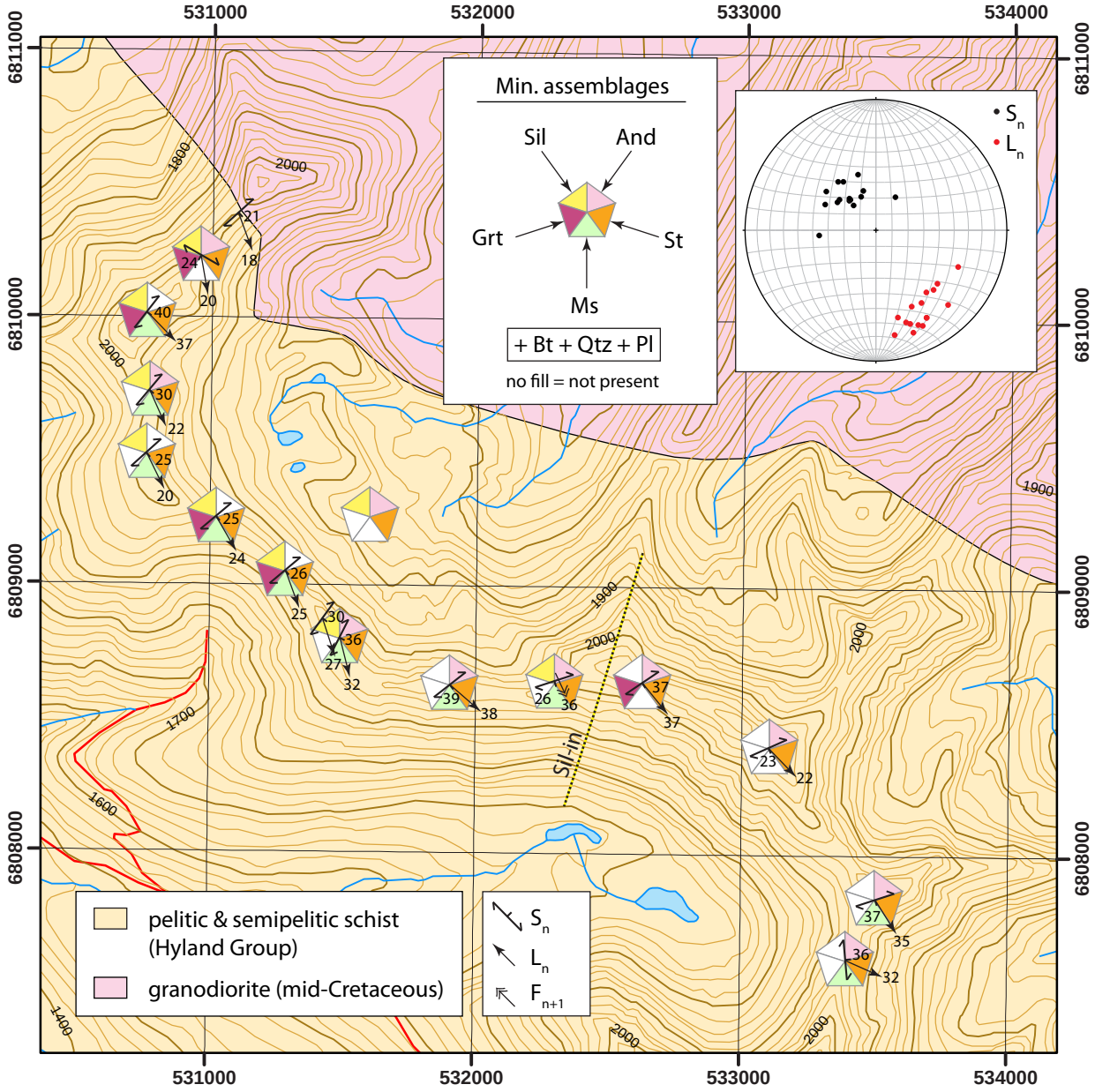

Figure 8. *Map of Area 2, east of the Mount Billings batholith showing mineral assemblages. Structural measurements are compiled on the equal area, lower hemisphere stereonet (inset). Grid lines spaced at 1 km intervals; UTM coordinates are NAD 83.*

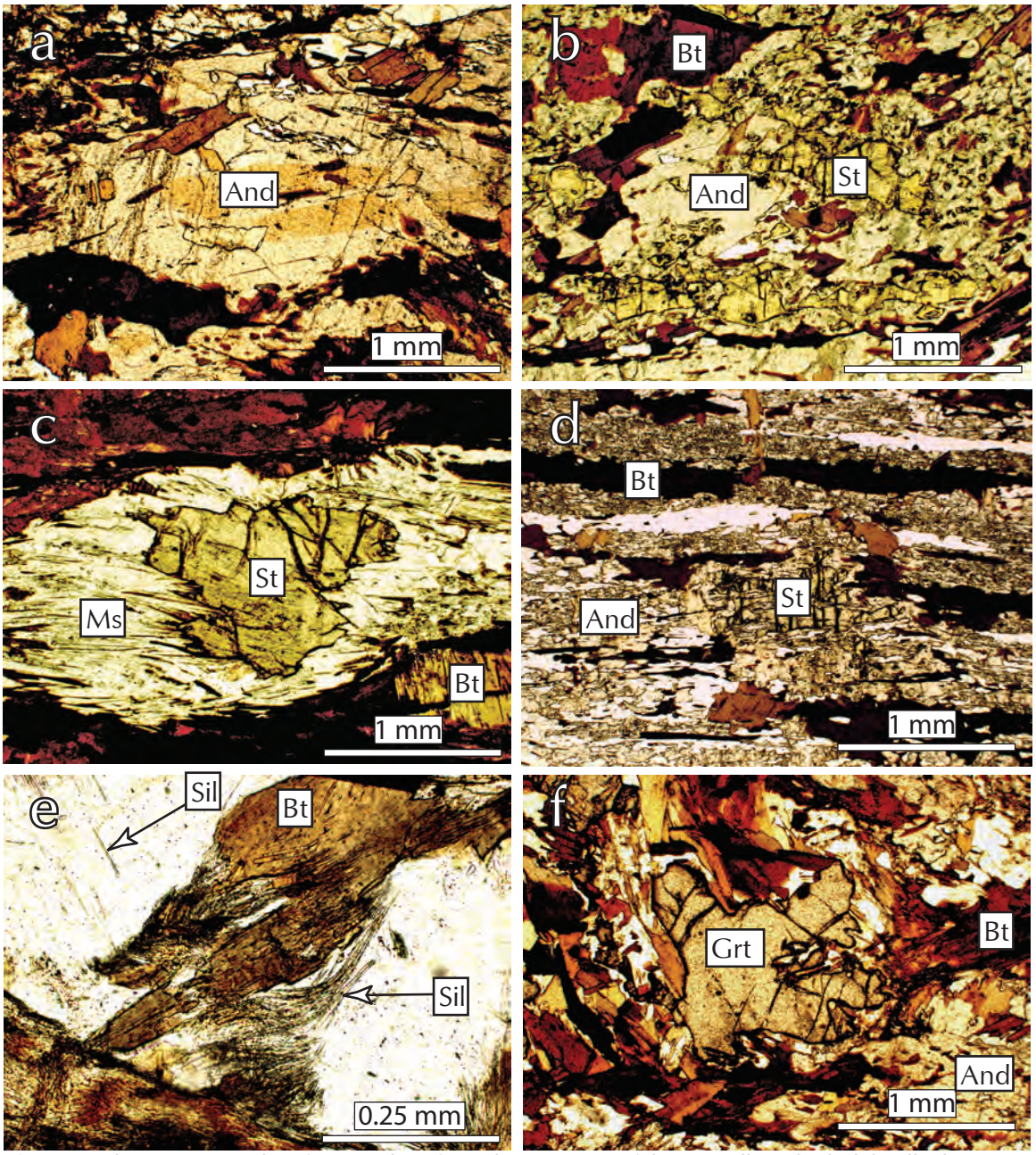

Figure 9. *Photomicrographs of metapelites from the area east of the Mt. Billings batholith, all taken in PPL. a) Andalusite displaying pink core and colourless rim. b) Embayed staurolite remnants surrounded by andalusite. c) Staurolite surrounded by a reaction rim of muscovite. d) Poikiloblastic andalusite with staurolite inclusion. e) Fibrolitic sillimanite on biotite and as inclusions in quartz. f) Embayed garnet crystal in metapelitic schist. Garnet is a minor constituent or is absent from schists in the area.*

REACTION HISTORY AND PRESSURE-TEMPERATURE CONDITIONS

Metapelites in Area 2 have low-variance assemblages and contain abundant non-equilibrium textures. Two Al_2SiO_5 polymorphs are present in most samples and staurolite is generally only preserved where mantled by andalusite, or locally muscovite.

The assemblage And + St + Bt + Ms, which occurs in the southeastern part of the area, is stable at intermediate temperatures (~550-575 °C) at a pressure of 3-4 kbar (Fig. 5b). Andalusite is predicted to grow at the expense of staurolite with increasing temperature in this field, and its high-T boundary marks the point at which staurolite is fully consumed. St + And (Sil-free) samples may have

reached their peak temperature in the And + St field, but the fact that staurolite occurs solely as inclusions in andalusite leaves open the possibility that staurolite was preserved above its predicted upper temperature limit as a result of its isolation from the remainder of the rock. In this case, the St + And field represents a lower bound on peak temperature conditions. The presence of sillimanite in otherwise similar samples from the northwest part of the area demonstrates further heating after St + And growth. The widespread preservation of andalusite in this area, in schists and quartz veins, suggests that the And-Sil boundary was not greatly overstepped. Significantly higher temperatures (T>625-650 °C) are ruled out by the widespread occurrence of the sub-assemblage Ms + Qtz (Fig. 5b).

In samples that contain sillimanite but lack andalusite, staurolite is surrounded by pseudomorphous aggregates of muscovite. This muscovite is aligned in the plane of S_n and there is no evidence that the muscovite is a late retrograde phase, or other evidence for retrogression in the rock (no replacement of minerals such as biotite or garnet). The muscovite pseudomorphs are interpreted to have formed during growth of sillimanite from staurolite breakdown, as described by Guidotti (1968). Rocks in the area thus contain evidence for independent growth of andalusite and sillimanite during staurolite breakdown.

Aluminosilicate growth from staurolite breakdown is accounted for by a whole rock equivalent of the divariant KFMASH metamorphic reaction:

$$St + Ms + Qtz = Al_2SiO_5 + Bt + H_2O$$

Garnet is also present in some samples and may be a product of a similar (univariant in KFMASH) reaction.

The Al_2SiO_5-producing reaction intersects the polymorphic transition:

$$And = Sil$$

at approximately 4 kbar (Fig. 5b). Above this pressure sillimanite is predicted to grow at the expense of staurolite whereas below this pressure andalusite is produced. This intersection is equivalent to the boundary between bathozones 2-3 of Carmichael (1978), and facies series 2B-3 of Pattison and Tracy (1991). The evidence for independent growth of andalusite and sillimanite from staurolite within the small area studied suggests that the pressure coincided with this intersection at or close to the peak metamorphic temperature (Fig. 5b). The spatial overlap of samples with different reaction histories can be accounted for by small variations in bulk composition (Fig. 5b). The intersection point between the Al_2SiO_5-producing reaction and the And-Sil boundary occurs at a slightly higher pressure in rocks with a relatively high bulk rock Mg/(Mg + Fe) (Fig. 5b). Growth of sillimanite directly from staurolite breakdown is therefore favoured by relatively Fe-rich bulk compositions, while andalusite growth is predicted in more Mg-rich rocks at the same pressure. Similarly, the intersection point occurs at a slightly higher pressure in Al-rich rocks.

DISCUSSION

The sensitivity of mineral assemblages in metapelites to small differences in pressure within the andalusite stability field facilitates recognition of otherwise indistinguishable contrasts in the depths of metamorphism. While the absolute depths implied by these mineral assemblages are subject to ongoing refinement to thermodynamic databases and activity models, the relative depths implied by the assemblages are well established (*cf.*, Pattison and Vogl, 2005).

The Hyland pluton was intruded late syn-kinematically at 97.1 Ma and, based on its And + Crd-bearing aureole assemblage, was emplaced at ~2.5-3 kbar, equivalent to a depth of ~9-11 km. The absence of andalusite from metapelite in the aureole of the Boundary pluton suggests it was intruded at <~9 km, though a meaningful lower depth limit is not provided by the And + Crd assemblage. The largely post-kinematic nature of the Boundary pluton, combined with the evidence in favour of a lower emplacement depth suggests that the Boundary pluton is slightly younger than the Hyland pluton; however, there is insufficient geochronological data to test this interpretation. A general point, applicable to metapelites here and elsewhere is that, whereas rocks with Crd + Bt-bearing aureoles may be prospective for shallow-level mineralizing processes, the presence of andalusite in metapelite typically indicates a greater depth of emplacement.

Staurolite ± andalusite ± sillimanite-bearing assemblages in the area to the east of the *ca.* 106 Ma Mount Billings batholith record metamorphism at ~4 kbar, equivalent to a depth of ~15 km. The spatial pattern, whereby amphibolite-facies rocks are restricted to the margins of the Mount Billings and Logan batholiths suggests low-pressure metamorphism in this area is related to plutonism, as does the reported presence of migmatite along batholith-country rock boundaries. This interpretation conflicts with that of Roots *et al.* (1966), who suggested

that syn-kinematic metamorphism was unrelated to Cretaceous plutonism and took place prior to deposition of the Devonian-Mississippian Earn Group, rocks belonging to which are "essentially non-schistose".

Mapping is required to establish the spatial and timing relationships among deformation, metamorphism, and plutonism in the area. While Roots *et al.* (1966) provided no indication that rocks of the Mt. Billings batholith are deformed, according to Archibald *et al.* (1982) they are at least locally foliated. The high strain that accompanied heating is not typical of contact metamorphism, but regional deformation, burial, and radiogenic heating alone generally cannot account for the elevated geothermal gradient required for low-pressure, amphibolite-facies metamorphism (England and Thompson, 1984). Whereas structures outside this belt follow the NW-NNW orogenic trend, structures in the schist/gneiss have more variable orientations (Roots *et al.*, 1966), and in the area studied, the foliation is orogen-perpendicular. The timing relationships between medium-grade fabrics and low grade structures outside this belt remain to be determined, as does the tectonic significance of the metamorphic and structural variation.

ACKNOWLEDGEMENTS

Thanks to Nikollet Kovacs for assistance in the field, and to Terralogic Ltd. who provided logistical support for the field work. Doug Tinkham (Laurentian University) translated the thermodynamic data base and solution models of Spear and Pyle (2010) into a form compatible with Theriak/Domino. Thanks to Lee Pigage for reviewing the manuscript and suggesting improvements.

REFERENCES

Ague, J.J., 1991. Evidence for major mass transfer and volume strain during regional metamorphism of pelites. Geology, vol. 19, p. 855-858.

Archibald, D., James, D., and Toohey, J., 1982. The Hyland pluton Tungsten prospect, Tuna claim group, NTS 105H/16. Energy, Mines and Resources, Government of Yukon, Assessment Report 091014.

Blusson, S.L., 1968. Geology and tungsten deposits near the headwaters of Flat River, Yukon, and southwest District of MacKenzie, Canada. Geological Survey of Canada, Paper 67-22, 77 p.

Carmichael, D.M., 1978. Metamorphic bathozones and bathograds: a measure of the depth of post-metamorphic uplift and erosion on the regional scale. American Journal of Science, vol. 278, p. 769-797.

de Capitani, C. and Brown, T.H., 1987. The computation of chemical equilibrium in complex systems containing non-ideal solutions. Geochimica et Cosmochimica Acta, vol. 51, p. 2639-2652.

de Capitani, C. and Petrakakis, K., 2010. The computation of equilibrium assemblage diagrams with Theriak/Domino software. American Mineralogist, vol. 95, p. 1006-1016.

England, P.S. and Thompson, A.B., 1984. Pressure-temperature-time paths of regional metamorphism I. Heat transfer during the evolution of regions of thickened continental crust. Journal of Petrology, vol. 24, p. 894-928.

Gordey, S.P. and Anderson, R.G., 1993. Evolution of the Northern Cordilleran Miogeocline, Nahanni map area (105I), Yukon and Northwest Territories. Geological Survey of Canada, Memoir 428, 214 p.

Gordey, S.P. and Makepeace, A.J. (comp.), 2003. Yukon Digital Geology (version 2). Geological Survey of Canada Open File 1749 and Yukon Geological Survey, Open File 2003-9(D), 2 CD-ROMs.

Guidotti, C.V., 1968. Prograde muscovite pseudomorphs after staurolite in the Rangeley-Oquossoc areas, Maine. American Mineralogist, vol. 53, p. 1368-1376.

Hart, C.J.R., Goldfarb, R.J., Lewis, L.L., and Mair, J.L., 2004. The Northern Cordillera mid-Cretaceous plutonic province: ilmenite/magnetite-series granitoids and intrusion-related mineralisation. Resource Geology, vol. 54, p. 253-280.

Hart, C.J.R. and Lewis, L.L., 2006. Gold mineralization in the upper Hyland River area: A non-magmatic origin. *In:* Yukon Exploration and Geology 2005, D.S. Emond, G.D. Bradshaw, L.L. Lewis and L.H. Weston (eds.), Yukon Geological Survey, p. 109-125.

Heffernan, S., 2004. Temporal, geochemical, isotopic and metallogenic studies of mid-Cretaceous magmatism in the Tintina gold province, southeastern Yukon and southwestern Northwest Territories. Unpublished MSc thesis, University of British Columbia, Vancouver, British Columbia, Canada, 83 p.

Kretz, R., 1983. Symbols for rock-forming minerals. American Mineralogist, vol. 68, p. 277-279.

MacLeod, W.A., 1982. Cal 81-144 mining claims, Watson Lake mining district, 105H/8W. Energy, Mines and Resources, Government of Yukon, Assessment Report 090867.

Pattison, D.R.M. and Tracy, R.J., 1991. Phase equilibria and thermobarometry of metapelites. *In*: Contact metamorphism, D.M. Kerrick (ed.), Reviews in Mineralogy, vol. 26, p. 105-206.

Pattison, D.R.M. and Vogl, J.J., 2005. Contrasting sequences of metapelitic mineral-assemblages in the aureole of the tilted Nelson batholith, British Columbia: implications for phase equilibria and pressure determination in andalusite-sillimanite-type settings. The Canadian Mineralogist, vol. 43, p. 51-88.

Rasmussen, K.L., Mortensen, J.K., and Falck, H., 2006. Geochronological and lithogeochemical studies of intrusive rocks in the Nahanni region, southwestern Northwest Territories and southeastern Yukon. *In:* Yukon Exploration and Geology 2005, D.S. Emond, G.D. Bradshaw, L.L. Lewis, and L.H. Weston (eds.), Yukon Geological Survey, p. 287-298.

Read, P.B., Woodsworth, G.J., Greenwood, H.J., Ghent, E.D., and Evenchick, C.A., 1991. Metamorphic Map of the Canadian Cordillera, Geological Survey of Canada, "A" Series Map 1714A, scale 1:2 000 000.

Roots, E.F., Green, L.H., Roddick, J.A., and Blusson, S.L., 1966. Geology, Frances Lake, Yukon Territory and District of Mackenzie. Geological Survey of Canada, Preliminary Map 6-1966, 1:253440 scale.

Spear, F.S., 1993. Metamorphic phase equilibria and pressure-temperature-time paths. Mineralogical Society of America Monograph, 799 p.

Spear, F.S. and Pyle, J. M., 2010. Theoretical modelling of monazite growth in a low-Ca metapelite. Chemical Geology, vol. 273, p. 111-119.

Strekheisen, A.L., 1973. Plutonic rocks – classification and nomenclature recommended by the IUGS's subdivision on the systematics of igneous rocks. Geotimes, vol. 18, p. 26-30.

Field-portable x-ray fluorescence spectrometer use in volcanogenic massive sulphide exploration with examples from the Touleary occurrence (MINFILE Occurrence 115O 176) in west-central Yukon

Patrick J. Sack[1], Lara L. Lewis
Yukon Geological Survey, Whitehorse, YT

Sack, P.J. and Lewis, L., 2013. Field-portable x-ray fluorescence spectrometer use in volcanogenic massive sulphide exploration with examples from the Touleary occurence (MINFILE Occurrence 115O 176) in west-central Yukon. *In:* Yukon Exploration and Geology 2012, K.E. MacFarlane, M.G. Nordling, and P.J. Sack (eds.), Yukon Geological Survey, p. 115-131.

ABSTRACT

Field-portable x-ray fluorescence analysers (pXRF) are becoming a common tool in the savvy mineral explorer's tool kit. Benefits include portability and ease of use, real-time acquisition of XRF data with minimal processing, immediate availability and analysis of data in the field, and a reasonably large number of elements that can be measured reliably. The findings indicate that data for 15 elements obtained with an Innov-X Omega pXRF analyser (2010 version) correlate well with lithogeochemical whole-rock analyses with R^2 values generally ≥0.7. The difference in elemental abundances between pXRF analyses of thin section off-cuts (a proxy for drill core) and pulps from the whole-rock analyses are generally ±35%, indicating that no sample preparation is needed for the rock samples analysed in this study. The uncorrected pXRF values of some elements can be very similar to whole-rock analytical abundances; however, it is recommended that uncorrected pXRF data only be used semi-quantitatively, such as for downhole elemental plots in which relative patterns or trends are more informative than individual data points. For more sophisticated plots such as those combining elements into ratios to form alteration indices, corrected pXRF data should be used. The pXRF data are also adequate for construction of simple volcanic composition plots that can be used to aid in identification of protolith compositions of altered samples. The pXRF is well suited to volcanogenic massive sulphide exploration as the analytical data obtained from drill core (using thin section off-cuts as a proxy) are comparable to whole-rock analyses and the range of immobile and mobile, major and trace elements should be versatile enough for most exploration programs. However, pXRF shouldn't be viewed as a replacement to traditional whole-rock geochemical methods.

[1]*patrick.sack@gov.yk.ca*

INTRODUCTION

Field-portable x-ray fluorescence analyzers (pXRF) are proving to be a valuable tool for exploration as they are portable, simple to use, can simultaneously analyse over 20 elements, and depending on conditions, can produce meaningful results (Peter *et al.*, 2009). As part of a larger project investigating the recently discovered Touleary volcanogenic massive sulphide (VMS) occurrence (MINFILE Occurrence 115O 176), 15 samples of diamond drill core were analysed using both traditional laboratory whole-rock lithogeochemical and pXRF analytical methods; both thin section off-cuts (a proxy for cut diamond drill core) and the pulps from the whole-rock geochemical samples were analysed with the pXRF. The goal of the pXRF study was to evaluate the precision and accuracy of such analyses against those of traditional whole-rock methods, determine if sample preparation (off-cuts vs. pulps) is important, and evaluate the usefulness of the pXRF for VMS exploration.

GEOLOGY

The Touleary occurrence (63°0′24.48″N, 139°8′11.85″W) is located within Yukon-Tanana terrane rocks, approximately 125 km south of Dawson City (Fig. 1). The occurrence is located between the north and south forks of Kirkman Creek in a fault-bound block of southeast dipping amphibolite schist/gneiss metabasites interlayered with minor metafelsite (Ryan and Gordey, 2001a,b).

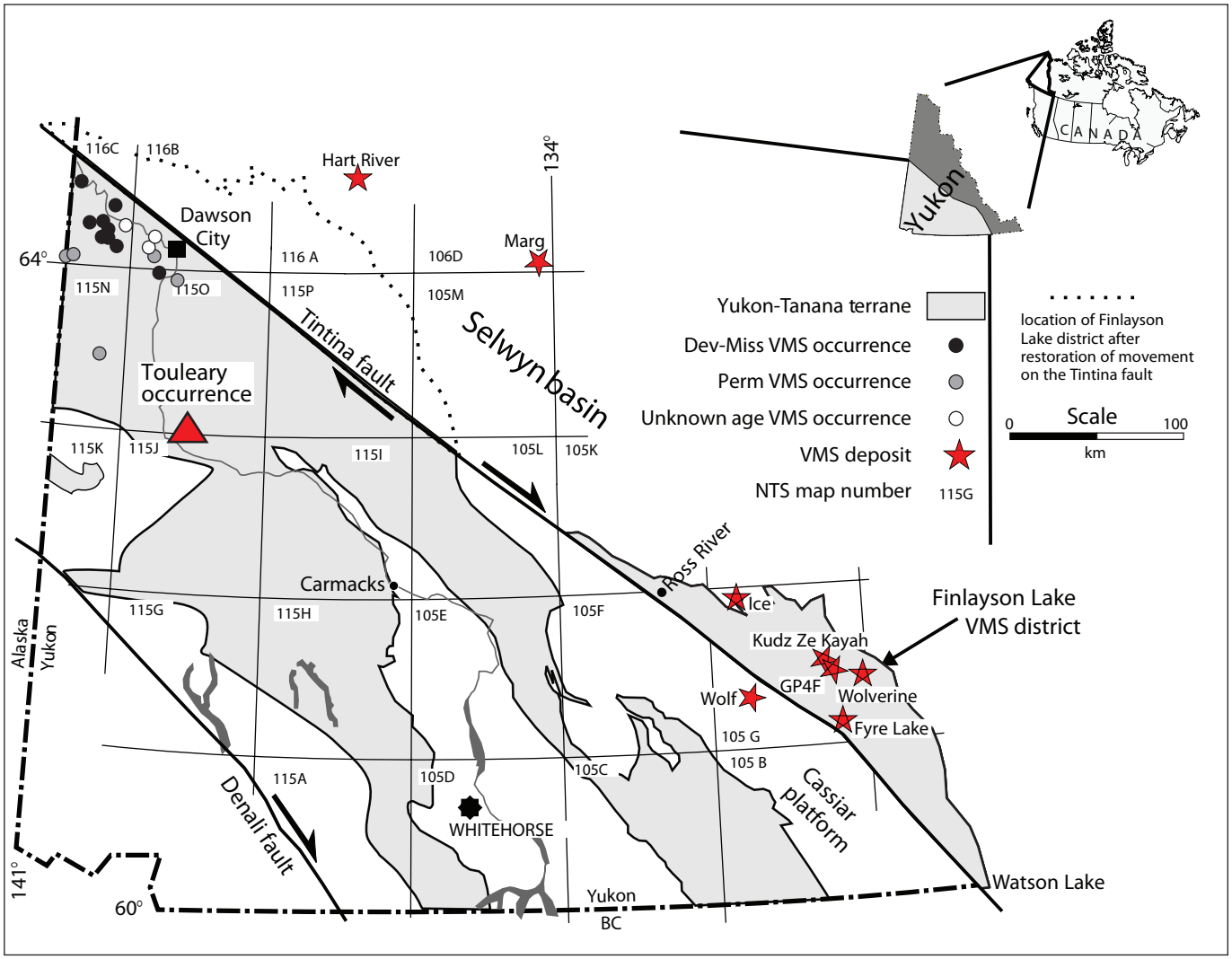

Figure 1. *Location of significant VMS deposits in Yukon and VMS occurrences in the Dawson City area (modified from Hunt, 2002). Also shown are the locations of the Yukon-Tanana terrane (YTT), the Finlayson Lake VMS district, and the approximate location of the Finlayson Lake VMS district after restoration of movement along the Tintina fault. Dev-Miss = Late Devonian to mid-Mississippian VMS occurrences, Perm = Permian VMS occurrences; based on Hunt (2002).*

Intense regional deformation and garnet amphibolite-facies metamorphism have hindered identification of the protolith of these rocks; however, they are interpreted to be of volcanic and volcaniclastic origin. The interfingering of metabasite and metafelsite suggests a bimodal nature, possibly in an arc setting (Ryan and Gordey, 2001a,b). These rocks are thought to be Devonian to Mississippian in age (Gordey and Ryan, 2005) and may correlate with rocks of a similar age in the Finlayson Lake VMS district (Fig. 1). However, several plutonic and hypabyssal rocks in the vicinity of the study area have yielded only Permian ages; therefore, it is also possible that these metavolcanic rocks are correlative locally with the Permian Klondike Schist in the Dawson Range near the Boulevard mineral occurrence, 24 km southwest of Touleary (J. Ryan, pers. comm., 2012).

SUMMARY OF DIAMOND DRILL CORE LOGGING

Diamond drilling in 2011 by Arcus Development Group Inc. targeted a linear magnetic low anomaly that is coincident with the contact between mafic schist (Unit 8) and amphibolite (Unit 6) on the map of Ryan and Gordey (2001a) (H. Burrell, pers. comm., 2012). This drilling intersected stratiform, semi-massive to massive sulphide mineralization dominated by pyrite and chalcopyrite. The 15 samples used in this study are from diamond drill hole TL11-05 that cored two semi-massive to massive sulphide intersections. The upper intersection is 2.25 m, grading 7.2% Cu, 116 g/t Ag, 3.6 g/t Au, and 4.3% Zn; the lower is 14.15 m thick and grades 1.4% Cu, 17 g/t Ag, 0.8 g/t Au, and 0.3% Zn (Arcus news release, October 4, 2011). Hydrothermal alteration is characterized by an intense quartz + pyrite ± sericite assemblage below mineralization that gradually transitions to chlorite ± sericite above and below mineralization. The nature of mineralization, alteration, and the host volcanic rocks are consistent with Touleary having a volcanogenic massive sulphide genetic origin.

Diamond drill hole TL11-05 is 246.28 m long with bedrock intersected at 3.0 m. The rocks are fine to coarse-grained schist with a grain size typically ranging from 0.5 mm to 5 mm; a few crystals can be larger than 1 cm. Layering, where present, is thin to thick (1 cm to 50 cm) and likely represents both primary features (bedding) and metamorphic features. Figure 2 shows a graphic lithologic log with accompanying photos and a log of the dominant hydrothermal alteration minerals. The rocks are commonly pale to dark green and are dominated by chlorite ± muscovite; garnet porphyroblasts up to 1 cm are common in places. The rock textures are heavily modified by hydrothermal alteration and subsequent regional metamorphism and deformation. Most primary textures have been destroyed; however, these rocks are interpreted to have a volcanic and volcaniclastic origin. Based on rock textures and mineralogy the succession is divided into two series: 1) an upper massive to weakly stratified, pale green felsic volcanic series and 2) a lower, thinly to thickly layered dark green mafic volcanic series (Fig. 6).

ANALYTICAL METHODS

WHOLE-ROCK METHODS

Diamond drill core samples were split and only fresh rock free of oxidized surfaces were submitted for analysis. Whole-rock analyses were conducted at Activation Laboratories Ltd., Ancaster, Ontario, using their 4Lithoresearch analytical package, a lithium metaborate/tetraborate fusion followed by analysis using Inductively Coupled Plasma Mass Spectrometry (ICPMS). For major elements, the quality of these data meets or exceeds fusion x-ray fluorescence data. For trace elements, the fusion process provides total dissolution of refractory minerals such as zircon, sphene, and monazite, and gives accurate rare earth and high field strength element data. Using this analytical package, detection limits for major elements are 0.001% to 0.01% and trace elements are typically better than 1 ppm. However, in order to lower detection limits for As, Au, Br, Cr, Ir, Sc, and Se, these elements were analysed by Instrumental Neutron Activation Analysis (INAA), and for Cd, Cu, Ni, S, and Zn, a multi-acid digestion followed by ICPMS analysis was used. A complete list of elements, analytical method and respective detection limits is reported in Table 1.

PXRF METHODS

The hand-held pXRF analyzer used in this study is an Innov-X Omega analyser manufactured by Innov-X-Systems Inc. (now Olympus Corporation) that was purchased in 2010. This instrument is equipped with a silver anode x-ray tube that operates at 40 kV and a maximum of 4 watts with a silicon positive-intrinsic negative (SiPIN) detector. The SiPIN detector technology has now been surpassed by silicon drift detectors (SDD) that have better detection limits; however, pXRF with SiPIN detectors are still common and are less expensive than SDD models.

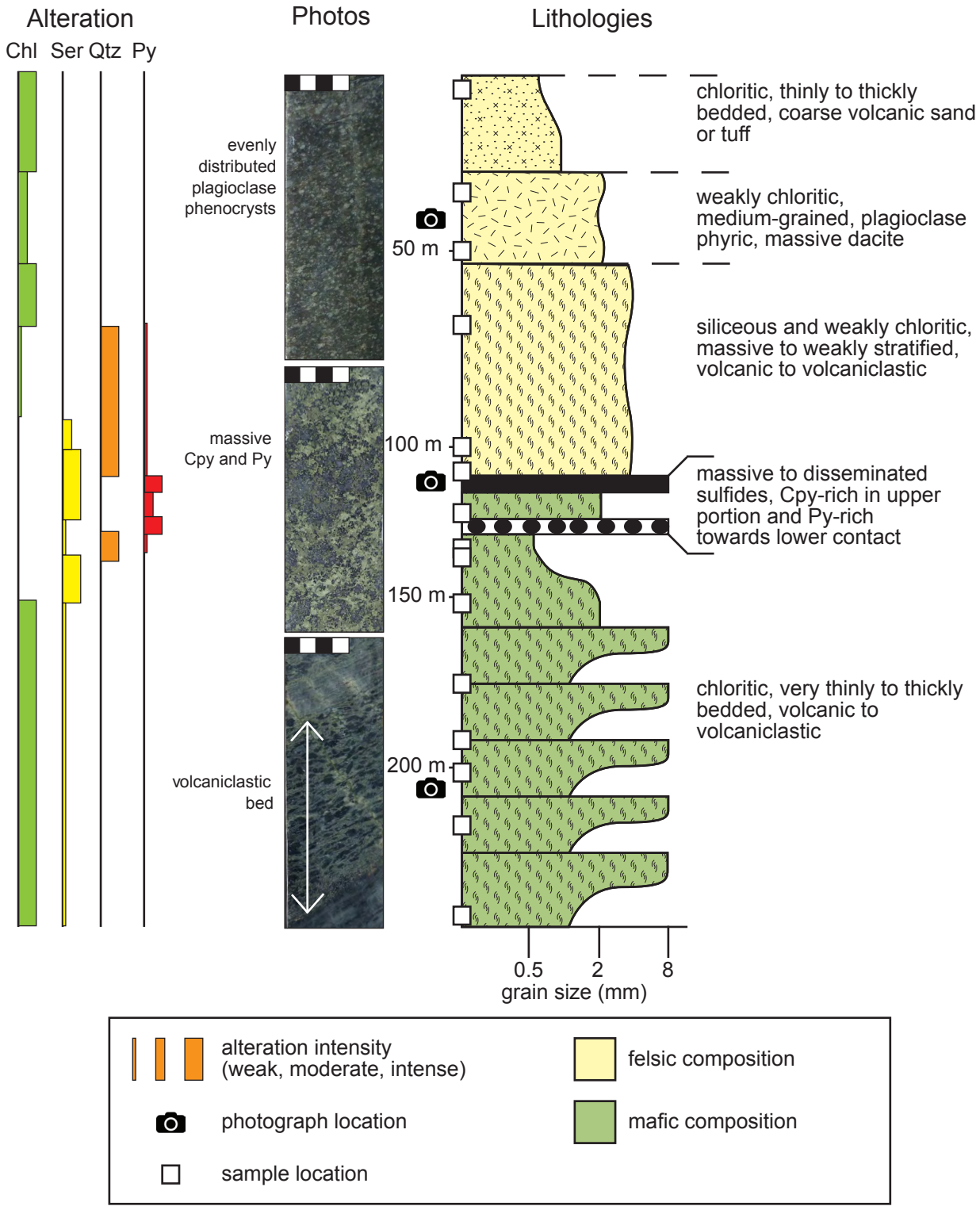

Figure 2. *Graphic log of TL11-05 with representative photos and a log of visual alteration mineralogy and intensity. Scale bars in photos are cm divisions. Chl = chlorite, Ser = sericite, Qtz = quartz, Py = pyrite, and Cpy = chalcopyrite. Composition based on Ti /Zr vs. Nb/Y (Winchester and Floyd, 1977) using whole-rock data.*

Table 1. *Detection limits (in ppm except major oxides) for elements analysed by Activation Laboratories Ltd. using whole-rock methods described in text. White = fusion digestion, light grey = INAA, and dark grey = multi-acid digestion.*

Element	Detection Limit	Element	Detection Limit
Al2O3	0.01%	Rb	1
CaO	0.01%	S	100
Fe2O3	0.01%	Sb	0.2
K2O	0.01%	Sc	0.1
MgO	0.01%	Se	3
MnO	0.001%	Sn	1
Na2O	0.01%	Sr	2
P2O5	0.01%	Ta	0.01
SiO2	0.01%	Th	0.05
TiO2	0.001%	Tl	0.05
Ag	0.5	U	0.01
As	0.5	V	5
Au	0.002	W	0.5
Ba	3	Y	0.5
Be	1	Zn	1
Bi	0.1	Zr	1
Br	0.5	La	0.05
Cd	0.5	Ce	0.05
Co	1	Pr	0.01
Cr	5	Nd	0.05
Cs	0.1	Sm	0.01
Cu	10	Eu	0.005
Ga	1	Gd	0.01
Ge	0.5	Tb	0.01
Hf	0.1	Dy	0.01
In	0.1	Ho	0.01
Ir	0.005	Er	0.01
Mo	2	Tm	0.005
Nb	0.2	Yb	0.01
Ni	1	Lu	0.002
Pb	5		

The pXRF is capable of measuring elements with atomic numbers between 15 (phosphorus) and 82 (lead), excluding the lanthanide elements and noble gases (Fig. 3). The pXRF analyses were conducted in 'soil mode', which is a two-beam mode employing an internal Compton Normalization calibration. This mode is optimized for sample types with a predominantly light element matrix (*e.g.*, soils, tills, and rocks) and has detection levels between 5 and 200 ppm with the exception of P and Al which are 0.5% and 1.0% respectively (Innov-X-Systems, 2009). Each analysis was two minutes in total with one minute using beam 1 conditions (heavy option: Ti and heavier elements) and one minute using beam 2 (light and transition elements: Fe and lighter elements).

Samples in this study were collected in the field and analysed with the pXRF in Whitehorse. Thin section off-cuts (minimum 5 mm thick) were dried and analysed such that the analyser window was oriented perpendicular to foliation, giving a cross sectional analysis not confined to a single foliation surface. The analysing window was positioned on a visually representative, fine-grained portion of the off-cut, avoiding unrepresentative features such as porphyroblasts. Pulps from the laboratory geochemical samples and a diorite gneiss Canadian Certified Reference Material pulp (SY-4) were compacted to form a compressed sample at least 5 mm thick as recommended by the manufacturer (Innov-X-Systems, 2009); three different spots were analysed through the plastic sample bag and the results were averaged for each element; no correction was made for potential contamination from the sample bags.

To evaluate the reliability of the data for each element, the pXRF off-cut and pulp data were plotted against the laboratory whole-rock data and the slope of a best fit line through the data and its corresponding coefficient of determination (R^2) and y-intercept value were calculated. Elements with a strong coefficient of determination ($R^2 \geq 0.7$) are deemed reliable and are corrected using the slope and intercept of the line of best fit to the pulp data (Table 2).

RESULTS

Geochemical studies of VMS deposits tend to utilize elements useful for determining primary geochemical features (immobile elements) or alteration geochemical features (mobile elements) (*e.g.*, Barrett *et al.*, 1993; Chapman *et al.*, 2009; Large *et al.*, 2001; MacLean and Barrett, 1993; Mireku and Stanley, 2006). In consideration of both element mobility (Pearce, 1996) and the element range possible with the pXRF used, the focus was on the following immobile elements: Ti, V, Cr, Y, Zr, and Nb; elements with variable behaviour (mobile to immobile): P, Mn, Fe, Ni, As, Sn, and Sb; and mobile elements: K, Ca, Cu, Zn, Rb, Sr, Ba, Au, and Pb (Fig. 3). In the discussion, variable and mobile elements are grouped into a single category. For both immobile and mobile elements, R^2 of

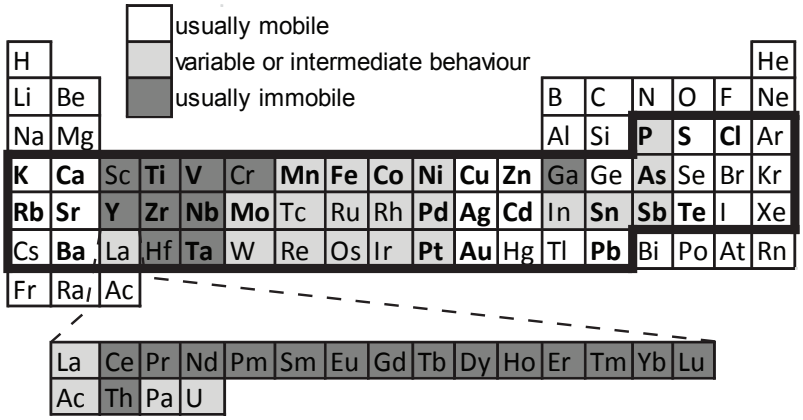

Figure 3. *Periodic table with elements coded according to mobility during alteration (modified from Pearce, 1996). Outline shows the range of elements that can be analysed with the pXRF analyser used in this study. Elements in bold are those included in the 'soil mode'.*

the pulp data is generally slightly higher than that for the thin section off-cut data; ascribed as a subtle nugget effect in the off-cuts that is nullified in the pulps when they are pulverized and homogenized. However, the difference between pXRF analytical data for thin section off-cuts (a proxy for drill core) and pulps from the whole-rock analyses is generally ≤35%, indicating that no sample preparation is needed for the rock samples analysed in this study. Whole-rock and pXRF (raw and corrected) data are included, respectively, in Appendices 1 and 2.

IMMOBILE ELEMENTS

The immobile elements Ti, V, Cr, Y, Zr, and Nb are part of the pXRF analytical package used (Fig. 3). Figure 4 a-e shows the correlation between the laboratory whole-rock and pXRF analyses of both pulps and thin section off-cuts, and Table 2 summarizes elemental variations for all three sets of analyses. For both pulps and off-cuts, Ti, Zr, Y, and Cr have $R^2 \geq 0.7$, suggesting good correlation between the data for the two pXRF sample types and between pXRF and whole-rock data. Vanadium has R^2 of 0.07 and 0.05 for pulps and off-cuts, respectively, as a result of interference with Ba when laboratory whole-rock Ba values are >2000 ppm. Nb values determined by laboratory whole-rock analysis range between 1 and 17 ppm, and this is below the pXRF lower limit of detection (20 ppm) which is too high to be of use in this study. Of the six immobile elements investigated in this study, only Ti and Zr are routinely above detection in pXRF analyses of thin section off-cuts with good determination coefficients (Table 2).

MOBILE ELEMENTS

Figure 5 a-f shows the correlation between selected whole-rock and pXRF analyses of both pulps and thin section off-cuts. Data from precious metals Au and Ag are not usable as the pXRF detection limit for Au is 10 ppm, much too high to be of use in this study, and the Ag anode in the analyser used causes over estimation of Ag. Nickel, chlorine, and niobium can be analysed on the pXRF used in this study, but their abundances in the samples studied are below the lower limits of detection (*e.g.*, Ni ranges from 2 to 39 ppm in whole-rock analyses, but was not detected in off-cuts). Cadmium, phosphorus, tin, and tantalum all have $R^2<0.5$ and slopes ranging from -0.01 to +7.36 demonstrating that these elements are poorly correlated and cannot be corrected using a linear correction. The following elements are found to have good determination coefficients (mostly ≥0.7): As, Ba, Ca, Co, Cu, Fe, K, Mn, Pb, Rb, S, and Sr (Table 2).

DISCUSSION

The primary aim of this study was to evaluate the utility of determining gross lithogeochemical characteristics in the field, such as mobile element variation due to hydrothermal alteration. For this purpose, a simple approach to the treatment of the pXRF data has been devised: 1) a focus on elements with high determination coefficients ($R^2 \geq 0.7$) that can be corrected using a simple linear equation of a best fit line; 2) major element data in this paper are elemental rather than in oxide form as is the norm in whole-rock data sets; and 3) focusing only on simple geochemical features that should be robust enough for preliminary interpretations. More sensitive uses, such as tectonic discrimination diagrams and alkalinity diagrams, are better suited to high-quality laboratory whole-rock data.

IMMOBILE ELEMENTS AND IGNEOUS COMPOSITION

Volcanogenic massive sulphide deposits commonly have spatially and temporally associated zones of hydrothermally altered host rocks that have obscured primary protolith textures and compositions (Gifkins *et al.*, 2005; Ishikawa *et al.*, 1976; Newberry *et al.*, 1989). Thus, a common application of whole-rock lithogeochemical data is the identification of precursor volcanic rock type

Table 2. *Summary of elemental data collected with ICP and pXRF. Elements shaded grey are determined to be reliable and are the focus of discussion. All elements are in ppm except Au which is in ppb. N = number of samples above detection limit. BD = below lower limit of detection. NA = no analysis. R^2, slope, and intercept values are calculated using the equation of a line of best fit through the whole-rock data versus the pulp or thin section off-cut data.*

Elements	Whole-rock ICP		pXRF (pulps)					pXRF (thin section off-cut)				
	Range	N	Range	N	R^2	slope	intercept	Range	N	R^2	slope	intercept
Ag	BD - 1.7	1	104 - 240	15	NA	NA	NA	114 - 283	15	NA	NA	NA
As	BD - 16.5	9	BD - 60	11	0.63	0.31	1.70	BD - 17	11	0.59	1.03	0.24
Au	BD - 412	4	1000 - 19000	15	0.29	NA	NA	BD - 14000	14	0.16	NA	NA
Ba	52 - 4702	15	237 - 2939	15	0.81	1.45	128	220 - 3238	15	0.87	1.58	51
Ca	357 - 59606	15	BD - 58013	14	0.97	1.11	3168	BD - 95467	13	0.83	0.61	7241
Cd	BD - 0.9	5	BD - 30	13	0.46	0.01	0.25	4 - 63	15	0.19	-0.01	0.57
Cl	NA	0	BD	0	NA	NA	NA	BD	0	NA	NA	NA
Co	1 - 31	15	107 - 1332	15	0.75	0.02	-2.90	151 - 1077	15	0.59	0.02	-0.61
Cr	BD - 252	6	7 - 207	15	0.93	1.32	-40	BD - 192	14	0.94	1.38	-28
Cu	2 - 7430	15	BD - 7895	5	1.00	0.94	-5	BD - 7184	4	1.00	1.03	21
Fe	31614 - 166324	15	13013 - 73121	15	0.96	2.11	13287	9060 - 91830	15	0.67	1.42	46148
K	2075 - 25818	15	1490 - 22932	15	0.96	1.06	1931	3486 - 24177	15	0.90	0.90	1176
Mn	50 - 1321	15	79 - 1418	15	0.98	1.00	-22	20 - 1865	15	0.68	0.74	224
Mo	BD - 14	3	2 - 5	15	0.57	0.38	1.17	BD - 24	6	0.50	0.33	1.57
Nb	1 - 17	15	BD	0	NA	NA	NA	BD	0	NA	NA	NA
Ni	2 - 39	15	BD	0	NA	NA	NA	BD	0	NA	NA	NA
P	87 - 698	15	BD - 15577	8	0.06	-0.01	456	517 - 33025	15	0.04	0.01	362
Pb	BD - 230	14	11 - 356	15	0.93	0.68	-0.86	8 - 313	15	0.83	0.83	3.34
Pd	NA	0	BD - 394	13	NA	NA	NA	BD - 77	9	NA	NA	NA
Pt	NA	0	BD - 37	5	NA	NA	NA	BD - 17	6	NA	NA	NA
Rb	2 - 61	15	6 - 72	15	0.88	0.67	8.53	1 - 94	15	0.81	0.81	5.47
S	150 - 73700	15	BD - 32340	8	0.95	2.41	2444	BD - 64612	8	0.96	1.11	1757
Sb	BD - 19.5	6	BD - 20	4	0.04	0.18	1.60	BD - 4	3	NA	NA	NA
Sn	BD - 4	10	BD - 48	14	0.00	7.36	1.63	BD - 31	9	0.32	0.06	1.14
Sr	26 - 499	15	27 - 481	15	0.92	1.01	-7	22 - 502	15	0.94	0.88	23
Ta	BD - 1	14	5 - 13	15	0.37	0.01	0.07	2 - 63	15	0.23	0.01	0.17
Te	NA	0	BD - 44	5	NA	NA	NA	BD 32	4	NA	NA	NA
Ti	1280 - 6685	15	1422 - 5508	15	0.88	1.11	72	1809 - 5703	15	0.68	0.91	672
V	12 - 371	15	45 - 343	15	0.07	0.29	57	34 - 523	15	0.05	0.16	75
Y	10 - 64	15	BD - 365	8	0.66	0.17	0	BD - 337	7	0.71	0.09	32
Zn	33 - 245	15	27 - 545	15	0.78	0.42	55	22 - 169	15	0.18	0.68	61
Zr	51 - 296	15	62 - 572	15	0.87	0.83	2	60 - 362	15	0.80	0.49	75

(*e.g.*, Barrett *et al.*, 1993; MacLean and Barrett, 1993). The pXRF immobile element data can be used to classify volcanic compositions, however, trace element discriminant diagrams require laboratory quality data and a diverse array of elements such as Ti, Zr, Ta, Th, Nb, Yb, and Y (*e.g.*, Barrett and MacLean, 1999; Ross and Bedard, 2009). In the pXRF element suite, Ti and Zr are the most suitable, having reasonable determination coefficients and both are present in abundances above the lower limits of detection in all samples.

To aid in the field identification of volcanic compositions, the Zr/Ti boundary between the rhyolite+dacite and andesite+basaltic andesite fields were converted on the Zr/Ti *vs.* Nb/Y diagram, revised from Winchester and Floyd (1977) in Pearce (1996), into Ti *vs.* Zr space (Fig. 6). With the exception of one highly altered sample proximal to massive sulphide, this modified diagram adequately separates the lower mafic and upper felsic rocks and there are no major differences between pXRF data obtained from off-cuts and whole-rock data (Fig. 6).

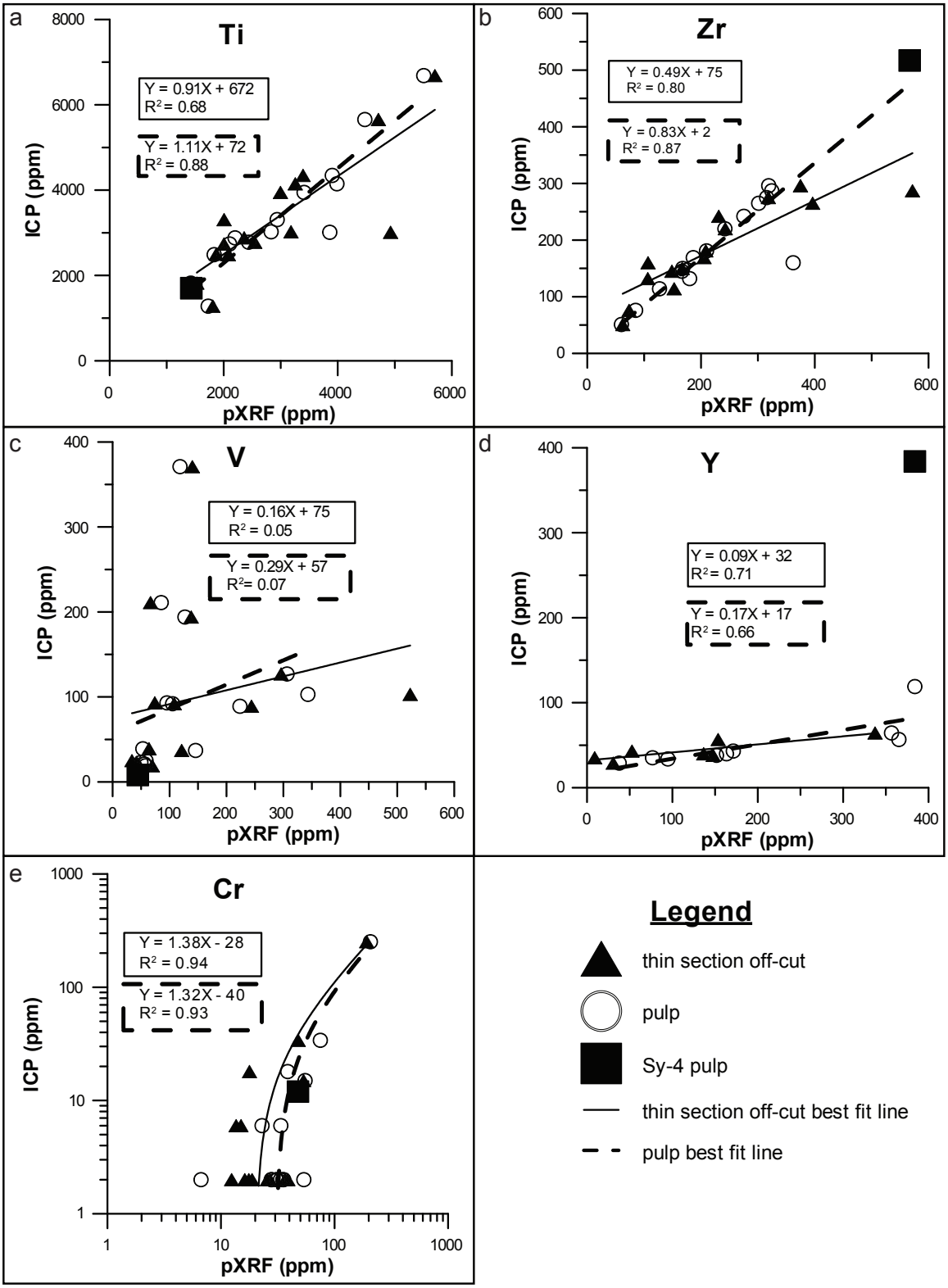

Figure 4. *Immobile element correlation plots of pXRF data (pulps and thin section off-cuts) versus laboratory ICP whole-rock data. Square symbol is a sample of Canadian Certified Reference Material SY-4, a diorite gneiss pulp.*

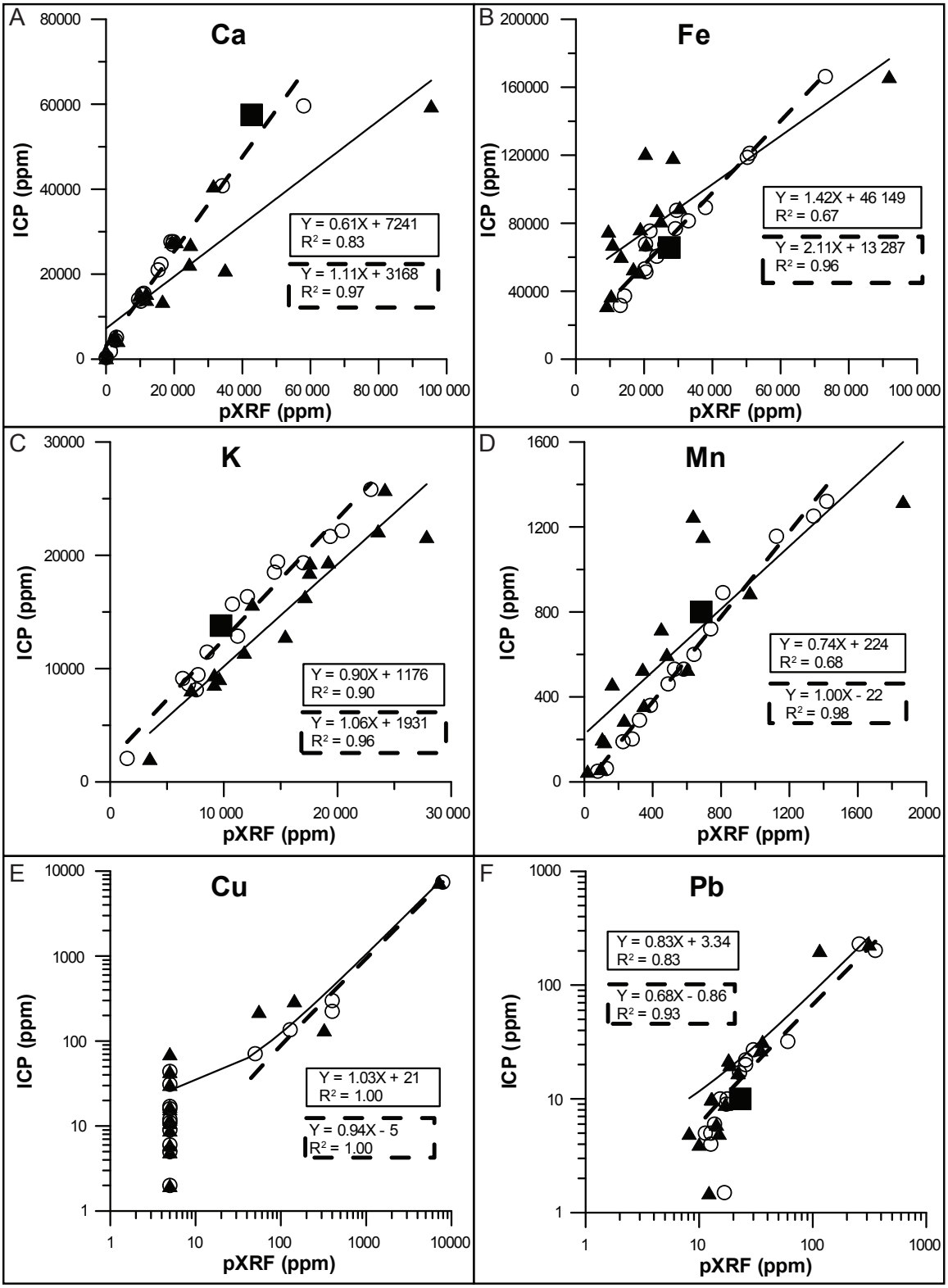

Figure 5. *Selected mobile element correlation plots of pXRF data (pulps and thin section off-cuts) versus laboratory whole-rock data. Square symbol is a sample of Canadian Certified Reference Material SY-4, a diorite gneiss pulp. Legend same as Figure 4.*

Based on this, it can be concluded that the diagram can be used as a composition discriminant to reliably separate felsic and mafic compositions. Finer subdivisions, such as intermediate compositions, require a more complete element suite and data with lower limits of detection.

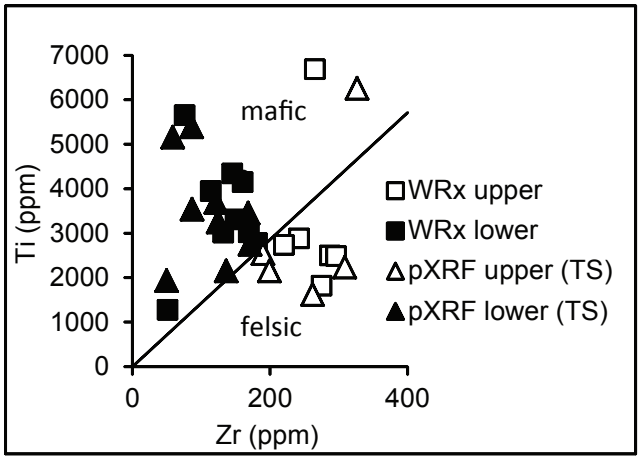

Figure 6. *Ti vs. Zr plot revised from Winchester and Floyd (1977) in Pearce (1996) using whole-rock (squares) and corrected pXRF (triangles) data from thin section off-cuts of diamond drill hole TL11-05.*

MOBILE ELEMENTS AND ALTERATION

The real-time acquisition of pXRF geochemical data in the field allows for optimization of strategies and plans. To demonstrate the usefulness of the pXRF in quantifying and mapping alteration geochemical signatures, elements that are mobile during hydrothermal alteration and traditionally employed by explorationists are evaluated using laboratory whole-rock analyses. Simple downhole plots of elements can commonly show geochemical trends relating to alteration that vary with proximity to mineralization (Gifkins *et al.*, 2005; Peter *et al.*, 2009). The data show that As, Ba, Ca, Co, Cu, Fe, K, Mn, Pb, Rb, S, and Sr mostly have good coefficients of determination ($R^2 \geq 0.7$) between both pXRF and laboratory whole-rock data. These elements are not universally present in abundances above their lower limits of detection, but because their distributions are an indicator of hydrothermal alteration intensity, abundances below the lower limits of detection are informative. The downhole patterns of both uncorrected pXRF and laboratory whole-rock data are similar for all 11 of the mobile elements mentioned above; however, the absolute values can be up to an order of magnitude different. Thus, for pXRF users who wish to use uncorrected analytical data obtained directly from the instrument, using the pXRF semi-quantitatively is recommended, such that abundance variation patterns for adjacent samples are more important than individual data values. Figure 7 shows selected downhole plots illustrating the changes in the alteration index (AI; Ishikawa *et al.*, 1976), Ca, Mn, and Pb against lithology and visually determined predominant hydrothermal alteration mineralogy. These plots reflect both lithology and alteration with the AI, Ca, and Pb plots, clearly showing geochemical anomalies proximal to mineralization.

To define alteration trends and visualize them, the alteration box plot of Large *et al.* (2001) was modified using elements deemed to be reliably determined with the pXRF. The alteration box plot of Large *et al.* (2001) plots the chlorite-carbonate-pyrite index (CCPI; see below) versus the alteration index (AI; see below) of Ishikawa *et al.* (1976). The CCPI measures the destruction and replacement of albite, K-feldspar, and sericite with Mg-Fe chlorite, whereas the AI measures the breakdown and replacement of sodic plagioclase and volcanic glass by sericite and chlorite (Large *et al.*, 2001).

The CCPI of Large *et al.* (2001) is defined as:

$$CCPI = 100(FeO+MnO)/(FeO+MnO+Na_2O+K_2O)$$

The AI of Ishikawa *et al.* (1976) is defined as:

$$AI = 100(MgO+K_2O)/(MgO+K_2O+CaO+Na_2O)$$

Because Na_2O and MgO cannot be analysed with the pXRF used, the AI formula was adapted by removing these elements. Removal of Na means the index under estimates albitic alteration (a diagenetic trend) and removal of Mg likely results in an under estimation of chlorite alteration (a hydrothermal trend) (Large *et al.*, 2001). This modified formula tends to slightly overestimate the AI value of a sample (Fig. 8). In the modified CCPI formula, Ca is assumed to have a similar behaviour to Na. The formulas modified for utilization of the pXRF data are:

$$AI = 100(K)/(K+Ca)$$

$$CCPI = 100(Fe+Mn)/(Fe+Mn+Ca+K)$$

Figure 8a shows values calculated with laboratory whole-rock data using both the original formulas (diamonds) and the modified formulas (squares). The modified values show similar patterns to the originals with the exception of several analyses from the upper part of the hole, which plot further to the lower left in the direction of diagenetic alteration (see Large *et al.*, 2001 for complete explanation of trends). Patterns to the upper right are similar, and these are the directions of hydrothermal alteration trends. Though the modified formulas slightly over estimate

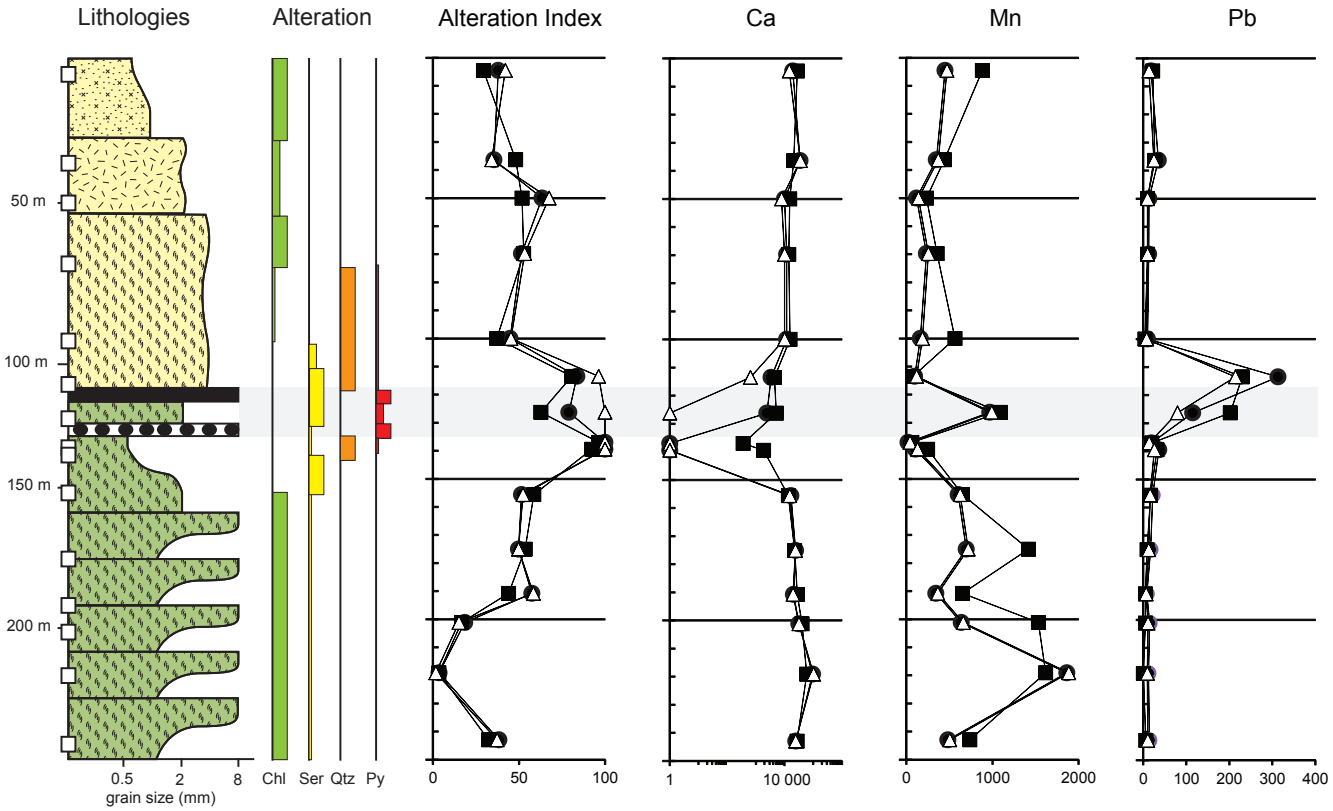

Figure 7. *Graphic log of TL11-05 with representative downhole plots using laboratory whole-rock data (black squares), uncorrected pXRF data (black circles), and corrected pXRF data (white triangles). Ca, Mn, and Pb in ppm. Lithology and alteration legend same as Figure 2, grey is mineralized and highly altered interval.*

AI values, they can be used to monitor the effects of hydrothermal alteration. Figure 8b plots the corrected pXRF analytical data using the modified formulas for thin section off-cuts. These values are similar to those derived from laboratory whole-rock data. Figure 8a and b both show a sericite hydrothermal alteration trend (1), followed by a sericite-chlorite-pyrite alteration trend (2) for the lower volcanic series, whereas the upper volcanic series shows either diagenetic trends (7 and 8) or a carbonate-sericite trend (5). This supports the observations in core that show increasing quartz + pyrite ± sericite underneath mineralization.

CONCLUSIONS

The main goals of this study were to evaluate the accuracy of the pXRF using diamond drill core samples and to evaluate the utility of pXRF generated data for VMS exploration. Portable XRF analyses generally have high determination coefficients ($R^2 \geq 0.7$) with laboratory whole-rock analyses for both pulps and thin section off-cuts and are reliably corrected by applying a linear correction.

Elements such as Cl, Nb, Ni, Pd, and Pt are below the lower limit of detection in all of the pXRF analyses; other elements are above the lower limit of detection but do not correlate well due to poor precision and accuracy as a result of either analyser issues (Ag and Au) or nugget effects (Cd, Mo, P, Sb, and Sn). This study found that pXRF data for off-cuts have slightly lower R^2 values for nearly every reliable element than pXRF data for pulps due to a subtle nugget effect in the off-cuts, but the difference in abundance is commonly ±35%. This study concludes that using diamond drill core (based on off-cuts as a proxy) is reasonable, but an effort must be made to avoid unrepresentative analysis sites (*e.g.*, clasts or phenocrysts). Of the elements available in 'soil mode' on the pXRF used, 13 of them are considered to be particularly suited to VMS exploration. Ti and Zr are reliable and are good discriminators of magmatic fractionation, allowing discrimination of felsic vs. mafic compositions. As, Ba, Ca, Co, Cu, Fe, K, Mn, Pb, Rb, S, and Sr are all reliable and, though not universally present in abundances above their lower limits of detection, their distributions generally vary with distance from mineralization, allowing the elements

to be used either individually or combined into ratios to monitor effects of hydrothermal alteration. The pXRF shows particular promise for use during VMS exploration field programs by allowing real-time acquisition of valuable geochemical data that could help direct concurrent exploration activities. However, results are not of high enough quality to allow the pXRF to replace traditional whole-rock analytical methods.

ACKNOWLEDGEMENTS

The authors wish to thank Arcus Development Group Inc. for allowing access to the property and core. Heather Burrell of Archer, Cathro and Associates (1981) Ltd. was a great help in getting us set up and telling us where the perfectly stacked core would be found. Mel and Will Fellers are thanked for their help with logistics, fine hospitality, and for renting us the 'ether hog' that got us around. Reviewers, Jan Peter and Jim Ryan of the Geological Survey of Canada, and Lee Pigage of the Yukon Geological Survey are thanked for critical reviews and discussion. Funding for the analytical portion of this study was provided by the Canadian Northern Economic Development Agency (CanNor) from the Strategic Investment in Northern Economic Development fund (SINED).

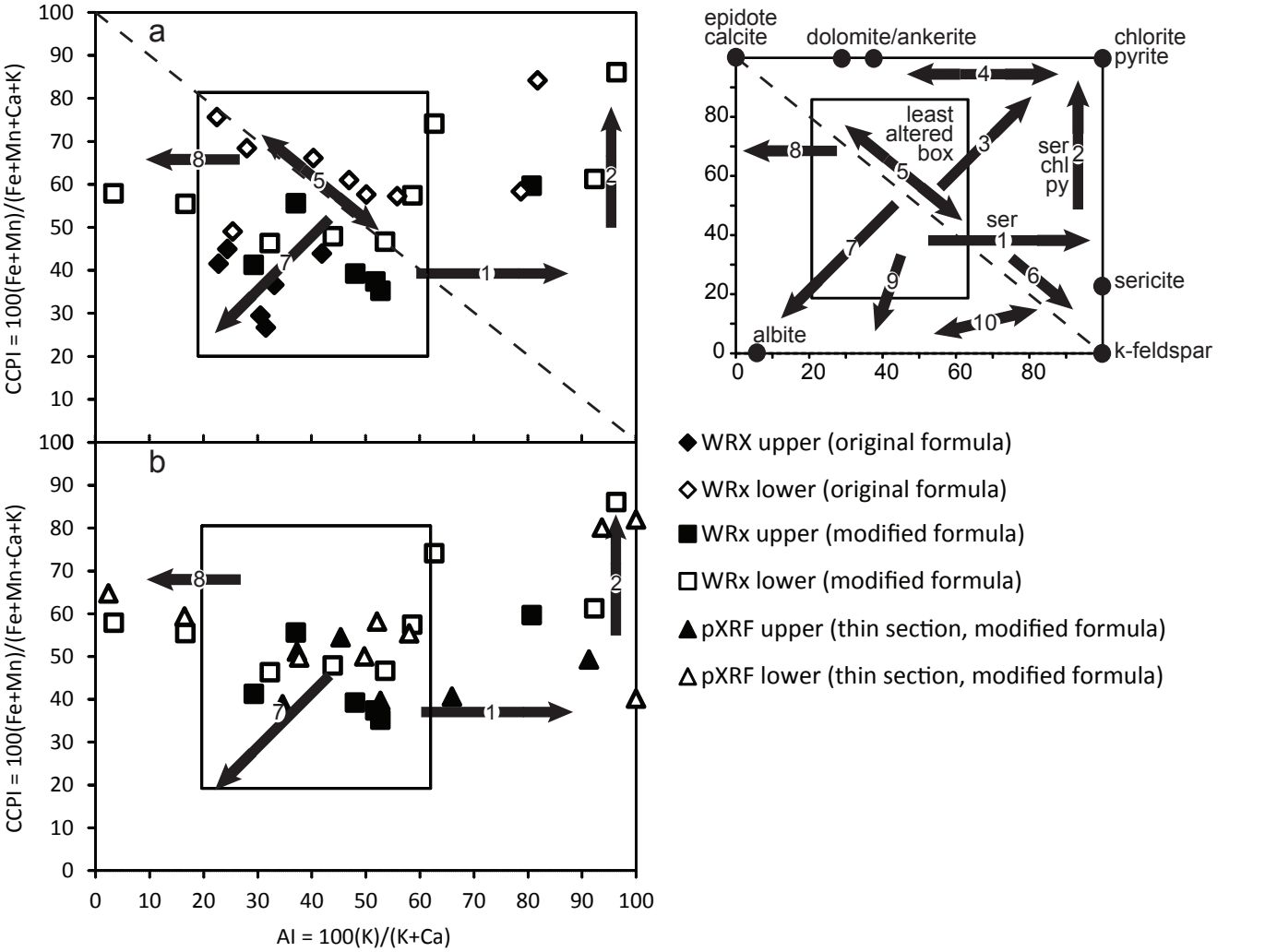

Figure 8. *Alteration box plot modified for pXRF elements. a) Points generated with formulas modified for pXRF data and the original formulas using whole-rock data; b) Points generated with pXRF modified formulas using corrected pXRF off-cut data and laboratory whole-rock data. Trends to the upper right of the dashed line are hydrothermal alteration trends (1 through 6) and trends to the lower left are diagenetic alteration trends (7 through 10), for further explanation of alteration trends see Large et al. (2001).*

REFERENCES

Barrett, T.J. and MacLean, W.H., 1999. Volcanic sequences, litho-geochemistry, and hydrothermal alteration in some bimodal volcanic-associated massive sulfide systems. *In:* Volcanic-associated massive sulfide deposits: processes and examples in modern and ancient settings, C.T. Barrie and M.D. Hannington (eds.), Society of Economic Geologists, vol. 8, p. 101-131.

Barrett, T.J., Cattalani, S., and Maclean, W.H., 1993. Volcanic lithogeochemistry and alteration at the Delbridge massive sulfide deposit, Noranda, Quebec. Journal of Geochemical Exploration, vol. 48, p. 135-173.

Chapman, J.B., Peter, J.M., Layton-Matthews, D., and Gemmell, J.B., 2009. Geochemistry of Archean sulfidic black shale horizons: combining data at multiple scales for improved targeting in VMS exploration. *In:* Proceedings of the 24th International Applied Geochemistry Symposium, D.R. Lentz, K.G. Thorne, and K.-L. Beal (eds.), Fredericton, New Brunswick, Canada, vol. 1, p. 19-22.

Gifkins, C., Herrmann, W., and Large, R., 2005. Altered volcanic rocks: A guide to description and interpretation, Centre for Ore Deposit Research (CODES), University of Tasmania, 275 p.

Gordey, S.P. and Ryan, J.J., 2005. Geology, Stewart River Area (115N, 115O and part of 115J), Yukon Territory. Geological Survey of Canada, scale 1:250 000.

Hunt, J.A., 2002. Volcanic-associated massive sulphide (VMS) mineralization in the Yukon-Tanana Terrane and coeval strata of the North American miogeocline, in the Yukon and adjacent areas. Exploration and Geological Services Division, Yukon Region, Indian and Northern Affairs Canada, 107 p.

Innov-X-Systems, 2009. Omega handheld XRF analyzer user manual, June 2009 edition.

Ishikawa, Y., Sawaguchi, T., Iwaya, S., and Horiuchi, M., 1976. Delineation of prospecting targets for Kuroko deposits based on modes of volcanism of underlying dacite and alteration haloes. Mining Geology, vol. 26, p. 105-117.

Large, R.R., Gemmell, J.B., Paulick, H., and Herrmann, W., 2001. The alteration box plot; a simple approach to understanding the relationship between alteration mineralogy and lithogeochemistry associated with volcanic-hosted massive sulfide deposits. Economic Geology and the Bulletin of the Society of Economic Geologists, vol. 96, p. 957-971.

MacLean, W.H. and Barrett, T.J., 1993. Lithogeochemical techniques using immobile elements. Journal of Geochemical Exploration, vol. 48, p. 109-133.

Mireku, L.K. and Stanley, C.R., 2006. Lithogeochemistry and hydrothermal alteration at the Halfmile Lake South Deep zone, a volcanic-hosted massive sulfide deposit, Bathurst mining camp, New Brunswick. Exploration and Mining Geology, vol. 15, p. 177-199.

Newberry, R.J., Brew, D.A., and Crafford, T.C., 1989. Zoned footwall alteration and original rock types at the Greens Creek volcanogenic massive sulfide (VMS) deposit, southeast Alaska. Proceedings to the Alaska Miners Association Juneau Conference, Juneau, Alaska, p. 29-31.

Pearce, J.A., 1996. A user's guide to basalt discrimination diagrams. *In:* Trace element geochemistry of volcanic rocks, D.A. Wyman (ed.), Volume Short Course Notes, Geological Association of Canada, Mineral Deposits Division, vol. 12, p. 79-113.

Peter, J.M., Mercier-Langevin, P., and Chapman, J.B., 2009. Application of field-portable x-ray fluorescence spectrometers in mineral exploration, with examples from the Abitibi Greenstone Belt. *In:* Proceedings of the 24th International Applied Geochemistry Symposium, D.R. Lentz, K.G. Thorne, and K.-L. Beal (eds.), Fredericton, New Brunswick, Canada, vol. 1, p. 83-86.

Ross, P.-S. and Bedard, J.H., 2009. Magmatic affinity of modern and ancient subalkaline volcanic rocks determined from trace-element discriminant diagrams. Canadian Journal of Earth Sciences, vol. 46, p. 823-839.

Ryan, J.J. and Gordey, S.P., 2001a. Geology, Thistle Creek area, Yukon Territory (115O/3). Geological Survey of Canada, scale 1:50 000.

Ryan, J.J. and Gordey, S.P., 2001b. New geological mapping in Yukon-Tanana terrane near Thistle Creek, Stewart River map area, Yukon Territory. Geological Survey of Canada, Current Research 2001-A2, 18 p.

Winchester, J.A. and Floyd, P.A., 1977. Geochemical discrimination of different magma series and their differentiation products using immobile elements. Chemical Geology, vol. 20, p. 325-343.

APPENDIX 1: Whole-rock analytical data.

	Detection Limit	Drillhole	TL11-05	TL11-05	TL11-05	TL11-05	TL11-05	TL11-05	TL11-05	TL11-05	TL11-05	TL11-05	TL11-05	TL11-05	TL11-05	TL11-05	TL11-05
		Depth (m)	4.50	36.36	50.00	69.76	99.97	113.50	126.25	137.00	139.45	155.60	175.07	190.75	201.20	219.10	243.00
		Sample No.	TL11-05-004.50m	TL11-05-036.36m	TL11-05-050.00m	TL11-05-069.76m	TL11-05-099.97m	TL11-05-113.50m	TL11-05-126.25m	TL11-05-137.00m	TL11-05-139.45m	TL11-05-155.60m	TL11-05-175.07m	TL11-05-190.75m	TL11-05-201.20m	TL11-05-219.10m	TL11-05-243.00m
SiO_2 (%)	0.01	FUS-ICP	71.48	69.76	73.39	71.72	74.55	56.81	74.48	78.73	70.17	69.38	66.56	66.95	62.36	54.62	71.1
Al_2O_3 (%)	0.01	FUS-ICP	13.44	13.75	14.24	14.25	12.41	24.77	12.83	4.96	12.1	12.57	14.23	14.36	13.73	15.23	13.46
Fe_2O_3* (%)	0.01	FUS-ICP	3.8	3.67	2.66	2.26	4.33	4.84	5.49	8.66	5.39	6.26	5.82	6.38	8.49	11.89	4.82
MnO (%)	0.001	FUS-ICP	0.114	0.057	0.03	0.046	0.073	0.01	0.141	0.008	0.032	0.084	0.183	0.084	0.198	0.209	0.095
MgO (%)	0.01	FUS-ICP	0.78	0.62	0.5	0.67	0.85	0.43	0.45	0.13	0.5	1.29	1.6	1.53	2.57	3.73	0.69
CaO (%)	0.01	FUS-ICP	3.87	2.94	2.13	1.97	2.17	0.62	0.72	0.05	0.26	1.91	3.13	3.87	5.71	8.34	3.78
Na_2O (%)	0.01	FUS-ICP	3.67	3.49	3.89	3.88	3.86	3.35	1.57	0.26	0.67	1.8	0.77	0.99	2.7	3.41	3.1
K_2O (%)	0.01	FUS-ICP	1.38	2.34	1.97	1.89	1.1	2.23	1.04	1.14	2.67	2.33	3.11	2.61	0.98	0.25	1.55
TiO_2 (%)	0.001	FUS-ICP	0.304	0.42	0.418	0.484	0.46	1.123	0.697	0.215	0.506	0.508	0.556	0.73	0.663	0.95	0.467
P_2O_5 (%)	0.01	FUS-ICP	0.07	0.11	0.1	0.08	0.09	0.03	0.07	0.02	0.15	0.09	0.13	0.13	0.13	0.16	0.11
LOI		FUS-ICP	1.96	2.33	1.55	1.74	0.73	5.25	3.25	5.2	5.41	3.89	2.58	1.92	1.52	0.88	1.32
Total			**100.9**	**99.49**	**100.9**	**98.98**	**100.6**	**99.45**	**100.7**	**99.37**	**97.85**	**100.1**	**98.67**	**99.56**	**99.06**	**99.67**	**100.5**
Sc (ppm)	1	FUS-ICP	9	11	8	14	11	23	13	6	14	15	25	20	25	36	14
Be (ppm)	1	FUS-ICP	2	2	2	< 1	1	2	< 1	< 1	< 1	1	< 1	< 1	< 1	< 1	1
V (ppm)	5	FUS-ICP	25	21	19	23	12	127	89	37	103	92	93	194	211	371	39
Sr (ppm)	2	FUS-ICP	153	111	98	94	86	310	140	26	71	82	63	120	129	499	104
Ba (ppm)	3	FUS-ICP	407	623	728	532	446	4175	2856	1873	4702	1112	887	1044	262	52	600
Cr (ppm)	20	FUS-MS	< 20	< 20	< 20	< 20	< 20	220	< 20	< 20	30	< 20	< 20	< 20	< 20	< 20	< 20
Co (ppm)	1	FUS-MS	3	1	1	1	2	12	4	10	6	6	9	11	20	31	6
Ga (ppm)	1	FUS-MS	17	19	19	17	15	28	19	10	13	14	15	18	17	20	16
Ge (ppm)	0.5	FUS-MS	1.7	1.5	1.6	1.3	1.7	2.6	6.1	1.1	0.6	0.8	1.3	1.6	1.8	2.2	1.5
As (ppm)	5	FUS-MS	< 5	< 5	< 5	< 5	< 5	8	19	< 5	10	< 5	< 5	< 5	< 5	< 5	< 5
Rb (ppm)	1	FUS-MS	31	59	41	45	20	40	24	20	61	49	56	54	26	2	37
Y (ppm)	0.5	FUS-MS	35.2	64.4	39.9	56.7	43.1	9.4	12.4	9.9	14.9	38.1	28.9	28.8	26.3	23.4	33.8
Zr (ppm)	1	FUS-MS	275	287	296	242	220	265	160	51	132	169	150	145	114	76	181
Nb (ppm)	0.2	FUS-MS	16.6	9.2	9.2	13.1	9.2	11.9	5.1	1.5	3.5	6.1	6.6	6.5	2.5	0.8	5.8
Mo (ppm)	2	FUS-MS	< 2	< 2	< 2	< 2	< 2	14	2	6	< 2	< 2	< 2	< 2	< 2	< 2	< 2
In (ppm)	0.1	FUS-MS	< 0.1	< 0.1	< 0.1	< 0.1	< 0.1	< 0.1	0.1	< 0.1	< 0.1	< 0.1	< 0.1	< 0.1	< 0.1	< 0.1	< 0.1
Sn (ppm)	1	FUS-MS	4	3	3	3	2	2	1	< 1	< 1	1	< 1	1	< 1	< 1	2
Sb (ppm)	0.2	FUS-MS	< 0.2	< 0.2	< 0.2	< 0.2	< 0.2	13.2	5.1	1.5	1	0.4	< 0.2	< 0.2	< 0.2	< 0.2	< 0.2
Cs (ppm)	0.1	FUS-MS	0.8	1.3	0.9	1.1	0.5	0.6	0.6	0.2	0.9	0.5	1.6	0.7	0.7	0.1	1.1
La (ppm)	0.05	FUS-MS	90.2	32.1	21.1	24.5	34.4	7.36	9.68	9.66	4.45	16.2	16.5	18.3	11.9	11.1	20.2
Ce (ppm)	0.05	FUS-MS	169	67.2	48	54	70.4	13.2	19.7	18.6	8.45	36.8	35.7	39.5	26.9	25.4	42.7
Pr (ppm)	0.01	FUS-MS	18.2	9.03	6.31	6.88	8.3	1.3	2.48	2.02	1.17	4.87	4.38	4.97	3.55	3.51	5.19
Nd (ppm)	0.05	FUS-MS	59.5	35.4	26.3	28.2	31.1	4.32	9.98	7.15	10.5	20.9	18	19.6	15.2	14.2	20.3
Sm (ppm)	0.01	FUS-MS	9.13	8.55	6.48	6.84	6.7	0.75	1.03	1.2	4.38	5.24	4.12	4.76	3.58	3.66	4.7
Eu (ppm)	0.01	FUS-MS	2.1	1.85	1.47	1.56	1.59	0.192	0.175	0.471	0.739	1.39	1.11	1.18	0.979	1.18	1.08
Gd (ppm)	0.01	FUS-MS	7.89	9.49	6.76	7.99	6.95	0.84	0.58	1.47	2.3	5.71	4.65	5.46	4.18	3.91	4.95
Tb (ppm)	0.01	FUS-MS	1.22	1.72	1.21	1.38	1.22	0.17	0.14	0.26	0.39	1	0.79	0.91	0.69	0.68	0.89
Dy (ppm)	0.01	FUS-MS	7.29	11	7.62	9.01	7.69	1.28	1.21	1.64	2.58	6.51	5.01	5.48	4.33	4.19	5.65
Ho (ppm)	0.01	FUS-MS	1.39	2.33	1.59	1.97	1.59	0.33	0.37	0.34	0.56	1.39	1.07	1.08	0.91	0.87	1.18
Er (ppm)	0.01	FUS-MS	3.97	7.05	4.82	6.2	4.67	1.23	1.52	1.02	1.76	4.23	3.29	3.02	2.77	2.61	3.58
Tm (ppm)	0.01	FUS-MS	0.567	1.09	0.723	0.955	0.701	0.243	0.316	0.154	0.286	0.637	0.508	0.422	0.425	0.389	0.546
Yb (ppm)	0.01	FUS-MS	3.76	7.17	4.88	6.53	4.68	2.02	2.71	1.02	2	4.27	3.39	2.66	2.84	2.61	3.7
Lu (ppm)	0.002	FUS-MS	0.592	1.17	0.784	1.03	0.743	0.357	0.486	0.162	0.343	0.682	0.552	0.4	0.451	0.426	0.609
Hf (ppm)	0.1	FUS-MS	8.1	7.7	7.5	6.7	6	7.7	4.2	1.4	3.6	4	3.9	3.8	3.1	2.2	5

APPENDIX 1 (continued): Whole-rock analytical data.

	Detection Limit	Drillhole	TL11-05	TL11-05	TL11-05	TL11-05	TL11-05	TL11-05	TL11-05	TL11-05	TL11-05	TL11-05	TL11-05	TL11-05	TL11-05	TL11-05	TL11-05
		Depth (m)	4.50	36.36	50.00	69.76	99.97	113.50	126.25	137.00	139.45	155.60	175.07	190.75	201.20	219.10	243.00
		Sample No.	TL11-05-004.50m	TL11-05-036.36m	TL11-05-050.00m	TL11-05-069.76m	TL11-05-099.97m	TL11-05-113.50m	TL11-05-126.25m	TL11-05-137.00m	TL11-05-139.45m	TL11-05-155.60m	TL11-05-175.07m	TL11-05-190.75m	TL11-05-201.20m	TL11-05-219.10m	TL11-05-243.00m
Ta (ppm)	0.01	FUS-MS	0.53	0.65	0.6	0.99	0.54	0.79	0.42	0.12	0.32	0.37	0.39	0.5	0.18	< 0.01	0.4
W (ppm)	0.5	FUS-MS	1.2	1.1	< 0.5	< 0.5	< 0.5	3.6	< 0.5	2	2.1	1	< 0.5	1.5	< 0.5	< 0.5	< 0.5
Tl (ppm)	0.05	FUS-MS	0.18	0.32	0.32	0.34	0.21	6.77	8.09	2.3	3.28	0.46	0.41	0.37	0.19	< 0.05	0.18
Bi (ppm)	0.1	FUS-MS	0.2	0.2	< 0.1	< 0.1	< 0.1	< 0.1	0.3	0.6	< 0.1	0.1	< 0.1	< 0.1	< 0.1	< 0.1	< 0.1
Th (ppm)	0.05	FUS-MS	11.8	7.42	6.81	6.12	6.03	1.44	3.05	1.58	0.59	5.01	4.11	4.16	2.47	1.17	4.93
U (ppm)	0.01	FUS-MS	0.99	1.88	1.87	1.65	1.32	3	0.75	0.94	3.72	1.85	1.24	1.16	0.76	0.36	1.35
Au (ppb)	2	INAA	4	< 2	< 2	< 2	< 2	< 2	8	412	62	< 2	< 2	< 2	< 2	< 2	< 2
As (ppm)	0.5	INAA	< 0.5	0.8	1.5	< 0.5	< 0.5	12.7	16.5	5.5	16	1.9	< 0.5	1.6	< 0.5	< 0.5	0.9
Br (ppm)	0.5	INAA	< 0.5	< 0.5	< 0.5	< 0.5	< 0.5	< 0.5	< 0.5	< 0.5	< 0.5	< 0.5	< 0.5	< 0.5	< 0.5	< 0.5	< 0.5
Cr (ppm)	5	INAA	< 5	< 5	< 5	< 5	6	252	15	< 5	34	< 5	18	< 5	6	< 5	< 5
Ir (ppb)	5	INAA	< 5	< 5	< 5	< 5	< 5	< 5	< 5	< 5	< 5	< 5	< 5	< 5	< 5	< 5	< 5
Sc (ppm)	0.1	INAA	8.3	10.8	7.4	13.2	10.5	23	11.3	6.4	14.2	15.3	23.8	19.5	26.2	34.9	13.5
Se (ppm)	3	INAA	< 3	< 3	< 3	< 3	< 3	< 3	< 3	9	< 3	< 3	< 3	< 3	< 3	< 3	< 3
Sb (ppm)	0.2	INAA	< 0.2	0.3	< 0.2	< 0.2	< 0.2	19.5	4.6	2	2	0.3	< 0.2	< 0.2	< 0.2	< 0.2	< 0.2
Ni (ppm)	1	TD-ICP	3	3	3	4	3	39	6	12	11	2	14	7	11	12	2
Cu (ppm)	1	TD-ICP	6	16	17	2	12	44	224	7430	299	9	31	11	71	136	5
Zn (ppm)	1	TD-ICP	90	69	56	33	93	62	245	104	209	44	192	103	101	89	73
Cd (ppm)	0.5	TD-ICP	< 0.5	< 0.5	< 0.5	< 0.5	< 0.5	< 0.5	0.7	0.9	0.8	< 0.5	0.7	< 0.5	< 0.5	0.6	< 0.5
S (%)	0.001	TD-ICP	0.024	0.016	0.182	0.015	0.106	2.71	0.427	7.37	3.97	3.38	0.61	0.036	0.069	0.062	0.027
Ag (ppm)	0.3	TD-ICP	< 0.3	< 0.3	< 0.3	< 0.3	< 0.3	< 0.3	< 0.3	1.7	< 0.3	< 0.3	< 0.3	< 0.3	< 0.3	< 0.3	< 0.3
Pb (ppm)	3	TD-ICP	22	27	10	10	4	230	202	20	32	17	9	5	5	< 3	6

**Total iron reported as Fe_2O_3*

Analytical methods described in Section 5.1

FUS-MS = lithium metaborate/tetraborate Fusion - Inductively Coupled Plasma Mass Spectrometry

FUS-ICP = lithium metaborate/tetraborate Fusion - Inductively Coupled Plasma Optical Emission Spectrometry

TD-ICP = Total Digestion - Inductively Coupled Plasma Optical Emission Spectrometry

INAA = Instrumental Neutron Activation Analysis of pulp (no digestion/fusion)

Samples were crushed, split and then pulverized in a mild steel mill

Analysis below lower detection limits shown with a "<" detection limit value

Details of diamond drill hole TL11-05:

UTM collar coordinates: 594353 E, 6987715 N, Zone 7, Datum NAD83

Azimuth: 360°

Dip: -45°

APPENDIX 2: Portable x-ray fluorescence spectrometer (pXRF) pulp and off-cut data.

Drillhole	TL11-05		TL11-05		TL11-05		TL11-05		TL11-05		TL11-05		TL11-05		TL11-05	
Depth (m)	4.50		36.36		50.00		69.76		99.97		113.50		126.25		137.00	
Sample No.	TL11-05-004.50m		TL11-05-036.36m		TL11-05-050.00m		TL11-05-069.76m		TL11-05-099.97m		TL11-05-113.50m		TL11-05-126.25m		TL11-05-137.00m	
	raw	corr.	raw	corr.	raw	corr.	raw	corr.	raw	corr.	raw	corr.	raw	corr.	raw	corr.
Ag-pulp	128	NA	117	NA	118	NA	104	NA	133	NA	147	NA	235	NA	240	NA
Ag-TS	148	NA	202	NA	129	NA	114	NA	118	NA	210	NA	127	NA	154	NA
As-pulp	2	BD	2	BD	1	BD	2	BD	2	BD	11	1.8	60	16.8	4	BD
As-TS	2.5	BD	1.8	BD	0.4	BD	2.5	BD	2.5	BD	17.2	3.6	8.4	0.9	1.7	BD
Au-pulp	BD	BD	BD	BD	BD	BD	BD	BD	BD	BD	BD	BD	BD	BD	BD	BD
Au-TS	BD	BD	BD	BD	BD	BD	BD	BD	BD	BD	BD	BD	BD	BD	BD	BD
Ba-pulp	319	334	285	285	332	353	240	220	237	216	1753	2413	2701	3788	828	1072
Ba-TS	298	304	383	428	375	416	226	200	220	192	2203	3066	1277	1724	786	1012
Ca-pulp	19025	17950	15285	13798	10613	8613	9538	7419	11072	9122	2749	BD	3060	228	25	BD
Ca-TS	19339	18298	34978	35657	9919	7843	11809	9940	11845	9980	3437	647	2439	BD	25	BD
Cd-pulp	24	BD	5	BD	22	BD	17	BD	28	0.03	11	BD	63	0.38	52	0.27
Cd-TS	9	BD	30	0.05	22	BD	21	BD	16	BD	18	BD	6	BD	4	BD
Co-pulp	316	9	287	9	167	6	151	6	346	10	420	11	860	20	1077	24
Co-TS	251	8	321	9	138	6	107	5	193	7	248	8	214	7	546	14
Cr-pulp	54	111	31	81	28	77	31	82	34	85	207	314	55	113	33	84
Cr-TS	19	65	12	57	37	89	18	64	15	60	192	294	53	111	39	92
Cu-pulp	BD	BD	BD	BD	BD	BD	BD	BD	BD	BD	BD	BD	400	381	7895	7427
Cu-TS	BD	BD	BD	BD	BD	BD	BD	BD	BD	BD	BD	BD	55	57	7184	6758
Fe-pulp	20228	29394	20516	30001	14256	16793	13013	14171	23707	36735	20427	29814	29166	48253	50956	94231
Fe-TS	16871	22311	18509	25768	10336	8522	9060	5830	13238	14646	10781	9460	18904	26601	20386	29727
K-pulp	8523	7103	14732	13685	12074	10867	10753	9467	6379	4831	14447	13383	6882	5364	7726	6258
K-TS	11795	10572	19199	18420	17144	16241	12499	11318	9610	8256	17543	16664	9155	7773	9167	7786
Mn-pulp	739	762	387	409	226	249	323	345	490	512	129	151	811	833	79	101
Mn-TS	450	473	349	371	118	141	234	256	163	185	95	118	969	991	20	42
Mo-pulp	BD	NA	BD	NA	BD	NA	BD	NA	BD	NA	18	NA	8	NA	14	NA
Mo-TS	BD	NA	BD	NA	BD	NA	BD	NA	BD	NA	22	NA	BD	NA	24	NA
Nb-pulp	BD	NA	BD	NA	BD	NA	BD	NA	BD	NA	BD	NA	BD	NA	BD	NA
Nb-TS	BD	NA	BD	NA	BD	NA	BD	NA	BD	NA	BD	NA	BD	NA	BD	NA
Ni-pulp	BD	NA	BD	NA	BD	NA	BD	NA	BD	NA	BD	NA	BD	NA	BD	NA
P-pulp	BD	NA	BD	NA	BD	NA	BD	NA	BD	NA	BD	NA	BD	NA	BD	NA
P-TS	BD	NA	BD	NA	BD	NA	BD	NA	BD	NA	BD	NA	BD	NA	BD	NA
Pb-pulp	26	18	30	21	15	11	18	13	13	9	257	175	356	243	26	18
Pb-TS	18	13	35	25	13	10	13	10	10	8	313	214	115	79	19	14
Rb-pulp	32	13	61	32	42	20	47	23	21	6	42	20	48	24	22	6
Rb-TS	35	15	72	40	43	20	36	16	18	4	56	29	23	7	21	6
S-pulp	BD	BD	BD	BD	BD	BD	BD	BD	BD	BD	8287	17528	1985	2341	32340	75495
S-TS	BD	BD	BD	BD	BD	BD	BD	BD	BD	BD	25080	57999	1173	382	64612	153270
Sb-pulp	BD	NA	BD	NA	BD	NA	BD	NA	BD	NA	7	NA	BD	NA	BD	NA
Sn-pulp	16	NA	21	NA	19	NA	25	NA	27	NA	47	NA	48	NA	41	NA
Sn-TS	28	NA	27	NA	4	NA	21	NA	17	NA	31	NA	9	NA	BD	NA
Sr-pulp	146	155	105	113	94	102	93	101	83	91	305	315	260	269	27	35
Sr-TS	96	104	167	176	89	97	76	84	73	80	377	387	83	91	22	29
Ta-pulp	33	NA	33	NA	39	NA	33	NA	30	NA	54	NA	33	NA	5	NA
Ta-TS	29	NA	40	NA	36	NA	28	NA	24	NA	63	NA	18	NA	2	NA
Ti-pulp	1422	1506	2006	2155	1832	1961	2198	2368	2102	2261	5508	6041	3985	4351	1727	1845
Ti-TS	1528	1623	1870	2003	2082	2239	2359	2546	2005	2153	5703	6258	3255	3541	1809	1935
V-pulp	59	NA	56	NA	58	NA	50	NA	45	NA	306	NA	224	NA	146	NA
V-TS	34	NA	45	NA	70	NA	42	NA	41	NA	296	NA	244	NA	121	NA
Y-pulp	77	13	357	61	163	28	365	62	171	29	BD	BD	BD	BD	BD	BD
Y-TS	9	2	337	57	137	23	154	26	53	9	BD	BD	BD	BD	BD	BD
Zn-pulp	75	BD	56	BD	43	BD	27	BD	77	BD	56	BD	545	174	92	BD
Zn-TS	56	BD	52	BD	22	BD	22	BD	50	BD	73	BD	69	BD	108	BD
Zr-pulp	315	260	324	267	319	263	275	226	242	199	301	248	362	298	60	48
Zr-TS	318	262	572	472	375	309	231	190	243	199	396	327	107	86	62	50

Analytical methods described in Section 5.2

BD = below lower limit of detection

corr. = corrected data using slope and y-intercept values in Table 2

NA in corrected column indicates data had R^2 value too low (<0.5) to apply linear correction

All data in ppm and elemental form

APPENDIX 2 (continued): Portable x-ray fluorescence spectrometer (pXRF) pulp and off-cut data.

Drillhole	TL11-05		TL11-05		TL11-05		TL11-05		TL11-05		TL11-05		TL11-05	
Depth (m)	139.45		155.60		175.07		190.75		201.20		219.10		243.00	
Sample No.	TL11-05-139.45m		TL11-05-155.60m		TL11-05-175.07m		TL11-05-190.75m		TL11-05-201.20m		TL11-05-219.10m		TL11-05-243.00m	
	raw	corr.	raw	corr.	raw	corr.	raw	corr.	raw	corr.	raw	corr.	raw	corr.
Ag-pulp	204	NA	167	NA	160	NA	178	NA	185	NA	227	NA	127	NA
Ag-TS	138	NA	138	NA	161	NA	153	NA	158	NA	283	NA	140	NA
As-pulp	18	4.0	BD	BD	BD	BD	BD	BD	3	BD	BD	BD	1	BD
As-TS	6.0	0.2	2.5	BD	2.5	BD	0.8	BD	0.2	BD	2.2	BD	2.5	BD
Au-pulp	BD	BD	BD	BD	BD	BD	BD	BD	BD	BD	BD	BD	BD	BD
Au-TS	BD	BD	BD	BD	BD	BD	BD	BD	BD	BD	BD	BD	BD	BD
Ba-pulp	2939	4133	591	728	489	581	583	717	389	436	691	873	276	272
Ba-TS	3238	4567	575	705	450	525	716	910	323	340	884	1154	371	410
Ca-pulp	1266	BD	10209	8164	16133	14740	19714	18714	34127	34713	58013	61226	19505	18483
Ca-TS	25	BD	16587	15243	24476	24000	20616	19716	31526	31826	95467	102800	24781	24339
Cd-pulp	13	BD	19	BD	23	BD	16	BD	15	BD	4	BD	6	BD
Cd-TS	0	BD	7	BD	1	BD	0	BD	7	BD	21	BD	14	BD
Co-pulp	718	17	542	14	529	13	605	15	775	18	1305	29	394	11
Co-TS	225	7	397	11	333	10	400	11	411	11	1332	30	331	10
Cr-pulp	75	139	36	87	39	91	28	77	23	71	7	49	35	87
Cr-TS	48	104	26	74	18	64	27	76	14	58	-8	30	16	62
Cu-pulp	400	381	BD	BD	BD	BD	BD	BD	50	52	128	126	BD	BD
Cu-TS	144	141	BD	BD	BD	BD	BD	BD	BD	BD	322	308	BD	BD
Fe-pulp	21713	32528	29535	49033	32943	56223	37980	66850	50238	92715	73121	140998	26060	41700
Fe-TS	9558	6881	23767	36861	24898	39247	30460	50983	28475	46796	91830	180475	20613	30207
K-pulp	20403	19696	16990	16079	22932	22377	19364	18594	7578	6102	1490	BD	11215	9957
K-TS	23573	23057	17574	16697	24177	23696	27844	27583	7128	5625	3486	1764	15414	14408
Mn-pulp	280	302	581	604	1124	1146	527	550	1341	1364	1418	1440	642	664
Mn-TS	106	128	603	626	694	717	342	364	637	660	1865	1887	483	505
Mo-pulp	12	NA	BD	NA	BD	NA	BD	NA	BD	NA	4	NA	BD	NA
Mo-TS	6	NA	BD	NA	BD	NA	BD	NA	BD	NA	3	NA	BD	NA
Nb-pulp	BD	NA	BD	NA	BD	NA	BD	NA	BD	NA	BD	NA	BD	NA
Nb-TS	BD	NA	BD	NA	BD	NA	BD	NA	BD	NA	BD	NA	BD	NA
Ni-pulp	BD	NA	BD	NA	BD	NA	BD	NA	BD	NA	BD	NA	BD	NA
P-pulp	BD	NA	BD	NA	BD	NA	BD	NA	BD	NA	BD	NA	BD	NA
P-TS	BD	NA	BD	NA	BD	NA	BD	NA	BD	NA	BD	NA	BD	NA
Pb-pulp	60	42	23	16	17	13	11	9	13	9	17	12	14	10
Pb-TS	36	25	22	16	17	12	8	6	15	11	12	9	14	11
Rb-pulp	94	55	53	27	61	32	56	29	26	9	1	-8	37	16
Rb-TS	66	35	46	22	52	27	64	34	19	4	6	-4	41	19
S-pulp	11220	24597	10151	22019	2095	2604	BD	BD	BD	BD	BD	BD	BD	BD
S-TS	23241	53567	34437	80549	BD	BD	BD	BD	BD	BD	BD	BD	BD	BD
Sb-pulp	BD	NA	BD	NA	BD	NA	BD	NA	BD	NA	20	NA	4	NA
Sn-pulp	11	NA	10	NA	11	NA	14	NA	16	NA	19	NA	10	NA
Sn-TS	BD	NA	BD	NA	BD	NA	8	NA	BD	NA	8	NA	BD	NA
Sr-pulp	101	109	81	89	62	70	115	123	128	136	481	493	97	105
Sr-TS	59	67	82	90	64	72	93	101	111	119	502	514	98	106
Ta-pulp	30	NA	18	NA	37	NA	34	NA	29	NA	37	NA	29	NA
Ta-TS	25	NA	33	NA	28	NA	30	NA	24	NA	35	NA	28	NA
Ti-pulp	3860	4212	2831	3070	2937	3188	3903	4260	3409	3712	4475	4895	2437	2633
Ti-TS	4925	5395	3180	3457	2005	2154	3391	3692	2994	3251	4713	5159	2544	2752
V-pulp	343	NA	105	NA	95	NA	127	NA	85	NA	118	NA	53	NA
V-TS	523	NA	108	NA	74	NA	138	NA	67	NA	140	NA	64	NA
Y-pulp	BD	BD	152	26	38	6	BD	BD	BD	BD	BD	BD	95	16
Y-TS	BD	BD	148	25	31	5	BD	BD	BD	BD	BD	BD	BD	BD
Zn-pulp	228	40	38	BD	173	17	89	BD	92	BD	96	BD	61	BD
Zn-TS	48	BD	40	BD	169	16	52	BD	43	BD	121	BD	48	BD
Zr-pulp	180	147	186	152	168	137	166	136	127	103	85	68	210	172
Zr-TS	107	86	205	168	167	136	149	121	153	125	73	59	208	171

Orogen-perpendicular magnetic segmentation of the western Yukon and eastern Alaska cordilleran hinterland: Implications for structural control of mineralization

Matías G. Sánchez[1], Murray M. Allan, Craig J.R. Hart, Jim K. Mortensen
Mineral Deposit Research Unit (MDRU), University of British Columbia, Vancouver, BC

Sanchez, M.G., Allan, M.M., Hart, C.J.R., and Mortensen, J.K., 2013. Orogen-perpendicular magnetic segmentation of the western Yukon and eastern Alaska cordilleran hinterland: Implications for structural control of mineralization. *In:* Yukon Exploration and Geology 2012, K.E. MacFarlane, M.G. Nordling, and P.J. Sack (eds.), Yukon Geological Survey, p. 133-146.

ABSTRACT

This contribution focuses on the analysis, characterization, and mineralization control of northeast-southwest oriented, magnetic heterogeneities of the allochthonous to parautochthonous Intermontane terranes of the North American Cordillera of western Yukon and eastern Alaska. Our interpretation of publically available magnetic datasets proposes sixteen zones of linear discontinuities oriented semi-perpendicular to the northwest-southeast Cordilleran deformation front and mid-Cretaceous Dawson Range magmatic arc. These magnetite-destructive corridors are interpreted as steeply dipping, brittle fault zones and fracture arrays of extensional, oblique-extensional, and strike-slip kinematics responsible for localized structural damage. Their spatial correlation with known mid to Late Cretaceous magmatic-hydrothermal mineralization suggests a first-order structural control in eastern Alaska, while a secondary role is interpreted for Yukon's Dawson Range.

[1]*msanchez@eos.ubc.ca*

INTRODUCTION

Across the western North American Laurentian margin, and specifically along the Canadian Cordillera, orogen-perpendicular, northeast-trending basement and upper crustal fault systems have been interpreted from regional aeromagnetic surveys (Logan *et al.*, 2010; Crawford *et al.*, 2010). We investigate this class of structure in the northern Yukon-Tanana terrane of west-central Yukon and east-central Alaska, using a seamless reduced-to-pole (RTP) magnetic grid generated by Fathom Geophysics LLC (Fig. 1; Buckingham and Core, 2012). The magnetic dataset is a compilation of publically available regional datasets from the U. S. Geological Survey (USGS), Alaska Division of Geological and Geophysical Surveys (DGGS), and Natural Resources Canada (NRCan).

Airborne magnetic surveys constitute one of the most widely used geophysical techniques for mineral exploration and geological interpretation (Gunn and Denith, 1997; Nabighian *et al.*, 2005; Purucker and Clark, 2011). Particular examples of its applications to western North American geology and structure include: (1) the mapping of strong magnetic anomalies caused by buried basement and cratonic structures (Crawford *et al.*, 2010); (2) analysis of weak signals assigned to Laurentian margin sedimentary basins (Lund, 2008); (3) mapping of high amplitude anomalies caused by buried Early Proterozoic magmatic arcs (Pilkington and Saltus, 2009); and (4) mineral exploration applications including the identification of structural controls on Mesoproterozoic massive sulphide and intrusion and fault-related Ag-Pb-Zn and Cu-Ag veins, as well as controls on Mesozoic lode gold and stratabound Cu-Ag deposits (McMechan, 2012). These and other applied magnetics studies have substantially contributed to the understanding of western North America's crustal structure and tectonic evolution (*e.g.*, Pilkington, *et al.*, 2006; Saltus, 2007).

Linear magnetic discontinuities have long been used as a guide to regional structural controls on magmatic-related mineralization within metallogenic provinces of diverse geological settings (*e.g.*, Domzalski, 1966; Henley and Adams, 1992; Sandirin *et al.*, 2007). In this study, we interpret linear magnetic discontinuities, mainly of magnetite-destructive character, corresponding to steeply dipping structures relevant to the structural control of magmatically-related mineralization. Structures of steeply dipping geometries, commonly of extensional or strike-slip kinematics, have frequently been correlated to the distribution of porphyry, mesothermal, and epithermal style mineralization (Hedenquist, 1996; Micklethwaite *et al.*, 2010; Sillitoe, 1997). World-class epithermal deposits controlled by normal faulting include the Comstock Lode in Nevada (Vikre, 1989), Hishikari in Japan (Izawa *et al.*, 1990) and the Kelian deposit in Indonesia (Van Leeuwen *et al.*, 1990). Epithermal mineralization associated with strike-slip systems include the Virginia City and Goldfield mining districts in Nevada (Berger, 2007), Mesquite mining district in southeast California (Willis and Tosdal, 1992), and the Baguio deposit in the Philippines (Cooke *et al.*, 1996; Sillitoe, 1997). Cases of steeply dipping faults controlling mineralization in mesothermal conditions include the strike-slip systems at St Ives goldfield and the Yilgarn craton of Western Australia (Cox, 1999; Cox and Running, 2004). At deeper crustal levels and elevated pressure-temperature conditions, regional scale, steeply dipping fault systems, such as the West Fissure in northern Chile, are broadly accepted to exert a first order structural control on some of the planet's largest porphyry copper deposits (Sillitoe, 1997).

We emphasize the spatial correlation between such linear magnetic discontinuities and the distribution of known Cretaceous magmatic related mineralization in western Yukon and eastern Alaska. The structural interpretation of regional geophysical datasets is part of a larger collaborative venture between the mining exploration industry and the Mineral Deposit Research Unit (MDRU) to improve constraints on metallogeny and generate knowledge relevant to mineral exploration in the region.

TECTONIC AND GEOLOGICAL SETTING

The interpreted magnetic dataset covers an area in the Intermontane terranes of the North American Cordillera of western Yukon and eastern Alaska between two Early Cenozoic, continental-scale dextral strike-slip faults, the Tintina and Denali faults (Fig. 1; Gabrielse *et al.*, 2006). This tectonic zone consists of a series of accreted parautochthonous to allochthonous terranes, including Slide Mountain, Quesnellia, Stikinia, and Yukon-Tanana terranes (Fig. 1; Mortensen, 1992; Colpron *et al.* 2007). The latter represents a mid to Late Paleozoic continental arc that was separated from the western margin of Laurentia by the coeval Slide Mountain back-arc basin during Late Devonian and Early to Middle Triassic time (Nelson *et al.*, 2006). The geometric array of the Intermontane terranes exhibit an overall semi-concentric distribution of mainly magmatic arc rocks, sedimentary

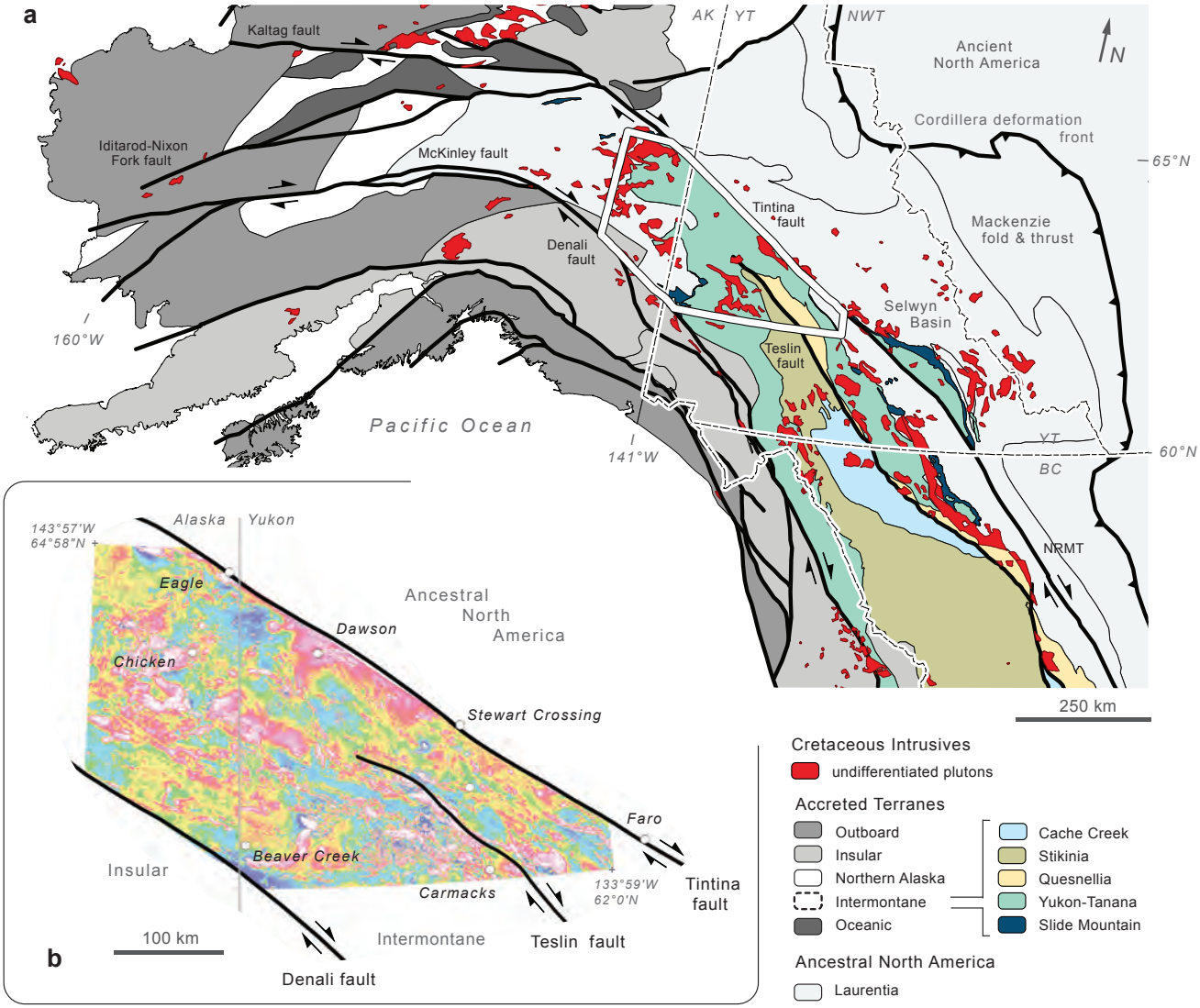

Figure 1. *(a) Tectonic map of the northern North American Cordillera, showing major tectonic boundaries (after Colpron, 2011) and Cretaceous post-accretionary intrusions (Garrity and Soller, 2009). (b) Location of the reduced-to-pole (RTP) magnetic grid.*

successions, and oceanic rocks bordering western Laurentia between mid-Paleozoic to Early Mesozoic times (Colpron *et al.*, 2007). In south-central Yukon, the exotic, Tethyan affinity oceanic rocks of the Cache Creek terrane comprise the core of the Intermontane terranes (Fig. 1; Cordey *et al.*, 1987). Its particular tectonic position has been proposed as the result of oroclinal entrapment by Quesnellia and Stikinia in Early Jurassic time (Mihalynuk *et al.*, 1992, 1994).

Early to Middle Jurassic accretion of the Intermontane terranes to the Laurentian margin, and related northwest-directed, margin-parallel shortening and fast cooling of upper plate rocks, locally switched to southeast-directed crustal extension by Early to mid-Cretaceous time (Dusel-Bacon *et al.*, 2002). In late Early Cretaceous time, extensional footwall exhumation took place in eastern Alaska (Dusel-Bacon *et al.*, 2002), whereas deformation in southern Yukon and northern British Columbia was dominated by dextral strike-slip displacement along the Northern Rocky Mountain Trench (NRMT) and Teslin fault (Fig. 1; Gabrielse *et al.*, 2006). During Early Cenozoic time (mainly Eocene) the Tintina fault propagated as a northern

fault segment of the NRMT through Yukon and eastern Alaska (Gabrielse, 1985; Gabrielse *et al.*, 2006). Tectonic restoration of the ~490 km dextral displacement along the Tintina fault to its pre-Cenozoic position, locates the study area within the hinterland zone of the Jurassic-Cretaceous Mackenzie fold and thrust belt to the northeast (Fig.1; Saltus, 2007).

Post-accretionary plutonic suites, caused by Cretaceous to Paleogene convergence, mainly intrude the Intermontane terranes and to a lesser extent the Laurentian margin and Insular terranes (Fig.1; Gabrielse *et al.*, 2006; Mair *et al.*, 2006). Early and mid-Cretaceous magmatism was widespread throughout Alaska and Yukon, with highly oxidized plutonic suites running in a northwest-southeast orientation and orogen-parallel (Fig. 1; Hart *et al.*, 2004; Mair *et al.*, 2006). In the study area, I-type plutons of the *ca.* 110-103 Ma Whitehorse plutonic suite are developed along the Dawson Range, while reduced coeval plutons occur across the back-arc (Fig. 2; Mortensen *et al.*, 2000; Baker and Lang, 2001).

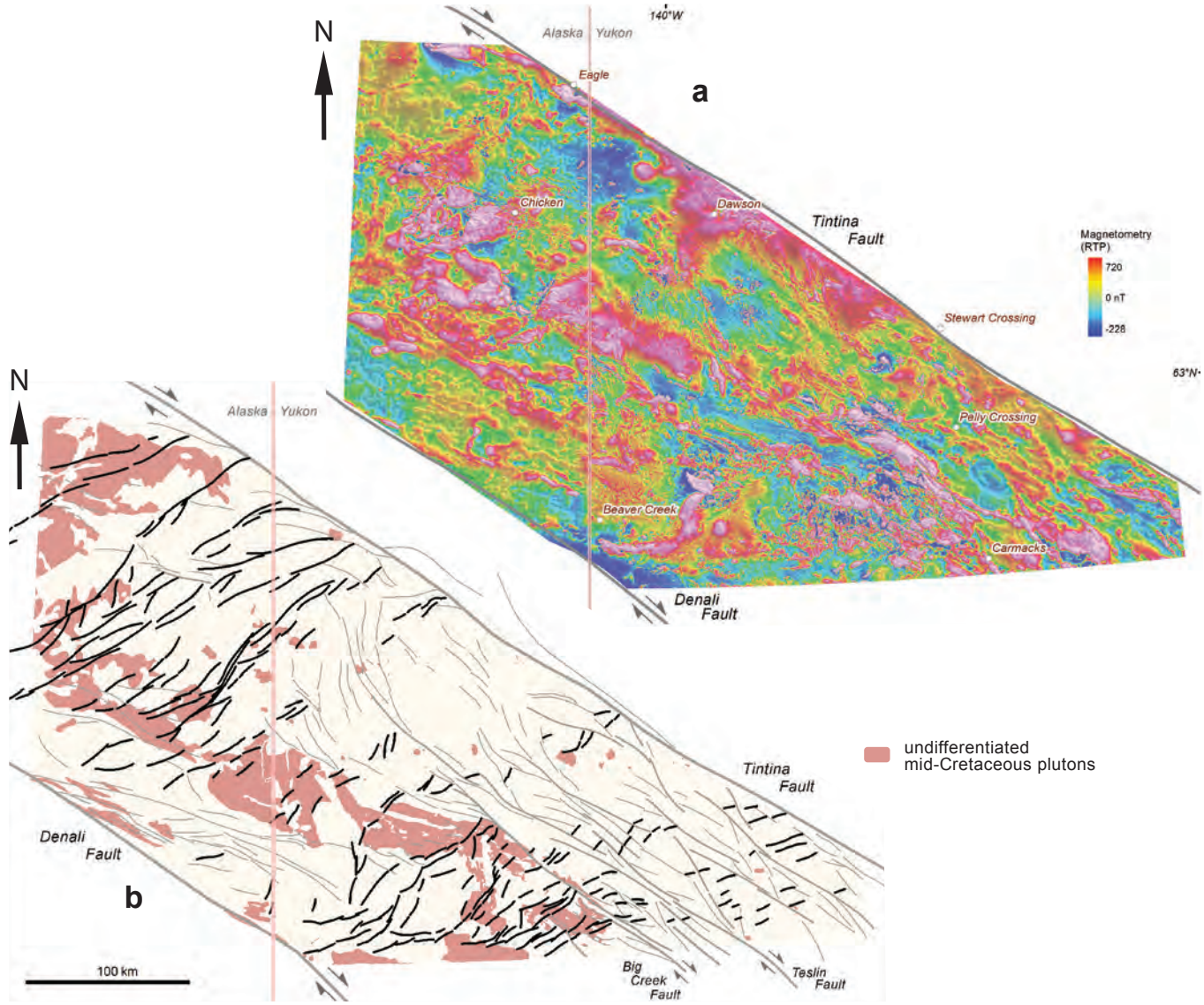

Figure 2. *(a) The levelled reduced-to-pole (RTP) magnetic grid generated by Fathom Geophysics LLC (Buckingham and Core, 2012). (b) Simplified map showing major magnetic discontinuities and magnetite-destructive lineaments of the magnetic dataset. Mid-Cretaceous plutonic rocks from the Whitehorse plutonic suite are shown in grey (modified from Gordey et al., 2005; Ryan et al., 2010; Beikman et al., 1980; and Gordey and Makepeace, 1999).*

METHODOLOGY

The magnetic dataset used in this study spans the northern Yukon-Tanana terrane and consists of a single, seamless reduced-to-pole (RTP) grid, with a 100 m grid cell for Alaska and Yukon (Buckingham and Core, 2012; Figs. 1 and 2). Source data includes regional datasets from the U.S. Geological Survey (USGS), Alaska Division of Geological and Geophysical Surveys (DGGS), and the recent NRCan Yukon Plateau compilation (Hayward *et al.*, 2011). Interpretation was carried out at a maximum scale of 1:300 000 and within a geographic information system platform (ArcGIS 10).

The current study focuses exclusively on linear magnetic discontinuities oriented at high angles to the regional northwest-southeast and orogen-parallel magnetic fabric (Fig. 2). Northwest-oriented magnetic signals correlate to the geometries of major geological contacts, the orientation of the Cretaceous magmatic arc, and to the presence of orogen-parallel fault systems. In the study area, orogen-perpendicular, linear, magnetic discontinuities are observed as magnetite-destruction trends of high-frequency and low-amplitude signals, which commonly border areas of distinct magnetic character (Fig. 3). Although our interpretation follows a similar methodology to ones previously reported (*e.g.*, Grant, 1985), we further emphasize a petrophysical approach (Clark, 1999; Clark *et al.*, 2004; Purucker and Clark, 2011). Our methodology considers common magnetic susceptibility ranges for rock types published in regional geological maps, as well as our own field measurements of magnetic susceptibility. Furthermore, end-member intensities of positive and

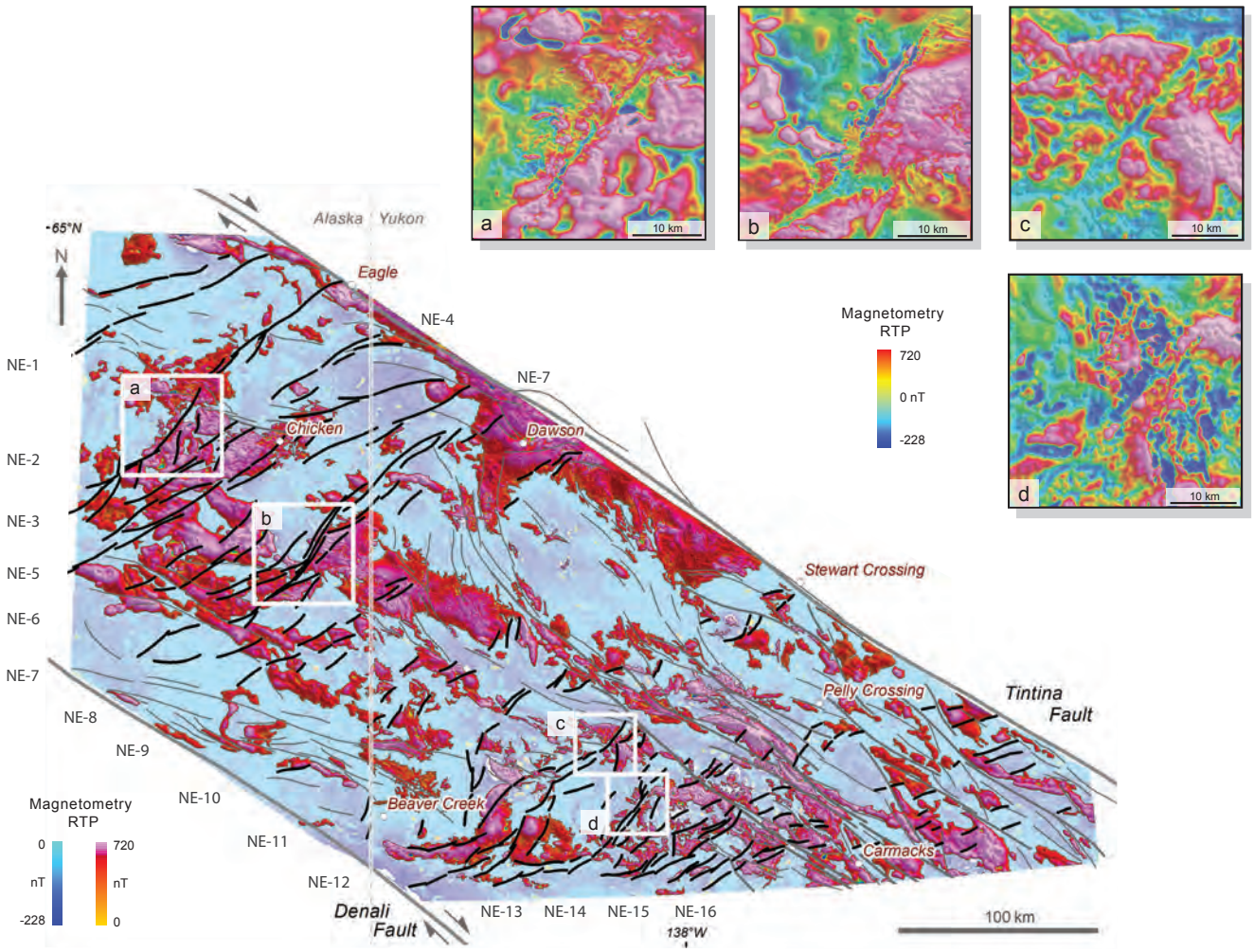

Figure 3. *Map-view examples of northeast-trending magnetic discontinuities of the reduced-to-pole grid. Bottom-left corner: Magnetic breaks and offsets in relation to extracted positive magnetic anomalies. Upper-right corner: Key examples of northeast-trending magnetite-destructive lineaments: (a) Ketchumstuk; (b) Sixtymile-Pika; (c) Dip Creek; and (d) Selwyn River.*

negative magnetic anomalies, as well as a series of range domains, were extracted from the RTP grid and compared to distinctive rock susceptibilities (*e.g.*, ultramafic rocks, magnetite-series plutonic suites) (Fig. 3).

The main objective in our structural-magnetometric interpretation focuses on the generation of a magnetic discontinuity map. This process consists of four main stages, beginning with tracing major linear features and discontinuities in the RTP magnetic grid (*i.e.*, magnetite-destructive lineaments and long axes of major magnetic anomalies). In the second stage, lineaments are compared against major structural geomorphology features from digital elevation models (regional 1 km resolution GEBCO 08 DEM and 30 m resolution Aster GDEM). In the third stage, possible structural offsets of geological contacts are evaluated from regional geological maps (Gordey and Ryan, 2005; Ryan *et al.*, 2010; Beikman *et al.*, 1980; Gordey and Makepeace, 1999). During the magnetic discontinuity map construction, a binary value is assigned to individual lineaments, according to whether they are also expressed in remote sensing datasets and geological maps. This quantified approach to multi-dataset interpretation results in a probability scale from which the most probable structures can be determined. Most plausible structures are represented by large scale magnetite-destructive lineaments, showing visible offsets of magnetic anomalies and geological contacts. These are commonly accompanied by a topographic trench and rarely offset drainages. In the final stage, lineaments have been grouped into sixteen zones of magnetic discontinuities according to their spatial distribution and density. These have been named consecutively, from north to south, as NE-1 to NE-16 (Fig. 3).

REGIONAL NE-SW MAGNETIC DISCONTINUITIES

Northeast-trending corridors of linear magnetite-destructive discontinuities truncate and offset some of the most prominent orogen and arc-parallel northwest-southeast oriented magnetic trends (Fig. 2). These high frequency and low intensity magnetic discontinuities are interpreted as the consequence of steeply-dipping fault systems oriented near perpendicular to the main regional magnetic signals (Fig. 3). Individual northeast oriented structural systems are composed of a series of linear segments of ~3 to 50 km in length that link and relay along strike. While these appear highly continuous and linear across the Alaskan part of the magnetometric grid, arcuate and highly segmented arrays commonly occur in the Yukon segment (Figs. 3 and 4). These regional geometric variations may result from shallower dips on fault surfaces in Yukon compared with steeper dips in Alaska. Major structural offsets and block segmentation are made evident when high intensity anomalies are extracted from the RTP dataset (Fig. 3). When the spatial distribution of lineaments and geological map units are compared, it is deduced that a series of major geological map patterns are constrained by northeast-southwest magnetic discontinuity corridors. An outstanding example is given by the along-strike block segmentation of the areal exposure of mid-Cretaceous igneous rocks of the Whitehorse plutonic suite (Fig. 2 and 5).

ALASKAN AREA

Across the Alaskan portion of the RTP magnetic grid, approximately eight major fault-fracture systems show highly continuous and linear patterns with major discontinuity zones reaching up to ~180 km in length (Figs. 2 and 4). Regional northeast-southwest oriented linear magnetic discontinuities are evident across the entire width of the Intermontane terrane block, *i.e.*, extending from the Denali to Tintina faults. Discrete, linear, magnetite-destructive discontinuities of up to ~60 km in length are responsible for the apparent truncation of orogen and arc-parallel shallow magnetic sources, as well as northwest-southeast elongated, high amplitude anomalies.

The most prominent magnetic truncations and offsets of high amplitude anomalies are observed in the Alaskan part of the study area. For example, a major geological and magnetic truncation is observed along the western edge of the Fortymile District, in Alaska, where the Ketchumstuk fault system runs for ~110 km in a northeast-southwest orientation (NE-3 in Figure 4a). This highly continuous structural system is composed of a linear central fault zone and associated oblique north-south oriented faults developed along a band of mid-Cretaceous intrusive rocks of the Whitehorse plutonic suite. Farther along strike to the north-east, this linear magnetic discontinuity defines the fault-bound margins of Late Triassic to Early Jurassic intrusions (Fig. 5). At least seven other regional scale discontinuities of similar orientation have been interpreted across the Alaskan portion of the RTP grid (Fig. 3). Additional examples of plan-view offsets of high amplitude anomalies, associated with mid-Cretaceous, oxidized plutonic rocks, are observed across NE-2 and NE-7 (Figs. 3 and 4).

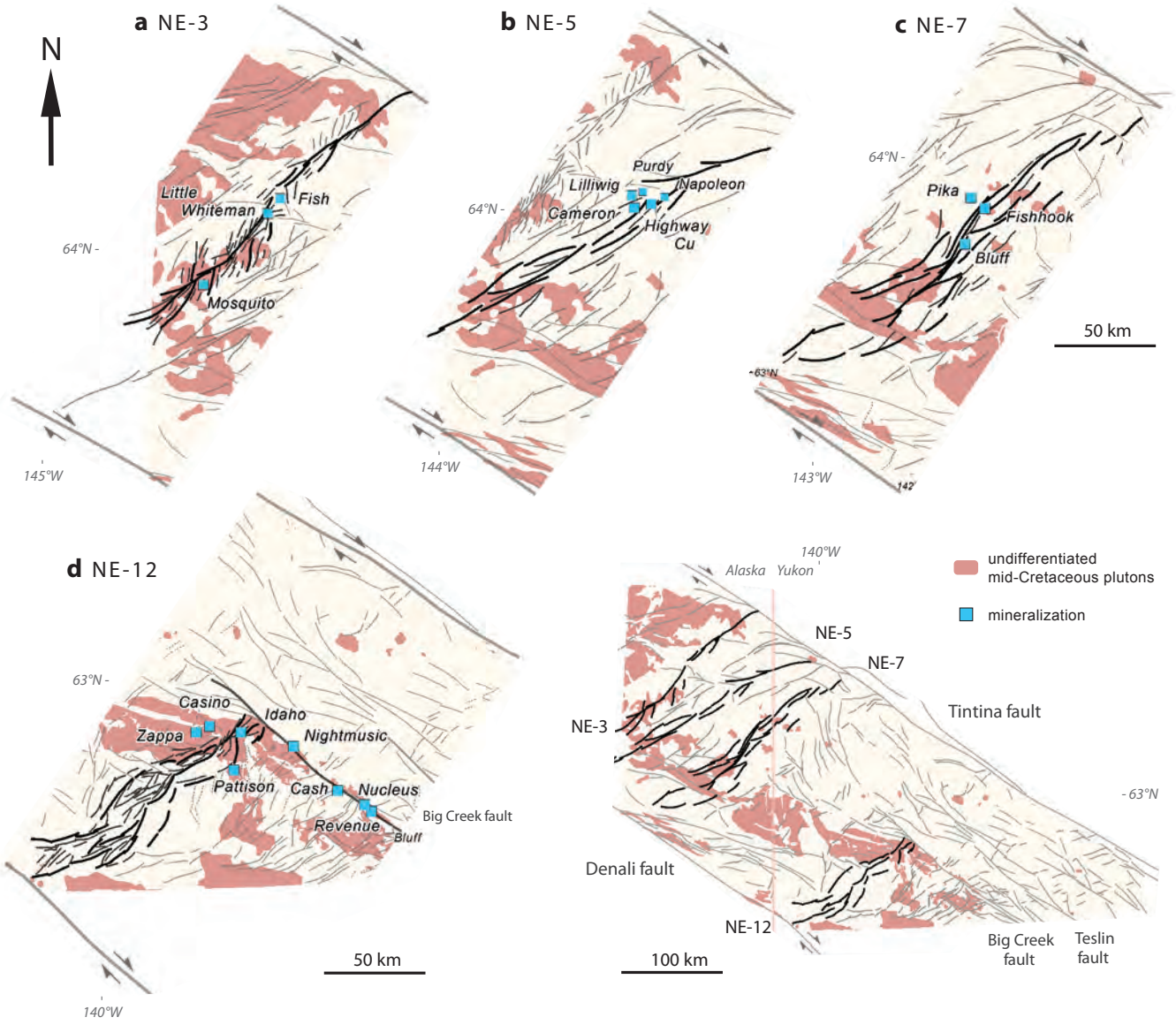

Figure 4. *Key examples of northeast-striking magnetic discontinuities, distribution of mid-Cretaceous plutons, and mainly Cretaceous magmatic-hydrothermal mineralization. The Alaska area shows continuous and linear northeast-trending "mag-breaks" (a, b, c), whereas the Yukon area is characterized by increased along-strike segmentation (d). Location map in bottom right corner. Mid-Cretaceous plutonic rocks modified from Gordey et al., 2005; Ryan et al., 2010; Beikman et al., 1980; and Gordey and Makepeace, 1999.*

YUKON AREA

Towards the center and south-eastern portion of the RTP magnetic grid and east of the Alaska-Yukon border, northeast-southwest oriented, magnetite-destructive lineaments display increasingly curvilinear geometry and increased along-strike segmentation (Figs. 3 and 4). These systems of linear magnetic discontinuities are frequently composed of a series of individual segments of 10 to 50 km in length that are interpreted to link and relay along strike. North of the Dawson Range, all five major structural corridors (NE-9 to NE-13 in Fig. 3) appear truncated by at least two major northwest-southeast oriented regional magnetic discontinuities. These correspond to the Big Creek and Teslin faults, both major, dextral, strike-slip structures of mid to Late Cretaceous age (Fig. 4; Colpron *et al.*, 2007; Gabrielse *et al.*, 2006).

The northeast-oriented Dip Creek fault (Johnston, 1999) is the most prominent orogen-perpendicular magnetic truncation of the Yukon area (Fig. 4d). We interpret this fault as extending for ~130 km from near the Denali fault to the northern flank of the Dawson Range, where it terminates immediately south of the Big Creek fault. The Dip Creek fault is interpreted as a highly segmented structural corridor composed of arcuate border faults and internal faults. This fault zone is up to ~16 km wide, with its narrower northeastern section generating a major offset across the Dawson Range batholith (Fig. 4d). In addition to the Dip Creek fault system, at least five other prominent examples of segmented northeast-southwest discontinuities are interpreted south of the Big Creek fault across the Dawson Range (Fig. 3).

IMPLICATIONS FOR MINERALIZATION

At the scale of the current interpretation, a number of established mid to Late Cretaceous porphyry and hydrothermal mineral occurrences and deposits cluster along the arc-perpendicular structures defined in this study (Figs. 4 and 5). These magnetic lineaments are interpreted to define zones of increased structural damage and enhanced permeability, which may consequently focus mid to Late Cretaceous magmatism, hydrothermal activity, and mineralization. While the northeast-southwest structures may represent a first order structural control across the Alaskan quadrant, a weaker, secondary role is interpreted for the Yukon segment of the Dawson Range. The most obvious correlations between northeast-trending structures and Late Cretaceous porphyry and polymetallic vein occurrences occur along the NE-3 (Ketchumstuk fault) and NE-7 structural corridors of the Fortymile and Sixtymile areas (Figs. 4a,c). A more complex scenario occurs along the Dawson Range, with examples of second order structural controls from the NE-12 zone of the Dip Creek fault (Fig. 4d).

ALASKAN AREA

Along the Ketchumstuk fault of the Fortymile District (Szumigala *et al.*, 2003), or in close proximity to it, a series of known mid to Late Cretaceous magmatic-related mineral occurrences and deposits occur (Fig. 4a). Known Cretaceous deposits along the western segment of NE-3 include the 70.5 Ma Fish massive sulphide prospect (Ag, Cu, Pb, Zn) (Dusel-Bacon *et al.*, 2007; Full Metal Minerals, 2012). The Little Whiteman carbonate replacement prospect (Zn, Pb, Ag) and the Mosquito porphyry Cu-Mo prospect may also be of similar age (Cox and Singer, 1986). Further examples of Cretaceous magmatic-related mineralization and northeast trending faults occur at the NE-7 of the Sixtymile River area in the vicinity of the Yukon/Alaska border (Fig. 4c). These include the Bluff/Taurus and Pika Canyon Cu-Mo-Au porphyry deposits (Cox and Singer, 1986), as well as the Fishhook Ag-Au (barite, Cu, Mo, Pb, Sb) prospect (http://www.mindat.org/loc-197486.html). A major cluster of age-unconstrained, magmatic-related lode gold mineralization and associated placer gold deposits occur where NE-5 intersects with a major northwest-trending magnetic discontinuity (Fig. 4b). Here, intrusion-related mineralization occurs in the Cameron (Chicken West; Opal), Highway Copper (Bruce), and Lilliwig Creek prospects, as well as a number of unnamed occurrences (Alaska ARDF, 2012). The Napoleon shear-hosted gold prospect (Werdon *et al.*, 2001) and Purdy epithermal gold veins (Cox and Singer (eds.), 1986) have been assigned an Early Jurassic mineralization age (*ibid*).

YUKON AREA

In central Yukon, the northwest-trending Big Creek fault controls the distribution of mid to Late Cretaceous magmatism and generates a highly linear magnetic discontinuity and morphologic trench which extends for ~120 km along the northeastern flank of the Dawson Range (Figs. 4 and 5). This dextral fault system exerts a first-order structural role in the emplacement of Late Cretaceous deposits and occurrences (Bennett *et al.*, 2010). Notable examples include the Cash (Cu, Mo) porphyry (Selby and Creaser, 2001), the Nightmusic zone of the Sonora Gulch porphyry prospect (Northern Tiger, 2012), and the Nucleus and Revenue Au porphyries (Northern Freegold, 2012a,b; Fig. 4d). Although northeast-southwest structures appear to play a secondary role in the area, their intersection with the Big Creek fault may generate zones of enhanced permeability and mineralization. The Dip Creek fault (NE-12), the most significant northeast-trending fault in the area, dislocates the mid-Cretaceous Dawson Range batholith and shows a regional-scale correlation with a series of Late Cretaceous porphyry-related systems (Figs. 4d and 5). Examples include: the mid-Cretaceous Idaho Au-Ag vein zone, Pattison Cu-Mo porphyry prospect, the Zappa Cu porphyry-style anomaly, and most notably, the Late Cretaceous Casino Cu-Mo-Au porphyry deposit (Fig. 4d; Selby and Creaser, 2001).

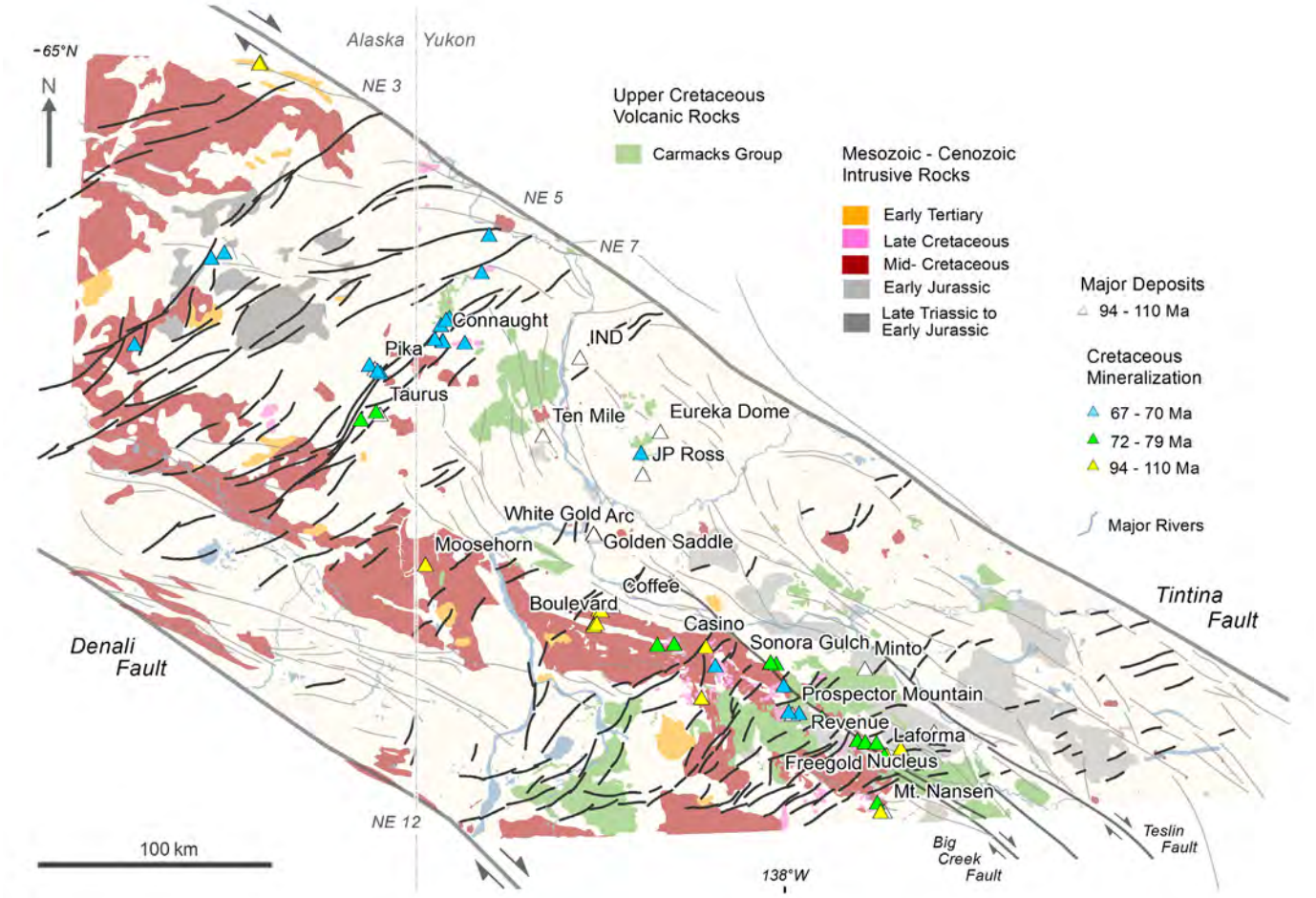

Figure 5. *Simplified geological map showing the along-strike northeast-trending segmentation of Mesozoic geologic units and the spatial distribution of major mineral deposits and mid to Late Cretaceous magmatic-hydrothermal mineralization (modified from Gordey et al., 2005; Ryan et al., 2010; Beikman et al., 1980; and Gordey and Makepeace, 1999). Magnetic discontinuities and geological offsets are most commonly observed across the mid-Cretaceous igneous arc and Upper Cretaceous Carmacks Group volcanics.*

DISCUSSION

We infer that the series of magnetite-destructive linear discontinuities interpreted from the reduced-to-pole grid (Buckingham and Core, 2012), correlate with steeply-dipping brittle fault systems of post-Jurassic age. Several of these discontinuities have been mapped as faults in regional geologic maps, although a much larger number of faults are inferred from the current study. Evidence of along-strike fault-block segmentation by northeast-trending magnetite-destructive discontinuities include: (1) abrupt variations in the orientation of geological contacts and map-view exposure of intrusive units; (2) map-view linear offsets of major geological units (e.g., Dawson Range batholith); (3) distribution of sedimentary basins (e.g., Paleogene volcano-sedimentary sediments) and volcanic units (e.g., Carmacks Group volcanics); and (4) the presence and offsets of geomorphologic trenches and ridges, as well as river systems (Fig. 5). In accordance to their linear geometry, these northeast-trending structural systems are interpreted as steep, brittle extensional, oblique-extensional or strike-slip fault systems. Their regional dimensions, regular spacing, and similar magnetic character and geometries suggest that they arise from a common tectonic process.

Structural controls on hydrothermal and subvolcanic ore systems largely derive from the role that deformation processes and fluid pressures play on generating and maintaining permeability within active faults, shear zones,

and associated fracture networks, at various crustal levels (Cox, 1999; Micklethwaite and Cox, 2004; Berger, 2007; Sibson, 1987). We infer that steeply dipping, northeast-trending, brittle structures have focused pervasive fracturing with the capability to generate a substantial increase in rock permeability and pressure gradients. Secondary permeability may be further enhanced at structural intersections with regional fault systems which controlled mid-Cretaceous magmatism (*e.g.*, Big Creek fault). World-class examples of magmatic hydrothermal Cu-Au deposits, located at zones of intersection between oblique structures and younger structurally-controlled magmatic arcs, have been proposed for the middle Eocene to early Oligocene metallogenic belt of northern Chile (Richards *et al.*, 2001; Richards, 2003; Sillitoe and Perello, 2005; Sillitoe, 2010). Within this belt, gigantic porphyry deposits (*e.g.*, La Escondida, El Salvador, Chiquicamata) and epithermal systems (*e.g.*, Pascua Lama, La Coipa) cluster at the junction of northwest-trending basement segments with north-south oriented magmatic arcs and structural systems (*e.g.*, West Fissure). In a similar manner to the northern Chilean Andes, the identification of structural systems, crosscutting at high angles to the mid-Cretaceous Dawson Range arc and regional fault systems, may provide relevant criteria for targeting porphyry and epithermal ore systems in the Northern Cordillera.

CONCLUSION

Northeast-oriented structures, as interpreted from a series of linear magnetic discontinuities, are orientated semi-perpendicularly to the regional northwest-trending magnetic grain, mid-Cretaceous magmatic arc, and overall Mesozoic to Cenozoic structural architecture. These magnetite-destructive corridors are interpreted as steeply dipping brittle fault zones and fracture arrays of extensional, oblique-extensional, and strike-slip kinematics, responsible for localized structural damage and along-strike block segmentation. Within these structural systems, substantial increments in rock permeability, fluid flow, and pressure gradients may favour the generation of mid to Late Cretaceous hydrothermal veins and subvolcanic stocks.

At the scale of observation in the current study, the spatial correlation between northeast-oriented steep dipping structural systems and known mid to Late Cretaceous magmatic-hydrothermal mineral deposits and occurrences suggests a first-order structural control in eastern Alaska. Arc-parallel structures like the Big Creek fault exert the first-order structural control on magmatic-hydrothermal systems in the Dawson Range, but northeast structures such as the Dip Creek fault system may play a second-order role. The relationship of northeast-oriented structures to exposures of Carmacks Group volcanic rocks and mineral prospects of known Late Cretaceous age, suggests that these structures were mainly active in Late Cretaceous time.

ACKNOWLEDGEMENTS

Funding for this research has been provided by grants from Natural Resources Canada (NRCan) and from the Natural Sciences and Engineering Research Council of Canada (NSERC). Additional support has been provided by the Yukon Gold Project, a collaborative research venture between the Mineral Deposit Research Unit (The University of British Columbia) and a consortium of industry participants. The authors are also grateful to Steve Israel for helpful comments on this manuscript.

REFERENCES

Alaska ARDF, 2012. Resource Data File - Alaska (ARDF). Alaska ARDF on the web, https://explore.data.gov/Geography-and-Environment/Resource-Data-File-Alaska-ARDF-/f9ps-ajhr, retrieved December, 20, 2012.

Baker, T. and Lang, J.R., 2001. Fluid inclusion characteristics of intrusion-related gold mineralization, Tombstone-Tungsten magmatic belt, Yukon Territory, Canada. Mineralium Deposita, vol. 36, p. 563-582.

Beikman, H.M., 1980. Geologic map of Alaska. U.S. Geological Survey, 1:2 500 000.

Bennett, V., Colpron, M., and Burke, M., 2010. Current thinking on Dawson Range Tectonics and Metallogeny. Yukon Geological Survey, Miscellaneous Report MR-2.

Berger, B.R., 2007. The 3D fault and vein architecture of strike-slip releasing- and restraining bends: evidence from volcanic-centre-related mineral deposits. Geological Society, London, Special Publications, vol. 290, p. 447-471.

Buckingham, A. and Core, D., 2012. Enhancement Filtering and Structure Detection Magnetic and Gravity Data, MDRU Project Area Yukon Alaska. Fathom Geophysics, internal report.

Clark, D., 1999. Magnetic petrology of igneous intrusions: implications for exploration and magnetic interpretation. Exploration Geophysics, vol. 30, p. 5–26.

Clark, D., Geuna, S., and Schmidt, P., 2004. Predictive magnetic exploration models for porphyry, epithermal, and iron oxide copper-gold deposits: implications for exploration. AMIRA International Ltd., P700 Final Report.

Colpron, M. and Nelson, J.L., 2011. A Digital Atlas of Terranes for the Northern Cordillera. British Columbia Geological Survey, GeoFile 2011-11.

Colpron, M., Nelson, J.L., and Murphy, D.C., 2007. Northern Cordilleran terranes and their interactions through time. GSA Today, vol. 17, p. 4-10.

Cooke, D.R., McPhail, D.C., and Bloom, M.S., 1996. Epithermal gold mineralization, Acupan, Baguio District, Philippines; geology, mineralization, alteration, and the thermochemical environment of ore deposition. Economic Geology, vol. 91, p. 243-272.

Cordey, F., Mortimer, N., DeWever, P., and Monger, J.W.H., 1987. Significance of Jurassic radiolarians from the Cache Creek terrane, British Columbia. Geology, vol. 15, p. 1151-1154.

Cox, S.F., 1999. Deformational controls on the dynamics of fluid flow in mesothermal gold systems. Geological Society, London, Special Publications, vol. 155, p. 123-140.

Cox, S.F. and Ruming, K., 2004. The St Ives mesothermal gold system, Western Australia—a case of golden aftershocks? Journal of Structural Geology, vol. 26, p. 1109-1125.

Cox D.P. and Singer D.A. (eds.), 1986. Mineral Deposit Models. US Geological Survey, Bulletin 1693, 379 p.

Crawford, B.L., Betts, P.G., and Aillères, L., 2010. An aeromagnetic approach to revealing buried basement structures and their role in the Proterozoic evolution of the Wernecke Inlier, Yukon Territory, Canada. Tectonophysics, vol. 490, p. 28-46.

Domzalski, W., 1966. Importance of Aeromagnetics in Evaluation of Structural Control of Mineralization. Geophysical Prospecting, vol. 14, p. 273-291.

Dusel-Bacon, C., Lanphere, M.A., Sharp, W.D., Layer, P.W., and Hansen, V.L., 2002. Mesozoic thermal history and timing of structural events for the Yukon-Tanana Upland, east-central Alaska: 40Ar/39Ar data from metamorphic and plutonic rocks. Canadian Journal of Earth Sciences, vol. 39, p. 1013-1051.

Dusel-Bacon, C., Slack, J.F., Aleinikoff, J.N., and Mortensen, J.K., 2007. Mesozoic magmatism and base-metal mineralization in the Fortymile mining district, eastern Alaska: initial results of petrographic, geochemical, and isotopic studies in the Mount Veta area. US Geological Survey, Professional Paper 1760-A, 50 p.

Full Metal Minerals, 2012. Full Metal Discovers a Second Massive Sulphide System at 40 Mile. Full Metal Minerals on the Web, http://www.fullmetalminerals.com/380/, retrieved December 20, 2012.

Gabrielse, H., 1985. Major dextral transcurrent displacements along the Northern Rocky Mountain Trench and related lineaments in north-central British Columbia. Geological Society of America, Bulletin 96, p. 1-14.

Gabrielse, H., Murphy, D.C., and Mortensen, J.K., 2006. Cretaceous and Cenozoic dextral orogen-parallel displacements, magmatism, and paleogeography, north-central Canadian Cordillera. *In:* Paleogeography of the North American Cordillera: Evidence For and Against Large-Scale Displacements, J.W. Haggart, R.J. Enkin, and J.W.H. Monger (eds.), Geological Association of Canada, Special Paper 46, p. 255-276.

Garrity, C.P. and Soller, D.R., 2009. Database of the Geologic Map of North America; adapted from the map by J.C. Reed, Jr. and others (2005), 1:5 000 000. U.S. Geological Survey Data Series 424, http://pubs.usgs.gov/ds/424/.

Gordey, S.P. and Makepeace, A.J. (comps.), 1999. Yukon Digital Geology. Indian & Northern Affairs Canada/ Department of Indian & Northern Development: Exploration & Geological Services Division, Open File 1999-1(D).

Gordey, S.P. and Ryan, J.J., 2005. Geology, Stewart River Area (115 N, 115 O, and part of 115 J), Yukon Territory. Geological Survey of Canada, Open File 4970, 1:250 000.

Grant, F.S., 1985. Aeromagnetics, geology and ore environments, I. Magnetite in igneous, sedimentary and metamorphic rocks: an overview. Geoexploration, vol. 23, p. 303-333.

Gunn, P. and Dentith, M., 1997. Magnetic responses associated with mineral deposits. AGSO Journal of Australian Geology and Geophysics vol. 17, p. 145–158.

Hart, C.J., Goldfarb, R.J., Lewis, L.L., and Mair, J.L., 2004. The Northern Cordilleran Mid-Cretaceous Plutonic Province: Ilmenite/Magnetite-series Granitoids and Intrusion-related Mineralization. Resource Geology, vol. 54, p. 253-280.

Hayward, N., Miles, W., and Oneschuk, D., 2011. Geophysical Series, regional geophysical compilation project, Yukon Plateau, Yukon, parts of NTS 105, 106, 115 and 116. Geological Survey of Canada, Open File 6959.

Hedenquist, J.W., Izawa, E., Arribas, A., and White, N.C., 1996. Epithermal gold deposits: Styles, characteristics, and exploration. Resource Geology Special Publication Number 1. Society of Resource Geology, Japan, 16 p.

Henley, R.W. and Adams, D.P.M., 1992. Strike-slip fault reactivation as a control on epithermal vein-style gold mineralization. Geology, vol. 20, p. 443-446.

Izawa, E., Urashima, Y., Ibaraki, K., Suzuki, R., Yokoyama, T., Kawasaki, K., Koga, A. and Taguchi, S., 1990. The Hishikari gold deposit: high-grade epithermal veins in Quaternary volcanics of southern Kyushu, Japan. Journal of Geochemical Exploration, vol. 36, p. 1-56.

Johnston, S.T., 1999. Large-scale coast-parallel displacements in the Cordillera: a granitic resolution to a paleomagnetic dilemma. Journal of structural geology, vol. 21, p. 1103-1108.

Logan, J.M., Schiarizza, P., Struik, L.C., Barnett, C., Nelson, J.L., Kowalczyk, P., Ferri, F., Mihalynuk, M.G., Thomas, M.D., Gammon, P., Lett, R., Jackaman, W., and Ferbey, T., 2010. Geoscience Map 2010-1: Bedrock Geology of the QUEST map area, central British Columbia. Geological Survey of Canada, Open File 6476.

Lund, K., 2008. Geometry of the Neoproterozoic and Paleozoic rift margin of western Laurentia: Implications for mineral deposit settings. Geosphere, vol. 4, p. 429.

Mair, J.L., Hart, C.J., and Stephens, J.R., 2006. Deformation history of the northwestern Selwyn Basin, Yukon, Canada: Implications for orogen evolution and mid-Cretaceous magmatism. Geological Society of America, Bulletin 118, p. 304-323.

McMechan, M.E., 2012. Deep transverse basement structural control of mineral systems in the southeastern Canadian Cordillera. Geological Survey of Canada, Contribution 20110294. Canadian Journal of Earth Sciences, vol. 49, p. 693-708.

Micklethwaite, S. and Cox, S.F., 2004. Fault-segment rupture, aftershock-zone fluid flow, and mineralization. Geology, vol. 32, p. 813-816.

Micklethwaite, S., Sheldon, H.A., and Baker, T., 2010. Active fault and shear processes and their implications for mineral deposit formation and discovery. Journal of Structural Geology, vol. 32, p. 151-165.

Mihalynuk, M.G., Nelson, J., and Diakow, L.J., 1994. Cache Creek terrane entrapment: Oroclinal paradox within the Canadian Cordillera. Tectonics, vol. 13, p. 575-595.

Mihalynuk, M.G., Smith, M.T., Gabites, J.E., Runkle, D., and Lefebure, D., 1992. Age of emplacement and basement character of the Cache Creek terrane as constrained by new isotopic and geochemical data. Canadian Journal of Earth Sciences, vol. 29, p. 2463-2477.

Mortensen, J.K., 1992. Pre-Mid-Mesozoic tectonic evolution of the Yukon-Tanana terrane, Yukon and Alaska. Tectonics, vol. 11, p. 836-853.

Mortensen, J.K., Hart, C.J.R., Murphy, D.C., and Heffernan, S., 2000. Temporal evolution of Early and mid-Cretaceous magmatism in the Tintina Gold Belt. *In:* The Tintina Gold Belt: Concepts, Exploration and Discoveries, T.L. Tucker and M.T. Smith (eds.), Vancouver, British Columbia and Yukon Chamber of Mines, Cordilleran Roundup, Special Volume 2, p. 49-57.

Nabighian, M.N., Grauch, V.J.S., Hansen, R.O., LaFehr, T.R., Li, Y., Peirce, J.W., Phillips, J.D., and Ruder, M.E., 2005. 75th Anniversary: The historical development of the magnetic method in exploration. Geophysics, vol. 70, p. 33ND-61ND.

Nelson, J.L., Colpron, M., Piercey, S.J., Dusel-Bacon, C., Murphy, D.C., and Roots, C.F., 2006. Paleozoic tectonic and metallogenic evolution of the pericratonic terranes in Yukon, northern British Columbia and eastern Alaska. *In:* Paleozoic Evolution and Metallogeny of Pericratonic Terranes at the Ancient Pacific Margin of North America, Canadian and Alaskan Cordillera, M. Colpron, and J.L. Nelson, (eds.), Geological Association of Canada, Special Paper 45, p. 323-360.

Northern Freegold, 2012a. Northern Freegold Extends the Nucleus Gold Deposit. Northern Freegold Resources on the web, http://www.northernfreegold.com/s/NewsReleases.asp?ReportID=551882, retrieved December 20, 2012.

Northern Freegold, 2012b. Northern Freegold Files Revenue Deposit NI 43-101 Technical Report at Freegold Mountain. Northern Freegold Resources on the web, http://www.northernfreegold.com/s/NewsReleases.asp?ReportID=511840, retrieved December 20, 2012.

Northern Tiger, 2012. Sonora Gulch Project. Northern Tiger Resources on the web, http://www.northern-tiger.com/s/Sonora.asp, retrieved December 20, 2012.

Pilkington, M. and Saltus, R.W., 2009. The Mackenzie River magnetic anomaly, Yukon and Northwest Territories, Canada—Evidence for Early Proterozoic magmatic arc crust at the edge of the North American craton. Tectonophysics, vol. 478, p. 78-86.

Pilkington, M., Snyder, D.B., and Hemant, K., 2006. Weakly magnetic crust in the Canadian Cordillera. Earth and Planetary Science Letters, vol. 248, p. 476-485.

Purucker, M.E. and Clark, D.A., 2011. Mapping and Interpretation of the Lithospheric Magnetic Field. Geomagnetic Observations and Models, vol. 5, p. 311-337.

Richards, J.P., 2003. Tectono-Magmatic Precursors for Porphyry Cu-(Mo-Au) Deposit Formation. Economic Geology, vol. 98, p. 1515-1533.

Richards, J.P., Boyce, A.J., and Pringle, M.S., 2001, Geological evolution of the Escondida area, northern Chile: A model for spatial and temporal localization of porphyry Cu mineralization. Economic Geology, vol. 96, p. 271–305.

Ryan, J.J., Colpron, M., and Hayward, N., 2010. Geology, southwestern Mcquesten and parts of northern Carmacks, Yukon. Geological Survey of Canada, Canadian Geoscience Map 7 (preliminary version), 1:125 000.

Saltus, R.W., 2007. Matching magnetic trends and patterns across the Tintina fault, Alaska and Canada - Evidence for offset of about 490 kilometers *In:* Recent U.S. Geological Survey Studies in the Tintina Gold Province, Alaska, United States, and Yukon, Canada. Results of a 5-Year Project, L.P. Gough, and W.C. Day, (eds.), U.S. Geological Survey, Scientific Investigations Report 2007-5289-C, 7 p.

Sandrin, A., Berggren, R., and Elming, S., 2007. Geophysical targeting of Fe-oxide Cu-(Au) deposits west of Kiruna, Sweden. Journal of Applied Geophysics, vol. 61, p. 92–101.

Selby, D. and Creaser, R.A., 2001. Late and mid-Cretaceous mineralization in the northern Canadian Cordillera: Constraints from Re-Os molybdenite dates. Economic Geology, vol. 96, p. 1461-1467.

Sibson, R.H., 1987. Earthquake rupturing as a mineralizing agent in hydrothermal systems. Geology, vol. 15, p. 701-704.

Sillitoe, R.H., 1997. Characteristics and controls of the largest porphyry copper-gold and epithermal gold deposits in the circum-Pacific region. Australian Journal of Earth Sciences, vol. 44, p. 373-388.

Sillitoe, R.H. and Perelló, J., 2005. Andean copper province: Tectonomagmatic settings, deposit types, metallogeny, exploration, and discovery. Economic Geology, 100th Anniversary Volume, p. 845–890.

Sillitoe, R.H., 2010. Porphyry copper systems. Economic Geology, vol. 105, p. 3-41.

Szumigala, D.J., Hughes, R.A., and Harris, R.H., 2003. Alaska Mineral Industry 2003. Division of Geological and Geophysical Survey, Fairbanks, Alaska, Special Report 58.

Van Leeuwen, T.M., Leach, T., Hawke, A.A., and Hawke, M.M., 1990. The Kelian disseminated gold deposit, east Kalimantan, Indonesia. Journal of Geochemical Exploration, vol. 35, p. 1-61.

Vikre, P.G., 1989. Fluid-mineral relations in the Comstock Lode. Economic Geology, vol. 84, p. 1574-1613.

Werdon, M.B., Newberry, R.J., Szumigala, D.J., and Burns, L.E., 2001. Reconnaissance bedrock geology of the Pogo area, Big Delta B-2 and B-3 Quadrangles, Alaska. Alaska Division of Geological and Geophysical Surveys, Preliminary Interpretive Report 2001-5, 1:63 360.

Willis, G.F. and Tosdal, R.M., 1992. Formation of gold veins and breccias during dextral strike-slip faulting in the Mesquite mining district, southeastern California. Economic Geology, vol. 87, p. 2002-2022.

Preliminary observations on the geology and mineralogy of the Rapid Creek Formation, Blow River and Davidson Mountains map area (NTS 117A/8 and NTS117 A/9), Yukon

Heidi Tomes
Department of Earth Sciences, University of Toronto, Toronto, ON

Kimberly Tait and Ian Nicklin
Royal Ontario Museum, Toronto, ON

Ronald Peterson
Department of Geological Sciences and Geological Engineering, Queen's University, Kingston, ON

Robert Beckett
Peterborough, Ontario

Tomes, H., Tait, K., Nicklin, I., Peterson, R., and Beckett, R., 2013. Preliminary observations on the geology and mineralogy of the Rapid Creek Formation, Blow River and Davidson Mountains map area (NTS 117A/8 and NTS117A/9), Yukon. *In:* Yukon Exploration and Geology 2012, K.E. MacFarlane, M.G. Nordling, and P.J. Sack (eds.), Yukon Geological Survey, p. 147-161.

ABSTRACT

The Rapid Creek Formation, exposed at Big Fish River and Rapid Creek, in the Richardson Mountains of Yukon is well known for its rare phosphate minerals. Mapping, geochemical sampling, and collection of phosphate minerals and nodules from this formation occurred over a three week field program in the summer of 2012. The Rapid Creek Formation is a phosphorite-rich ironstone facies composed of alternating beds of phosphate and siderite-rich mudstones and shale. Secondary minerals collected from crosscutting mineralized veins in this area include unusual apatite, augelite, arrojadite group minerals, dypingite, lazulite, and garyansellite-kryzhanovskite. Phosphate nodules with satterlyite, wolfeite, vivianite-barićite, wicksite, and arrojadite-group minerals have been identified and collected for study.

[1]*tomes@es.utoronto.ca*

INTRODUCTION

Phosphate minerals were first discovered in the Rapid Creek area when Campbell (1962) identified lazulite, $MgAl_2(PO_4)_2(OH)_2$, in samples collected by B. Cameron, but this early discovery was not followed up on. In the 1970s, F.G. Young, a geologist with the Geological Survey of Canada noted this occurrence which drew the attention of Welcome North Mines (Young, 1972; Young and Robertson, 1984). Subsequently Al Kulan, prospector and Director of Welcome North Mines, found large well-crystallized specimens of lazulite and other phosphate minerals while staking claims in the area (Young and Robertson, 1984; Robinson *et al.*, 1992). The incredible quality of the crystals of rare phosphates such as wardite, $NaAl_3(PO_4)_2(OH)_4{\cdot}2H_2O$, arrojadite-group minerals, and lazulite (now recognized as Yukon's official gemstone) prompted numerous collecting trips to the area by Royal Ontario Museum mineralogists throughout the 1970s (Robinson *et al.*, 1992). There have been fifteen new minerals discovered from this region, including barićite (Sturman and Mandarino, 1976), gormanite (Sturman *et al.*, 1981a), marićite (Sturman *et al.*, 1977), nahpoite (Coleman and Robertson, 1981), satterlyite (Mandarino *et al.*, 1978), and wicksite (Sturman *et al.*, 1981b). More recently, previously collected samples from this locality have been studied with modern instruments resulting in the description of bobdownsite (Tait *et al.*, 2011), and new arrojadite group end members (Tomes, in progress). Many studies in the 1970s and 1980s described these new minerals but only studies by Robertson (1980, 1982), Young and Robertson (1984) and Yeo (1992) have considered the geological setting of these minerals.

The Rapid Creek Formation is unusual in a number of respects: (1) the formation conditions for phosphorites and siderite-rich ironstones are not complementary to one another; (2) primary mineralogy in most phosphorite consists of carbonate-rich fluorapatite (commonly known as francolite), $Ca_5(PO_4,CO_3)_3(F,O)$; however, at Big Fish River the principal mineralogy consists of microcrystalline secondary phosphate minerals with an unknown Ca-Fe-Mg phosphate origin (Robertson, 1980, 1982). (3) The geological environment that allowed these assemblages of rare phosphates to form is unique; the sedimentary rocks host several mineral species previously known only from igneous and more highly metamorphosed environments.

The current study has set out to elucidate the relationships between the host ironstone and the unusual secondary phosphate minerals found at this locality. In the summer of 2012, the authors completed a three week, preliminary mapping and geochemical sampling field program of the Rapid Creek Formation at Big Fish River, Yukon and collected specimens from both Rapid Creek and Big Fish River. A preliminary study of the geological setting and mineralization observed during this field program is presented here.

GEOLOGICAL SETTING

The phosphatic ironstone deposit at Rapid Creek and Big Fish River lies within the Richardson Mountains in northeast Yukon (Fig. 1; Young *et al.*, 1976). The sediments were deposited as part of an Aptian-Albian flysch sequence in the Blow trough, a structural depression about 50 km wide that runs approximately north-south (Young and Robertson, 1984; Robinson *et al.*, 1992). The sequence was bordered by the Cache Creek High to the east, where the Richardson Mountains are now located, and uplift to the west (Young and Robertson, 1984; Robinson *et al.*, 1992). The combination of subsidence of the Blow trough and erosion due to the uplift to the west resulted in the formation of a thick sequence of turbidite sandstone, conglomerate, mudstone, and shale which thins towards the eastern structural high and grades into the Rapid Creek Formation (Young and Robertson, 1984; Robinson *et al.*, 1992). The flyschoid sequence was buried by approximately 1500 to 3000 m of sediment during the Late Cretaceous and Early Tertiary, and was later affected by the onset of Tertiary Laramide deformation, which caused faulting, compression, uplift, and erosion to occur, bringing the Albian portion of the sequence to the present day surface (Young and Robertson, 1984).

RAPID CREEK FORMATION

The strata studied here have been called various names such as the Aptian-Albian flysch division (Young *et al.*, 1976), the upper Aptian to lower Albian flysch (Jeletzky, 1971), the Albian flyschoid phase (Young, 1973; Norris and Yorath, 1981), and the Aptian-Albian flysch sequence (Young, 1972). Yeo (1992) notes that Robertson (1980, 1982) proposed the name the Rapid Creek Formation but disputes this title commenting that at least three units of formation rank are described within this by Norris (1981, 1983) and Young (1977). Yeo (1992) describes a Rapid Creek group that includes three map units from Norris (1981) Ksr, Krr, and Kbr and informally calls the unit of interest the Blow River Formation. However, Yeo (1992) overlooks the description by Young and Robertson (1984)

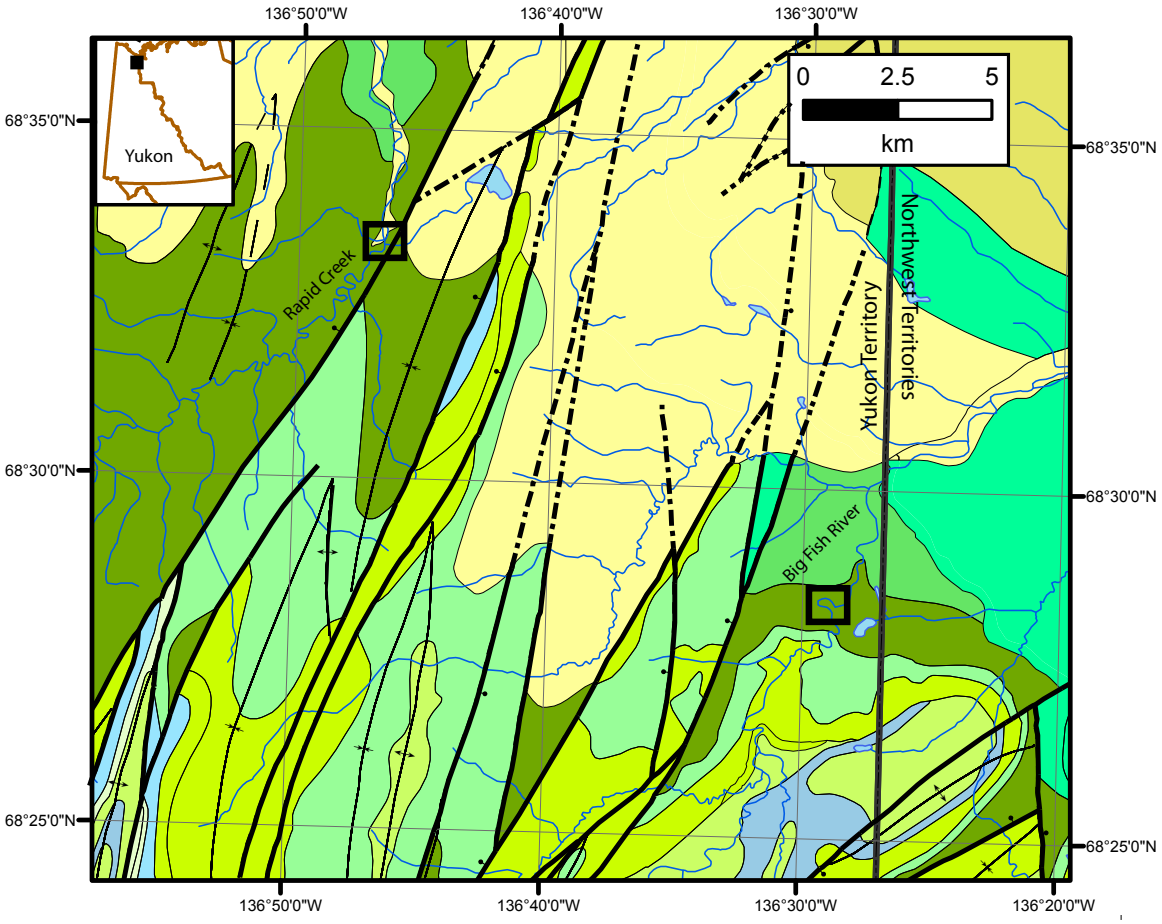

Legend

QUATERNARY

QUATERNARY: Hummocky or ridged moraine in area of Laurentide glaciation

UPPER CRETACEOUS AND LOWER TERTIARY

FISH RIVER GROUP: Moose Channel Formation: lower part: sandstone, conglomeritic, lithic; alluvial and deltaic

TENT ISLAND FORMATION: upper member: mudstone and sandstone; marine; includes Cuesta Creek Member

BOUNDARY CREEK FORMATION: mudstone, bituminous, bentonitic, ironstone concretions; marine

LOWER CRETACEOUS

Kbr: RAPID CREEK FORMATION: sandstone, conglomerate and shale; flyschoid

Krr: RAT RIVER FORMATION: interbedded units of sandstone and shale; marine

UNDIVIDED: shale, siltstone, sandstone and coal; marine and nonmarine; includes Mount Goodenough Formation

McGUIRE FORMATION: shale, siltstone and very fine grained argillaceous bioturbated sandstone; ironstone concretions in lower beds; marine

MARTIN CREEK FORMATION: sandstone, coal, and shale; marine and nonmarine

JURASSIC AND LOWER CRETACEOUS

KINGAK FORMATION: dark grey siltstone and shale; marine

PORCUPINE RIVER FORMATION: siltstone and fine to very fine grained sandstone; marine and nonmarine

HUSKY FORMATION: shale, siltstone and ironstone; marine

Symbols

geological boundary.....

syncline (defined, approximate).....

anticline (defined, approximate).....

fault, extention (solid cicle indicates downthrow side; defined, approximate).....

Figure 1. *General geology map showing the location of the Kbr unit from Norris (1981) which is equivalent to the Rapid Creek Formation. The study areas along Big Fish River and Rapid Creek from the 2012 field season are indicated by black squares. Inset shows general location of study area in Yukon. Modified from Norris (1981).*

which formally names the ironstone facies previously known as the Bedded ironstone and shale unit (Young, 1972, 1973, 1977; Young *et al.* 1976) of the Aptian-Albian flysch division as the Rapid Creek Formation. According to the outcrop map in Young and Robertson (1984) the Rapid Creek Formation is equivalent to, at minimum, parts of the Kbr formation from Norris (1981). Here the unit is called the Rapid Creek Formation based on the formal name and description published by Young and Robertson (1984).

The Rapid Creek Formation is about 1000 m thick in the eastern Blow trough, west of Rapid Creek (Young and Robertson, 1984; Robinson *et al.*, 1992). At Big Fish River the formation thins to approximately 60 m, however faulting has overlain the unit upon itself so correlation of beds in order to determine thickness is difficult (Young and Robertson, 1984; Robinson *et al.*, 1992). The Rapid Creek Formation consists of alternating thin to medium beds of phosphatic ironstone and iron-rich dark grey shale (Fig. 2a,b), which form a widespread yet low-grade iron deposit, with reserves calculated at 10^{10} tonnes of Fe_2O_3 equivalent (Young, 1977; Young and Robertson, 1984). The Upper Cretaceous shale of the Boundary Creek Formation overlies the Rapid Creek Formation everywhere the contact is exposed (Young and Robertson, 1984). The lower contact is more variable and is within the shale and siltstone of the general flyschoid sequence in the Blow trough (Fig. 3a; Young and Robertson, 1984). It lies immediately above a facies correlative with the Aptian-aged Rat River formation, consisting of concretionary dark grey shale, sandstone, and siltstone (Fig. 3b; Young and Robertson, 1984).

The sedimentology of the Rapid Creek Formation is of interest due to the unique composition of phosphate grains within some of the ironstone facies (Robertson, 1980, 1982; Young and Robertson, 1984). The phosphate grains within the coarser grained sediments consist of arrojadite-group minerals, satterlyite, $(Fe^{2+},Mg,Fe^{3+})_2(PO_4)$-$(OH,O)$, and gormanite, $(Fe^{2+},Mg)_3(Al,Fe^{3+})_4(PO_4)_4$-$(OH)_6{\cdot}2H_2O$, the latter two of which were first described from this formation (Robertson, 1980, 1982; Young and Robertson, 1984). Robertson (1980, 1982) suggests that the sediments originally contained an unknown Ca-Fe-Mg phosphate which was altered to these unusual phosphates during low-grade metamorphism. In the mudstones, the unknown phosphate altered to carbonate-apatite, occurring with siderite, as well as gormanite-souzalite alteration/replacement (Robertson, 1980, 1982). The ironstone unit at Big Fish River has a P_2O_5 content of approximately 14%, varying up to 30% (Young, 1977).

The Rapid Creek Formation at Big Fish River is exposed as high cliffs, often with a white coating of epsomite, $MgSO_4{\cdot}7H_2O$, or possibly dypingite, $Mg_5(CO_3)_4(OH)_2{\cdot}5H_2O$ (Fig. 4). It consists of siderite-rich ironstone units of interbedded mudstone and iron-rich shale and pelletal phosphate shale (Robertson, 1982; Young and Robertson, 1984). The mudstone layers, which sometimes appear pelletal and show evidence of gormanite-souzalite alteration, are 1 cm to 1 m thick, but are typically less than 20 cm thick (Fig. 5a). A steel-blue weathering patina is characteristically found on these mudstone layers (Fig. 5b). These layers are interbedded both with splintery iron-rich shale and pelletal phosphate shale, which are often thinly bedded (Fig. 6a,b). Near

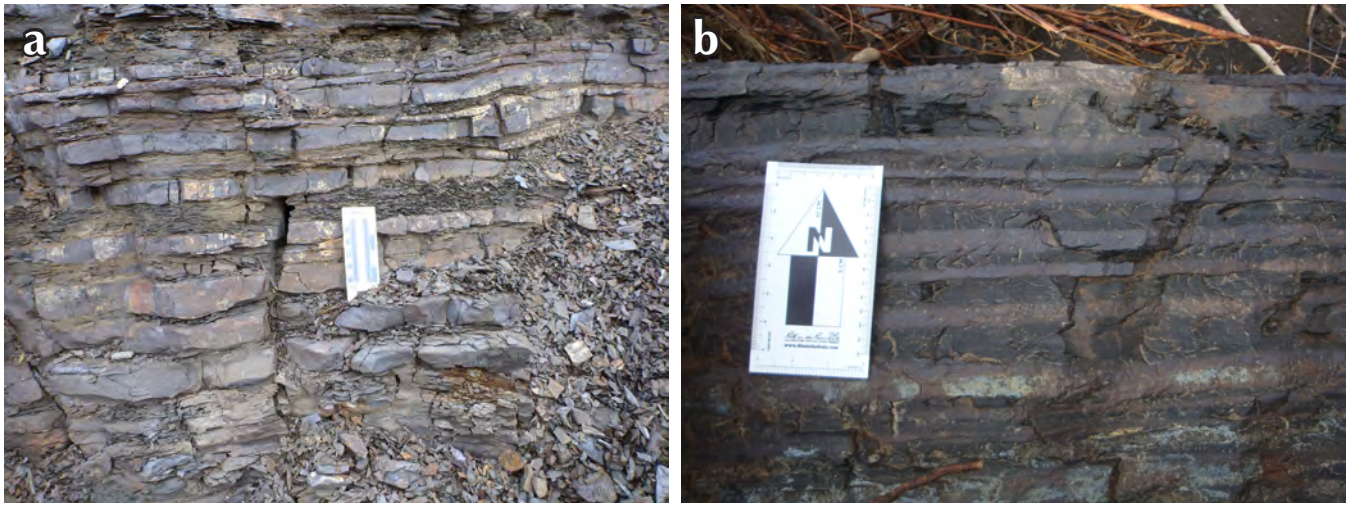

***Figure 2**. a) Intercalated thin to medium beds of phosphatic siderite-rich mudstone & shale and b) unweathered block at base of a rock slide (not in situ) showing fresh ironstone.*

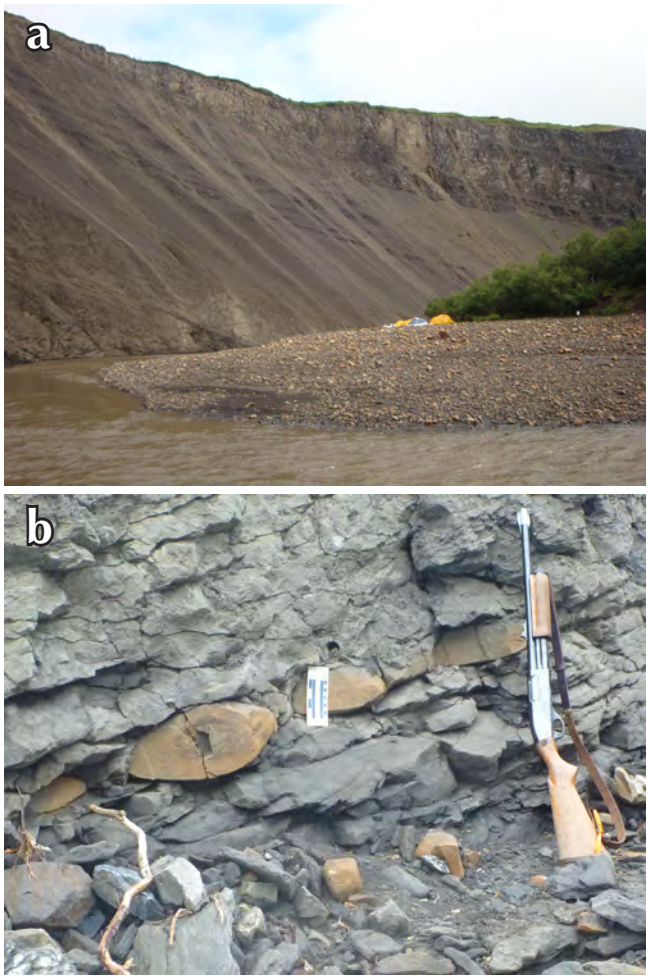

***Figure 3**. a) Lower contact between Rapid Creek Formation and the Rat River Formation dark grey concretionary shale and b) large concretions in sandstones of the Rat River Formation.*

fault zones, the thinly bedded shale is frequently host to bedding-parallel mineralization of vivianite-barićite (Fig. 7a). These mineralized layers show growth fibres, which occasionally show minor shearing (Fig. 7b). Dark grey shale, with white unidentified spherules and small concretions (Fig. 8a-d) was identified in the former river bed near the base of the Rapid Creek Formation at Big Fish River suggesting they are part of the underlying Rat River Formation. However, the gormanite-souzalite-siderite veins occurring in these strata and their occasional presence between pelletal shale layers in the lower strata suggest they are related to the Rapid Creek Formation. Bulk analysis of the dark grey shale is being performed to identify the quantity of iron and phosphorus in this unit and detailed petrography of each of these layers is currently in progress.

***Figure 4**. Cliffs of Rapid Creek Formation at Big Fish River with a white coating of epsomite, $MgSO_4 \cdot 7H_2O$, and/or dypingite, $Mg_5(CO_3)_4(OH)_2 \cdot 5H_2O$.*

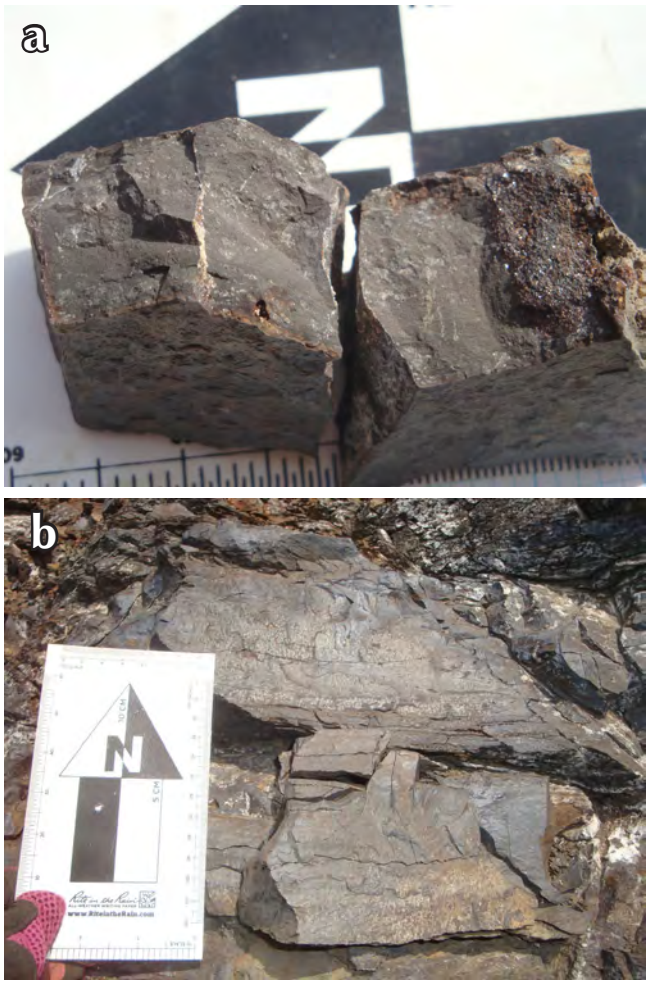

***Figure 5**. a) Iron-rich mudstone layers, sometimes appearing pelletal and b) mudstone with characteristic steel-blue weathering patina.*

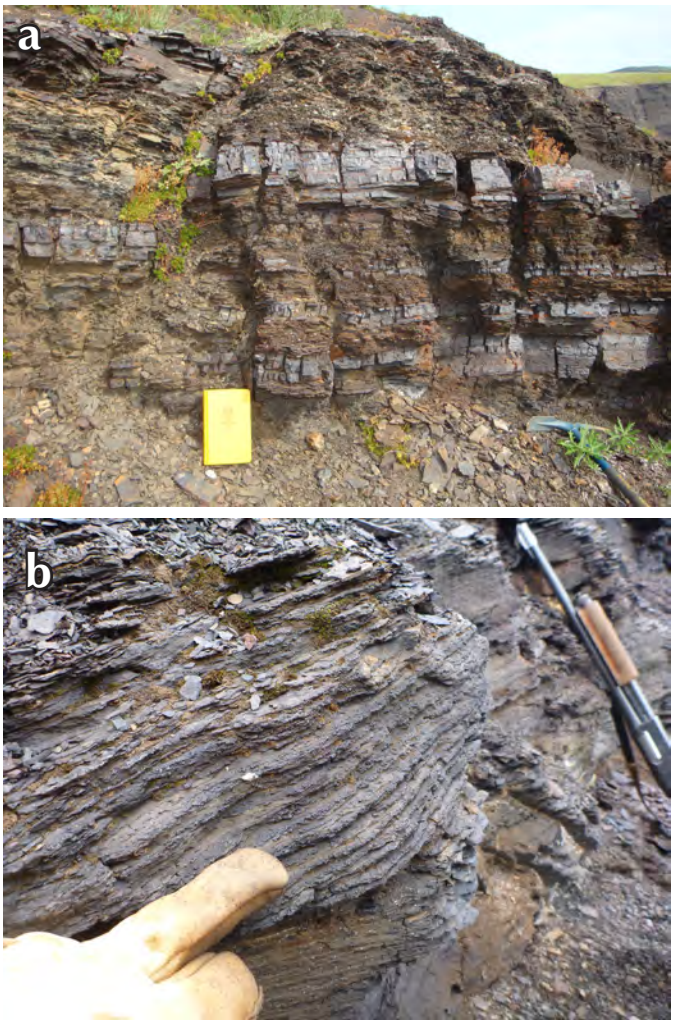

***Figure 6**. a) Interbedded mudstone and splintery iron-rich shale, notebook for scale and b) thinly bedded pelletal phosphate shale, shotgun for scale.*

SECONDARY MINERALS

The Rapid Creek and Big Fish River localities are most famous for their exceptional rare and unique mineral specimens. These minerals are generally found in thin fracture filling veins typically a few centimetres wide, with the most spectacular specimens plucked from wider pockets. These veins crosscut the strata of the Rapid Creek Formation and occur in specific mineralogical associations which are described in Robertson (1982). Generally, these veins are abundant with a greater variety of mineral species occurring near to fault zones. Descriptions of some of the minerals collected during the 2012 field program follow.

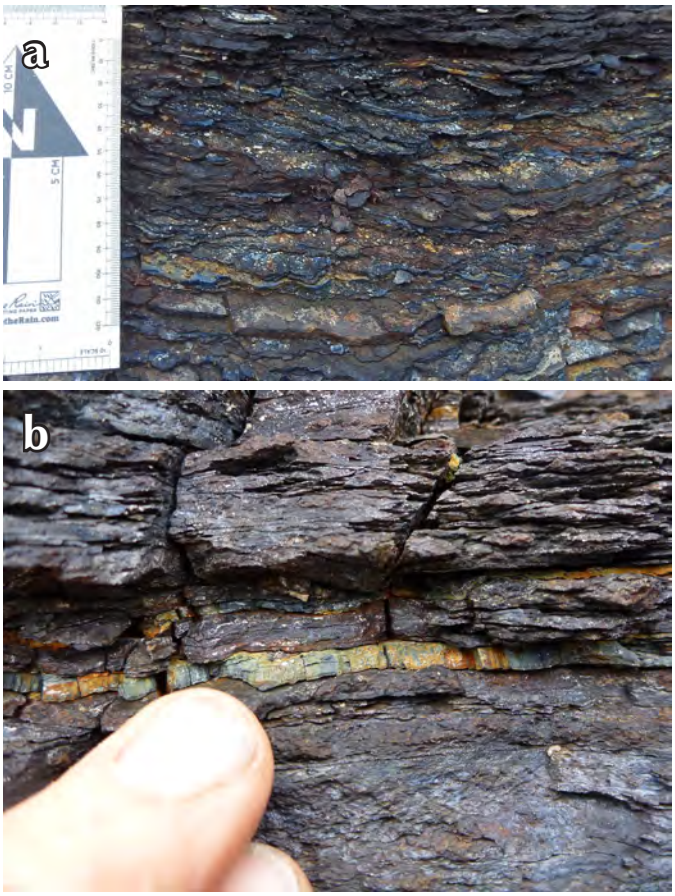

***Figure 7.** a) Thinly bedded shales hosting to bedding-parallel mineralization of vivianite-baricite (blue mineral in photo) and b) Fibrous growth of vivianite-baricite mineralization.*

APATITE-GROUP MINERALS

Although Rapid Creek is known more for the other rare-phosphates the area has yielded some spectacular purple crystals of apatite. These purple crystals have been found in three areas at this locality, with the finest ones from locality 8 as noted on the map in the Mineralogical Record 23, no. 4, 1992 paper. This find is on an unnamed creek, approximately 1.7 km south of the tributary to Rapid Creek, sometimes referred to as "Crosscut Creek" (68°32′30″N, 136°47′40″W).

In 1983, George Robinson collected some very pale mauve apatite crystals from locality 1, area 'A', 'Kulan camp' and in 1984 Joel Grice and Bob Gault collected pale mauve crystals from 'Grizzly Bear Creek', locality 14, area 'B', 'Stoneman camp'. Whereas these crystals were larger than those from locality 8, area A, they were much paler in colour. These apatite crystals are most commonly

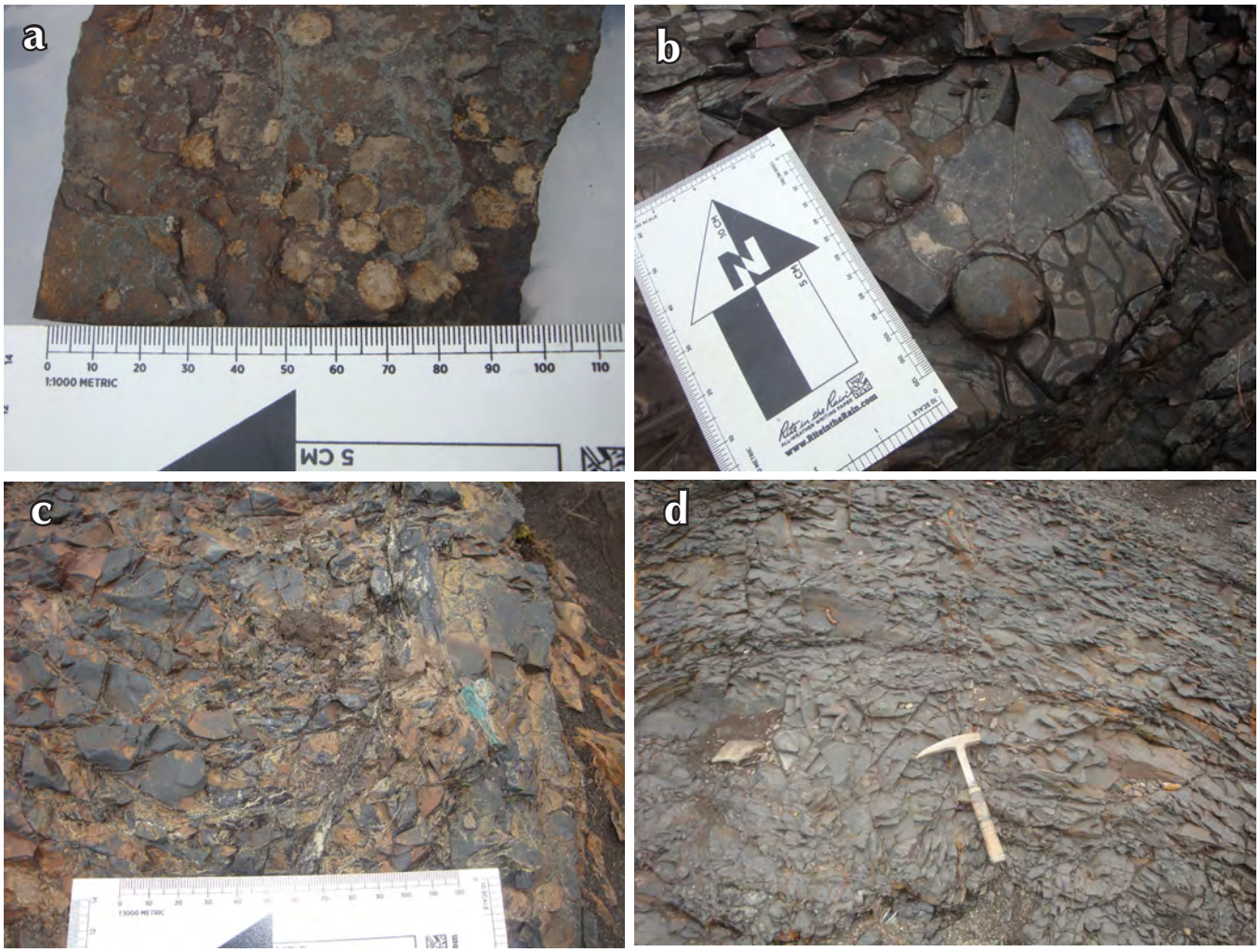

***Figure 8**. Dark grey shales: a) white unidentified spherules; b) small concretions; c) gormanite-siderite veins occurring in the dark grey shale; and d) weathered dark grey shale, no white spherules.*

associated with lazulite, quartz, and siderite and range in size from microscopic to nearly 2 cm across.

During the summer of 2012 another apatite association was noted here. The arrojadite-quartz-(±apatite) veins were part of a crosscutting system not part of, what appeared to be, the primary depositional sequence. In these veins, well crystallized arrojadite group minerals and quartz were common, but in the larger pockets, apatite crystals were common, but were quite small (3-7 mm). They are transparent, colourless, striated, hexagonal prisms.

Right at the base of the bobdownsite-whitlockite locality, along a cliff face in the water, a new vein was observed. The vein crosscuts the primary strata, with milky, opaque, tabular (~1.2 cm) hexagonal shaped crystals (Fig. 9). These crystals are shortened along their *c*-axis compared to more typical apatite from Rapid Creek or Big Fish River (or most

***Figure 9**. Tabular apatite from Big Fish River, FOV = 5x3 cm. Photo courtesy of the Royal Ontario Museum, ©ROM.*

other localities for that matter) and have virtually no discernible pinacoid faces. Under magnification they are actually composite crystals composed of multiple individuals in parallel growth which, none the less, maintain an overall hexagonal outline macroscopically.

ARROJADITE-GROUP MINERALS

Arrojadite-group minerals are a large group of phosphates with exhibiting complex chemical variations. They have the general formula $A_2 B_2 Ca_1 Na_{2+x} M_{13} Al (PO_4)_{11} (PO_3OH_{1-x}) W_2$ where *A* are monovalent cations (K, Na) or large divalent cations (Ba, Sr, Pb) plus vacancy; *B* are either monovalent (Na) cations or small divalent cations (Fe, Mn, Mg) plus vacancy; *M* can include Fe, Mn, Mg, Zn, or Li; and *W* is OH or F (Chopin *et al*., 2006). The base name "arrojadite" is used only when the *M* cation is predominantly Fe, whereas an Mg dominant species would be "dickinsonite". Dickinsonite end-members have not been identified from these localities. Members of this group were thought to be primarily found in granitic pegmatites until being discovered in the sedimentary ironstones at Rapid Creek in the 1970s (Chopin *et al.*, 2006; Robinson *et al.*, 1992). Group members have also been found more recently in metamorphic quartzite (Demartin *et al.*, 1996).

Rapid Creek is the type locality for the iron-rich end member arrojadite-KNa (KNa) $Na_2CaNa_2Fe_{13}Al(PO_4)_{11}(PO_3OH)(OH,F)_2$ (Cámara *et al.*, 2006) and recently Ba-rich and Sr-rich end members have been identified from Big Fish River samples (Tomes, 2011). The end members present here all show evidence of zoning in some samples, often alternating between arrojadite-KNa and the Ba-rich end member (Robinson *et al.*, 1992; Tomes, unpublished thesis). Crystals with Sr-rich zones are strongly zoned with the Ba-rich end member (Tomes, unpublished thesis).

Arrojadite-group minerals occur at both the Rapid Creek and Big Fish River exposures of the Rapid Creek Formation. Arrojadite-KNa is fairly common at both localities, while the Ba-rich end member has been found primarily at Big Fish River, although is present in some zoned crystals from Rapid Creek (Robinson *et al.*, 1992; Tomes, unpublished thesis). The Sr-rich end member has only been identified from Big Fish River (Tomes, unpublished thesis). Arrojadite-group minerals are found as 1-2 mm, tabular to bladed, clear to yellow to green crystals in 0.5 mm to 3 cm veins with occasional open pockets which crosscut the bedding planes. Crosscutting arrojadite veins were abundant near faulted zones at Big Fish River and the veins have brecciated the surrounding shale and mudstone layers up to approximately 3-5 cm away from the vein (Fig. 10a). Arrojadite-group minerals were associated with quartz and less frequently, small hexagonal apatite crystals (Fig. 10b). In contrast, Robertson (1980, 1982) noted the relative scarcity of veins along his stratigraphic sections at Big Fish River, when compared to the abundance of simple and complex veins at Rapid Creek. Robertson (1980, 1982) notes that arrojadite occurs with vivianite-barićite and quartz in bedding-plane parting surfaces and Robinson *et al.* (1992) report the presence of crystal lined fractures at Big Fish River. Robinson *et al.* (1992) also include kryzhanovskite, whiteite, and metavivianite as minerals associated with arrojadite; however these associations were not confirmed in the present study.

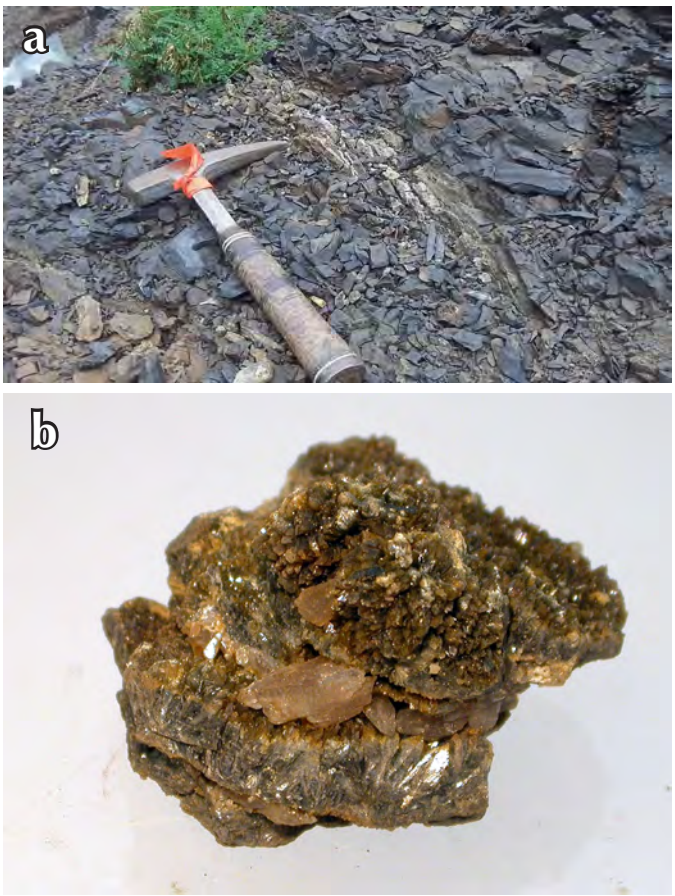

Figure 10. *Arrojadite-group minerals. a) Arrojadite-quartz-apatite vein in situ and (b) yellow-green arrojadite crystals with quartz, FOV 6 x 4 cm.*

AUGELITE

Just before the waterfall, mid-way up "Crosscut Creek", a steep defile cuts back into the southern wall of the creek's canyon at an approximate 45 degree angle. This narrow draw winds its way from the creek bed up to the tundra level and is clearly a drainage feature as water can be seen coming down a short cliff face and heard percolating through the jumbled rocks which form the floor of the canyon. A number of years ago an excellent occurrence of well crystallized lazulite specimens was discovered in a steeply dipping, heavily brecciated vein in the eastern wall of this canyon near the cliff face. The breccia zone runs parallel to the direction of the defile (approximately north-south) and reaches a maximum width of about 15 cm. Visiting the area again in 2012 an extensive amount of overburden was moved, following the course of the breccia zone, in search of more lazulite specimens. Unfortunately, the ground beneath the loose overburden was frozen, preventing further excavation. However, adjacent to the lazulite bearing vein and running approximately parallel to it were a number of tighter quartz/siderite veins which, upon closer inspection and excavation, were found to contain augelite crystals up to 5 mm in size formed on beds of childrenite and siderite crystals. The childrenite crystals reach a maximum length of 3 mm and width of approximately 1 mm and are a typical chocolate-brown colour. The augelite crystals are pale blue-green in colour.

DYPINGITE

Dypingite $Mg_5(CO_3)_4(OH)_2{\cdot}5H_2O$, closely associated with hydromagnesite $Mg_5(CO_3)_4(OH)_2{\cdot}4H_2O$ and lansfordite, was collected from an open fracture system above permafrost in the Rapid Creek — Big Fish River area in August 2012 (Fig. 11). Dypingite occurs in a botryoidal habit consisting of very fine radiating crystals forming a translucent crust of spheroidal aggregates (Fig. 12a-c). Some of the spheroids can be up to 1 mm in diameter. The fracture system is on a northwest facing slope and dypingite is found 10 cm or more below the surface coating surfaces on open fractures. The dypingite is often covered with loose and chalky hydromagnesite that is brittle and falls away from the fracture surface. The relationship suggests that the hydromagnesite forms as a dehydration product of dypingite at this locality. Elsewhere in Canada, dypingite has been observed as an alteration product of ultramafic rocks and forms through the breakdown of olivine and the introduction of CO_2 from the atmosphere (Wilson *et al.,* 2009). In some areas, the formation of hydrous magnesium carbonates is accelerated through biological activity (Power *et al.,* 2009). Several mineral species belong to the hydrous magnesium carbonate mineral group. Anhydrous magnesite $MgCO_3$ is followed by barringtonite $MgCO_3{\cdot}2H_2O$, nesquehonite $MgCO_3{\cdot}3H_2O$, and lansfordite $MgCO_3{\cdot}5H_2O$ as hydration increases. Pokrovskite $MgCO_3(OH)_2$ and Mcguinnessite (Mg, Cu)$CO_3(OH)_2$ have hydroxyl as an additional anion. Dypingite $Mg_5(CO_3)_4(OH)_2{\cdot}5H_2O$, hydromagnesite $Mg_5(CO_3)_4(OH)_2{\cdot}4H_2O$, and artinite $Mg_5(CO_3)_4(OH)_2{\cdot}3H_2O$ have both hydroxyl and water as essential components. All of these phases have the potential to participate in the sequestration of carbon dioxide from the environment and are the subject of recent research by many investigators (Mavromatis *et al.,* 2012). The Big Fish River occurrence of dypingite is unusual as it is not related to the alteration of ultramafic rocks but is located within a sequence of phosphate-rich sedimentary rocks. However, a magnesium sulfate, epsomite ($MgSO_4{\cdot}7H_2O$), is commonly coating cliff faces throughout the area.

Figure 11*. Botryoidal habit of dypingite (white mineral). Spheroids up to 1 mm in diameter.*

GARYANSELLITE-KRYZHANOVSKITE

The phosphoferrite group is a complex group of hydrated phosphate minerals. They have the general formula $A_3(PO_4)_2{\cdot}nH_2O$ where $A = Fe^{2+}$, Fe^{3+}, Mg, Mn^{2+} and n is dependent on the oxidation state of the cations and the presence of OH/H_2O (Gaines *et al.*, 1997). There are three ideal end members in this group — reddingite, $Mn^{2+}_3(H_2O)_3(PO_4)_2$, phosphoferrite, $Fe^{2+}_3(H_2O)_3(PO_4)_2$, and kryzhanovskite, $Fe^{3+}_3(OH)_3(PO_4)_2$ — and they form a

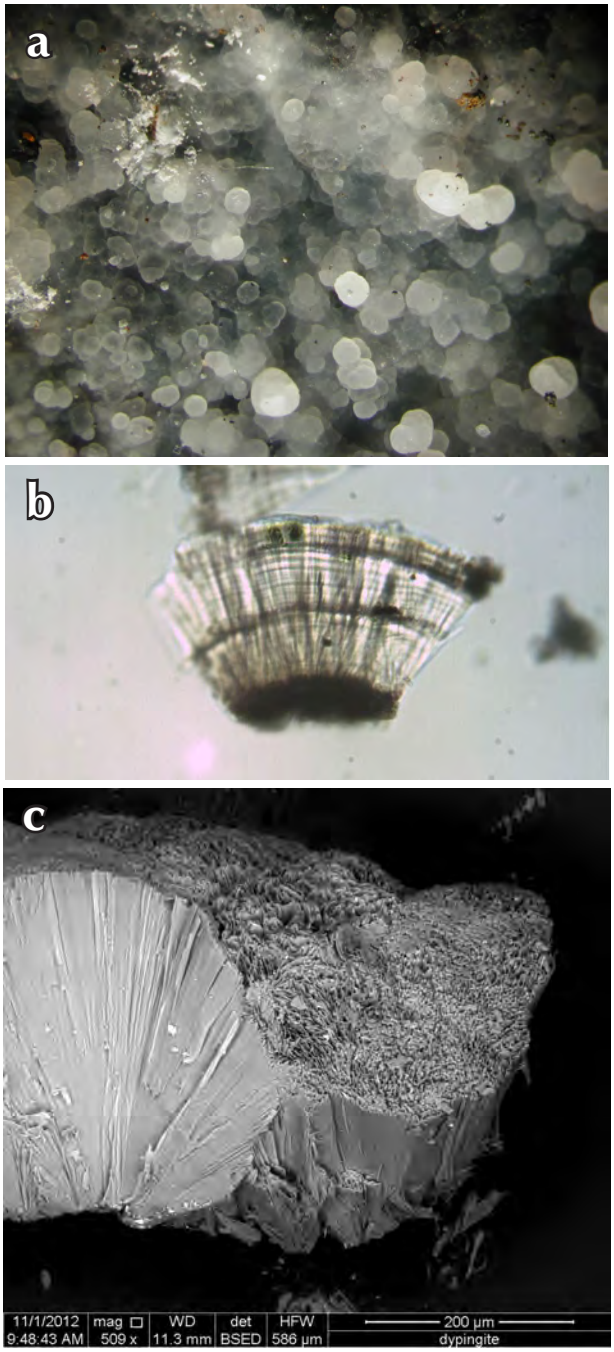

***Figure 12**. Crystals of dypingite: a) Botryoidal habit forming a translucent crust of spheroidal aggregates; FOV = 10 mm; b) very fine radiating crystals; FOV = 1 mm; and c) backscattered electron image of showing the fine radiating crystals, scale bar at the bottom of the image is 200 microns.*

complex triple series (Moore *et al.*, 1980). Other members include: garyansellite, $(Mg,Fe^{3+})_3(PO_4)_2(OH,O)\cdot 1.5H_2O$ and landesite, $(Mn^{2+}Mg)_9Fe^{3+}{}_3(PO_4)_8(OH)_3\cdot 9H_2O$. Minerals in the phosphoferrite group can be found in select regions in the world, but two key members of this group are found at Rapid Creek, with garyansellite first being described from here.

Up until now, kryzhanovskite (Fig. 13) and garyansellite are the two minerals within the phosphoferrite group that are described in the Rapid Creek region (Robinson *et al.*, 1992). The kryzhanovskite at this locality typically exist in its intermediate form, with the chemical formula $MnFe^{3+}{}_2(PO_4)_2(OH)_2\cdot H_2O$. The minerals are also relatively enriched in magnesium (Robinson *et al.*, 1992). Furthermore, most of the samples collected by Robinson *et al.* (1992) show evidence of zoning within individual crystals. They also suspected some samples may contain zones of garyansellite.

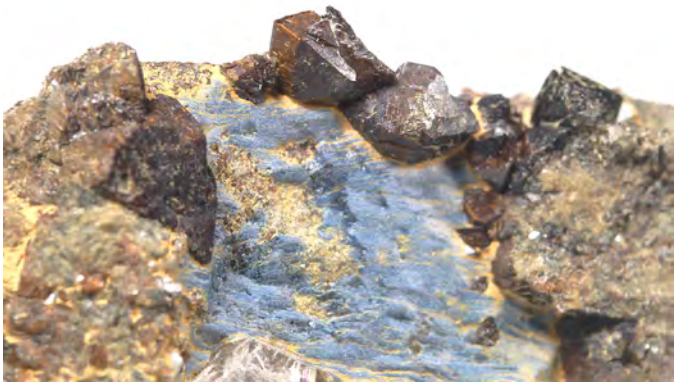

***Figure 13**. Kryzhanovskite crystals (dark brown) with vivianite (blue), metavivianite (yellow) on quartz (lighter brown) accession number M52270 from Rapid Creek, Yukon, FOV = 6x4 cm. Photo courtesy of the Royal Ontario Museum, © ROM.*

Veins of garyansellite and kryzhanovskite are found high above Rapid Creek (68° 34'N and 136° 46'W) about 1 km north of the junction of Lake Creek. Many samples were found loose in the talus slope leading up to the outcrop. On most specimens garyansellite-kryzhanovskite occurs as plates, 1-3 mm in size, associated with ludlamite, arrojadite-group minerals, quartz, vivianite, metavivianite, and souzalite. They range from chocolate to clove to reddish brown and typically exist as subhedral to euhedral crystals, with a characteristic bronze lustre.

LAZULITE

Lazulite, $MgAl_2(PO_4)_2(OH)_2$, specimens consisting of deep blue crystals, 3-5 mm in size, closely associated with siderite and quartz, were collected from ironstone beds in the cliffs along "Crosscut creek" (Fig. 14). Lazulite is the magnesium-rich end member of a series with scorzalite

***Figure 14**. Lazulite (blue) in ironstone (brown) from "Crosscut Creek", Rapid Creek area, Yukon.*

***Figure 15**. Highly weathered ammonite nodule, now replaced with pyrite, which has preferentially weathered out leaving holes in the nodule.*

$Fe^{2+}Al_2(PO_4)_2(OH)_2$, which is not found in the Rapid Creek and Big Fish River area. While lazulite is abundant at Rapid Creek in crosscutting veins both in "Crosscut Creek" and nearby the garyansellite-kryzhanovskite locality, it is noticeably absent from the mineralized crosscutting veins at Big Fish River.

PHOSPHATE NODULES

The lower portion of the Rapid Creek Formation at Big Fish River is well known by collectors as the location for unusual phosphate nodules that host a variety of rare phosphate minerals (Robertson, 1980, 1982; Young and Robertson, 1984; Robinson *et al.*, 1992). According to Robertson (1980, 1982) the phosphate nodules appear to be recrystallized replacement of ammonites and pelecypods, although some bear only a slight resemblance and some bear no resemblance at all to ammonites or pelecypods. Phosphatic nodules from Big Fish River are known to be dominantly composed of satterlyite, wolfeite, marićite, ludlamite, pyrite, and vivianite-barićite (Robertson, 1980, 1982). Big Fish River is the primary locality for these nodules, however Robertson (1980, 1982) reports that they also occur at Boundary Creek.

Nodules were identified both *in situ* and on talus slopes at all exposures along Big Fish River, although the type of nodules varied with position in the section. The lower portion of the Rapid Creek Formation is dominated by microcrystalline pyritic nodules (this study; Robertson, 1980, 1982). Phosphate nodules are highly weathered *in situ* making field identification of minerals difficult in some samples (Fig. 15). However, preliminary analyses of some nodules have found wicksite, arrojadite-group minerals, vivianite-barićite, satterlyite, and wolfeite. In nodules, these minerals are often found radiating from the center at the base of the nodule. Not all nodules are disc or ammonite shaped, as "cigar" shaped nodules are found at one exposure with similar "nodule-type" mineralization. Also, massive sprays of nodule-like mineralization (frequently satterlyite) were identified in large lenses parallel to the bedding planes (Fig. 16a,b) and found to be connecting small nodules within the shale layers (Fig. 17). Satterlyite was identified as radiating masses in crosscutting veins up to 15 cm wide (Fig. 18a-c). These veins are located in close proximity to fault zones. Small phosphate nodules were collected *in situ* with surrounding host rock in order to determine if these nodules are replacements, of ammonites for example, or if they grew in place, putting stress and causing small fractures in the surrounding shale (Fig. 19a,b). Extensive collection of phosphate nodules during the 2012 field season will allow determination of the distribution of mineralization in the phosphatic and pyrite nodules as well as insight into their relationship with the shale and mudstone layers.

SUMMARY

The Rapid Creek Formation, exposed at Big Fish River and Rapid Creek, in the Richardson Mountains of Yukon is well known for its rare phosphate minerals. The Rapid Creek Formation is a phosphorite-rich ironstone facies composed of alternating beds of phosphate and siderite-rich mudstones and shale. A three week field program in the

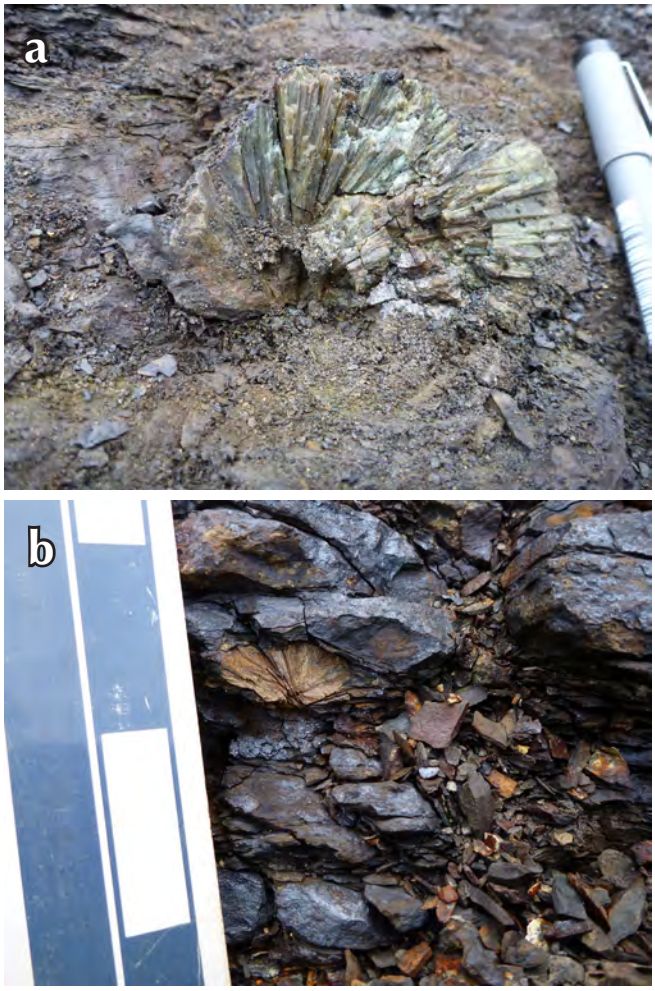

Figure 16. *Nodules showing the radiating mineralization of a) appears to be highly altered satterlyite/wolfeite and b) highly weathered wolfeite.*

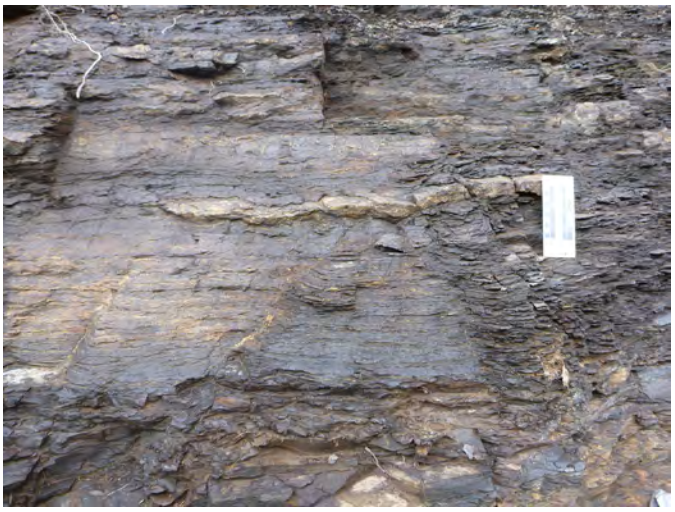

Figure 17. *Large lense of nodule material in ironstone.*

Figure 18. *a,b) Satterylite "nodule-like" vein in situ, vein is up to ~15 cm wide; and c) satterlyite (green radiating mineral) vein material, FOV = 3 x 2 cm. Photo courtesy of the Royal Ontario Museum. ©ROM*

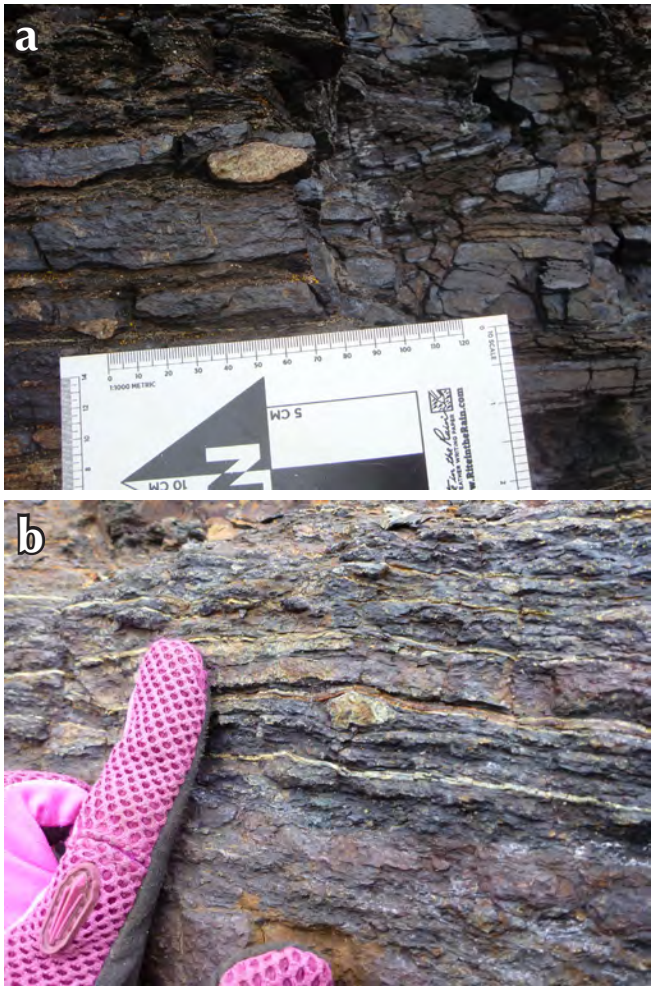

***Figure 19**. Small phosphate nodules in situ a) between layers of iron-rich shale and mudstone; nodule 3 cm long and b) In thinly bedded shale with bedding-parallel mineralization of vivianite-barićite; nodule 1.3 cm long.*

summer of 2012 was carried out to map this region, and collect specimens for a detailed geochemical survey of the region. The Rapid Creek Formation is unusual in a number of respects: (1) the formation conditions for phosphorites and siderite-rich ironstones are not complementary to one another; and (2) primary mineralogy in most phosphorites consists of carbonate-rich fluorapatite (commonly known as francolite), $Ca_5(PO_4,CO_3)_3(F,O)$ which are not observed in this region. The geological environment that allowed these assemblages of rare phosphates to form is unique; the sedimentary rocks host several mineral species previously known only from igneous and more highly metamorphosed environments. We anticipate many more discoveries with our field samples as we progress with a more detailed geochemical investigation.

ACKNOWLEDGEMENTS

The subject matter of this paper is part of H.T.'s PhD research. Yukon Geological Survey is gratefully acknowledged for their support of the field program. Further funding for this project was provided by the Young Patrons Circle, the Peer Review Fund, and the Department of Natural History Fieldwork Fund at the Royal Ontario Museum. Additional funding was provided by the D.H. Gorman Explorers Fund Graduate Scholarship and the Arctic Institute of North America's Grant-in-aid program. The Polar Continental Shelf program provided logistical support in the field. An NSERC Discovery grant supported the participation of R. Peterson. Thank you to Natalie Chu for her lab work on this project and to Maurice Colpron for his review of this paper.

REFERENCES

Cámara, F., Oberti, R., Chopin, C., and Medenbach, O., 2006. The arrojadite enigma: I. A new formula and a new model for the arrojadite structure. American Mineralogist, vol. 91, p. 1249-1259.

Campbell, F.A., 1962. Lazulite from Yukon, Canada. American Mineralogist, vol. 47, p. 157-160.

Chopin, C., Oberti, R., and Cámara, F., 2006. The arrojadite enigma: II. Compositional space, new members and nomenclature of the group. American Mineralogist, vol. 91, p. 1260-1270.

Coleman, L.C. and Robertson, B.T., 1981. Nahpoite Na_2HPO_4, a new mineral from the Big Fish River area, Yukon Territory. Canadian Mineralogist, vol. 19, p. 373-376.

Demartin, F., Gramaccioli, C.M., Pilati, T., and Sciesa, E., 1996. Sigismundite, (Ba,K,Pb) Na3 (Ca,Sr) $(Fe,Mg,Mn)_{14}(OH)_2(PO_4)_{12}$, a new Ba-rich member of the arrojadite group from Spluga valley, Italy. Canadian Mineralogist, vol. 34, p. 827-834.

Gaines, R.V., Skinner, H.C.W., Foord, E.E., Mason, B., and Rosenzweig, A., 1997. Dana's New Mineralogy, John Wiley & Sons, Inc., p. 706-712.

Jeletzky, J.A., 1971. Stratigraphy, facies and paleogeography of Mesozoic rocks of northern and west-central Yukon. *In:* Report of Activities, 1970, Part A, Geological Survey of Canada Paper, 71-1A, 18 p.

Mandarino, J.A., Sturman, B.D., and Corlett, M.I., 1978. Satterlyite, a new hydroxyl-bearing ferrous phosphate from the Big Fish River area, Yukon Territory. Canadian Mineralogist, vol. 16, p. 411-413.

Mavromatis, V., Pearce, C.R., Shirokova, L.S., Bundeleva, I.A., Pokrovsky, O.S., Benezeth, P., and Oelkers, E.H., 2012. Magnesium isotope fractionation during hydrous magnesium carbonate precipitation with and without cyanobacteria. Geochimica et Cosmochimica Acta, vol. 76, p. 161-174.

Moore, P.B., Araki, T., and Kampf, A.R., 1980. Nomenclature of the phosphoferrite structure type: refinements of landesite and kryzhanovskite. Mineralogical Magazine, vol. 43, p. 789-795.

Norris, D.K., 1981. Blow River and Davidson Mountains. Geological Survey of Canada, Map 1516A.

Norris, D.K., 1983. Geotectonic Correlation Chart 1532A – Operation Porcupine Area. Geological Survey of Canada, "A" Series Map 1532A, 1 sheet.

Norris, D.K. and Yorath, C.J., 1981. The North American Plate from the Arctic Archipelago to the Romanzoff Mountains. *In*: The Ocean Basins and Margins, Vol. 5 The Arctic Ocean, A.E.M Nairn, M. Churkin, and F. Stehli, (eds), Plenum Press, New York and London, p. 37-103.

Power, I.M., Wilson, S.A., Thom, J.M., Dipple, G.M., Gabites, J.E., and Southam, G., 2009. The hydromagnesite playas of Atlin, British Columbia, Canada: A biogeochemical model for CO_2 sequestration. Chemical Geology, vol. 260, p. 286-300.

Robertson, B.T., 1980. Stratigraphic setting of some new and rare phosphate minerals in the Yukon Territory. Unpublished MSc Thesis, University of Saskatchewan, Saskatoon, Saskatchewan, Canada.

Robertson, B.T., 1982. Occurrence of epigenetic phosphate minerals in a phosphatic iron-formation, Yukon Territory. Canadian Mineralogist, vol. 20, p. 177-187.

Robinson, G.W., van Velthuizen, J., Ansell, H.G., and Sturman, B.D., 1992. Mineralogy of the Rapid Creek and Big Fish River area, Yukon Territory. Mineralogical Record, vol. 23, p. 1-47.

Sturman, B.D. and Mandarino, J.A., 1976. Barićite, the magnesium analogue of vivianite from Yukon Territory, Canada. Canadian Mineralogist, vol. 14, p. 403-406.

Sturman, B.D., Mandarino, J.A., and Corlett, M.I., 1977. Marićite, a sodium iron phosphate, from the Big Fish River area, Yukon Territory, Canada. Canadian Mineralogist, vol. 15, p. 396-398.

Sturman, B.D., Mandarino, J.A., Mrose, M.E., and Dunn, P.J., 1981a. Gormanite, $Fe_3^{2+}Al_4(PO_4)_4(OH)_6 \cdot 2H_2O$, the ferrous analogue of souzalite, and new data for souzalite. Canadian Mineralogist, vol. 19, p. 381-387.

Sturman, B.D., Peacor, D.R., and Dunn, P.J., 1981b. Wicksite, a new mineral from northeastern Yukon Territory. Canadian Mineralogist, vol. 19, p. 377-380.

Tait, K.T., Barkley, M.C., Thompson, R.M., Origlieri, M.J., Evans, S.H., Prewitt, C.T., and Yang, H. (2011). Bobdownsite, a new mineral species from Big Fish River, Yukon, Canada, and its structural relationship with whitlockite-type compounds. Canadian Mineralogist, vol. 49, p. 1065-1078.

Tomes, H., 2011. Arrojadite-(BaNa), a new arrojadite-group mineral from Big Fish River, Yukon Territory, Canada. Unpublished MSc thesis, University of Toronto, Ontario, Canada.

Wilson, S.A., Dipple, G.M., Power, I.M., Thom, J.M., Anderson, R.G., Raudsepp, M., Gabites, J.E., and Southam, G., 2009. Carbon dioxide fixation within mine wastes of ultramafic-hosted ore deposits: Examples form the Clinton Creek and Cassiar Chrystotile Deposits, Canada. Economic Geology, vol. 104, p. 95-112.

Yeo, G.M., 1992. Phosphorites, ironstones, and secondary phosphates in mid-Cretaceous Flysch of the Blow Trough, Northern Yukon. *In*: Yukon Geology, Vol. 3; Exploration and Geological Services Division, Yukon, Indian and Northern Affairs Canada, p. 27-36.

Young, F.G., 1972. Cretaceous stratigraphy between Blow and Fish Rivers, Yukon Territory. Report of Activities, Part A, Geological Survey of Canada Paper 72-1A, p. 229-235.

Young, F.G., 1973. Mesozoic epicontinental, flyschoid and molassoid depositional phase of Yukon's North Slope. *In*: Canadian Arctic Geology, J.D. Aitkin and D.J. Glass (eds.), Proceedings of the Geological Association of Canada-Canadian Society of Petroleum Geologist Symposium on Geology of the Canadian Arctic, Saskatoon, p. 181-202.

Young, F.G., 1977. The Mid-cretaceous flysch and phosphatic ironstone sequence, Northern Richardson Mountains, Yukon Territory. Geological Survey of Canada Paper, 77-1C, p. 67-74.

Young, F.G., Myhr, D.W., and Yorath, C.J., 1976. Geology of the Beaufort-Mackenzie Basin. Geological Survey of Canada Paper, 76-11.

Young, F.G. and Robertson, B.T., 1984. The Rapid Creek Formation: An Albian flysch-related phosphatic iron formation in Northern Yukon Territory. *In*: The Mesozoic of Middle North America, D.F. Smith and D.J. Glass (eds.), Canadian Society of Petroleum Geologists Memoir, vol. 9, p. 361-372.

Geology, alteration, and mineralization of the Carlin-type Conrad zone, Yukon

Michael J. Tucker[1], Craig J.R. Hart,
Mineral Deposits Research Unit, Department of Earth and Ocean Sciences, University of British Columbia

Robert C. Carne
ATAC Resources Ltd.

Tucker, M.J., Hart, C.J.R., and Carne, R.C., 2013. Geology, alteration, and mineralization of the Carlin-type Conrad zone, Yukon. *In:* Yukon Exploration and Geology 2012, K.E. MacFarlane, M.G. Nordling, and P.J. Sack (eds.), Yukon Geological Survey, p. 163-178.

ABSTRACT

The Conrad zone, east-central Yukon is a newly discovered gold prospect. It is strongly analogous to Carlin-type mineralization, and represents the first Carlin-type gold deposit discovered in Yukon. The regional geological framework and style of mineralization bear similarities to the Carlin trend in Nevada. Structurally, the Conrad area is bounded to the south by the regional-scale Dawson thrust and the Kathleen Lakes fault to the north. This structural setting lies at the interface between the dominantly clastic Neoproterozoic to Paleozoic rocks of Selwyn basin and coeval carbonate rocks of Mackenzie platform. The principal host rock to mineralization is a variably decarbonatized silty limestone, although where permeability has been enhanced by shearing, siliciclastic rocks may also contain significant amounts of gold. Alteration and associated processes related to mineralization include decarbonatization of host limestone with subsequent silicification and brecciation. Gold is hosted within arsenic-rich pyrite growth rims around pre-existing pyrite. Significant post-mineralization realgar, orpiment, calcite, and trace stibnite are found locally as open-space minerals.

[1]*mike.tucker.geo@gmail.com*

INTRODUCTION

The Conrad zone (Fig. 1) is a new Carlin-type gold discovery in Yukon. The Nadaleen trend, which hosts the Conrad zone, lies in the eastern part of ATAC Resources Limited's Rackla Gold Property (Fig. 2). The Conrad zone drilled prospect is located in east-central Yukon, 185 km northeast of the town of Mayo (Fig. 1). Significant Carlin-type mineralization discovered thus far at Conrad includes diamond drill intersections of 42.9 m of 18.44 g/t Au (ATAC Resources Ltd., 2012a). The discovery of a Carlin-type deposit in Yukon has wide ranging implications for the area given the immense size and clustered nature of Carlin deposits as recognized in Nevada.

Carlin deposits are characterized by sediment-hosted micron-scale gold within disseminated arsenian pyrite (Arehart, 1996). Deposits are typically found as replacement deposits in silty-carbonate, and have both structural and stratigraphic controls with strong relationships to deep seated crustal-scale structures (Cline *et al.,* 2005; Muntean *et al.,* 2011). Carlin fluids are typically weakly acidic, which results in the dissolution of carbonate. This is followed by precipitation of quartz and gold-bearing arsenian pyrite as well as trace metal enrichments of As-Tl-Hg-Sb-(Te) (Muntean *et al.,* 2011). At the Conrad zone, mineralization occurs within slope and basinal facies carbonate and clastic rocks. Mineralization is found associated with disseminated sulphides and is classified as carbonate replacement, associated with silicification and brecciation. The Conrad zone is strongly analogous to Carlin-type mineralization, and does not resemble nearby intrusion related deposits of the Tombstone suite as described by Stephens *et al.* (2004) or the recently discovered intrusion-related carbonate replacement Tiger zone (100 km to the west) as described by Theissen *et al.* (2011).

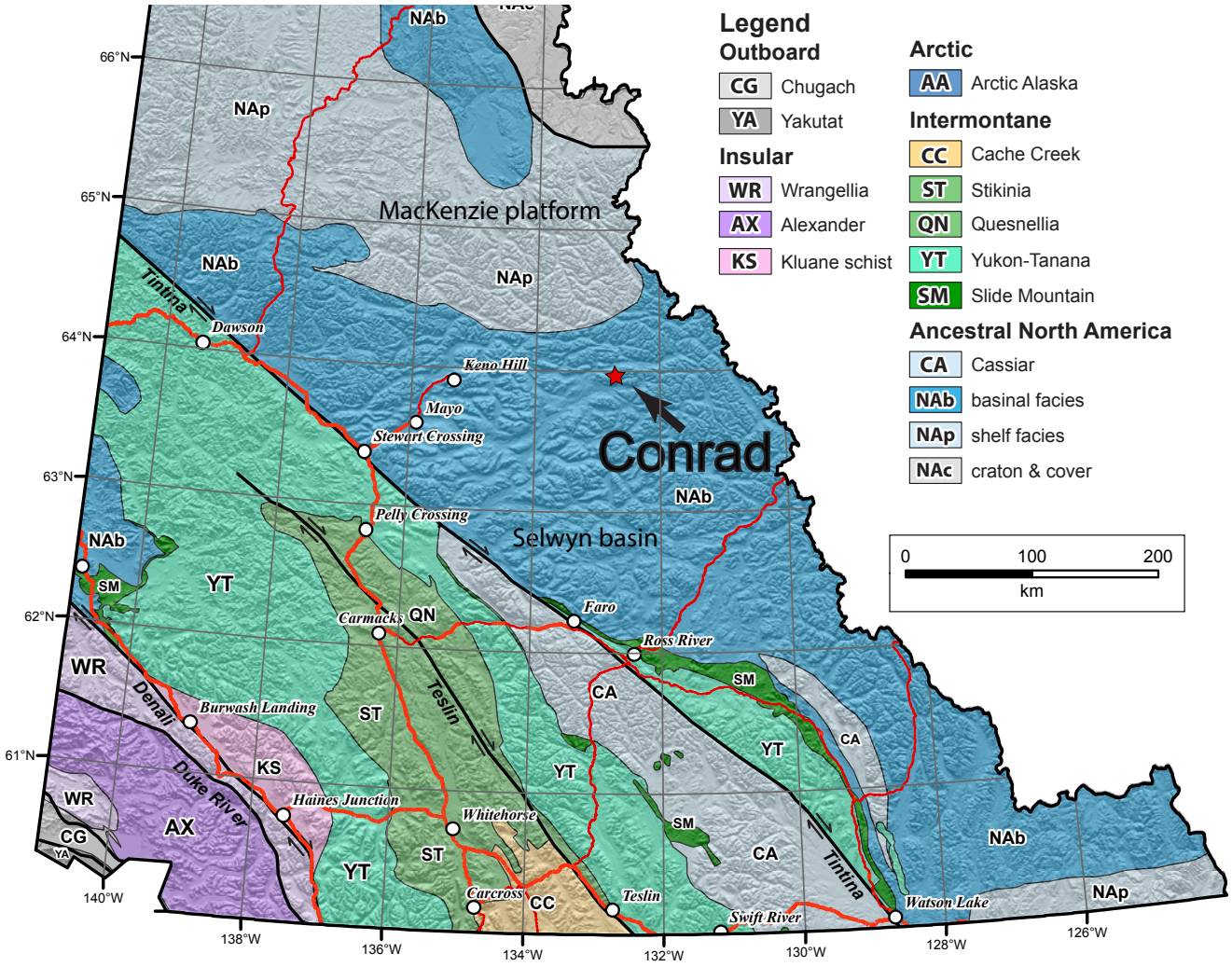

Figure 1. *Terrane map of Yukon showing the location of the Conrad zone in the northern Selwyn basin.*

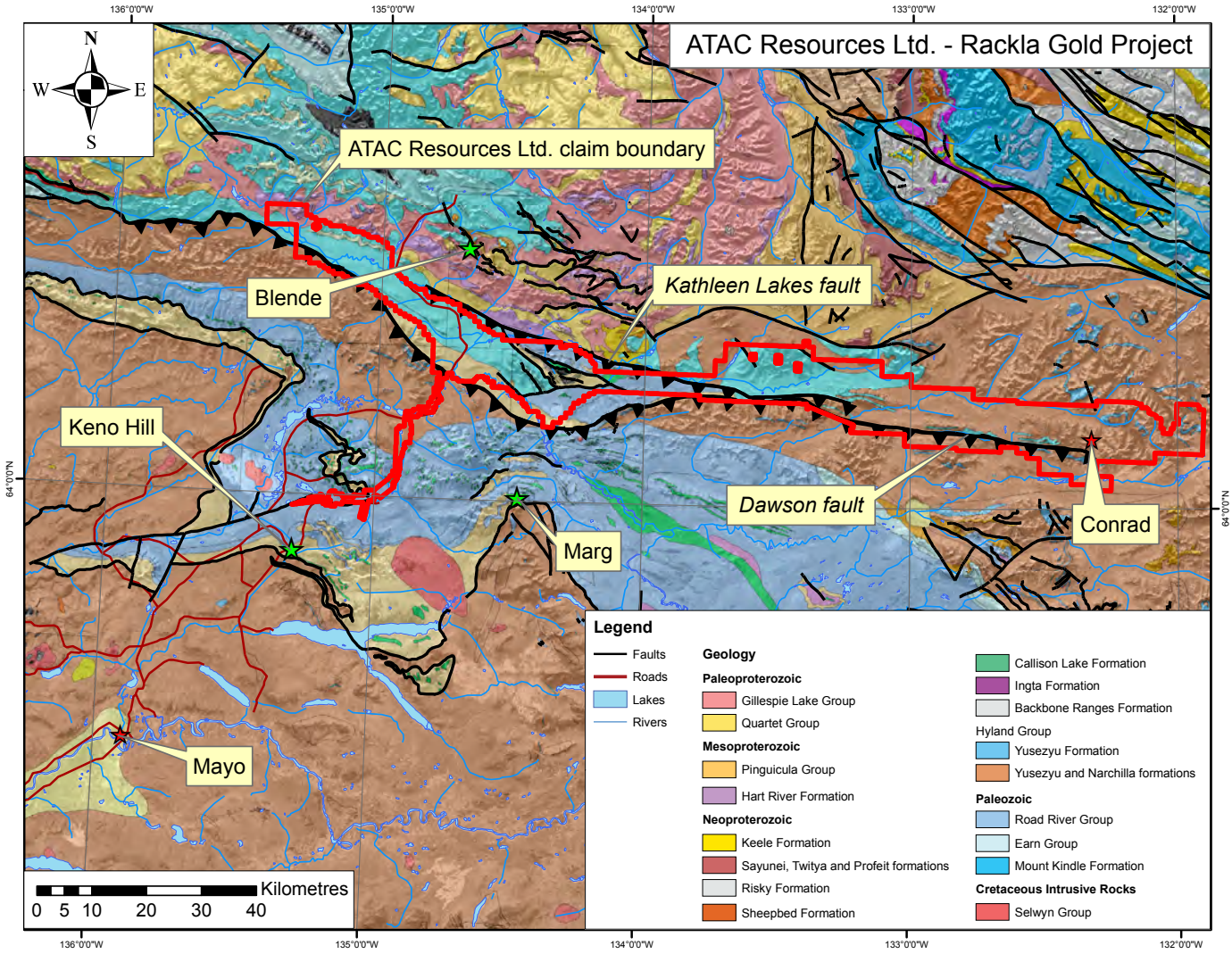

Figure 2. *Regional geology of the Rackla Gold Project (red outline). Major faults are indicated as well as some significant mineral occurrences in the region (as green stars).*

This study is part of an MSc project that will characterize the geology, alteration, and mineralization of the Conrad zone in order to develop a deposit and exploration model. This paper presents detailed characterization of lithologies, mineralization, and observed timing relationships. A preliminary paragenesis is presented based upon field observation of outcrops and detailed core-logging. Additionally, petrographic and Scanning Electron Microscope (SEM) analysis of the major rock types and the various stages of mineralization were utilized to constrain the paragenetic sequence presented here.

EXPLORATION HISTORY

The Nadaleen Trend was discovered in the summer of 2010 by ATAC Resources Ltd. during follow-up of arsenic anomalies in stream sediment. This resulted in the discovery of multiple mineralized zones with the season culminating in drilled intersections of mineralization at the Orisis, Conrad, and Isis zones within the Nadaleen trend (Fig. 3). During 2011, exploration and drilling of the area resulted in the expansion of the Conrad and Osiris zones and the discovery of the Amon and Isis East zones. Drilling projects in 2012 further expanded known mineralized zones, and led to the discovery of the Sunrise zone (ATAC Resources Ltd., 2012b). Follow up from prospecting in 2011 and subsequent drilling in 2012 discovered the Anubis prospect, located 10 km west of the Osiris and Conrad zones (ATAC Resources Ltd., 2012c).

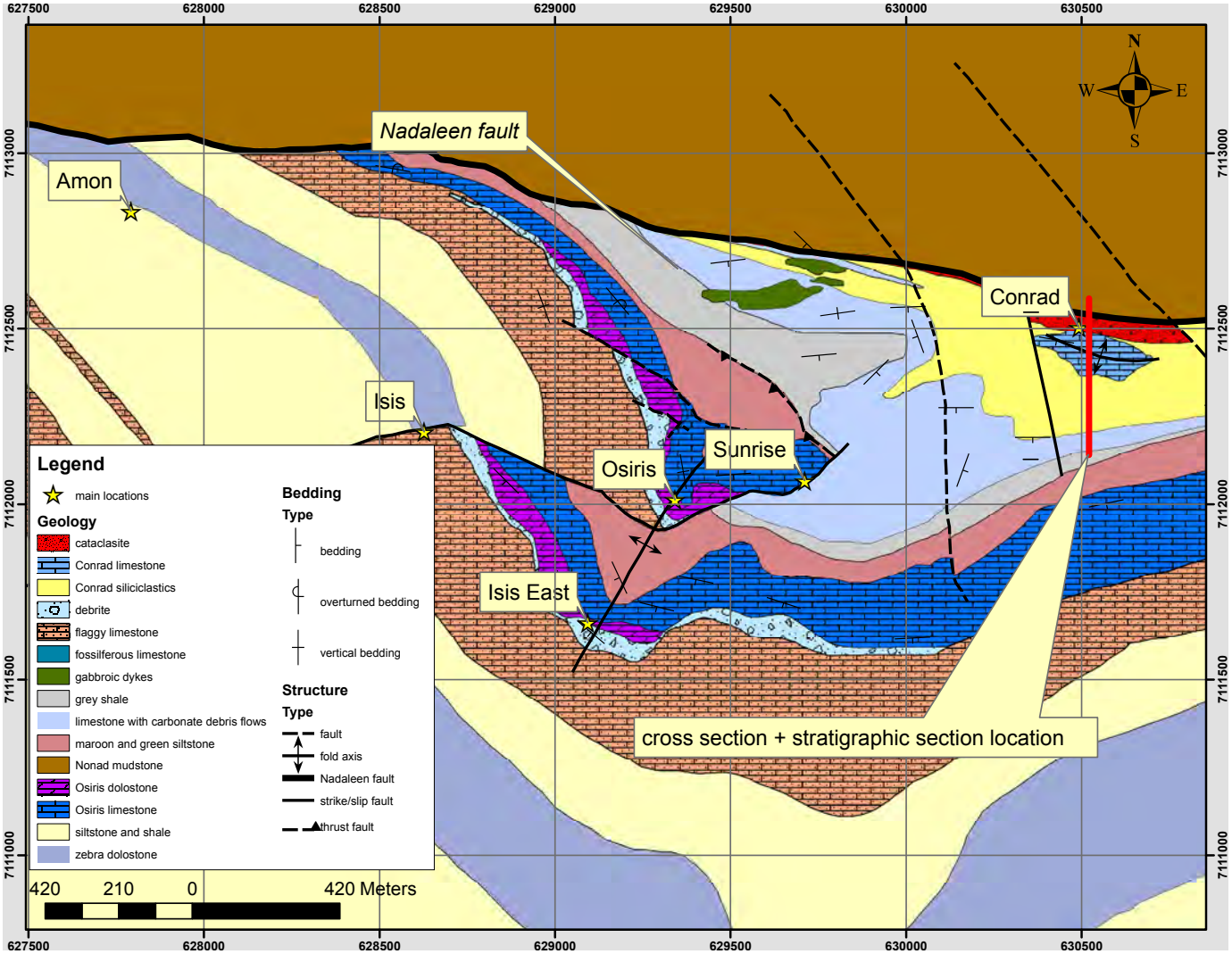

***Figure 3**. Local geology of the Nadaleen trend. Major faults are indicated along with other mineral occurrences on the property. The location of the stratigraphic section shown in Figure 4 is indicated by red line.*

REGIONAL GEOLOGY

The Nadaleen trend lies at the interface between the Neoproterozoic to Paleozoic rocks of the Selwyn basin and MacKenzie platform (Fig. 2). Rocks of Selwyn basin in the area are dominated by slope and basin facies carbonate, clastic rocks, and siltstone with significant deep water black shale and chert, whereas the Mackenzie platform is dominated by shallow water platformal carbonate (Abbott *et al.,* 1986). The area is bound structurally to the south by the Dawson thrust and to the north by the Kathleen Lakes fault. The Dawson thrust is believed to be a reactivated Neoproterozoic normal fault that lies at the northernmost boundary of the Selwyn basin and is marked by an abrupt facies change to the Mackenzie platform (Mair *et al.,* 2006). Structures in Selwyn basin are dominated by a fold and thrust belt associated with north directed Mesozoic convergence (Mair *et al.,* 2006). The Nadaleen trend and its association with the Dawson thrust and the Kathleen Lakes fault may be analogous to the Roberts Mountain thrust in the Carlin trend where the majority of giant deposits lie within 100 km of the thrust (Cline *et al.,* 2005).

No intrusive units have been documented thus far in the vicinity of the mineralization, with the exception of small mafic dykes (described below). Two regionally developed intrusive suites are found in the area surrounding the Nadaleen trend. The Mayo suite to the south of the Nadaleen trend consists of felsic to mafic, sub-alkalic

intrusions dated between 96-90 Ma. This suite is part of the larger Tombstone suite associated with post-collisional extension in the Selwyn basin (Hart *et al.,* 2004). The small granitic Rackla pluton lies 100 km to the west; it has associated aplite dykes and pegmatites that have yielded $^{40}Ar/^{39}Ar$ muscovite ages of 62.3 ± 0.7 Ma, 62.4 ± 1.8 Ma, and 59.1 ± 2.0 Ma (Kingston *et al.,* 2009). A U-Pb date of 62.9 ± 0.5 Ma for the Rackla pluton was also reported by Theissen *et al.* (2011). Although these two intrusive packages exist throughout Selwyn basin, a Cretaceous granodiorite pluton of the Mayo suite ~50 km to the southwest is the intrusion identified closest to the Nadaleen trend.

PROPERTY GEOLOGY

The Nadaleen trend consists of a southward-younging sequence of sedimentary rocks that is in faulted contact with a large mudstone package to the north (Fig. 3). Two different sedimentary packages can be separated in the strata to the south of the Nadaleen fault; Conrad and Osiris. The thick package to the north of the Nadaleen fault is an argillaceous mudstone to siltstone with isolated debris flow lenses. The Conrad strata, which underlies the Osiris strata consists of silty limestone with siltstone and sandstone as well as large carbonate debris flows inter-bedded with black shale/siltstone (Fig. 4). The Osiris strata consist of maroon and green siltstone underlying a main limestone package. A sequence of silty limestone and siltstone, diamictite, and dolomite overlie the main limestone unit. Small, east-west trending, mafic dykes have been identified trending parallel to the Nadaleen fault. The overall stratigraphy of the area remains unclear as little regional mapping has been carried out in the area. Ongoing mapping by the Yukon Geological Survey (YGS) is designed to improve the understanding of the regional stratigraphy.

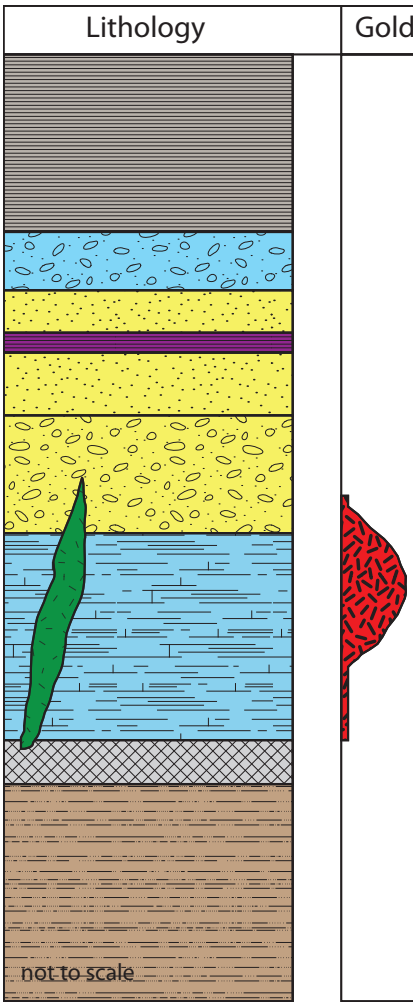

Lithology	Gold	Informal Name	Description
		Black shale/siltstone	thinly laminated, fine-grained shale interbedded with thin lenses of quartz sandstone
		Carbonate debris flows	carbonate debris flows interbedded with shales and silty limestones
		Conrad siliciclastics (hydrothermal dolostone)	siltstone: laminated siltstone to sandstone with disseminated pyrite throughout; small lense of dolostone with crackle breccia
		Conrad siliciclastics (gabbroic dykes)	conglomerate: matrix supported quartz-pebble conglomerate; disseminated pyrite throughout
		Conrad limestone (gabbroic dykes)	light grey weathering, massive to silty laminated limestone with cone-in-cone calcite lenses as well as beef calcite; some wispy, fine-grained quartz-sandstone layers; unit intruded by gabbroic dykes
		Nadaleen fault	strongly sheared interval up to 50 m wide
		"Nonad" argillaceous mudstone	rusty weathering, light green to teal to maroon and brown mudstone with minor interbedded granule to pebble diamictite

Figure 4. *Simplified stratigraphic section of the Conrad zone. The sequence youngs to the south.*

The Nadaleen trend has a complicated structural history, having been affected by several generations of faults and folds. The most prominent structural feature in the trend is the Nadaleen fault which separates the Conrad and Osiris strata from the argillaceous mudstone package to the north (Fig.5). The Osiris strata define two large scale antiforms that plunge steeply to the southwest. These two antiforms are separated by an east-west trending dextral strike-slip fault. The Conrad strata, on the other hand, are complexly folded. The Conrad limestone lies at the core of a doubly plunging antiform trending north-northeast. Evidence for other larger scale folds in the Conrad strata is not easily recognized, though small-scale chevron folds are observed within all siltstone and shale packages. The area is also cut by late, steeply dipping, northwest-trending faults that off-set mineralization locally. North-northwest bounding structures through valleys exist on the eastern and western extents of the area, separating the Conrad and Osiris strata from different sequences.

Numerous gold showings have been identified within the Nadaleen trend. An area approximately 4 by 2.5 km contains the mineralized zones known as Conrad, Osiris, Isis, Isis East, Amon, and Sunrise (Fig. 3). These zones occur within various carbonate packages across the trend, commonly containing realgar and orpiment with local decalcification and silicification. The Amon zone is hosted in dolomite and contains significant arsenic sulphides, but with minimal gold mineralization. The abundance and clustered natured of these showings and deposits signifies the metallogenic potential of the Nadaleen trend.

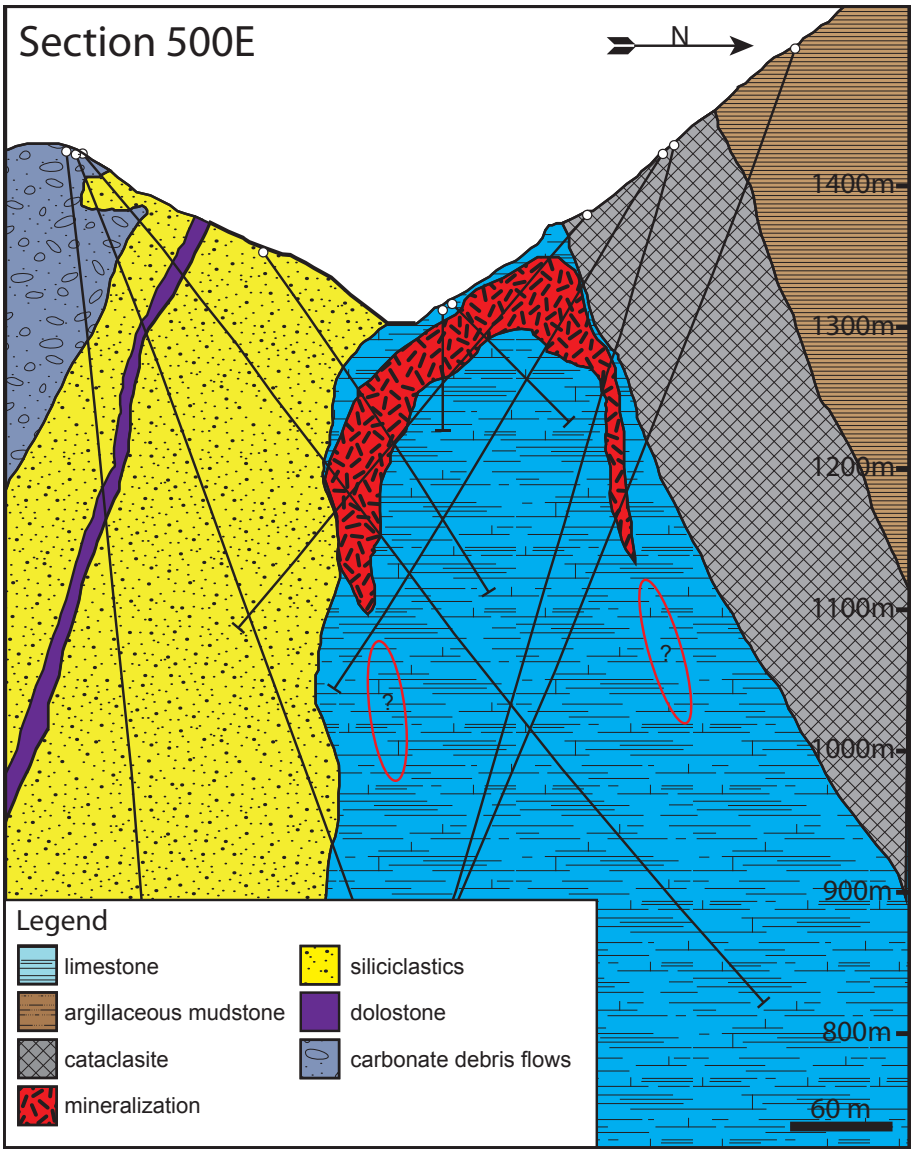

***Figure 5**. Simplified cross section through line indicated on Figure 3. Typical rock types are indicated with mineralization in an antiformal structure.*

GENERAL LITHOLOGIES

ARGILLACEOUS MUDSTONE - NONAD

The argillaceous mudstone known colloquially as "Nonad" is a thick sequence that underlies the northernmost part of the property and extends beyond currently mapped units to the east, west, and north. The unit is separated from Conrad and Osiris strata by the east-trending Nadaleen fault. The unit is a moderately to readily weathering sequence, producing fine talus on slopes yet remaining resistant on ridges. The unit has a distinctive tan to rusty-brown weathering colour. Fresh surfaces are dominantly grey-green though can be maroon locally. Lithologies consist of very thinly bedded mudstone to siltstone with minor sandy beds (<1 cm) (Fig. 6a). Locally, there are lenses of diamictite with rounded sedimentary granules to pebbles in a sandy, calcareous matrix. Grains are dominantly angular to subrounded sub-millimetric quartz in layers alternating with silt and mud (Fig. 6b). The unit contains trace (<1%) amounts of pyrite disseminated

throughout silty beds. Distinctly maroon coloured layers can contain up to 5% disseminated hematite with rare chalcopyrite. The unit has been subjected to minor faulting throughout with well-developed cleavage locally. Thin, (3-15 mm) en-echelon calcite and dolomite veinlets are abundant throughout the unit; these veins tend to weather recessively. The Nonad mudstone contrasts starkly with all units to the south of the Nadaleen fault; the superposition of this package with sedimentary sequences to the south is a defining characteristic of the Nadaleen trend.

CONRAD LIMESTONE

The Conrad limestone is a small, lenticular package with limited erosional exposure within an area of 300 by 70 m. It lies in faulted contact with the Nadaleen fault to the north and is in gradational contact on all other sides with the overlying siliciclastic package. The unit resists weathering and has a light grey weathering color. In hand specimen and in core, it is fine to medium grained, dark grey and crystalline (Fig. 6c). Thin bedding in the unit is visible in both hand specimen and core. Quartz and silt-rich interbeds up to 3 m thick are observed locally, typically close to contacts with above lying siliciclastic rocks. Areas of higher silt content within the limestone can have bedding parallel features such as "beef calcite" and "cone in cone calcite". These features are found locally and range up to 4 cm in thickness. The limestone is dominantly calcite (60-95%), with silt and detrital quartz content varying from 5-30%, increasing towards the contact with the siliciclastic package.

Three generations of stylolites are present within the Conrad limestone. First generation stylolites are parallel to bedding and the most abundant. Second generation stylolites crosscut earlier bedding parallel stylolites, typically perpendicular to bedding planes. Third generation stylolites occur at many angles to bedding and crosscut all earlier phases along with early calcite veins. These stylolites have small enrichments of residual quartz grains as well as framboidal pyrite (Fig. 6d). Calcite surrounding the stylolites is typically recrystallized. As many as four generations of calcite veins and veinlets are present throughout the unit with the most dominant set being a conjugate set of veins with widths from 1 to 20 mm at high angles to bedding. Small and large scale chevron and open folds are present throughout the unit.

SILICICLASTIC PACKAGE

The siliciclastic package has a large areal extent with limited outcrop. The unit has a northeast elongation of approximately 1.5 km with the narrowest, northeast dimension being only 800 m within the mapped extent. The package is folded into an east and west-plunging antiformal dome with the Conrad limestone package at its core. Contacts with the limestone are all gradational. To the north, the unit is in faulted contact with the argillaceous mudstone across the Nadaleen fault. All southern portions of the unit are in gradational contact with an overlying carbonate debris flow unit. The package is very rusty brown in outcrop and typically weathers recessively. Fresh surfaces are dark grey to black. The unit is a siltstone to sandstone with lenses and interbeds of matrix and clast supported quartz-granule to pebble conglomerate (Figs. 6e,f and 7a). Siltstone to sandstone portions of this unit show regular bedding at 0.5-1 cm. Conglomerate lenses are typically matrix supported, though isolated zones of clast supported conglomerate are observed. Clasts are granule sized with some lenses of pebble conglomerates. Clasts are subrounded to rounded frosted quartz, chert, carbonate, and siltstone; whereas the matrix is dominantly silt and trace carbonate (Fig. 6b). Siltstone portions are dominated by quartz (85-95%). Typically, the quartz grains are small (<0.5 mm) and subrounded. Subrounded quartz grains dominate the coarser grained portions of beds (80-95%) with the remainder being dominated by silt (Fig. 7b). Pyrite is disseminated throughout both siltstone and conglomerate portions of the unit (2-6%) but localized layers of massive (>60%) pyrite have been observed. Sparse dolomite and calcite veinlets (<1 cm) are observed throughout the unit.

CARBONATE DEBRIS FLOWS

The carbonate debris flow package is an irregularly shaped unit in gradational contact with the underlying siliciclastic package to the north. It is a resistive weathering sequence that is tan to buff colour on weathered surfaces. Fresh surfaces vary from dark grey to beige with a dark brown matrix. The unit consists of a series of megaclastic carbonate debris flows interbedded with black shale and limestone. The debris flows are large lenses of clastic material with blocks of carbonate as big as 2 m in diameter. These lenses typically occur at the base of the unit, transitioning to bedded limestone interbedded with black siltstone upwards in section. Debris flow lenses persist upward in section though thickness reduces considerably. Limestone towards the top of the section is thinly bedded with abundant bedding parallel "beef" calcite features. Ooids and cortoids are found locally throughout the matrix of the debris flows in between large carbonate fragments (Fig 7c). Clasts are primarily angular

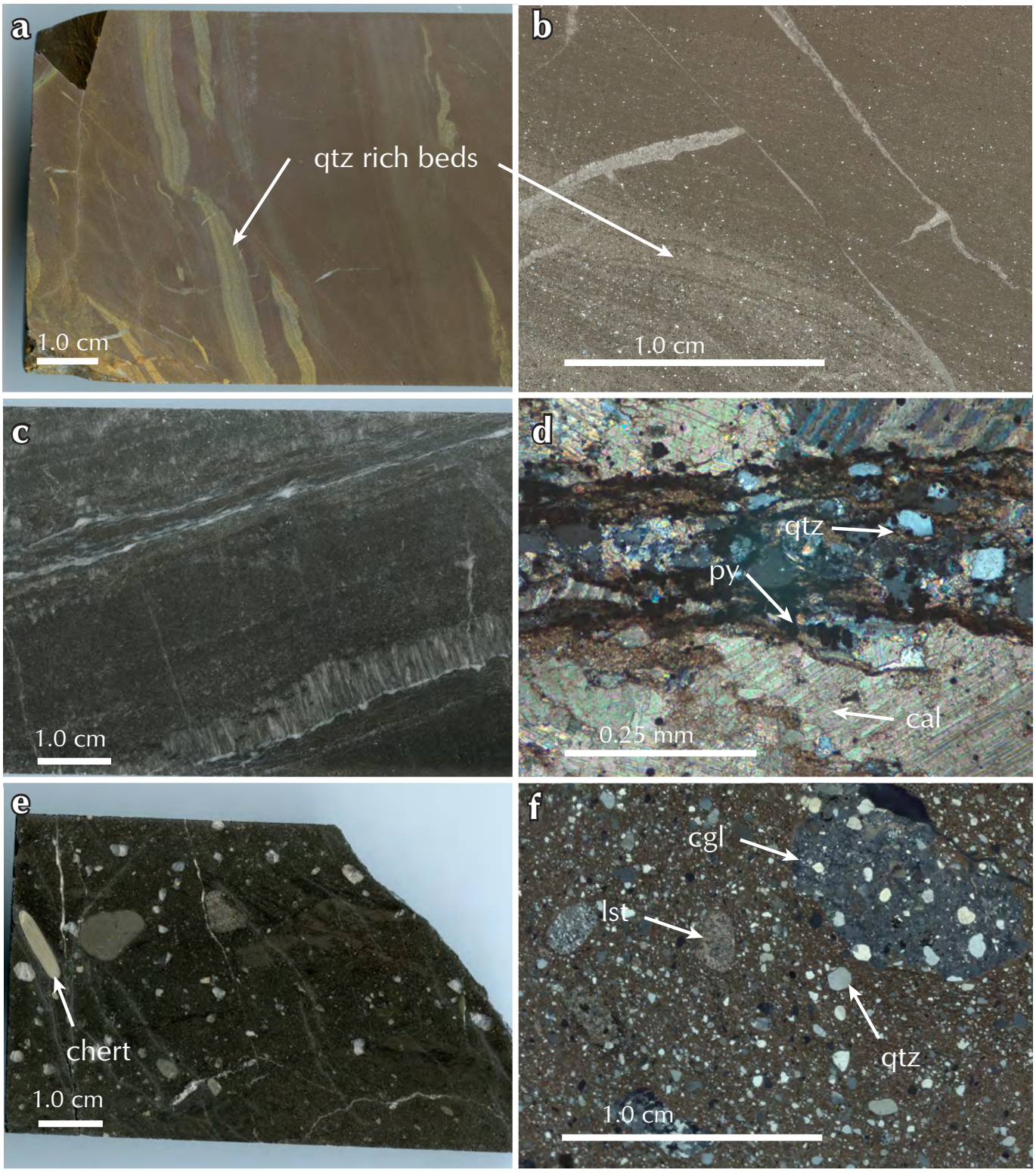

Figure 6. *Typical Conrad lithologies: (a) photograph sample of argillaceous mudstone; (b) photomicrograph illustrating bedding textures; (c) photograph of limestone (lst) illustrating bedding textures; (d) photomicrograph of stylolite in limestone (cal=calcite) illustrating pyrite (py) and quartz (qtz) within seam; (e) photograph of siliciclastic conglomerate (cgl) illustrating clast size and variety; and (f) photomicrograph of siliciclastic conglomerate illustrating varied fragment compositions and silty matrix.*

fragments of dolostone, limestone, and siltstone-mudstone with angular to rounded quartz grains (Fig. 7c). Lithic fragments are large, ranging from centimetre to metre scale. Quartz grains dominate the smaller sized clasts present (2-10 mm). Matrix is dominantly silt-mud with trace carbonate (Fig. 7d). Matrix content varies from 15-50%. The unit has small sets of thin (<1 cm) calcite veinlets cutting throughout. The carbonate debris flow package is a unique and identifiable unit, and is an important marker horizon where present.

BLACK SILTSTONE/SHALE

The black siltstone/shale unit lies stratigraphically above the carbonate debris flow package forming a thin, wispy border at the top of the section. The unit is interbedded with the underlying package. The unit weathers recessively and is rarely observed in outcrop. Where visible, it is black with some minor rust staining, and is commonly only observed as small chips. On fresh surfaces, the unit is light grey to black in color. Thin laminations are present throughout (Fig. 7e). The unit is dominated by silt to mud with small contributions of 1-2 mm subrounded quartz grains locally (Fig. 7f). Trace disseminated pyrite is observed within quartz-rich beds. The unit is highly cleaved and also shows well-developed local chevron folding. Fracture surfaces are often conchoidal in nature. This unit has complex internal structures such as cleavage and folds, making it an important package for identifying key structures.

DOLOSTONE

A horizon of hydrothermal dolostone occurs within the siliciclastic package that underlies the carbonate debris flow unit. This is a very thin band parallel to stratigraphy that only outcrops in two locations within the Conrad strata. Where observed, it is resistive weathering with a dull, buff-grey colour. In hand specimen it is beige-grey and finely crystalline. Thin bedding is present locally. The unit is primarily composed of 80-90% sub-millimetre intergrown dolomite crystals (Fig. 7h). Pyrite is abundant throughout the unit, both disseminated and in veinlets (5-10%), trace (<1%) sphalerite is also observed. Distinct black crackle breccia veinlets (Fig. 7g) are found throughout consisting of sparry black-dolomite (20-50%) and quartz (50-80%) with minor pyrite. Although the dolostone appears to be hydrothermal in nature, it distinctly follows a specific horizon that is traceable in drill core as well as on surface. This unit appears to represent an early hydrothermal event associated with minor zinc mineralization.

NADALEEN FAULT CATACLASITE

The Nadaleen fault is a distinctive feature of the Nadaleen trend. It is a steeply north dipping, east-trending structure that separates two distinct lithologic packages. It presents in drill core as a complex zone of cataclasite. This cataclastic zone can be up to 50 m in thickness and is only found directly adjacent to the fault (Fig. 5). In outcrop, it is a recessively weathering unit that is rusty brown in color. In hand specimen and in core, the unit ranges from light to dark grey. The zone contains deformed fragments of all of the rock types found in proximity to the fault. Fragments are highly variable in size with abundant, small 1-5 cm fragments as well as occasional fragments larger than 2 m. Composition of fragments is highly variable although abundance of fragment types corresponds to the nearest, non-deformed lithology. A fabric defined by rotated and elongated clasts and fine silt is well developed locally (Fig. 8a). The fine-grained silty groundmass is composed primarily of muscovite, much of which defines shear fabrics (Fig. 8b). Up to 5% disseminated and blebby pyrite is found within the cataclasite (Fig. 8b). The kinematics of this fault are inconsistent, as both sinistral and dextral indicators are observed, indicating multiple generations of movement. The complexity of the cataclasite and enigmatic nature of the movement along the fault zone may indicate that the Nadaleen fault was a long lived structure, subject to multiple generations of movement.

MAFIC INTRUSIVE ROCKS

A series of mafic dykes have been identified in the Nadaleen trend. These are found within an area where no intrusive rocks have previously been observed. The dykes are steeply dipping, east-trending and sub-parallel to the Nadaleen fault, ranging in thickness from 25 cm to 25 m. The majority of dykes found thus far have been drill core intersections as very few outcrops of the unit are present. Within the Conrad zone the dykes crosscut the limestone and siliciclastic packages. One particular dyke parallels the lower contact of the Nadaleen fault zone. Locally, fragments of this dyke are incorporated into the cataclasite. Where intersected in drill core, the dykes contain abundant xenoliths of proximal country rocks. The dykes intrude along fault zones; their proximal nature to the Nadaleen fault as well as incorporation into the cataclasite locally indicating that there is some movement along the fault post dyke emplacement.

The mafic dykes are greyish green with a slight rusty coating on weathered surfaces. Fresh surfaces are

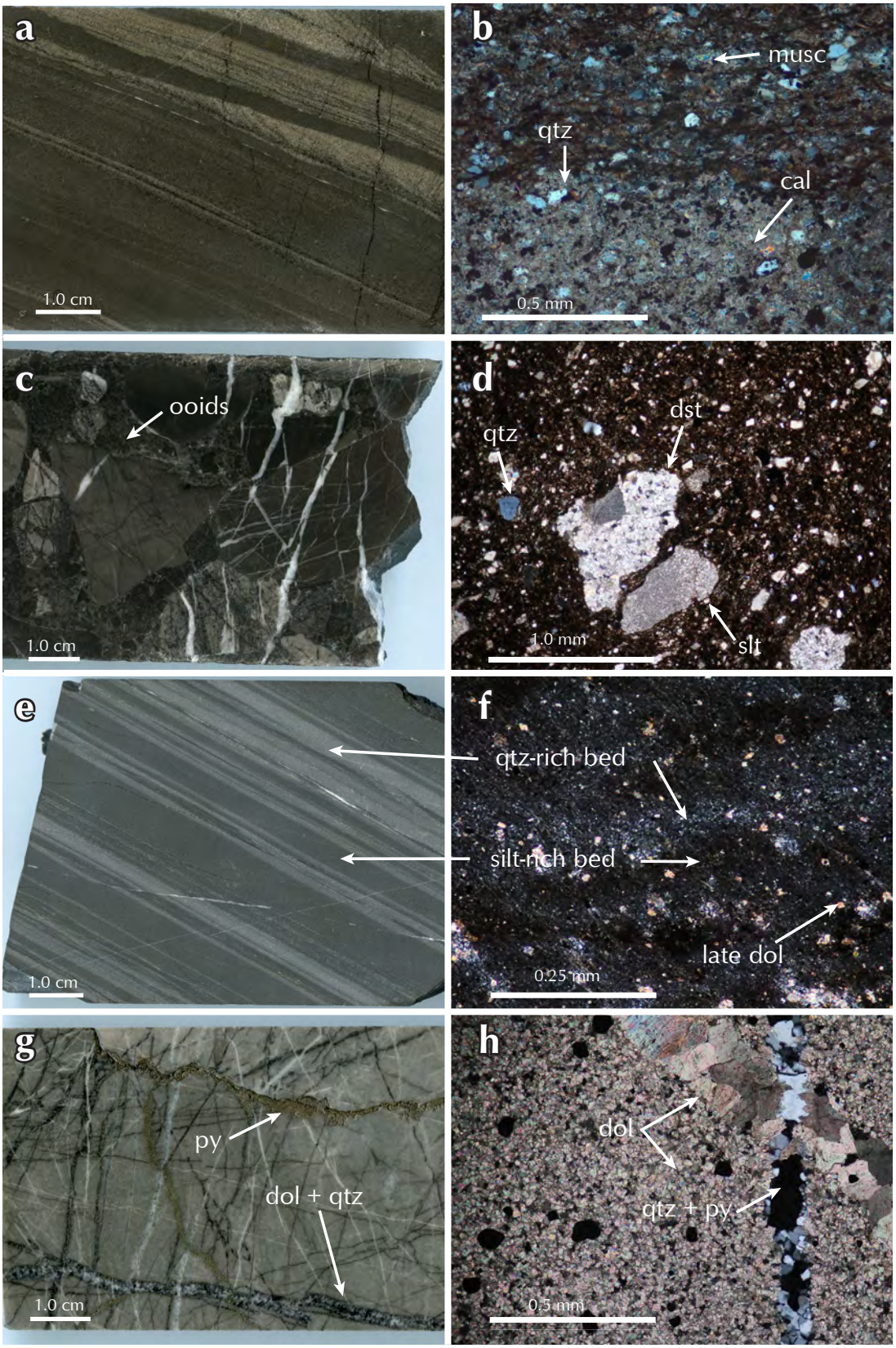

***Figure 7**. Typical Conrad lithologies: (a) photograph of pyrite rich siltstone; (b) photomicrograph of siltstone illustrating abundant quartz and variable bedding (musc=muscovite); (c) photograph of carbonate debris flow package with ooids and cortoids in matrix; (d) photomicrograph of carbonate debris flow unit illustrating high silt content in matrix and varied clast compositions (dst=dolostone, slt=siltstone); (e) photograph of black shale unit with quartz-rich beds; (f) photomicrograph of black shale package showing thin beds and late stage dolomite (dol); (g) photograph of hydrothermal dolostone illustrating crackle breccia texture and abundant pyrite; and (h) photomicrograph of dolostone showing fine grained dolomite with abundant pyrite.*

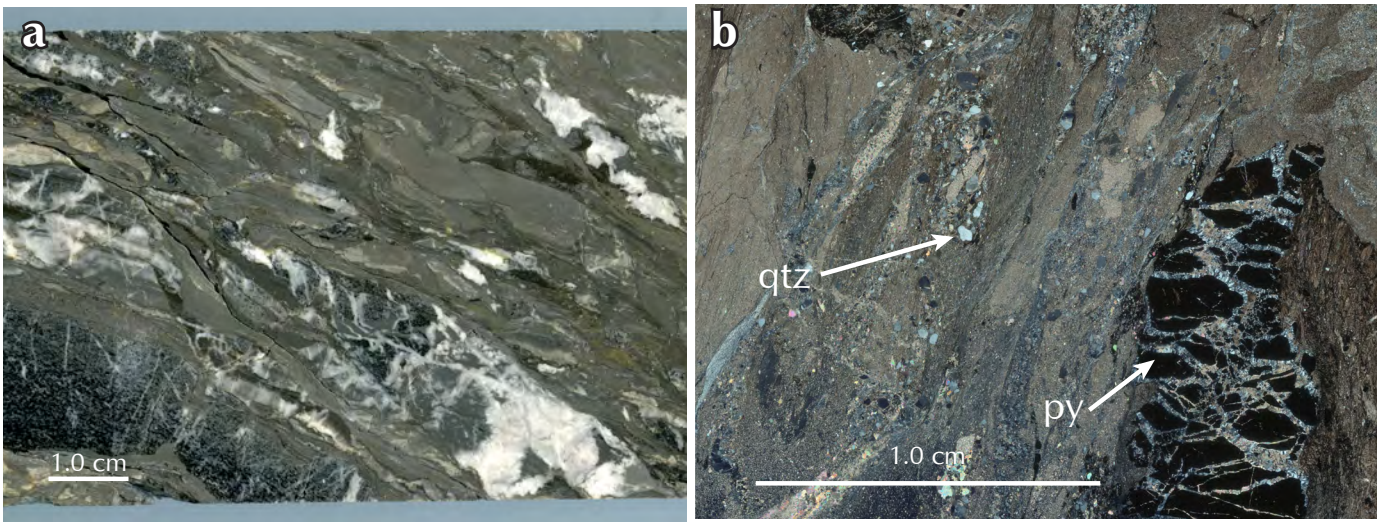

***Figure 8**. Nadaleen fault cataclasite zone lithologies and textures: (a) photograph of cataclasite illustrating well-developed shear textures; and (b) photomicrograph illustrating shear textures and pyrite content.*

dark grey and coarsely crystalline (Fig. 9a). Chilled margins are common along dyke margins. The dykes are gabbroic in composition, dominated by amphibole (30-45%) and plagioclase (25-40%) with minor clinopyroxene (10-15%), trace pyrite is observed disseminated throughout (Fig. 9b). Texturally, large euhedral amphibole crystals enclose interstitial plagioclase with laths of some minor plagioclase (0.5-2mm). One dyke identified has similar composition but is very distinct texturally. Carbonate amygdules are abundant (10-25%), as well as lesser (<10%) plagioclase phenocrysts up to 8 mm (Fig. 9c). These phenocrysts occur within a very fine grained groundmass dominated by very fine-grained amphibole and plagioclase with trace pyrite (Fig. 9d).

The gabbroic dykes show little evidence of deformation. No discernible fabric or folding has been identified but there are small fractures and very minor faulting present throughout. All dykes are altered to some extent. Least altered rocks are distinctly green and show amphibole replacement by chlorite. Plagioclase typically shows patchy sericite alteration. Secondary pyrite is also present; disseminated throughout sites previously occupied by mafic minerals. The most highly altered dykes are proximal mineralization and are characterized by strong, pervasive sericite alteration. Mafic minerals have been replaced by carbonate, pyrite, and sericite. Porphyritic and amygdaloidal dykes exhibit sericitic alteration of plagioclase phenocrysts and carbonate, sericite, and pyrite alteration of mafic groundmass. Small calcite and quartz veinlets are rarely observed. The mafic dykes are also locally mineralized with abundant pyrite and trace realgar. The gabbroic dykes pre-date mineralization, possibly preserving a record of alteration induced by the mineralizing fluid.

ALTERATION AND MINERALIZATION

The primary style of alteration associated with mineralization is decarbonatization of host limestone (Fig. 10a). Large amounts of carbonate are removed from the host limestone creating large amounts of insoluble residue, consisting primarily of detrital materials from within the host carbonate. In hand specimen, this is manifested as a very fine grained, sooty, black material, which is commonly found within early stylolites. Stylolites observed near areas of mineralization are thick (0.5-1.5 cm) and are powdery and unconsolidated. The majority of this material (>80%) is very fine grained brown to black residue with 5-10% detrital quartz and 1-5% pyrite (Fig. 10b). The composition of the black residuum is a combination of fine silt and carbonaceous material.

Decarbonatization of host limestone occurs synchronously with silicification. Quartz in silicified and mineralized zones is typically black in color with a distinct, sugary texture. Quartz can be abundant in mineralized areas, locally up to 95% by volume. Quartz crystals are variable, including both euhedral and anhedral crystals. The quartz crystals are typically very small, rarely greater than 1 mm with an average size of 0.05-0.4 mm. Anhedral crystals typically

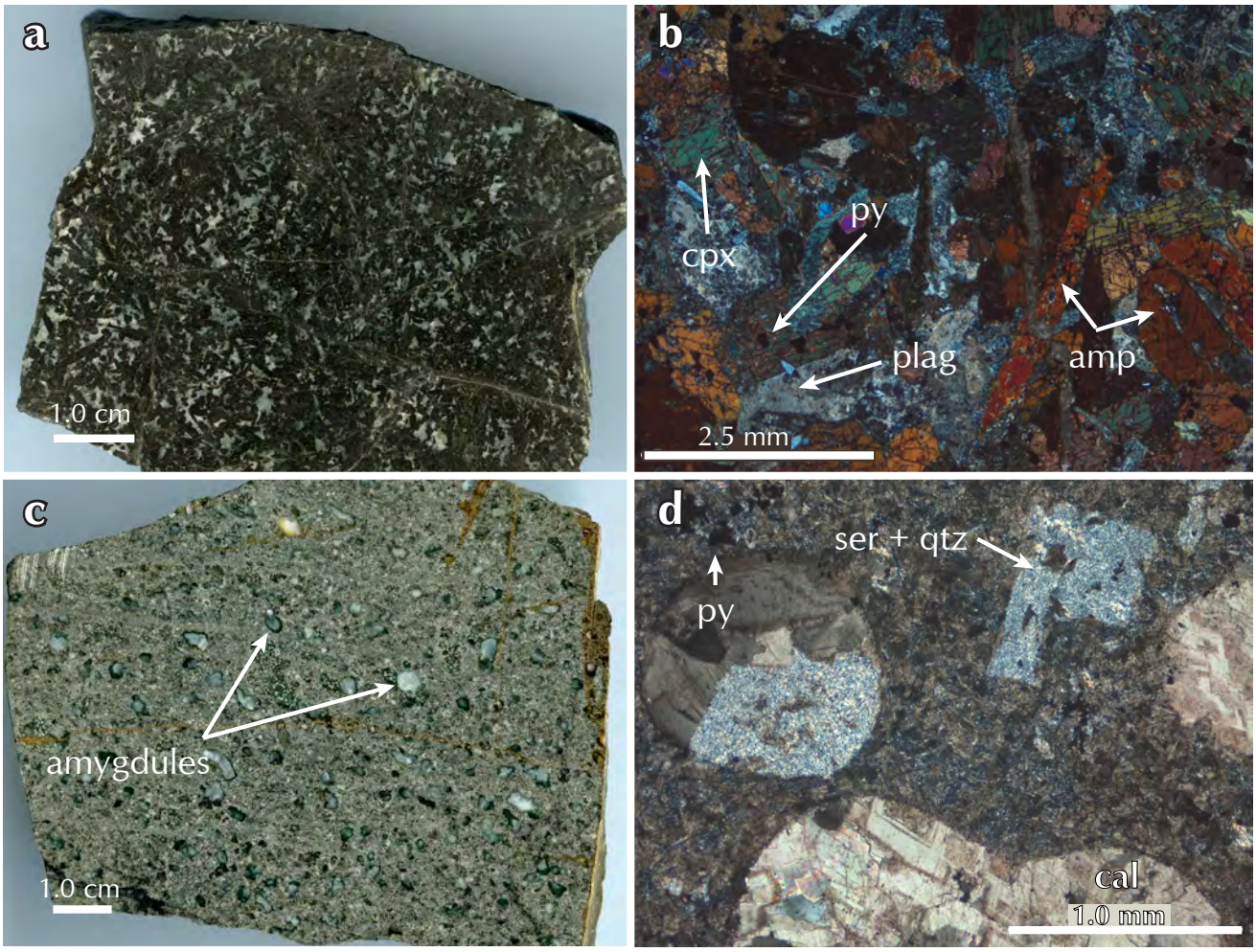

***Figure 9**. Gabbroic dyke units in Conrad: (a) photograph of gabbroic dyke with coarse crystalline amphibole; (b) photomicrograph of gabbroic dyke with coarse grained amphibole (amp; cpx=clinopyroxene, plag=plagioclase); (c) photograph of amygdaloidal unit with porphyritic plagioclase; and (d) photomicrograph of dyke illustrating carbonate amygdules and sericite (ser) altered plagioclase phenocrysts.*

have inclusions of carbonate or dark colored residuum (Fig. 10c). Areas of mineralization are dominated by strong silicification, allowing areas of complete decarbonatization to remain moderately competent, permeable, and porous.

Pyrite can be abundant in mineralized zones. Pre-ore stage pyrite is concentrated within these zones as residuum from decarbonatization. Pyrite crystals are very small (<0.5mm), occurring as very small framboids, euhedral crystals, or anhedral grains/masses. Pyrite content within mineralized zones can be around 5-10% (Fig. 10e). The large increase in the amount of pyrite provides a suitable nucleus for later trace-element and gold-rich pyrite (Fig. 10e). Secondary growth around early crystals of pyrite is commonly visible (Fig. 10f). This secondary growth can be arsenic and trace-element enriched. Arsenian pyrite forms as secondary growths around early pyrite crystals (Fig. 10h).

The secondary arsenian pyrite is very small, commonly only 1-5 microns in size; and locally forms anhedral buds or euhedral growths around pre-existing pyrite crystals (Fig. 10h,g). Despite a significant abundance, pyrite is not readily visible in hand specimens, probably because of its dark, sooty colour. Where observed petrographically, the highest abundance of pyrite is commonly associated with areas of increased illite content.

Visible gold is not present within the Conrad zone, although other minerals that can be recognized in hand specimen can be key indicators of gold enrichments. Realgar and orpiment are key spatial indicators of gold mineralization. In silicified and brecciated mineralized zones these arsenian sulphides are commonly observed disseminated within pore spaces or filling interstices (Fig. 10d). Massive realgar, orpiment, and fluorite are

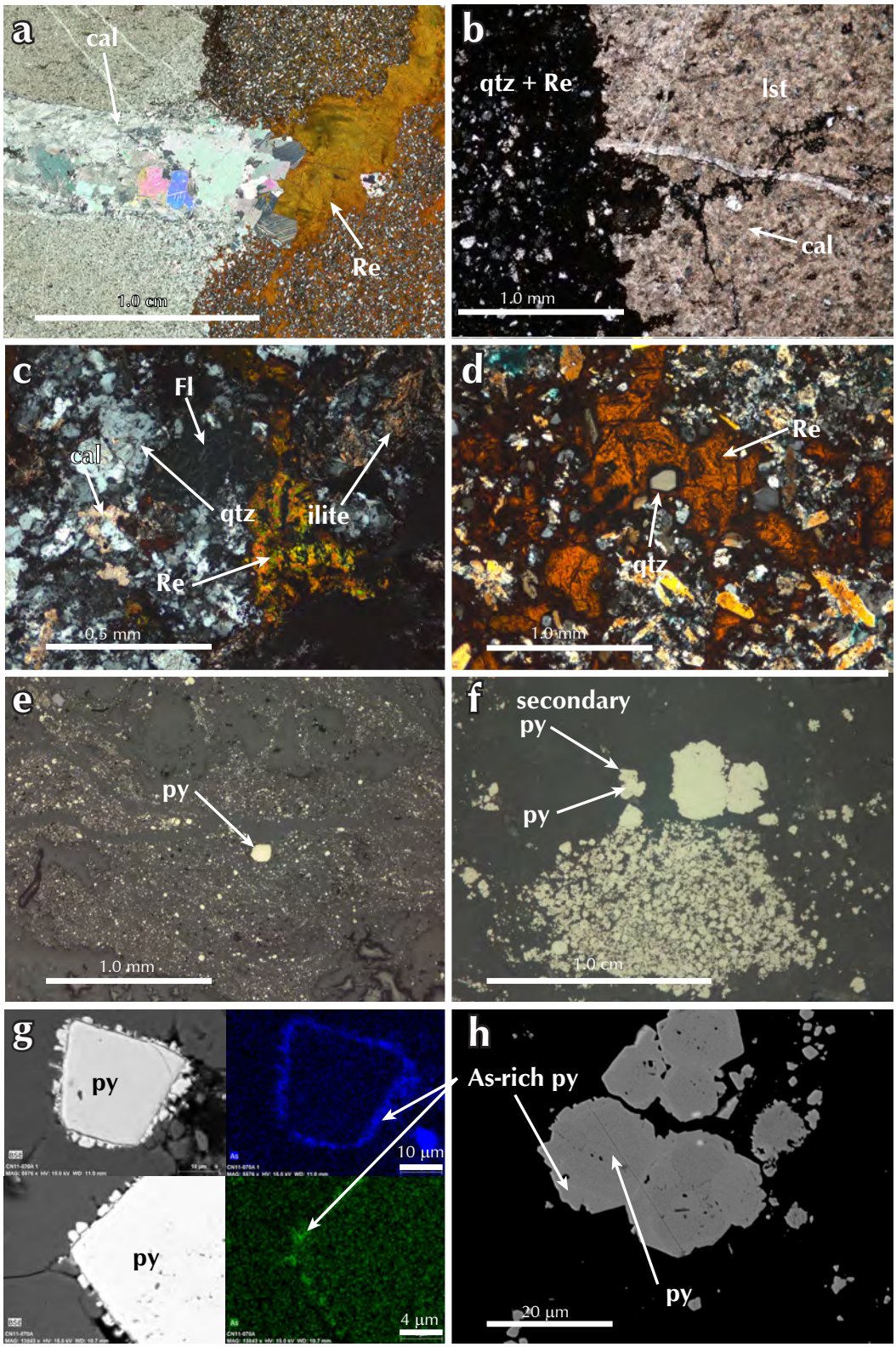

***Figure 10**. Styles of mineralization in the Conrad zone: (a) photomicrograph of silicification and decarbonatization front next to un-altered limestone; (b) photomicrograph of alteration along stylolites and vein selvages (Re=realgar); (c) photomicrograph of mineralized textures and mineral varieties (Fl=fluorite); (d) photomicrograph illustrating early quartz surrounded by late realgar; (e) photomicrograph showing pyrite abundance in mineralized zones; (f) photomicrograph showing secondary growth around earlier pyrite; (g) SEM backscattered electron microscope images and corresponding arsenic map illustrating arsenic-rich overgrowths around early pyrite; and (h) SEM backscattered electron microscope image illustrating early pyritic cores with secondary trace element rich pyrite overgrowths.*

commonly observed, but rarely contain significant gold. Massive realgar can be associated with peripheral rhombohedral calcite veins up to 3 m thick. Rare, narrow stibnite veins and veinlets are also present within siliciclastic packages. Although not always directly associated with gold, stibnite veins containing realgar, orpiment, and fluorite, serve as important indicators of possible gold mineralization. The pathfinder element mineral suite associated with mineralization in the Conrad zone is a key indicator to otherwise non-visible gold.

DISCUSSION

Gold mineralization within the Conrad zone is intimately associated with decarbonatization of host limestone and subsequent silicification. It is associated with a variety of minerals including realgar, orpiment, quartz, illite, fluorite, and calcite (Fig. 11). Very fine grained arsenic-rich pyrite typifies areas of gold mineralization. Texturally, zones of gold mineralization appear as black breccias or replacement/dissolution zones, typically occurring with abundant visible realgar.

DISTRIBUTION OF MINERALIZED ZONES

The factor controlling the distribution of alteration and mineralization is permeability. The core of mineralization appears to define a large antiformal structure within the Conrad limestone (Fig. 5); however, a combination of factors controls the permeability of the rock. Apart from primary fluid conduits such as fault and shear zones,

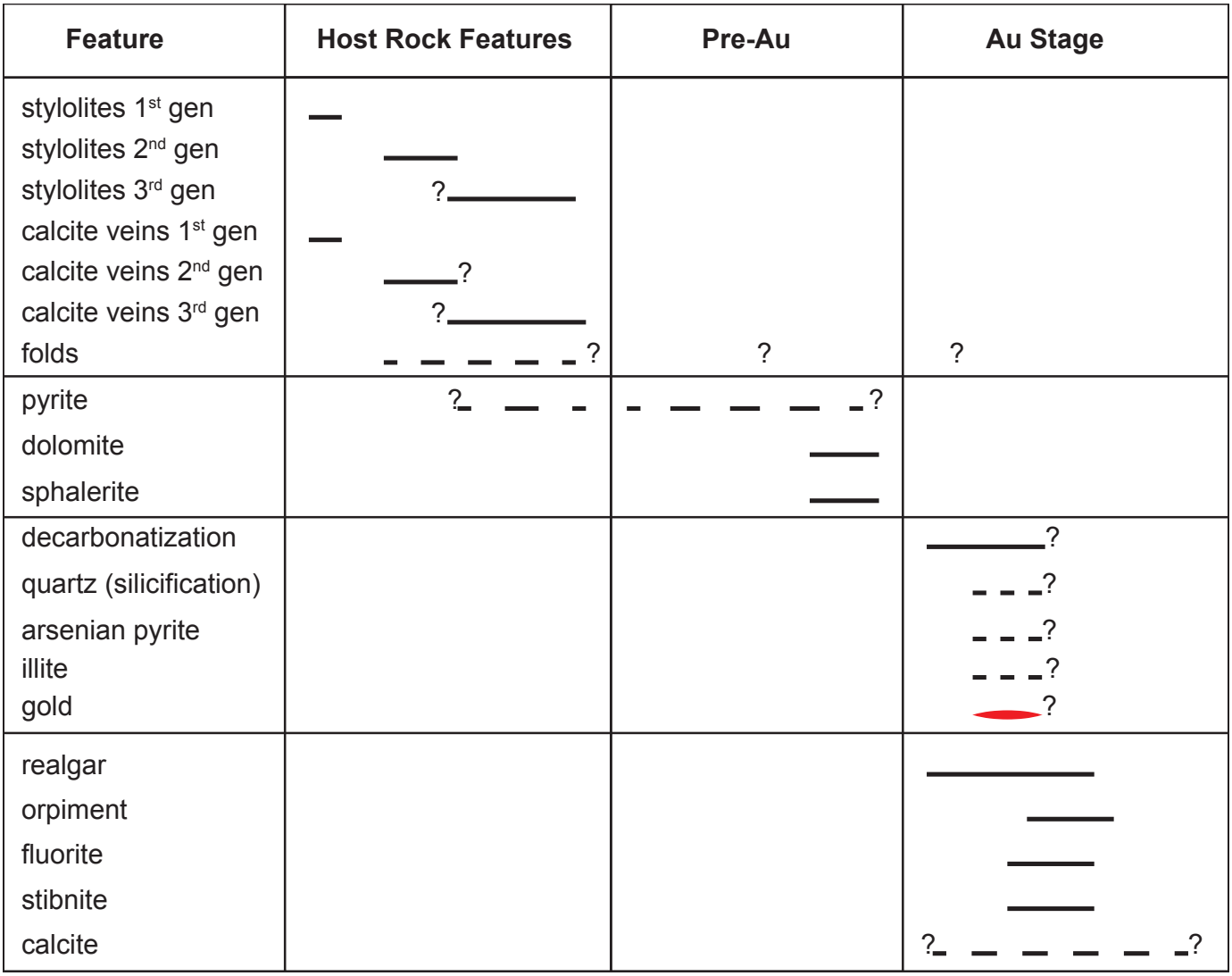

Figure 11. *Preliminary paragenetic scheme for Conrad zone mineralization, illustrating early rock preparation events followed by late ore stage mineralization.*

features controlling permeability are stylolites, veinlets, fold hinges and faults (Fig. 10b). Three generations of stylolites are present within the Conrad limestone. Up to four generations of calcite veins and veinlets are also present within the host limestone. Small scale folds are readily observed throughout the Conrad limestone package, many of which have faults and fractures propagating through fold hinges. These features create preferential fluid pathways for mineralizing fluids. The network of porosity created by the stylolites, vein sets, fold hinges, and isolated shears and faults control the distribution and intensity of mineralization and alteration. Permeability is possibly further enhanced in the limestone within the axial area of the anticline by the hydraulic barrier presented by the overlying siliciclastic package.

FLUID EVOLUTION MODEL

Alteration associated with gold mineralization at the Conrad zone consists of two primary phases: decarbonatization and silicification (Fig. 12). The strongest control on the distribution of mineralization is porosity and permeability. Exploitation of the porosity network by the mineralizing fluid has enabled reaction with and removal of carbonate from the host limestone. As this process progressed, varying amounts of carbonate were removed and quartz crystallized into space created by the removal of carbonate. The quartz that is present is commonly euhedral, indicating precipitation after space was created (Fig. 10d). The process of gradual removal of carbonate around areas of high porosity resulted in the local formation of collapse breccias (Fig. 12). Euhedral as well as finely crystalline quartz now forms the matrix of these brecciated zones along with illite and late realgar, calcite, and fluorite (Fig. 11). Fluid exploitation of porosity networks gave rise to extensive decalcification, followed by silicification of the host carbonate rocks. In extreme cases, this process resulted in the formation of mineralized breccias (Fig. 12). These areas form the core of mineralized zones identified at Conrad.

CONCLUSIONS

This paper presents the first descriptions of the host rocks and mineralized rocks from the Conrad zone, a newly discovered sediment hosted gold prospect in east-central Yukon. The Conrad zone is located in on the northern margin of the Selwyn basin proximal to the Dawson thrust, a major structure at the interface of Selwyn basin and MacKenzie platform. Geology of the Conrad zone is dominated by slope facies carbonate and clastic rocks with gold preferentially hosted within secondary arsenian pyrite in the carbonate rocks. Mineralization consists of

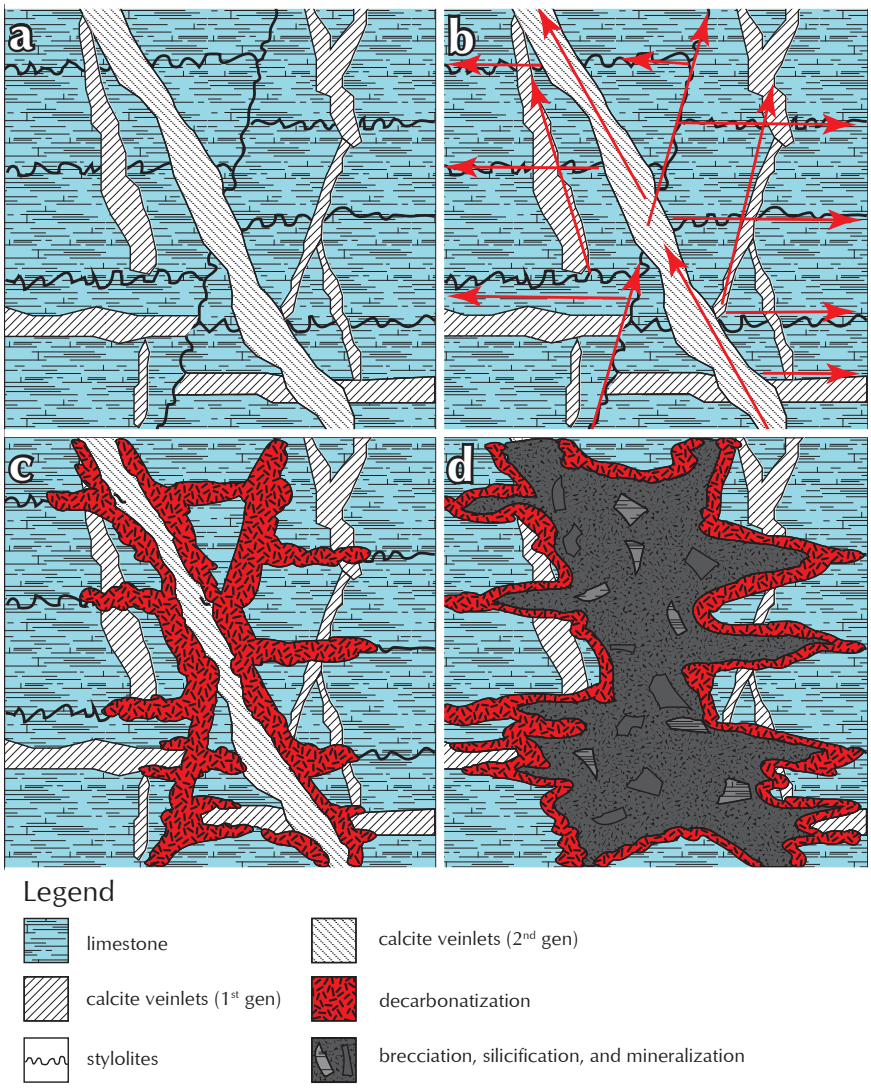

***Figure 12**. Fluid evolution model showing sequential stages of alteration and mineralization, including, (a) early deformation events modifying the original permeability structure of the host rock; (b) preferential fluid flow along early veins and stylolites; (c) early phase of decarbonatization along early fluid pathways; and (d) final stages of decarbonatization, mineralization, silicification and brecciation.*

decarbonatization, silicification, and subsequent gold deposition; realgar, orpiment, calcite, and fluorite are commonly observed as post mineralization open space minerals. The regional tectonic setting and local features at Conrad are similar to sediment hosted gold deposits found in the Carlin trend of Nevada in that gold is hosted in silty carbonate and intimately associated with arsenian pyrite growth rims around early pyrite. Based on detailed core logging, surface mapping, and laboratory work on both host rocks and mineralized zones we suggest the Conrad zone is a Carlin-type gold deposit.

ACKNOWLEDGEMENTS

The author would like to thank Rob Carne of ATAC Resources Ltd. for financial and logistical support of this project. Special thanks to Joan Carne and Julia Lane for their helpful geologic discussions and continued help and support through the duration of this project. The author would also like to thank Murray Allan for his many suggestions on how to improve this paper as well as Jim Mortensen for his critical review. Many thanks are owed to Patrick Sack of the YGS for his editorial assistance and suggestions on how to improve the quality of this paper.

REFERENCES

Abbott, J.G., Gordey, S.P., and Tempelman-Kluit, D.J., 1986. Setting of stratiform, sediment-hosted lead-zinc deposits in the Yukon and northeastern British Columbia. *In:* Mineral deposits of the northern Cordillera, J.A. Morin (ed.), Canadian Institute of Mining and Metallurgy, Special vol. 37, p. 1-18.

Arehart, G.B., 1996. Characteristics and origin of sediment-hosted disseminated gold deposits: a review. Ore Geology Reviews, vol. 11, p. 383-403.

ATAC Resources Ltd., 2012a. ATAC Resources Ltd. Intersects 42.93 m of 18.44 g/t Gold at its Rackla Gold Project – Yukon. August 21, 2012. Retrieved from http://www.atacresources.com/s/NewsReleases.asp. Web. August 21, 2012.

ATAC Resources Ltd., 2012b. ATAC Resources Drills 19.85 g/t Gold over 8.51 Metres at its Newest Carlin-type Gold Discovery Located 10 km West of Osiris. September 17, 2012. Retrieved from http://www.atacresources.com/s/NewsReleases.asp.Web. September 17, 2012.

ATAC Resources Ltd., 2012c. ATAC Resources Ltd. Drills 14.86 m of 10.54 g/t Gold at the New Sunrise Zone Discovery in the Osiris area of the Rackla Gold Project – Yukon. October 12, 2012. Retrieved from http://www.atacresources.com/s/NewsReleases.asp.Web. October 12, 2012.

Cline, J.S., Hofstra, A., Muntean, J.L., Tosdal, R.M., and Hickey, K.A., 2005. Carlin-Type Gold Deposits in Nevada: Critical Geologic Characteristics and Viable Models. Economic Geology 100th Anniversary Volume, p. 451-484.

Hart, J.R., Mair, J.L., Goldfarb, J.R., and Groves, I.G., 2004. Source and redox controls on metallogenic variations in intrusion-related ore systems, Tombstone-Tungsten Belt, Yukon Territory, Canada. Transactions of the Royal Society of Edinburgh. Earth Sciences, vol. 95, p. 339-356.

Kingston, S., Mortensen, J., Dumala, M., and Gabites, J., 2009. Ar-Ar geochronology and Pb isotopic constraints on the origin of the Rau gold-rich carbonate replacement deposit, central Yukon. *In*: Yukon Exploration and Geology 2009, K.E. MacFarlane, L.H. Weston, and L.R. Blackburn (eds.), Yukon Geological Survey, p. 213-222.

Mair, J.L., Hart, C.J.R., and Stephens, J.R., 2006. Deformation history of the northwestern Selwyn Basin, Yukon, Canada: Implications for orogeny evolution and mid-Cretaceous magmatism. Geological Society of America Bulletin, vol. 118, p. 304-323.

Muntean, J.L., Cline, J.S., Simon, A.C., and Longo, A.A., 2011. Magmatic-hydrothermal origins of Nevada's Carlin-type gold deposits. Nature, vol. 4, p. 122-127.

Stephens, J.R., Mair, J.L., Oliver, N.H.S., Hart, C.J.R., and Baker, T., 2004. Structural and mechanical controls on intrusion-related deposits of the Tombstone Gold Belt, Yukon, Canada, with comparisons to other vein-hosted ore-deposit types. Journal of Structural Geology, vol. 26, p. 1025-1041.

Thiessen, E.J., Gleeson, S.A., Dufrane, S.A., Carne, R.C., and Dumala, M., 2011. Upper age constraint and paragenesis of the Tiger zone, Rau property, central Yukon. *In*: Yukon Exploration and Geology 2011, K.E. MacFarlane and P.J. Sack (eds.), Yukon Geological Survey, p. 151-164.